

Stability of Hypervelocity Boundary Layers

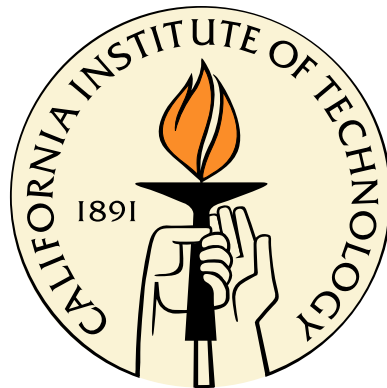
Thesis by

Neal Phillip Bitter

In Partial Fulfillment of the Requirements

for the Degree of

Doctor of Philosophy



California Institute of Technology

Pasadena, California

2015

(Defended May 15, 2015)

Abstract

The early stage of laminar-turbulent transition in a hypervelocity boundary layer is studied using a combination of modal linear stability analysis, transient growth analysis, and direct numerical simulation. Modal stability analysis is used to clarify the behavior of first and second mode instabilities on flat plates and sharp cones for a wide range of high enthalpy flow conditions relevant to experiments in impulse facilities. Vibrational nonequilibrium is included in this analysis, its influence on the stability properties is investigated, and simple models for predicting when it is important are described.

Transient growth analysis is used to determine the optimal initial conditions that lead to the largest possible energy amplification within the flow. Such analysis is performed for both spatially and temporally evolving disturbances. The analysis again targets flows that have large stagnation enthalpy, such as those found in shock tunnels, expansion tubes, and atmospheric flight at high Mach numbers, and clarifies the effects of Mach number and wall temperature on the amplification achieved. Direct comparisons between modal and non-modal growth are made to determine the relative importance of these mechanisms under different flow regimes.

Conventional stability analysis employs the assumption that disturbances evolve with either a fixed frequency (spatial analysis) or a fixed wavenumber (temporal analysis). Direct numerical simulations are employed to relax these assumptions and investigate the downstream propagation of wave packets that are localized in space and time, and hence contain a distribution of frequencies and wavenumbers. Such wave packets are commonly observed in experiments and hence their amplification is highly relevant to boundary layer transition prediction. It is demonstrated that such

localized wave packets experience much less growth than is predicted by spatial stability analysis, and therefore it is essential that the bandwidth of localized noise sources that excite the instability be taken into account in making transition estimates. A simple model based on linear stability theory is also developed which yields comparable results with an enormous reduction in computational expense. This enables the amplification of finite-width wave packets to be taken into account in transition prediction.

Contents

Abstract	iii
Contents	v
List of Figures	x
List of Tables	xv
1 Introduction	1
1.1 Motivation	1
1.2 Paths to transition	3
1.2.1 Receptivity	4
1.2.2 Linear Growth	5
1.2.3 Nonlinear Breakdown	6
1.3 Modal Instabilities	7
1.4 Non-modal Amplification	11
1.5 Wave Packets	12
1.6 Scope of present work	14
2 Physical Models	16
2.1 Governing Equations	18
2.2 Vibrational Nonequilibrium Modeling	18
2.3 Transport Properties	22
2.3.1 Thermal Conductivity	22
2.3.2 Viscosity	23

2.4	Dimensionless governing equations	24
3	Mean Flow Calculation	26
3.1	Boundary Layer Equations	26
3.1.1	Boundary Conditions	27
3.1.2	Freestream Flow Behavior	28
3.1.3	Coordinate transformation	31
3.1.4	Flow Timescales	32
3.2	Self-Similar Solutions	33
3.3	Non-Similar Solutions	36
3.4	Verification	38
3.4.1	Air	39
3.4.2	Carbon Dioxide	40
3.5	Mangler Transform	43
4	Modal Stability Analysis	48
4.1	Global Method	50
4.2	Local Method	54
4.2.1	Fundamental Solutions	55
4.2.2	Orthonormalization	58
4.3	Freestream Boundary Conditions	60
4.4	Model Verification	64
4.4.1	Low enthalpy flow	64
4.4.2	High enthalpy flow	64
4.4.3	Chemical Reactions	66
5	Modal Stability Results	69
5.1	Stability Characteristics	69
5.1.1	Dispersion curves	69
5.1.2	The N Factor	72
5.2	High and low enthalpy flows	75

5.3	Supersonic Unstable Modes	77
5.3.1	Shape of Dispersion Curve	77
5.3.2	Effect of Reynolds and Mach Numbers	83
5.4	Stability Trends in Air	84
5.4.1	Growth Rates	85
5.4.2	Scaling of instability parameters	87
5.4.3	Comparison with experiments	92
5.4.4	Stability map	94
5.5	Effects of Vibrational Nonequilibrium	94
5.5.1	Vibrational Relaxation in Air	95
5.5.2	Vibrational Relaxation in CO ₂	99
5.6	Vibrational Nonequilibrium Estimates	102
5.6.1	Vibrational energy fluctuations	103
5.6.2	Effective vibrational specific heat	105
5.6.3	Second Mode Frequency Estimates	106
5.6.4	Damköhler numbers	107
6	Transient Growth	111
6.1	Introduction	111
6.2	Background	111
6.3	Simple Transient Growth Example	114
6.4	Methodology	117
6.4.1	Energy Norm	118
6.4.2	Transient growth calculation	121
6.5	Results	124
6.5.1	Optimal Perturbations	124
6.5.2	Wall Cooling	129
6.5.3	Effects of Mach Number and Wall Temperature	131
6.5.4	Temporal vs. Spatial	132
6.5.5	Optimization for prescribed downstream distance	134

6.5.6	Effect of Energy Norm	136
6.5.7	Effect of Vibrational Nonequilibrium	139
6.5.8	Modal vs. Non-modal	143
7	Linearized DNS Calculations	147
7.1	Introduction	147
7.2	Previous Work	151
7.3	Governing Equations	155
7.4	Numerical Methods	159
7.4.1	Base Flow Solution	160
7.4.2	Boundary conditions	163
7.4.3	Convergence Study	167
7.5	Flow Conditions and Linear Stability Analysis	169
7.6	Validation	170
7.7	Results: Spatial DNS	175
7.8	Results: Second mode wave packets	177
7.9	Incoming Acoustic Wavepackets	189
7.9.1	Freestream waves	190
7.9.2	Receptivity considerations	193
7.9.3	Results	195
7.10	Simple Wave Packet Model	201
7.10.1	Equations of motion	202
7.10.2	Laplace Transform	203
7.10.3	Solutions near the initial point	205
7.10.4	Solutions away from the initial point	210
7.10.5	Single mode solution	213
7.10.6	Simplification	214
7.10.7	Results	216
7.11	Conclusion	221

8	Conclusions	223
8.1	Modal Stability Analysis	223
8.2	Transient Growth Analysis	226
8.3	Wave Packet Analysis	228
8.4	Future Work	230
	Bibliography	232
	Appendices	249
A	Stability Equations	250
A.1	General Linearized Stability Equations	251
A.2	Locally Parallel Flow	253
A.3	Normal Modes	255
A.4	Second order equations	259
A.5	First order equations	262
B	Mean Flow Jacobian	267
C	Multiple-Scales Model	272
C.1	Governing equations	272
C.2	Adjoint Boundary Conditions	278

List of Figures

1.1	Paths to transition	3
1.2	Pressure eigenfunctions for higher modes	9
1.3	Pressure contours for higher modes	10
1.4	Experimental measurements of wave packets	13
2.1	Limitations of chemically frozen analysis	17
2.2	Viscosity models	24
3.1	Vibrational relaxation in freestream	29
3.2	Simple model of relaxation in freestream	31
3.3	Verification of boundary layer code for air	39
3.4	Base flow profiles for low enthalpy CO ₂	41
3.5	Base flow profiles for high enthalpy CO ₂	42
4.1	Temporal and spatial global eigenvalue spectra	53
4.2	Comparison of eigenfunctions from local and global analysis	60
4.3	Effect of freestream boundary conditions on growth rates	62
4.4	Effect of freestream boundary conditions on eigenfunctions	63
4.5	Effect of freestream boundary conditions on streamwise velocity eigen- function	63
4.6	Low enthalpy validation of stability analysis	64
4.7	High enthalpy validation of stability analysis	66
4.8	Effect of chemistry on stability analysis	67
5.1	Low enthalpy dispersion curves	70

5.2	Low enthalpy growth rates	72
5.3	Low enthalpy stability diagram	73
5.4	Low enthalpy N factors	74
5.5	High enthalpy dispersion curve	76
5.6	Growth rates of supersonic unstable modes	78
5.7	Eigenfunctions of supersonic unstable modes	79
5.8	Temperature contours of supersonic unstable modes	80
5.9	Complex phase velocities of supersonic unstable modes	81
5.10	N factors of supersonic unstable modes	84
5.11	Effect of Mach number on supersonic unstable modes	85
5.12	Effect of Mach number and wall temperature on spatial growth rates for air	86
5.13	Effect of Mach number and wall temperature on second mode frequencies	88
5.14	Scaled dispersion curves	89
5.15	Scaled N factor curves	91
5.16	Effect of Mach number and wall temperature on 2D N factors	92
5.17	First and second mode stability map	95
5.18	Nonequilibrium base flow profiles for air	96
5.19	Effect of vibrational relaxation in base flow for air	97
5.20	Effect of vibrational relaxation in disturbances for air	98
5.21	Effects of vibrational relaxation in air for various Mach numbers and wall temperatures	99
5.22	Effect of vibrational relaxation in base flow for CO ₂	100
5.23	Effect of vibrational relaxation in disturbances for CO ₂	101
5.24	Schematic of relaxation times in a boundary layer	110
6.1	Modal growth example	115
6.2	Transient growth example	116
6.3	Verification of transient growth analysis	124
6.4	Energy growth for adiabatic boundary layers	125

6.5	Optimal disturbances for adiabatic boundary layers	126
6.6	Amplified disturbances for adiabatic boundary layers	126
6.7	Disturbance contours for adiabatic boundary layers	127
6.8	Modes participating in transient growth	129
6.9	Energy growth with $T_w/T_e = 1$	130
6.10	Energy growth with $T_w/T_e = 0.3$	130
6.11	Transient growth map	132
6.12	Spatial transient growth	133
6.13	Energy amplification at fixed downstream distance	135
6.14	Optimal disturbances for $x < x_{opt}$	136
6.15	Disturbance contours for $x < x_{opt}$	137
6.16	Effect of energy norm on transient growth	138
6.17	Effect of energy norm on optimal disturbance	139
6.18	Nonequilibrium base flow profiles for transient growth analysis	140
6.19	Effect of vibrational energy on transient growth	141
6.20	Effect of vibrational energy on optimal disturbances	141
6.21	Effect of vibrational energy on disturbance contours	142
6.22	Comparison of modal and non-modal growth at Mach 2.5	144
6.23	Comparison of modal and non-modal growth at Mach 0.5 and 5.0	146
7.1	Examples of experimental wave packet measurements	149
7.2	Examples of pressure fields from three DNS configurations	152
7.3	DNS flow domain	159
7.4	DNS convergence	168
7.5	Base flow profiles for linearized DNS	170
7.6	Stability characteristics for DNS conditions	171
7.7	Stability diagram for DNS conditions	171
7.8	Comparison of DNS vs LST for a parallel boundary layer	172
7.9	Verification of DNS	173
7.10	Comparison of phase speeds and growth rates from DNS and LST	175

7.11	Spatial DNS amplification	177
7.12	Spatial DNS growth rates and phase speeds	178
7.13	Initial conditions for second mode wave packet simulations	179
7.14	Pressure contours of second mode wave packet	180
7.15	X-t diagram for second mode wave packet	181
7.16	Amplification and frequency of second mode wave packet	182
7.17	Frequency of second mode wave packets on a stability diagram	183
7.18	Frequency and wavenumber spectra of second mode wave packet	184
7.19	Frequency spectrum on a stability diagram	185
7.20	Comparison of Fourier amplitude growth with spatial DNS	186
7.21	Pressure contours for wide wave packet	187
7.22	Pressure contours for narrow wave packet	188
7.23	Effect of wave packet width on amplitude growth	189
7.24	Initial condition and wavenumber spectrum for acoustic waves in freestream	193
7.25	Relationship between freestream acoustic waves and boundary layer modes	195
7.26	Pressure contours for boundary layer modes excited by fast acoustic waves	196
7.27	Pressure contours for boundary layer modes excited by slow acoustic waves	198
7.28	Amplification and frequency of second mode waves excited by slow acoustic waves from freestream	199
7.29	Pressure contours for second mode waves excited by a wide packet of slow acoustic waves	200
7.30	Effect of freestream wave width on second mode wave amplification	201
7.31	Initial pressure profiles from simple model	217
7.32	x-t diagram from simple wave packet model	218
7.33	Effect of wave packet width from simple wave packet model	219
7.34	Maximum N factor from simple wave packet model for fixed width of initial condition	220
7.35	Maximum N factor from simple wave packet model for fixed number of waves in initial condition.	221

8.1	Effect of Mach number and wall temperature on spatial growth rates	224
8.2	Schematic of relaxation times in a boundary layer	225
8.3	Dispersion curves for unstable supersonic modes	226
8.4	Transient growth map	227
8.5	Comparison between modal and non-modal N factors	228
8.6	Effect of wave packet width on amplification	229

List of Tables

2.1	Characteristic vibration temperatures and degeneracies for CO ₂ and air	20
2.2	Vibrational energy transfer rates for nitrogen and oxygen	21
2.3	Sutherland model for CO ₂ and air	23
5.1	Comparison of measured and computed second mode frequencies . . .	93
5.2	Typical Damköhler numbers for CO ₂ and air	108
6.1	Summary of temporal transient growth characteristics	127
7.1	Flow conditions for DNS	169

Chapter 1

Introduction

1.1 Motivation

Air-breathing hypersonic aircraft have the potential to offer access to space with many advantages over conventional, rocket-based launch systems. As detailed by [Bilardo et al. \(2003\)](#), these benefits include reductions in launch and maintenance costs, improvements in turn-around time, and increased reliability and mission flexibility. However, these benefits are accompanied by serious challenges which have thus far prevented air-breathing launch systems from being realized. One such challenge is coping with the enormous surface heating loads, which are much larger for the ascent trajectories of proposed air-breathing launch systems that take off horizontally than for conventional launch systems ([Tauber et al., 1987](#), [Bilardo et al., 2003](#)). The larger heating load anticipated for air-breathing vehicles is the result of extended flight at higher density, which is needed to develop sufficient thrust to accelerate to orbital speeds ([Tauber et al., 1987](#)).

These heating loads must be accommodated by a suitably-designed Thermal Protection System (TPS). Proposed air-breathing launch systems employ slender vehicles for which the heat transfer rate is governed by the flow characteristics within the thin boundary layer. The heat flux to the vehicle's surface depends strongly on whether the boundary layer flow is laminar or turbulent, with heating loads increasing by a factor of 2-10 for turbulent flow ([White, 1974](#), [Lin, 2008](#), [Lau, 2008](#)) in comparison to laminar flow. This must be taken into account to design an effective TPS, and

care must be taken to provide sufficient margins to accommodate uncertainties in the heating load while avoiding the extraneous weight of an overly-conservative design. Predicting the location or region over which transition to turbulence takes place is therefore a key design consideration, yet it remains extremely challenging to predict reliably. The difficulties in predicting hypersonic boundary transition lie in the enormous parameter space involved, the high sensitivity of boundary layer transition to each parameter, uncertainties regarding the disturbance environment that initiates transition, and the inherent complexity of the nonlinear processes involved in the final stages of transition to turbulence.

Because the subsystems of hypersonic aircraft are highly-integrated, boundary layer transition can have a significant influence on an overall vehicle design. As an example, boundary layer transition was identified as a major source of design uncertainty in the National Aerospace Plane (NASP) program, one of the early scramjet technology demonstrators. After reviewing the NASP program, the Defense Science Board found that aircraft designs based on different assumptions about the transition location differed by about a factor of two in takeoff weight ([Defense Science Board, 1988, 1992](#)). The members of the Defense Science Board concluded that “[Boundary layer transition] is by far the single area of greatest technical risk in the aerodynamics of the NASP program.” They furthermore recommended that “It would seem prudent to delay initiation of detailed vehicle design until that effort [a proposed analytical and experimental program] has narrowed the uncertainty in location of the transition point to an acceptable tolerance.” This project demonstrated how uncertainty in the prediction of boundary layer transition can impede the development of an entire aircraft system.

Since the end of the NASP program in the early 1990s, much progress has been made in the prediction of boundary layer transition. Because of the enormous increase in computational resources over the last two decades, boundary layer stability calculations can now be made for more complicated geometries, and various high-temperature phenomena can be included, such as chemical reactions and thermochemical nonequilibrium flow. However, even with modern computational tools

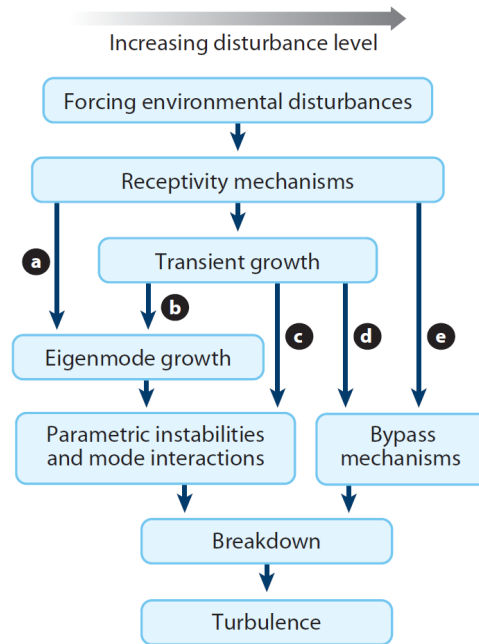


Figure 1.1: Diagram of pathways by which a boundary layer might transition to turbulence (reproduced with permission from Fedorov (2011)).

and massively-parallel computing facilities, high fidelity direct numerical simulation (DNS) of boundary layer transition remains infeasible for all but the simplest geometries and is far too expensive for use as a design tool. Instead, transition prediction is usually carried out using linear stability theory (LST), in which unstable, exponentially-growing eigenmodes of the linearized Navier-Stokes equations are identified, their growth rates are computed, and their amplification is correlated with boundary layer transition.

1.2 Paths to transition

The current understanding of boundary layer transition is graphically portrayed in Figure 1.1, which was originally conceived by Morkovin et al. (1994) and is reproduced here from Fedorov (2011). According to this framework, boundary layer transition consists of three stages, which are known as receptivity, linear growth, and nonlinear breakdown.

1.2.1 Receptivity

Interactions between environmental disturbances and the smooth, laminar boundary layer excite oscillatory modes within the boundary layer, a process which is called receptivity. These environmental disturbances can take the form of wall roughness, particle impacts, acoustic waves impinging from the freestream, or nonuniformities of the freestream velocity and temperature (vorticity and entropy spots). The extent to which these disturbance sources excite waves in the boundary layer depends on the frequency and wavelength of the disturbances and the local properties of the boundary layer.

For low speed boundary layers, there is a large disparity between the frequencies and length scales of boundary layer modes and the forcing of environmental disturbances in the freestream, and hence a scale-conversion mechanism is needed in order to excite the boundary layer modes (Saric et al., 2002). Potential scale-conversion mechanisms are wall roughness (Goldstein, 1985) and regions of the flow where the boundary layer thickness varies rapidly, such as near the leading edge of a plate or cone (Goldstein, 1983). In contrast, for high speed flows the boundary layer modes and freestream disturbances can have similar length scales and hence receptivity can potentially occur without such a scale conversion mechanism (Fedorov, 2003, Fedorov and Khokhlov, 1991, 1993).

Under flight conditions, acoustic waves in the freestream are known to have small amplitudes, so transition on smooth surfaces is thought to result from vorticity and entropy disturbances in the freestream. However, waves that are initially of the vorticity or entropy type can produce acoustic waves upon crossing the oblique shock wave at the leading edge of the body (McKenzie and Westphal, 1968), so all types of disturbances are relevant to boundary layer transition in free flight. Nevertheless, the amplitudes of forcing waves from the freestream in free flight are hypothesized to be quite small. Comparatively, in conventional wind tunnels the level of acoustic noise in the freestream is quite high, since the turbulent boundary layers that develop on the walls of the nozzle and test section radiate acoustic waves into the flow. Experiments

have demonstrated high sensitivity of transition measurements to the level of acoustic noise in the tunnel (Schneider, 2001, 2015), which suggests that the boundary layer transitions much earlier in wind tunnel experiments than it would in real flight. This has led to considerable difficulties in drawing meaningful conclusions about transition in real flight from ground-based measurements (Reshotko, 1976). A major source of difficulty is that current computational methods of predicting boundary layer transition, which are calibrated against experimental data, do not yet take into account the amplitudes or frequency spectra of environmental disturbances that participate in boundary layer transition. Therefore computational transition estimates that are calibrated against ground-based wind tunnel data are not predictive of transition in free flight.

Because environmental disturbances in the freestream feature a large parameter space of possible wave types, wavelengths, frequencies, and angles of incidence, the problem of receptivity remains largely unsolved for hypersonic boundary layers. No general framework for performing receptivity calculations exists, but many DNS calculations (Balakumar, 2009, Fedorov et al., 2013, Ma and Zhong, 2003a,b, 2005, Zhong and Ma, 2006) and asymptotic analyses (Fedorov and Khokhlov, 1991, 1993, Fedorov, 2003, Fedorov and Tumin, 2003) have clarified various features of the receptivity problem for simple geometries like a flat plate or sharp cone. Nevertheless, an enormous amount of work remains since the effects of realistic flow features on receptivity, such as angle of attack and boundary layer three-dimensionality, remain for the most part unexplored.

1.2.2 Linear Growth

After the small-amplitude, oscillatory modes in the boundary layer have been excited, they may amplify by a variety of different mechanisms as indicated in Figure 1.1. Path A refers to unstable modes of the boundary layer, which consist of a fixed mode shape that grows exponentially as it travels downstream. This path is called “modal growth” and has historically received the most attention in the literature, especially

for compressible flows.

Paths B, C, and D involve the transient growth, or non-modal growth, of disturbances. Unlike modal growth, this amplification mechanism involves a collection of boundary layer modes (an “optimal disturbance”) that are all damped, but superpose in such a way that their linear combination grows for a short time despite the eventual exponential decay of all modes involved. This amplification mechanism first began to be appreciated after the work of [Trefethen et al. \(1993\)](#), who showed that transient growth offers a potential transition mechanism for flows like Couette flow and pipe flow that are completely stable according to path A.

Paths B, C, and D in [Figure 1.1](#) refer to three different manifestations of transition growth. Path B describes the situation in which transient growth excites a mode that is linearly unstable, which then grows exponentially. This mechanism appears to not be important in boundary layers because unstable modes and optimal disturbances from transient growth have very different frequencies, wavenumbers, and mode shapes, and hence it is unlikely that optimal disturbances will strongly excite unstable modes. Nevertheless, in [Chapter 6](#), some examples of interactions between modal and non-modal amplification are observed. Path C refers to pure transient growth leading directly to secondary instabilities and production of nonlinear harmonic waves. Path D refers to the transient growth that occurs when a boundary layer is excited by a broad spectrum of disturbances rather than a particular optimal disturbance ([Reshotko, 2001](#)).

1.2.3 Nonlinear Breakdown

As the disturbances amplify according to the above-mentioned mechanisms, their amplitude eventually becomes large enough to modify the laminar flow profile and cause non-linear interactions between modes. Because of these nonlinear interactions, additional length and time scales are excited at harmonics of the dominant disturbance frequencies and the flow rapidly breaks down into the chaotic motion and broad-band frequency spectrum of turbulence. Path E in [Figure 1.1](#) accounts for disturbances

that are initially of such large amplitude that no amplification is needed in order to reach the nonlinear regime, which is often called bypass transition.

1.3 Modal Instabilities

The most widely-studied amplification mechanism for disturbances is modal instability, path A in Figure 1.1. Modal stability analysis was pioneered for incompressible flows by Rayleigh (1879, 1880), Tollmien (1936), and Lin (1944). Although linear stability theory was initially met with some skepticism, a significant advancement of the theory was made by the experiments of Schubauer and Skramstad (1947), who immersed a vibrating ribbon in an incompressible boundary layer and conclusively demonstrated the downstream growth of instability waves using hot wire measurements. Because they qualitatively confirmed many of the results predicted by linear stability theory, these experiments were largely responsible for the acceptance of linear stability theory as a useful description of the flow characteristics leading up to transition (Mack, 1977).

The first major theoretical effort to study linear instabilities in compressible boundary layers was undertaken by Lees and Lin (1946). Rayleigh (1879) and Tollmien (1936) had previously shown that incompressible flows are stable to inviscid, temporally-growing disturbances unless the mean velocity profile $\bar{U}(y)$ contains an inflection point, $\bar{U}'' = 0$, where primes designate differentiation in the wall normal direction. Lees and Lin (1946) extended this result to compressible flows by examining the balance of kinetic and internal energy integrated over the boundary layer. They showed that the 2D, inviscid boundary layer cannot be unstable unless the mean velocity and density profiles feature a generalized inflection point defined by:

$$\frac{\partial}{\partial y} \left(\bar{\rho} \frac{\partial \bar{U}}{\partial y} \right) = 0 \quad (1.1)$$

where y is the wall-normal height. Lees and Lin observed that when the wall is highly cooled, the laminar boundary layer over a flat plate or cone does not have a generalized

inflection point, which led to the remarkable conclusion that such boundary layers are absolutely stable under the action of inviscid disturbances. However, in arriving at this result Lees and Lin had to assume that the local Mach number of the disturbances relative to the mean flow velocity was everywhere less than one, and hence their analysis applies only to a subset of the possible modes in a boundary layer. In a subsequent paper, [Lees \(1947\)](#) extended his previous work to include the effects of viscosity, which can be important because Tollmien-Schlichting waves can be more unstable at finite Reynolds numbers than in the inviscid limit ([Lin, 1944](#)). Lees found that stabilization of the boundary layer by wall cooling was also possible at finite Reynolds numbers, a finding that was confirmed by the calculations of [Van Driest \(1952\)](#).

Only after [Mack \(1969, 1984, 1975, 1987\)](#) began to produce numerical simulations of the dispersion relation was it realized that an additional class of modes was also present in the boundary layer, and these so-called “Mack modes” could be highly unstable at high Mach numbers. These modes travel supersonically with respect to the mean flow over some portion of the boundary layer, thus violating the assumptions originally made by Lees and invalidating their proof that the boundary layer is completely stabilized by wall cooling. It has since been realized that the analyses of Lees and Lin only apply to compressible Tollmien-Schlichting waves, which Mack called “first mode” waves. The additional modes, which Mack called the “second mode” and “higher modes”, behave differently and in fact can experience growth rates that are many times larger than those of the Tollmien-Schlichting waves at high Mach numbers. Nevertheless, the prediction of Lees that compressible Tollmien-Schlichting waves are stabilized by wall cooling have indeed been born out for first mode waves ([Masad et al., 1992](#)).

The calculations of [Mack \(1969, 1984, 1975, 1987\)](#) revealed that the “Mack modes” are acoustic waves reflecting between the wall and the relative sonic line. This interpretation follows from the behavior of the disturbance pressure, which is shown in [Figure 1.2](#) for the first three of the acoustic modes. The quantity plotted in the figure is the real part of the complex pressure mode shape as a function of wall normal

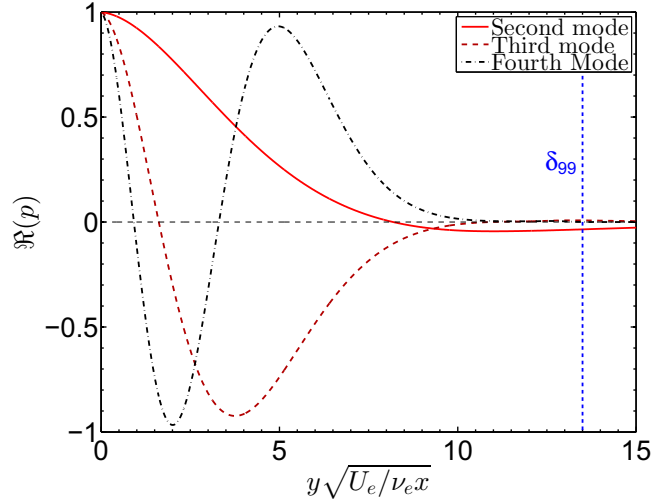


Figure 1.2: Pressure eigenfunctions for second, third, and fourth mode instabilities. Flow is air over a flat plate at Mach 5 with an adiabatic wall. Reynolds number is $Re_x = 4$ million.

distance y , and the flow is Mach 5 air flowing over a flat plate. As shown in the figure, the higher acoustic modes experience increasing numbers of oscillations inside the boundary layer, with each successive mode featuring an additional zero of the pressure mode shape.

These acoustic modes exist because the relative sonic line serves as an acoustic waveguide that traps the disturbances within the boundary layer (Fedorov, 2011). The disturbances propagate subsonically with respect to the mean flow above the relative sonic line and supersonically below it. As a result, acoustic waves transition from being oscillatory waves inside of the sonic line to being evanescent waves outside of it, which leads to a partial reflection of the wave back into the boundary layer.

This behavior is illustrated in Figure 1.3, which shows contours of the pressure mode shape for an unstable, second mode disturbance. The three dashed lines in the figure indicate the boundary layer thickness δ_{99} , the critical layer at which the real part of the disturbance phase velocity c_r equals the base flow velocity \bar{U} , and the relative sonic line $c_r = \bar{U} + \bar{a}$, where \bar{a} is the mean sound speed profile. The contour plot shows that the disturbance experiences a change in phase across the relative sonic line, which is indicative of the partial reflection of the wave back into the interior of

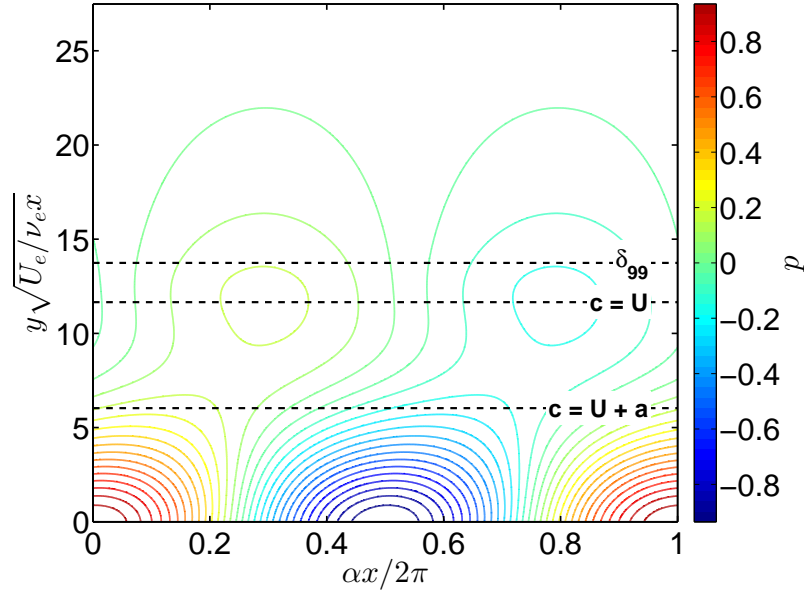


Figure 1.3: Contours of the pressure eigenfunction for second mode instability at Mach 5 with an adiabatic wall.

the boundary layer.

Unlike the Tollmien-Schlichting waves mentioned above which can be stabilized by wall cooling, the acoustic modes are destabilized, an effect which is mainly caused by the reduction in boundary layer thickness that occurs when the wall is cooled. This destabilization can be thought of in the following way: as the boundary layer becomes thinner, the wavelength of the second mode waves also decreases since they are reverberating within the boundary layer. The amplification per unit wavelength remains approximately constant, and hence the amplification per unit distance (the growth rate) increases as the boundary layer is made thinner, since there are more waves per unit distance. This explanation is demonstrated quantitatively in Section 5.4.2.

For boundary layer flows that have a high stagnation enthalpy, the temperature in the interior of the boundary layer can become large enough that the vibrational energy of polyatomic molecules becomes significant, such that the gas cannot be treated as calorically perfect. Dissociation reactions can also become significant at sufficiently high enthalpies. Furthermore, the rates of chemical reactions or vibrational-translational energy transfer can be comparable to flow timescales, leading to a nonequilibrium flow. A number of researchers have considered these nonequilib-

rium flow effects on the stability of boundary layers, and in some cases conflicting results were obtained. For example, [Hudson et al. \(1997\)](#) concluded that “...thermal nonequilibrium has a destabilizing effect”, whereas [Bertolotti \(1998\)](#) determined that “Vibrational relaxation has a large destabilizing influence.” [Johnson et al. \(1998\)](#) concluded that “translational-vibrational energy transfer can be either stabilizing or destabilizing.” As will be shown in Chapter 5, vibrational relaxation produces two competing effects which can result in net stabilization or destabilization, depending on the flow conditions. Chapter 5 investigates these mechanisms and clarifies the flow conditions under which net stabilization or destabilization can be expected.

1.4 Non-modal Amplification

Although initial efforts to predict transition to turbulence focused on the modal instability mechanisms described above, it was soon realized that modal instabilities could not explain all the phenomena observed in experiments. In particular, certain canonical flows, such as pipe flow and Couette flow, have no unstable modes, and yet transition to turbulence is readily achieved in experiments ([Schmid and Henningson, 2001](#)). Other flows, like plane Poiseuille flow, transition at low Reynolds numbers for which the linear theory predicts that the flow is stable.

It was eventually realized that modal analysis only takes into account the long-time fate of disturbances, which may be exponentially growing or decaying, but entirely neglects their short-time dynamics. [Ellingsen and Palm \(1975\)](#) was one of the first to report the growth of disturbances in flows that are exponentially stable. Similar results were obtained by [Landahl \(1980\)](#) and [Hultgren and Gustavsson \(1981\)](#), who showed that inviscid parallel shear flows can experience a particular class of linearly-growing disturbances. Such algebraic growth of disturbances was subsequently popularized by [Trefethen et al. \(1993\)](#), who developed a framework for analyzing algebraically-growing disturbances. This type of amplification is now referred to by the names “non-modal amplification” or “transient growth.”

Transient growth of disturbances is usually largest when streamwise vortical per-

turbations appears in the flow, for instance, behind a small, sharp-edged roughness element. The vertical velocity generated by these vortices then carries low momentum fluid up from the wall and high momentum fluid down from the freestream, thereby producing streaks of high and low streamwise velocity. The existence of this mechanism has been demonstrated in experiments involving roughness elements placed in incompressible boundary layers. Such experiments have reproduced many features predicted by transient growth calculations, including the downstream evolution of disturbance kinetic energy and the shape of the amplified disturbances (White, 2002, White et al., 2005, Ergin and White, 2006).

1.5 Wave Packets

Time traces from hot wire probes, pressure transducers, and interferometers have shown that in hypersonic wind tunnel experiments the second mode instability waves leading up to boundary layer transition consist of many isolated, localized wave packets. A good example of this was reported by Heitmann et al. (2011) and is reproduced in Figure 1.4. Although that paper also considered the excitation of disturbances using laser-generated shock waves, the traces shown in Figure 1.4 correspond to “natural” transition of the boundary layer. Two packets of second mode waves are clearly visible in the time traces, and similar results have been observed in many other experiments. Pulsed laser Schlieren photographs of high speed boundary layers have also captured full-field images of disturbance wave packets of this type (Parziale, 2013, Laurence et al., 2012, 2014, Casper et al., 2013a,b). These images show that the structure of these wave packets, including the wavelength and wall-normal density profile, closely matches the predictions of linear stability theory, indicating that these are indeed packets of second mode instability waves.

If boundary layer transition is triggered by a succession of isolated wave packets, as is suggested by Figure 1.4 and many other similar results, then the amplification of a particular wave packet moving downstream is highly relevant for transition prediction. Although both experimental (Gaster and Grant, 1975, Cohen et al., 1991, Cohen,

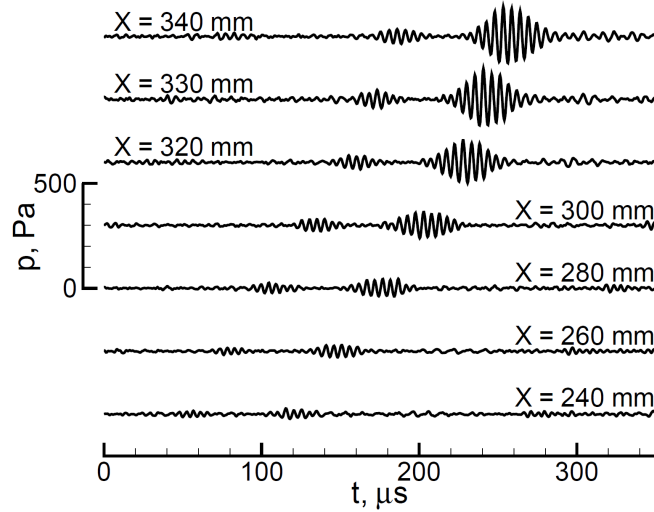


Figure 1.4: Experimental surface pressure traces for flow over a sharp cone at Mach 6, reproduced with permission from [Heitmann et al. \(2011\)](#).

1994) and theoretical ([Gaster, 1975, 1982a,b](#)) studies of wave packet development exist for incompressible boundary layers, these efforts have never been extended to high speed flow. In spite of the fact that wave packets frequently appear in hypersonic flow experiments, their downstream evolution has never been analyzed and reported. Instead, the data sets are usually Fourier-transformed and the downstream growth of individual Fourier modes is reported. Only a few direct numerical simulations, such as those of [Mayer et al. \(2011\)](#) and [Sivasubramanian and Fasel \(2014\)](#), have considered packets of waves. Like the experiments, these simulations deal primarily with the amplification of Fourier modes rather than the growth of the wave packet in physical space. Theoretical analysis by [Forgoston and Tumin \(2006\)](#) did consider the propagation of a physical wave packet, but only in a perfectly parallel boundary layer, so they could not analyze the development of the wave packet over large downstream distances for which boundary layer growth is significant.

Because there have been no detailed studies of wave packet propagation in non-parallel, compressible boundary layers, it is unknown how wave packets develop, how their amplification relates to linear stability theory, or ultimately how their development influences boundary layer transition. Current methods of predicting boundary layer transition are based entirely on the downstream amplification of Fourier modes,

rather than on the amplification of physical wave packets. However, Figure 1.4 suggests that wave packet amplification may in fact be more relevant to boundary layer transition than that of Fourier modes. There is of course a connection between these two points of view, since the wave packet itself consists of an integration over many modes, each corresponding to a particular frequency. However, using knowledge of the Fourier mode amplification to reconstruct the wave packet evolution has not been attempted for compressible flow. In Chapter 7, linearized direct numerical simulations (LDNS) are used to clarify the downstream evolution of second mode wave packets.

1.6 Scope of present work

This work is divided into three parts, which focus on the three mechanisms of disturbance amplification described above. After the physical models and base flow calculation are described in Chapters 2-3, the first mechanism, modal instability, is investigated in Chapters 4 and 5. The results presented in Chapter 5 significantly extend the set of flow conditions for which linear stability calculations are available, and this comprehensive assessment of the stability characteristics enables several new trends to be identified. The influence of vibrational nonequilibrium on the stability results is also discussed in detail, and simplified yet predictive models that clarify the various nonequilibrium processes involved are discussed.

The second mechanism of disturbance amplification, transient growth, is investigated in Chapter 6. The simulations detailed in that chapter again provide unprecedented coverage of the parameter space and the identification of new trends. Of particular value are results relevant to experiments in high enthalpy impulse facilities, for which transient growth calculations have not been made in the past. Direct comparisons between modal and non-modal growth are also carried out to clarify the relative importance of these mechanisms in different flow regimes.

The third mechanism of disturbance amplification is the downstream propagation of localized wave packets. Although these packets involve the same modal instability mechanism from Chapter 5, the wave packet evolution combines results from

many different frequencies, which obscures the connection with spatial linear stability theory. Chapter 7 clarifies the downstream evolution of linear wave packets in the boundary layer over a flat plate using linearized DNS, and a simple model is proposed that enables wave packet evolution to be accounted for in transition prediction.

Chapter 2

Physical Models

This chapter describes the governing equations, thermochemical models, and transport properties that are used to simulate the gasdynamics of high enthalpy compressible flows. The focus is on gas mixtures containing nitrogen, oxygen, and carbon dioxide. Nitrogen and oxygen are chosen because of the many engineering applications involving air, and carbon dioxide is chosen because of its large vibrational energy capacity and short relaxation time, which make highly nonequilibrium flow situations possible at relatively modest flow enthalpies. This enhances the influence of nonequilibrium processes on boundary layer transition and enables the physics involved to be more easily characterized.

In this work, vibrational nonequilibrium is included in the modeling, but chemical reactions are neglected. This limits the peak temperatures for which the present model is applicable. A simple estimate of the temperature limitation can be found by comparing the enthalpy h_{fr} of a chemically inert gas with the enthalpy h_{eq} under conditions of thermal equilibrium:

$$err = \frac{h_{eq} - h_{fr}}{h_{eq}} \quad (2.1)$$

This metric compares the energy released by dissociation reactions to the total energy of the flow, and hence is an estimate of the maximum relative error in enthalpy that could be incurred by neglecting chemistry. The results obtained depend on the reference enthalpy used in calculating Equation 2.1; here we set the enthalpies to zero

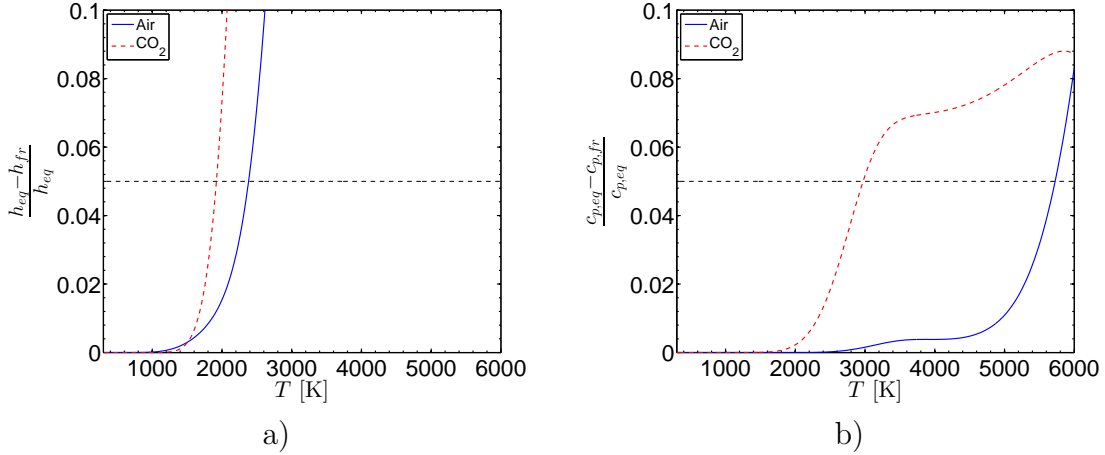


Figure 2.1: a) Relative difference in enthalpy for chemically frozen (h_{fr}) and chemical equilibrium (h_{eq}) gases. Pressure is 20 kPa. Enthalpies are zero at 300 K. b) Relative difference in c_p of chemically frozen ($c_{p,fr}$) and chemical equilibrium ($c_{p,eq}$) gases at 20 kPa.

at 300 K, and the results have been found to be reasonably insensitive to this choice. Equation 2.1 is plotted in Figure 2.1a as a function of temperature for air and CO₂. The results suggest that the chemically frozen analysis will be acceptable up to about 2400 K for air and 1900 K for CO₂, which are the temperatures at which the enthalpy error first reaches 5%. These estimates depend slightly on the pressure, which was taken to be 20 kPa. The results of Figure 2.1 were calculated using the Cantera software package (Goodwin, 2003) with reaction data taken from a high temperature version of the GRI30 mechanism, which extends its range to 6000 K.

For stability analysis, in which the equations of motion are linearized about a base configuration, the specific heat c_p is more important than the actual enthalpy of the flow. This is because one is interested in fluctuations in enthalpy rather than its absolute magnitude. Figure 2.1b shows the relative difference between the c_p of chemically frozen and equilibrium flows. It is observed that the assumption of chemically frozen flow results in much smaller errors for the c_p than for the enthalpy. This suggests that the chemically frozen assumption may perform better in stability analysis than in calculating a mean boundary layer profile. This possibility is explored in Section 4.4.3, where chemically frozen stability calculations are compared with a reacting analysis.

2.1 Governing Equations

For a chemically inert gas mixture, the nonlinear equations describing the transport of mass, momentum, vibrational energy, and total energy are the following (Park, 1990):

$$\frac{\partial \rho^*}{\partial t^*} + \nabla \cdot (\rho^* \mathbf{u}^*) = 0 \quad (2.2a)$$

$$\rho^* \frac{D\mathbf{u}^*}{Dt^*} + \nabla p^* = \nabla \cdot \boldsymbol{\tau}^* \quad (2.2b)$$

$$\rho^* \frac{De_v^*}{Dt^*} = -\nabla \cdot \mathbf{q}_v^* + Q^* \quad (2.2c)$$

$$\rho^* \frac{Dh_{tr}^*}{Dt^*} + \rho^* \frac{De_v^*}{Dt^*} - \frac{Dp^*}{Dt^*} = -\nabla \cdot (\mathbf{q}_{tr}^* + \mathbf{q}_v^*) + \boldsymbol{\tau}^* : \nabla \mathbf{u}^* \quad (2.2d)$$

Here asterisks denote dimensional quantities, boldface symbols refer to vectors, and $\boldsymbol{\tau}$ is the viscous stress tensor. The system is closed by the equation of state:

$$p^* = \rho^* \mathcal{R}^* T^* \quad (2.3)$$

Thermal nonequilibrium is included in the model by dividing the flow enthalpy into a translational/rotational enthalpy h_{tr}^* and a vibrational energy e_v^* . Likewise, the heat flux vector is split into a vibrational part \mathbf{q}_v^* and a translational part \mathbf{q}_{tr}^* . The exchange of energy between translational and vibrational modes is taken into account by the source term Q^* .

2.2 Vibrational Nonequilibrium Modeling

It is convenient to express the vibrational energy e_v^* in terms of a vibrational temperature T_v^* . The relationship between these two variables is defined using equilibrium statistical mechanics and treating molecules as simple harmonic oscillators (Vincenti and Kruger, 1967). Under conditions of thermal equilibrium, the flow is characterized by a single temperature T^* , and this temperature is related to the vibrational energy

by:

$$e_v^* = \frac{g\mathcal{R}^*\Theta_v^*}{e^{\Theta_v^*/T^*} - 1} \quad (2.4)$$

This equation provides a monotonic, invertible relationship between vibrational energy and the temperature. Therefore we define the temperature in Equation 2.4 to be the vibrational temperature T_v^* . The vibrational temperature simply parameterizes the vibrational energy while satisfying the intuitive property that the translational and vibrational temperatures should be equal under conditions of thermal equilibrium.

In Equation 2.4, \mathcal{R}^* is the gas constant, g is the degeneracy of the vibration mode, and Θ_v^* is the characteristic temperature of the vibration mode. Symmetric diatomic molecules like N_2 and O_2 have a single vibrational mode with a degeneracy of 1, whereas more complicated polyatomic molecules like CO_2 can have multiple vibrational modes with degeneracies greater than 1. Carbon dioxide is a linear, triatomic molecule which has three modes of vibration: symmetric stretching along its axis, asymmetric stretching along its axis, and bending transverse to its axis. The last of these modes has a degeneracy of $g = 2$ since transverse bending can occur along two orthogonal planes. The multiplicity of vibrational modes gives carbon dioxide the ability to store a larger fraction of its total internal energy in vibrational modes compared to diatomic molecules. Table 2.1 lists the characteristic vibration temperatures and degeneracies relevant to mixtures of carbon dioxide and air.

The total vibrational energy of a gas mixture is computed by summing Equation 2.4 over all species and all vibrational energy modes, weighting the sum by the species mass fractions Y .

$$e_v^* = \sum_{i=1}^{n_{sp}} \sum_{m=1}^M Y_i \frac{g_m \mathcal{R}_i^* \Theta_{v,i,m}^*}{\exp(\Theta_{v,i,m}^*/T_v^*) - 1} \quad (2.5)$$

In this equation the species is indexed by i and the vibrational modes (of which there are M total) are indexed by m . The model used in Equation 2.5 assumes that

Table 2.1: Characteristic vibration temperatures and degeneracies for carbon dioxide (McQuarrie, 1976) and air (Vincenti and Kruger, 1967).

Species	Mode	g	Θ_v^* (K)
N ₂	1	1	3390
O ₂	1	1	2270
CO ₂	1	2	960
	2	1	1997
	3	1	3382

the vibrational energy states of each molecule satisfy a Boltzmann distribution characterized by the vibrational temperature T_v^* . By using a single value of T_v^* during this summation, one also assumes that all species share the same vibrational temperature, T_v^* . This is true only if the rate of vibration-vibration (V-V) energy exchange between unlike molecules (e.g., N₂ and O₂) is much faster than vibration-translation (V-T) energy exchange.

Taylor and Bitterman (1969) compiled vibrational energy transfer rates for a number of different vibrational energy exchange processes involving mixtures of carbon dioxide and air. Selected energy exchange rates are listed in Table 2.2 at temperatures of 1000 - 3000 K, which represents the range of temperatures of interest in this study. In the reactions listed in this table, asterisks are used to designate vibrationally excited states and M is either N₂ or O₂; each of these molecules deactivates nitrogen and oxygen at a similar rate, so only one rate is given in the table. The tabulated data reveal that V-V transfer between N₂ and O₂ is several orders of magnitude faster than V-T transfer for N₂, but is slightly slower than V-T transfer for O₂. This suggests that for pure air, the use of a single vibrational temperature is a reasonable first approximation, but more accurate results would be obtained if separate vibrational temperatures were used and the V-V exchange process were explicitly included in the model. For simplicity, a single vibrational temperature is assumed here.

With the assumption of a single vibrational temperature, the rate Q^* of V-T energy exchange is computed using the Landau-Teller model (Vincenti and Kruger,

Table 2.2: Vibrational energy transfer rates for several V-V and V-T processes relevant to high temperature air. Data from [Taylor and Bitterman \(1969\)](#).

Reaction	Rate at 1000 K [cm ³ /s]	Rate at 2000 K [cm ³ /s]	Rate at 3000 K [cm ³ /s]
N ₂ [*] + M ⇌ N ₂ + M	< 10 ⁻¹⁷	4 × 10 ⁻¹⁶	4 × 10 ⁻¹⁵
O ₂ [*] + M ⇌ O ₂ + M	2 × 10 ⁻¹⁵	4 × 10 ⁻¹⁴	2 × 10 ⁻¹³
N ₂ [*] + O ₂ ⇌ N ₂ + O ₂ [*]	6 × 10 ⁻¹⁶	8 × 10 ⁻¹⁵	4 × 10 ⁻¹⁴

1967, [Park, 1990](#)):

$$Q^* = \rho^* \sum_{i=1}^{n_{sp}} Y_i \frac{e_{v,i}^*(T^*) - e_{v,i}^*(T_v^*)}{\tau_i^*} \quad (2.6)$$

Here Y_i is the species mass fraction and τ_i^* is the effective relaxation time for species i , which accounts for collisions between molecules of type i and all other types of molecules. The effective relaxation time τ_i^* is given by ([Millikan and White, 1963](#)):

$$\tau_i^* = \left[\sum_{j=1}^{n_{sp}} \frac{X_j}{\tau_{ij}^*} \right]^{-1} \quad (2.7)$$

where X_i is the mole fraction of species i and τ_{ij}^* is the relaxation time for a dilute species i in an isothermal bath of molecules j . For N₂ and O₂, the relaxation time is computed using the correlations of [Millikan and White \(1963\)](#). They fitted the relaxation times with a semi-empirical relation of the form:

$$\ln(\tau_{ij}^* p^*) = A_{ij} T^{*-1/3} + B_{ij} \quad (2.8)$$

where A_{ij} and B_{ij} are constants which are determined based on the collision partners involved. [Millikan and White \(1963\)](#) experimentally determined the following correlations for these coefficients:

$$A_{ij} = 1.16 \times 10^{-3} \sqrt{\mu_{ij}} \Theta_{v,i}^{*4/3} \quad (2.9a)$$

$$B_{ij} = -0.015 A_{ij} \mu_{ij}^{1/4} - 18.42 \quad (2.9b)$$

where Θ_v^* is the vibrational activation temperature and μ_{ij} is the reduced mass of the colliding pair based on the molecular weights W :

$$\mu_{ij} = \frac{W_i W_j}{W_i + W_j}$$

The model above is used for air, but for pure carbon dioxide the values of A and B are determined instead from the experimental measurements of [Camac \(1966\)](#). These measurements are more accurate than the correlation of [Millikan and White \(1963\)](#), which was intended primarily for diatomic molecules.

2.3 Transport Properties

2.3.1 Thermal Conductivity

With the assumption of a single vibrational temperature, the vibrational and translational heat flux vectors can be written in terms of the temperature gradients:

$$\mathbf{q}_v^* = -k_v^* \nabla T_v^* \quad (\text{Translational/rotational}) \quad (2.10a)$$

$$\mathbf{q}_{tr}^* = -k^* \nabla T^* \quad (\text{Vibrational}) \quad (2.10b)$$

where k^* is the translational thermal conductivity and k_v^* is its vibrational counterpart. For each species, the thermal conductivity is evaluated using Eucken's relation ([Vincenti and Kruger, 1967](#)), in which the total conductivity is split into translational/rotational and vibrational parts:

$$k_i^* = \frac{5}{2} \mu_i^* c_{v,tr,i}^* \quad (2.11a)$$

$$k_{v,i}^* = \mu_i^* c_{v,v,i}^* \quad (2.11b)$$

Here $c_{v,tr,i}$ is the translational/rotational specific heat of species i and $c_{v,v,i}$ is its vibrational specific heat. After evaluating the thermal conductivities for each species, the effective conductivity of the mixture is obtained using Wilke's mixing rule ([Wilke,](#)

Table 2.3: Sutherland model coefficients fitted to data of [Cole and Wakeham \(1985\)](#) and [Trengove and Wakeham \(1987\)](#).

Species	μ_{ref} [$\mu\text{Pa}\cdot\text{s}$]	T_{ref} [K]	S [K]
N ₂	18.50	300	123.8
O ₂	21.28	300	153.4
CO ₂	15.14	300	266.5

1950). At low temperatures, the vibrational thermal conductivity vanishes and the Prandtl number reduces to a constant value of 0.737.

2.3.2 Viscosity

Separate viscosity models are needed for each species in order to apply Eucken’s relation in Equation 2.11. Sutherland models for N₂ and O₂ were deduced by fitting Sutherland’s coefficient to the correlations of [Cole and Wakeham \(1985\)](#), which are suitable for the temperature range of 110-2100 K for nitrogen and 110-2500 K for oxygen. For carbon dioxide, the Sutherland model was fitted to the data of [Trengove and Wakeham \(1987\)](#), which is valid for $200 < T < 1500$ K. Values of the fitted coefficients are given in Table 2.3 and conform to Sutherland’s model in the form:

$$\frac{\mu}{\mu_{ref}} = \left(\frac{T}{T_{ref}} \right)^{3/2} \frac{S + T_{ref}}{S + T} \quad (2.12)$$

After determining the species viscosities from the Sutherland models mentioned above, the viscosity of the mixture is calculated using Wilke’s mixing rule. To verify that mixture viscosity calculated in this way is suitable, the mixture viscosity is compared for air with the measurements of [Kadoya et al. \(1985\)](#) in Fig. 2.2. The agreement is within 4% over the temperature range 85-2000 K. Also shown in the figure are the commonly-used viscosity model of [White \(1974\)](#) (originally from [Hilsenrath \(1955\)](#)), which is accurate only for low temperatures, and the viscosity model used in the Cantera software package ([Goodwin, 2003](#)).

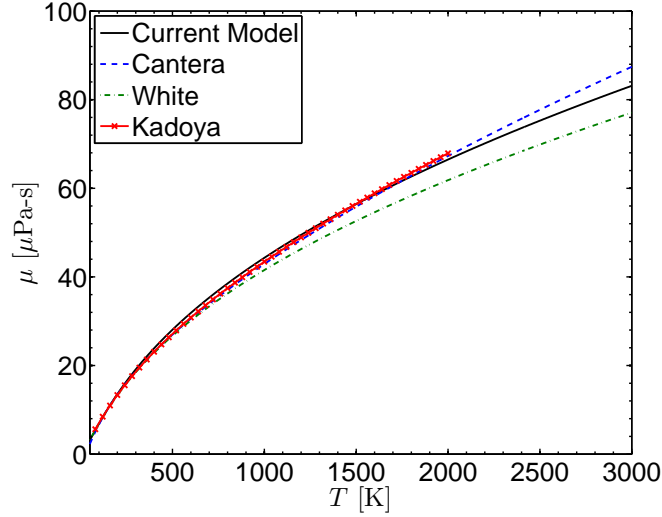


Figure 2.2: Comparison of current viscosity model with several other models. Cantera: Viscosity determined by Cantera using chemically frozen air with GRI30 mechanism. White: Sutherland model given by [White \(1974\)](#). Kadoya: empirical correlations determined by [Kadoya et al. \(1985\)](#).

2.4 Dimensionless governing equations

Equations [2.2](#) are made dimensionless using the following nondimensional variables:

$$\begin{aligned} \rho &= \frac{\rho^*}{\rho_e^*} & T &= \frac{T^*}{T_e^*} & T_v &= \frac{T_v^*}{T_e^*} & \mathbf{u} &= \frac{\mathbf{u}^*}{U_e^*} & p &= \frac{p^*}{\rho_e^* U_e^{*2}} & t &= \frac{t^* U_e}{L^*} \\ c_{v,v} &= \frac{c_{v,v}^*}{c_{p,tr}^*} & \mathbf{x} &= \frac{\mathbf{x}^*}{L^*} & k &= \frac{k^*}{k_e^*} & k_v^* &= \frac{k_v^*}{k_e^*} & \tau &= \frac{\tau^*}{\mu_e^* U_e^* / L^*} & Q &= \frac{Q^* \nu_e^*}{\rho_e^* c_{p,tr}^* T_e^* U_e^{*2}} \end{aligned} \quad (2.13)$$

In these equations, subscript e refers to the edge conditions and L^* is a reference length. The translational specific heat $c_{p,tr}^*$ is a constant since the gas composition is fixed. The vibrational source term Q is nondimensionalized using the volumetric energy density $\rho_e^* c_{p,tr}^* T_e^*$ and the timescale ν_e^* / U_e^{*2} .

After re-writing the governing equations ([2.2](#)) in terms of these nondimensional parameters and subtracting the vibrational energy equation from the total energy

equation, the result is:

$$\frac{\partial \rho}{\partial t} + \nabla \cdot (\rho \mathbf{u}) = 0 \quad (2.14a)$$

$$\rho \frac{D\mathbf{u}}{Dt} + \nabla p = \frac{1}{Re_L} \nabla \cdot \boldsymbol{\tau} \quad (2.14b)$$

$$\rho c_{v,v} \frac{DT_v}{Dt} = \frac{1}{Re_L \sigma_e} \nabla \cdot (k_v \nabla T_v) + Re_L Q \quad (2.14c)$$

$$\begin{aligned} \rho \frac{DT}{Dt} - M^2(\gamma_e - 1) \frac{Dp}{Dt} &= \frac{1}{Re_L \sigma_e} \nabla \cdot (k \nabla T) \\ &+ \frac{M^2(\gamma_e - 1)}{Re_L} (\boldsymbol{\tau} : \nabla \mathbf{u}) - Re_L Q \end{aligned} \quad (2.14d)$$

$$\gamma_e M^2 p = \rho T \quad (2.14e)$$

Here M is the frozen Mach number in the freestream, $\sigma_e = c_{p,tr}^* \mu_e^* / k_e^*$ is the Prandtl number, γ_e is the ratio of frozen specific heats, and Re_L is the Reynolds number. The equations for the vibrational and translational temperatures are coupled only by the vibrational source term Q (c.f. Equation 2.6) and the dependence of k_v on the temperature T . The dimensionless equations (2.14) form the basis of the mean flow calculations and stability analysis presented in the chapters that follow.

Chapter 3

Mean Flow Calculation

The first step in the linear stability analysis is to compute the steady, laminar base flow for which the stability characteristics are desired. For flows having low stagnation enthalpy, the classical similarity solution obtained using the Levy-Lees transformation ([Schlichting and Gersten, 2000](#)) provides an excellent representation of the flow over a flat plate. However, flows at higher stagnation enthalpies can experience thermal and/or chemical non-equilibrium and similarity solutions are no longer admissible. In this chapter, a method for computing boundary layer profiles in thermal non-equilibrium flows over flat plates and cones is described.

3.1 Boundary Layer Equations

By applying Prandtl's boundary layer scaling arguments ([Schlichting and Gersten, 2000](#)) and assuming zero pressure gradient, the compressible Navier-Stokes equations

(2.14) are reduced to the boundary-layer equations:

$$\frac{\partial}{\partial x}(\bar{\rho}\bar{U}) + \frac{\partial}{\partial y}(\bar{\rho}\bar{V}) = 0 \quad (3.1a)$$

$$\bar{\rho}\bar{U}\frac{\partial\bar{U}}{\partial x} + \bar{\rho}\bar{V}\frac{\partial\bar{U}}{\partial y} = \frac{1}{Re_L}\frac{\partial}{\partial y}\left(\bar{\mu}\frac{\partial\bar{U}}{\partial y}\right) \quad (3.1b)$$

$$\begin{aligned} \bar{\rho}\left(\bar{U}\frac{\partial\bar{T}}{\partial x} + \bar{V}\frac{\partial\bar{T}}{\partial y}\right) &= \frac{1}{Re_L\sigma_e}\frac{\partial}{\partial y}\left(\bar{k}\frac{\partial\bar{T}}{\partial y}\right) \\ &+ \frac{(\gamma_e - 1)M^2}{Re_L}\bar{\mu}\left(\frac{\partial\bar{U}}{\partial y}\right)^2 - Re_L\bar{Q} \end{aligned} \quad (3.1c)$$

$$\bar{\rho}\bar{c}_{v,v}\left(\bar{U}\frac{\partial\bar{T}_v}{\partial x} + \bar{V}\frac{\partial\bar{T}_v}{\partial y}\right) = \frac{1}{Re_L\sigma_e}\frac{\partial}{\partial y}\left(\bar{k}_v\frac{\partial\bar{T}_v}{\partial y}\right) + Re_L\bar{Q} \quad (3.1d)$$

where over-bars are used to indicate mean flow quantities. These are the classical compressible boundary layer equations supplemented by a vibrational energy equation (3.1d) and a vibrational source term $Re_L\bar{Q}$ which couples the two energy equations.

3.1.1 Boundary Conditions

The velocity boundary conditions at the wall are $\bar{U} = \bar{V} = 0$. For temperature, the two most common boundary conditions at the wall are those of isothermal and adiabatic flow:

$$\bar{T}(0) = T_w \quad (\text{Isothermal}) \quad (3.2a)$$

$$\bar{k}_v\frac{\partial\bar{T}_v}{\partial y}\Big|_{y=0} + \bar{k}\frac{\partial\bar{T}}{\partial y}\Big|_{y=0} = 0 \quad (\text{Adiabatic}) \quad (3.2b)$$

Here T_w is an imposed wall temperature. The adiabatic or isothermal condition by itself is insufficient to completely specify the problem, and an additional boundary condition relating the vibrational and translational temperatures at the wall is required. A common assumption is that the wall catalyzes energy exchange between translational and vibrational modes, such that $\bar{T}_v(0) = \bar{T}(0)$, and this assumption is adopted in this work. There is, however, some evidence that a slip condition on the vibrational temperature can develop at the wall for conditions that are relevant

to high enthalpy shock tunnels. For example, [Nompelis et al. \(2003\)](#) found that a vibrational temperature slip was needed to match experimentally measured heat flux data in double-cone experiments.

The relevant boundary conditions in the freestream are that the flow variables approach their edge values:

$$\begin{aligned}\bar{U} &= 1 \\ \bar{T} &= 1 \\ \bar{T}_v &= T_{v,e}^*/T_e^*\end{aligned}\quad y \rightarrow \infty \quad (3.3)$$

The form of the boundary condition on \bar{T}_v arises from the fact that all temperatures are nondimensionalized using the edge translational temperature T_e^* .

3.1.2 Freestream Flow Behavior

It must be noted that the freestream flow is not necessarily uniform in the streamwise direction. For example, in a reflected shock tunnel as the gas from the high temperature reservoir expands through the nozzle, the translational temperature can decrease much more rapidly than the vibrational temperature, leading to a “vibrationally hot” flow with $T_{v,e}^* > T_e^*$. These two edge temperatures gradually approach one another as one moves downstream. Conversely, in free flight if the shock wave emanating from the leading edge of the body is fairly strong, the translational temperature will rise quickly and the vibrational temperature can take some time to follow, leading to a “vibrationally cold” freestream with $T_e^* > T_{v,e}^*$. Again, the freestream vibrational and translational temperatures approach one another as the gas moves downstream.

To a good approximation, the relaxation of the freestream is described by the one

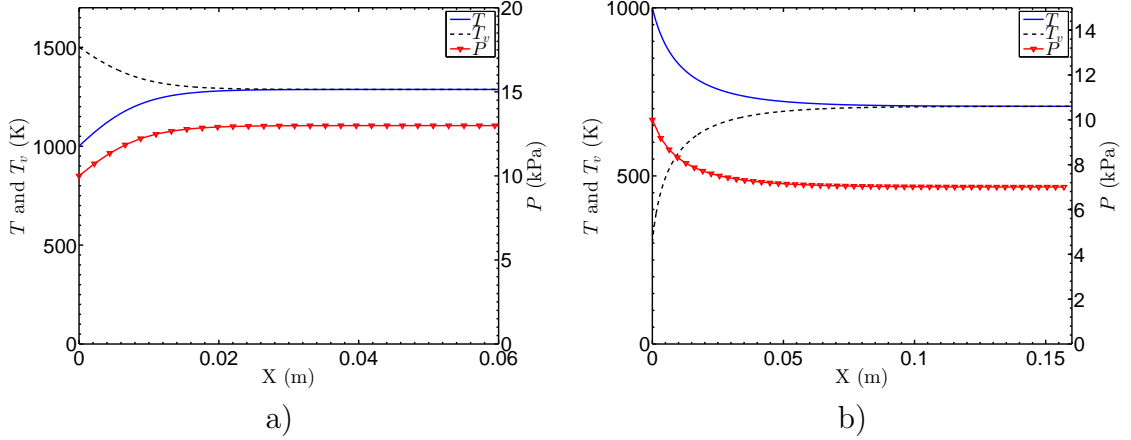


Figure 3.1: Variation of freestream properties with streamwise distance for a) vibrationally hot flow; b) vibrationally cold flow. In both cases, the flow is CO_2 with a Mach number of 5 based on $\gamma = 9/7$, and $P_e^* = 10$ kPa.

dimensional inviscid flow problem:

$$\frac{D\rho}{Dt} + \rho \frac{\partial u}{\partial x} = 0 \quad (3.4a)$$

$$\frac{Du}{Dt} + \frac{1}{\rho} \frac{\partial p}{\partial x} = 0 \quad (3.4b)$$

$$c_v \frac{DT}{Dt} + c_{v,v} \frac{DT_v}{Dt} + p \frac{\partial u}{\partial x} = 0 \quad (3.4c)$$

$$c_{v,v} \frac{DT_v}{Dt} = Q \quad (3.4d)$$

which is supplemented by the equation of state $p = \rho \mathcal{R}T$. For steady flow, this system of equations can be easily solved numerically. The results of two numerical simulations are given for carbon dioxide in Figure 3.1. In Figure 3.1a, the flow is vibrationally hot: the edge temperature is $T_e^* = 1000$ K while the vibrational temperature is $T_{v,e}^* = 1500$ K. This is representative of a reflected shock tunnel in which the translational temperature of the gas flowing out of a high temperature reservoir decreases too rapidly for the vibrational temperature to maintain equilibrium. Figure 3.1b is the opposite situation of vibrationally cold flow: the edge temperature is $T_e^* = 1000$ K while the vibrational temperature is 300 K.

An important observation from these simulations is that the pressure changes significantly as the freestream flow relaxes toward vibrational equilibrium. In fact, the

velocity and density (not shown) remain nearly constant while the pressure varies in proportion to the translational temperature. This pressure gradient in the freestream is inconsistent with our original assumption of a zero pressure gradient boundary layer. Therefore the boundary layer calculation employed here is restricted to situations for which the freestream is either near equilibrium or relaxing slowly in the downstream direction, such that the pressure gradient can be ignored.

In practice this is not too prohibitive a restriction. For flows that relax rapidly towards equilibrium, such as the carbon dioxide flows considered in Figure 3.1, the gas emanating from a nozzle or passing through a bow shock will reach equilibrium over a short distance (a few cm for the examples in the figure) and hence the pressure gradient is only important upstream or at the leading edge of the body. For flows having longer relaxation times, such as those involving nitrogen, the pressure gradient associated with vibrational relaxation is small and our zero pressure gradient approximation is good.

As mentioned previously, the velocity in the freestream is nearly constant during the relaxation process. Consequently, the energy equations (3.4c-3.4d) are approximately decoupled from the rest of the system:

$$\frac{DT_v}{Dt} = \frac{Q}{c_{v,v}} \qquad \frac{DT}{Dt} \approx -\frac{c_{v,v}}{c_v} \frac{DT_v}{Dt} = -\frac{Q}{c_v} \qquad (3.5)$$

In essence, this approximation neglects flow work associated with dilatation of the fluid ($p\nabla\cdot\vec{u}$), which is small given the uniformity of the freestream velocity. Figure 3.2 compares the temperature profiles computed using this reduced model with those from the full equations (3.4). The agreement is quite good, although there is a slight difference in relaxation rate which is associated with the pressure gradient described above. The full model includes the rising pressure in the downstream direction, which reduces the vibrational relaxation time ($\tau \propto p^{-1}$), whereas the reduced model assumes that the freestream pressure is constant. Given the good agreement between the simple model (3.5) and the full model (3.4), the simple model is used in all boundary layer calculations involving a nonequilibrium freestream.

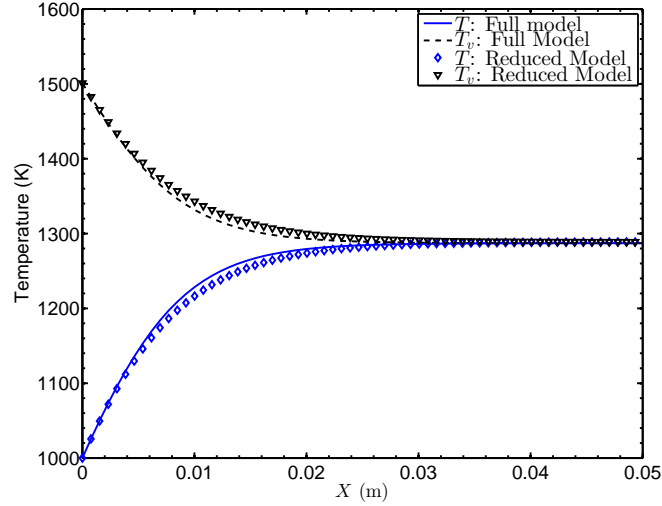


Figure 3.2: Relaxation of translational and vibrational temperatures for a vibrationally hot flow of CO_2 at $M=5$ and $P_e^* = 10$ kPa. Full model is Equations 3.4, whereas the reduced model is Equation 3.5 with the assumption of constant freestream pressure.

3.1.3 Coordinate transformation

Since the boundary layer equations (3.1) are singular at the leading edge of a flat plate or cone, it is convenient re-scale the vertical coordinate y by the local Blasius boundary layer thickness, introducing the similarity variable η :

$$\eta = y^* \sqrt{\frac{U_e^*}{\nu_e^* x^*}} \quad (3.6)$$

Even though the flow is generally not self-similar, this transformation is beneficial since it removes the leading-edge singularity and enables the use of a fixed grid and a fixed computational domain size. When the boundary layer equations (3.1) are

rescaled in this manner, the result is:

$$\left(x^* \frac{\partial}{\partial x^*} - \frac{\eta}{2} \frac{\partial}{\partial \eta}\right) (\bar{\rho}\bar{U}) + \sqrt{Re_x} \frac{\partial}{\partial \eta} (\bar{\rho}\bar{V}) = 0 \quad (3.7a)$$

$$\bar{\rho}\bar{U} \left(x^* \frac{\partial \bar{U}}{\partial x^*} - \frac{\eta}{2} \frac{\partial \bar{U}}{\partial \eta}\right) + \bar{\rho}\bar{V} \sqrt{Re_x} \frac{\partial \bar{U}}{\partial \eta} = \frac{\partial}{\partial \eta} \left(\bar{\mu} \frac{\partial \bar{U}}{\partial \eta}\right) \quad (3.7b)$$

$$\begin{aligned} \bar{\rho}\bar{U} \left(x^* \frac{\partial \bar{T}}{\partial x^*} - \frac{\eta}{2} \frac{\partial \bar{T}}{\partial \eta}\right) + \bar{\rho}\bar{V} \sqrt{Re_x} \frac{\partial \bar{T}}{\partial \eta} &= \frac{1}{\sigma_e} \frac{\partial}{\partial \eta} \left(\bar{k} \frac{\partial \bar{T}}{\partial \eta}\right) \\ &+ (\gamma_e - 1) M_e^2 \bar{\mu} \left(\frac{\partial \bar{U}}{\partial \eta}\right)^2 - Re_x \bar{Q} \end{aligned} \quad (3.7c)$$

$$\bar{\rho}\bar{U} \bar{c}_{v,v} \left(x^* \frac{\partial \bar{T}_v}{\partial x^*} - \frac{\eta}{2} \frac{\partial \bar{T}_v}{\partial \eta}\right) + \bar{\rho}\bar{V} \bar{c}_{v,v} \sqrt{Re_x} \frac{\partial \bar{T}_v}{\partial \eta} = \frac{1}{\sigma_e} \frac{\partial}{\partial \eta} \left(\bar{k}_v \frac{\partial \bar{T}_v}{\partial \eta}\right) + Re_x \bar{Q} \quad (3.7d)$$

3.1.4 Flow Timescales

In general, the vibrational source term \bar{Q} in Equations 3.7 precludes self-similar solutions of the boundary layer profiles. The non-similarity of the flow is caused by the presence of multiple timescales (viscous, convective, and vibrational), as opposed to frozen or equilibrium boundary layers which involve only the viscous and convective timescales.

In practice, one is often interested in using a frozen or equilibrium flow model wherever possible since a self-similar solution is then admissible, which can be computed relatively easily. In doing so, one must determine whether frozen or equilibrium flow is in fact a good approximation for the flow of interest. Intuitively, one expects the frozen and equilibrium flow solutions to perform well when the vibrational relaxation time is very large or very small; however, the largeness or smallness of the relaxation time must be judged in comparison with flow timescales. There are in fact two flow timescales in this problem: one is the viscous timescale $\tau_{visc} = \nu_e^*/U_e^{*2}$ and the other is the convection timescale $\tau_{conv} = x^*/U_e^*$. However, since we are interested in high Reynolds number flows and $\tau_{conv}/\tau_{visc} = Re_x$, the convective timescale is the

timescale to which the vibrational relaxation time should be compared. One then expects the frozen flow approximation to be appropriate when $U_e^* \tau^* / x^* \gg 1$ (and vice versa for equilibrium flow).

The same result can be derived directly from the equations of motion. For example, in a gas consisting of a single diatomic species, the dimensionless source terms in Equations 3.7 are (c.f. Equation 2.6):

$$\begin{aligned}
 Re_x \bar{Q} &= Re_x \frac{Q^* \nu_e^*}{\rho_e^* c_{p,tr}^* T_e^* U_e^{*2}} \\
 &= \left(\frac{x^*}{U_e^* \tau^*} \right) \left(\frac{\bar{\rho}^*}{\rho_e^*} \right) \left(\frac{e_v^*(\bar{T}) - e_v^*(\bar{T}_v)}{c_{p,tr}^* T_e^*} \right) \\
 &\approx \left(\frac{x^*}{U_e^* \tau^*} \right) \left(\frac{\bar{\rho}^*}{\rho_e^*} \right) \left(\frac{c_{v,v}^*}{c_{p,tr}^*} \right) \left(\frac{\bar{T}^* - \bar{T}_v^*}{T_e^*} \right) \tag{3.8}
 \end{aligned}$$

The dimensionless density ($\bar{\rho}^*/\rho_e^*$) is usually on the order of 0.1-10. From the rest of the terms, it is concluded that vibrational nonequilibrium is negligible if:

1. The flow is already close to vibrational equilibrium, $|\bar{T}^* - \bar{T}_v^*| \ll T_e^*$;
2. The temperature is low enough that only a small fraction of the internal energy is contained in vibrational modes ($c_{v,v}^*/c_{p,tr}^* \ll 1$);
3. The relaxation time is long compared to the convective timescale, $x^*/U_e^* \tau^* \ll 1$.

Given that the relaxation time τ^* is nearly constant as one moves downstream, it is to be expected that a high enthalpy boundary layer always begins with vibrationally frozen flow at the leading edge ($x^*/U_e^* \tau^* \ll 1$), features a non-equilibrium region further downstream, and then approaches equilibrium flow as $Re_x \rightarrow \infty$.

3.2 Self-Similar Solutions

For situations in which there is a large disparity between the vibrational and convective timescales, Equations 3.7 admit self-similar solutions that have no explicit dependence on x^* . Rather than using the usual density-weighted Levy-Lees transformation (Schlichting and Gersten, 2000), it is convenient here to perform the boundary

layer calculation using un-stretched coordinates. By integrating the continuity equation (3.7a) with respect to η and using integration by parts, one finds the relation

$$\bar{\rho}\bar{V} = -\frac{1}{\sqrt{Re_x}} \left(2x^* \frac{\partial g}{\partial x^*} - \frac{1}{2} [\bar{\rho}\bar{U}\eta - 2g] \right) \quad (3.9)$$

where g is defined following the notation of Klunker and McLean (1953):

$$g \equiv \frac{1}{2} \int_0^\eta (\bar{\rho}\bar{U}) d\eta' \quad (3.10)$$

Using (3.9) to eliminate the vertical velocity, the momentum and energy equations (3.7b-3.7d) can be written in terms of the similarity variable as follows:

$$\bar{\rho}\bar{U}x^* \frac{\partial \bar{U}}{\partial x^*} - \frac{\partial}{\partial \eta} \left(\bar{\mu} \frac{\partial \bar{U}}{\partial \eta} \right) - \frac{\partial \bar{U}}{\partial \eta} \left(g + 2x^* \frac{\partial g}{\partial x^*} \right) = 0 \quad (3.11a)$$

$$\bar{\rho}\bar{U}x^* \frac{\partial \bar{T}}{\partial x^*} - \frac{1}{\sigma_e} \frac{\partial}{\partial \eta} \left(\bar{k} \frac{\partial \bar{T}}{\partial \eta} \right) - (\gamma_e - 1) M^2 \bar{\mu} \left(\frac{\partial \bar{U}}{\partial \eta} \right)^2 + Re_x \bar{Q} - \frac{\partial \bar{T}}{\partial \eta} \left(g + 2x^* \frac{\partial g}{\partial x^*} \right) = 0 \quad (3.11b)$$

$$\bar{\rho}\bar{U}\bar{c}_{v,v}x^* \frac{\partial \bar{T}_v}{\partial x^*} - \frac{1}{\sigma_e} \frac{\partial}{\partial \eta} \left(\bar{k}_v \frac{\partial \bar{T}_v}{\partial \eta} \right) - Re_x \bar{Q} - \bar{c}_{v,v} \frac{\partial \bar{T}_v}{\partial \eta} \left(g + 2x^* \frac{\partial g}{\partial x^*} \right) = 0 \quad (3.11c)$$

The flow can be treated as vibrationally frozen if the vibrational source term $Re_x \bar{Q}$ is small. This occurs at the leading edge $x^* \rightarrow 0$ or when the temperature is low enough that the vibrational energy is small. In either case, the source terms are neglected and terms involving derivatives with respect to x^* are ignored. This produces the self-similar equations of Klunker and McLean (1953) along with a de-

coupled vibrational energy equation:

$$g \frac{\partial \bar{U}}{\partial \eta} + \frac{\partial}{\partial \eta} \left(\bar{\mu} \frac{\partial \bar{U}}{\partial \eta} \right) = 0 \quad (3.12a)$$

$$g \frac{\partial \bar{T}}{\partial \eta} + \frac{1}{\sigma_e} \frac{\partial}{\partial \eta} \left(\bar{k} \frac{\partial \bar{T}}{\partial \eta} \right) + (\gamma_e - 1) M^2 \bar{\mu} \left(\frac{\partial \bar{U}}{\partial \eta} \right)^2 = 0 \quad (3.12b)$$

$$g \bar{c}_{v,v} \frac{\partial \bar{T}_v}{\partial \eta} + \frac{1}{\sigma_e} \frac{\partial}{\partial \eta} \left(\bar{k}_v \frac{\partial \bar{T}_v}{\partial \eta} \right) = 0 \quad (3.12c)$$

These equations can be solved using the method of successive approximations described by [Klunker and McLean \(1953\)](#). This technique begins with an initial guess of the flow profiles; for instance, the uniform profiles $\bar{U}(\eta) = 1$, $\bar{T}(\eta) = 1$, $\bar{T}_v(\eta) = T_{v,e}^*/\bar{T}_e^*$ work quite well as an initial guess. With the help of an integrating factor the X momentum, energy, and vibrational energy equations (3.12) can then be written in the form:

$$\frac{\partial}{\partial \eta} \left[\bar{\mu} \frac{\partial \bar{U}}{\partial \eta} \exp \left(\int_0^\eta \frac{g(\xi)}{\bar{\mu}(\xi)} d\xi \right) \right] = 0 \quad (3.13a)$$

$$\begin{aligned} \frac{\partial}{\partial \eta} \left[\frac{\bar{k}}{\sigma_e} \frac{\partial \bar{T}}{\partial \eta} \exp \left(\int_0^\eta \frac{g(\xi) \sigma_e}{\bar{k}(\xi)} d\xi \right) \right] = \\ -(\gamma_e - 1) M^2 \bar{\mu} \left(\frac{\partial \bar{U}}{\partial \eta} \right)^2 \exp \left(\int_0^\eta \frac{g(\xi) \sigma_e}{\bar{k}(\xi)} d\xi \right) \end{aligned} \quad (3.13b)$$

$$\frac{\partial}{\partial \eta} \left[\frac{\bar{k}_v}{\sigma_e} \frac{\partial \bar{T}_v}{\partial \eta} \exp \left(\int_0^\eta \frac{g(\xi) \bar{c}_{v,v}(\xi) \sigma_e}{\bar{k}_v(\xi)} d\xi \right) \right] = 0 \quad (3.13c)$$

Each of these equations can be numerically integrated twice to yield the profiles of velocity, temperature, and vibrational temperature. In computing these integrals, the profiles of $\bar{\mu}$, \bar{k} , \bar{k}_v , g , and $\bar{c}_{v,v}$ are evaluated using the current guess of the solution. The evaluation of the integrals then provides a new solution estimate. The integrals above are evaluated repeatedly until convergence is reached. The convergence criterion used in this work is that the L2 norm of the difference between successive iterations must be less than 10^{-7} . This procedure provides a fast and robust means of calculating self-similar boundary layer profiles.

For equilibrium flow situations in which the rate of vibrational energy exchange is rapid enough that $\bar{T}_v = \bar{T}$, the translational and vibrational energy equations (3.12b-3.12c) can be added together to obtain the result:

$$g \frac{\partial \bar{U}}{\partial \eta} + \frac{\partial}{\partial \eta} \left(\bar{\mu} \frac{\partial \bar{U}}{\partial \eta} \right) = 0 \quad (3.14a)$$

$$g(1 + \bar{c}_{v,v}) \frac{\partial \bar{T}}{\partial \eta} + \frac{1}{\sigma_e} \frac{\partial}{\partial \eta} \left((\bar{k} + \bar{k}_v) \frac{\partial \bar{T}}{\partial \eta} \right) + (\gamma_e - 1) M^2 \bar{\mu} \left(\frac{\partial \bar{U}}{\partial \eta} \right)^2 = 0 \quad (3.14b)$$

These equations again admit self-similar solutions which can be computed using the method of successive approximations described above.

3.3 Non-Similar Solutions

Because of the source term \bar{Q} , Equations 3.11 do not in general admit self-similar solutions. However, since the boundary layer equations are parabolic, the steady laminar boundary layer can be solved as an initial-value problem in the streamwise direction with solutions determined by downstream marching. As $x^* \rightarrow 0$, the vibrational source terms in Equations 3.11 disappear because they are pre-multiplied by the Reynolds number. Therefore the self-similar, vibrationally frozen solutions from Equations 3.12 can be used as initial conditions to start the downstream march.

To proceed with the non-similar analysis, Equations (3.11) are discretized using fourth order finite differences in the wall-normal direction and implicit, first-order finite differences in the streamwise direction. The low order of accuracy in the streamwise direction is acceptable because the slow evolution of the boundary layer profiles in the streamwise direction is easily captured by a low order method. The discretized

boundary layer equations (3.7) are:

$$E = 0 = \frac{x}{\Delta x} \left(\frac{\bar{U}}{\bar{T}} - \frac{\bar{U}^{(k-1)}}{\bar{T}^{(k-1)}} \right) - \frac{\eta}{2} \frac{\partial}{\partial \eta} \left(\frac{\bar{U}}{\bar{T}} \right) + \frac{\partial}{\partial \eta} \left(\frac{\bar{V}}{\bar{T}} \right) \quad (3.15a)$$

$$F = 0 = \frac{\bar{U}x}{\Delta x} (\bar{U} - \bar{U}^{(k-1)}) + \left(\bar{V} - \frac{\eta \bar{U}}{2} \right) \frac{\partial \bar{U}}{\partial \eta} - \bar{T} \frac{\partial}{\partial \eta} \left(\bar{\mu} \frac{\partial \bar{U}}{\partial \eta} \right) \quad (3.15b)$$

$$G = 0 = \frac{\bar{U}x}{\Delta x} (\bar{T} - \bar{T}^{(k-1)}) + \left(\bar{V} - \frac{\eta \bar{U}}{2} \right) \frac{\partial \bar{T}}{\partial \eta} - \frac{\bar{T}}{\sigma_e} \frac{\partial}{\partial \eta} \left(\bar{k} \frac{\partial \bar{T}}{\partial \eta} \right) - \bar{T} (\gamma_e - 1) M_e^2 \bar{\mu} \left(\frac{\partial \bar{U}}{\partial \eta} \right)^2 + \bar{T} Re_x \bar{Q} \quad (3.15c)$$

$$H = 0 = \frac{\bar{U} \bar{c}_{v,v} x}{\Delta x} (\bar{T}_v - \bar{T}_v^{(k-1)}) + \bar{c}_{v,v} \left(\bar{V} - \frac{\eta \bar{U}}{2} \right) \frac{\partial \bar{T}_v}{\partial \eta} - \frac{\bar{T}}{\sigma_e} \frac{\partial}{\partial \eta} \left(\bar{k}_v \frac{\partial \bar{T}_v}{\partial \eta} \right) - \bar{T} Re_x \bar{Q} \quad (3.15d)$$

In these equations, E , F , G , and H are residuals corresponding to the continuity, x momentum, energy, and vibrational energy equations. The variable $\bar{V} = \bar{V} \sqrt{Re_x}$ is the vertical velocity re-scaled by the Reynolds number. Superscripts indicate the stream-wise grid location with local grid spacing Δx ; however, for clarity we omit the superscripts corresponding to marching step k , at which most of the terms are evaluated, and indicate only the terms that are evaluated at the previous stream-wise point $k - 1$. All terms without superscripts are evaluated at the marching step k . Wall-normal differentiation is carried out using either 4th order finite differences or differentiation matrices based on the Chebyshev polynomials collocated at the Gauss-Lobatto points (Canuto et al., 1988).

Suppose that a column vector \mathbf{X} contains the current guess of \bar{U} , \bar{V} , \bar{T} , and \bar{T}_v at location k along the boundary layer, and a column vector \mathbf{R} contains the residuals E , F , G , and H defined by Equation 3.15. The residual vector \mathbf{R} is then driven to zero using Newton iteration, in which the solution vector \mathbf{X} is updated according to

the formula:

$$\mathbf{J}(\mathbf{X}^{n+1} - \mathbf{X}^n) = -\mathbf{R} \quad (3.16)$$

where \mathbf{J} is the Jacobian matrix and n is the Newton iteration number. These iterations are repeated until the L_2 norm of the residual vector \mathbf{R} falls below 10^{-10} . At each iteration the Jacobian matrix is evaluated analytically, and its elements are provided in Appendix B.

3.4 Verification

Verification of the boundary layer calculation was carried out by making comparisons with Navier-Stokes simulations which were conducted using the STABL stability software package developed at the University of Minnesota (Johnson et al., 1998, Wright et al., 1998, Johnson, 2000). This software package includes a shock-capturing finite volume solver that models non-equilibrium, chemically reacting flows. The Navier-Stokes simulations shown here were conducted using a grid of 450×450 points, with exponential clustering of points at the wall and near the leading edge of the plate. Convergence was checked using a finer grid of 600 streamwise by 650 wall-normal points, which led to no significant differences in the flow profiles. For cases with air, the Navier-Stokes simulations employed a 5 species air model containing N_2 , O_2 , NO, N, and O, with a freestream composition of 78% N_2 and 22% O_2 by mole. For simulations with carbon dioxide, a 5 species model was also used with CO_2 , CO, C, O_2 , and O included in the model, and with a pure CO_2 freestream.

For the present non-similar boundary-layer solver described in the preceding sections, the mesh resolution was 300 wall-normal points and 150 marching steps in the streamwise direction, which has been found to produce a converged solution. Verification was carried out for flows of both air and carbon dioxide; in both cases the geometry is a flat plate with a sharp leading edge.

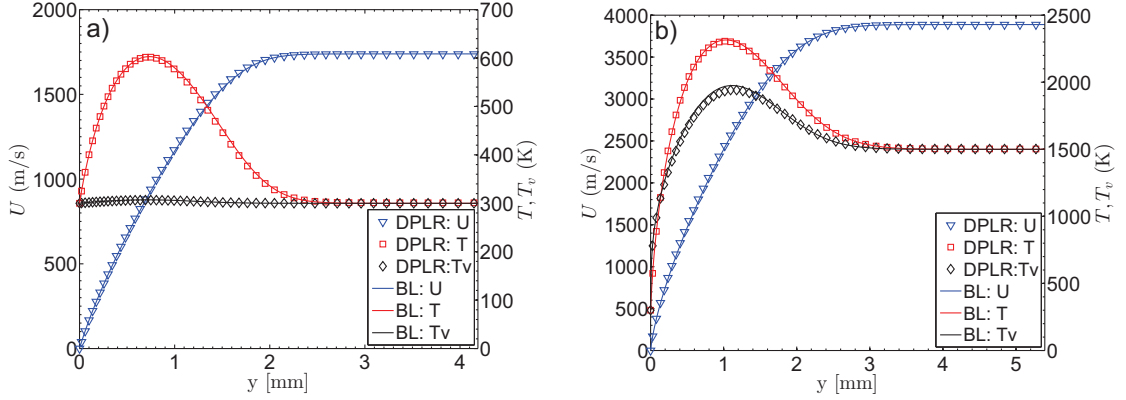


Figure 3.3: Comparison of boundary layer profiles at $Re_x = 2.25$ million from STABL Navier-Stokes solver (symbols) and boundary layer code (solid lines). Profiles are velocity (∇), translational/rotational temperature (\square), and vibrational temperature (\diamond). a) Low enthalpy, $P_e^* = 5$ kPa, $M = 5$, $T_w^* = 300$ K, $T_e^* = T_{v,e}^* = 300$ K. b) High enthalpy, $P_e^* = 20$ kPa, $M = 5$, $T_w^* = 300$ K, $T_e^* = T_{v,e}^* = 1500$ K.

3.4.1 Air

Examples of temperature and velocity profiles for flows of air at $Re_x = 2.25 \times 10^6$ are given in Figure 3.3. Figure 3.3a is a fairly low enthalpy flow that is representative of a slender body in free flight, with $T_e^* = T_{v,e}^* = 300$ K. At $Re_x = 2.25 \times 10^6$, the vibrational temperature remains close to its initial value and the translational temperature distribution is close to that of a self-similar frozen flow. Because of the slow vibrational relaxation times of N_2 and O_2 at low temperatures, the vibrational temperature does not approach the translational temperature until the Reynolds number is very large.

Figure 3.3b is a much higher enthalpy case that is representative of a shock tunnel, with $T_e^* = T_{v,e}^* = 1500$ K. In this case the rate of vibrational energy transfer is more significant, so that by $Re_x = 2.25 \times 10^6$ the vibrational temperature is fairly close to the equilibrium temperature distribution. As Re_x increases further, the vibrational and translational temperature profiles both approach a single equilibrium temperature profile.

In the figure, solid lines are taken from the present boundary layer calculations, while symbols correspond to the shock capturing Navier-Stokes simulations. For both

flow conditions shown, excellent agreement between the boundary layer solver and the Navier-Stokes solver is seen, and similarly good agreement has been found for other Reynolds numbers and flow conditions.

3.4.2 Carbon Dioxide

Figure 3.4 compares the boundary layer profiles from the present boundary layer solver with Navier-Stokes simulations for carbon dioxide at $M = 5$ and with a fairly low edge temperature of 300 K . In making this comparison, the vibrational relaxation time in the present boundary layer simulations was adjusted to match the model used by STABL. Specifically, the relaxation time was calculated using the correlation of Millikan and White (1963) given in Equations 2.8 and 2.9 rather than using the experimental data of Camac (1966). In using Equations 2.9 one must choose a value for the vibrational activation temperature Θ_v^* , and this choice is ambiguous for carbon dioxide, which has three vibrational modes. To match the model used in STABL, the value $\Theta_v^* = 960\text{ K}$ corresponding to the bending mode was used. This change to the relaxation time was used only for making comparisons with STABL; unless stated otherwise, the experimentally measured rates of Camac (1966) are used in the remainder of this work.

Figure 3.4 shows the boundary layer profiles for a progression of Reynolds numbers from $R = \sqrt{Re_x} = 200 - 1500$. The evolution of the temperature profiles from flow that is nearly frozen to flow that is in vibrational equilibrium is evident. At all Reynolds numbers, excellent agreement between the boundary-layer solver (lines) and the Navier-Stokes simulations (symbols) is observed.

Figure 3.5 shows a similar progression of mean flow profiles, but for a higher enthalpy flow that is relevant to reflected shock tunnels: here the Mach number is 5 and the edge temperature is 1000 K . The qualitative behavior is the same as that shown in the preceding cases, but because of the higher temperature the flow relaxation is quite fast, and the temperature profiles already reach equilibrium at a low Reynolds number of about $R = 400$. This Reynolds number is much smaller than

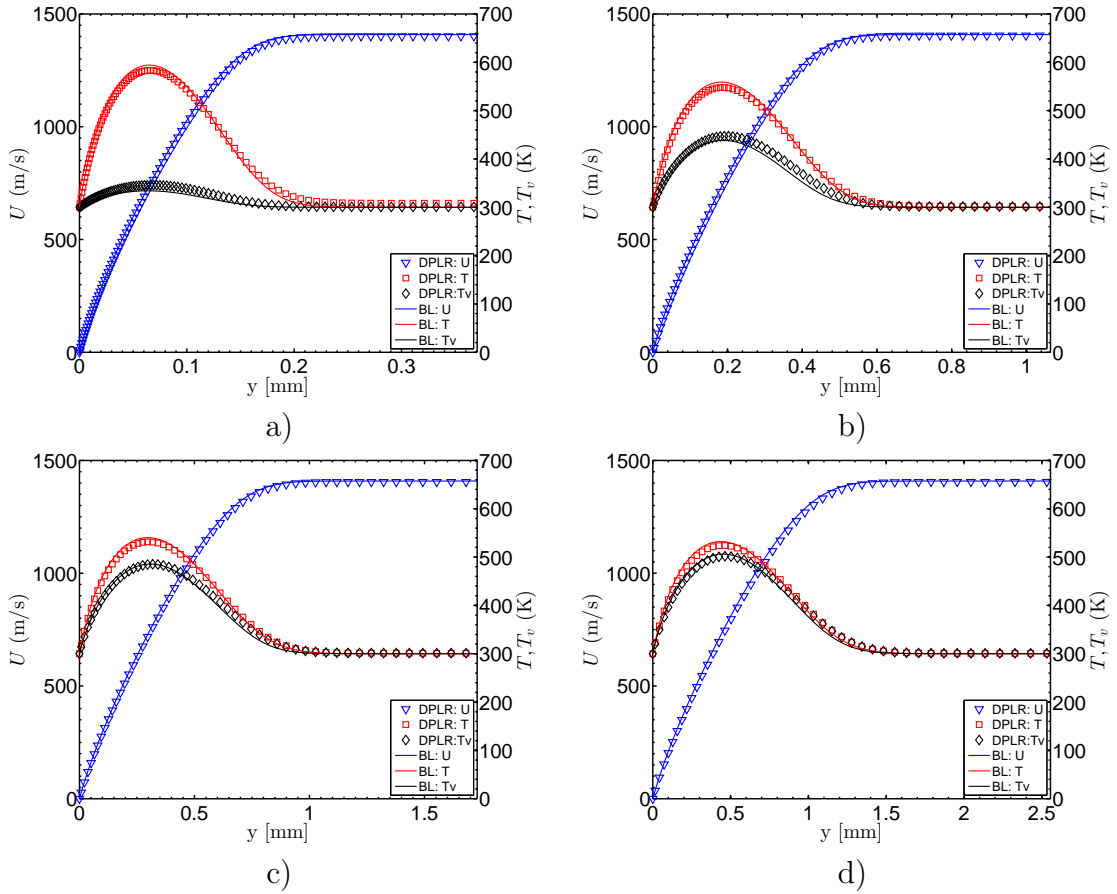


Figure 3.4: Comparison of boundary layer profiles at four Reynolds numbers from STABL Navier-Stokes solver (symbols) and boundary layer code (solid lines). Profiles are velocity (∇), translational/rotational temperature (\square), and vibrational temperature (\diamond). Flow is at $M = 5$, $P_e^* = 5$ kPa, $T_e^* = T_{v,e}^* = 300$ K. The Reynolds numbers $R = \sqrt{Re_x}$ are a) 200, b) 600, c) 1000, and d) 1500.

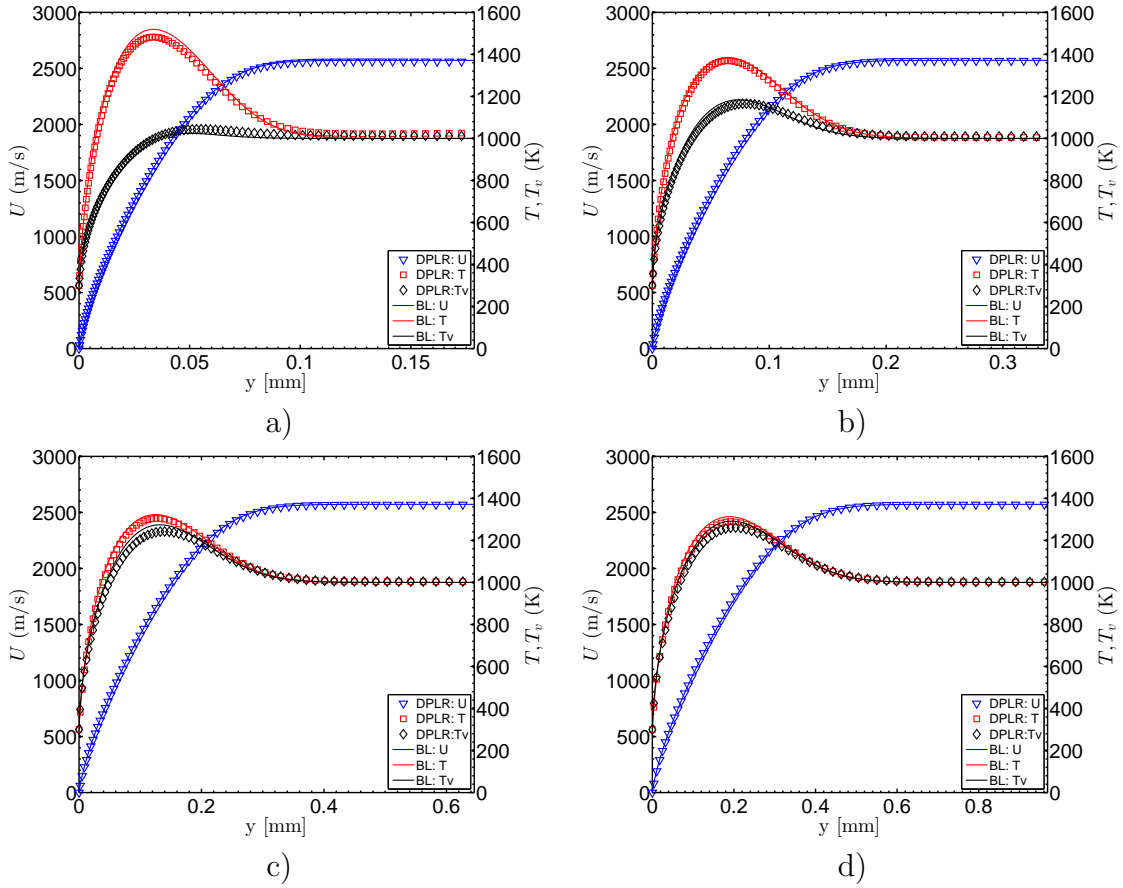


Figure 3.5: Comparison of boundary layer profiles at four Reynolds numbers from STABL Navier-Stokes solver (symbols) and boundary layer code (solid lines). Profiles are velocity (∇), translational/rotational temperature (\square), and vibrational temperature (\diamond). Flow is at $M = 5$, $P_e^* = 20$ kPa, $T_e^* = T_{v,e}^* = 1000$ K, $T_w^* = 300$ K. The Reynolds numbers $R = \sqrt{Re_x}$ are a) 100, b) 200, c) 400, and d) 600.

the typical transition Reynolds number. This suggests that in performing stability analysis of high enthalpy flows of CO_2 , it is an excellent approximation to assume that the mean boundary layer is in a state of vibrational equilibrium.

The preceding simulations have been carried out for particular choices of the edge pressure, but when the boundary layer profiles are presented nondimensionally in terms of the Reynolds number and the scaled vertical coordinate $\eta = y^*/\delta$, they apply for any pressure. As shown in Equation 2.8, the vibrational relaxation time is inversely proportional to the pressure, but the viscous timescale ν_e^*/U_e^{*2} is inversely proportional to pressure as well. As the pressure is increased, vibrational relaxation proceeds more rapidly in terms of physical distance downstream of the leading edge, but the boundary layer also grows more rapidly. As a result, the boundary layer profiles are always the same at a given Reynolds number, regardless of the pressure. This result can also be derived from the dimensionless equations of motion (2.14) in which the edge pressure appears only through the Reynolds number. This behavior contrasts with flows involving chemical reactions, in which the three-body recombination reactions often prevent the pressure from scaling out of the problem.

3.5 Mangler Transform

The methods described so far apply to a zero pressure gradient flat plate, which is the geometry of interest for most of the work presented in this thesis. However, in some cases it is of interest to make comparisons with experiments involving flow over sharp cones. For flows that are vibrationally frozen or in vibrational equilibrium, the similarity solutions described in Section 3.2 can be used in combination with the Mangler transformation (White, 1974, Schlichting and Gersten, 2000) to model flow past sharp cones. As will be shown below, the Mangler transformation reveals that the boundary layer profiles on a cone are equivalent to those of a flat plate at a larger Reynolds number where the boundary layer thickness is a factor of $\sqrt{3}$ larger. Specifically, if the wavenumber α and frequency ω of disturbances in the boundary layer are normalized using the local boundary layer thickness δ as the length scale

and δ/U_e as the time scale, then the results from stability calculations on cones and flat plates are related by

$$R_c = \sqrt{3}R_{fp} \quad (3.17a)$$

$$\omega_c = \sqrt{3}\omega_{fp} \quad (3.17b)$$

$$\alpha_c = \sqrt{3}\alpha_{fp} \quad (3.17c)$$

where subscript ‘c’ refers to a cone, ‘fp’ refers to a flat plate, and $R = \sqrt{Re_x}$ is the Reynolds number based on boundary layer thickness.

The Mangler transformation described above is a good approximation only at high Reynolds numbers where the transverse curvature of the boundary layer is small and the effects of flow divergence are negligible, i.e., the boundary layer is approximately planar. The influence of flow divergence and transverse curvature on the stability properties has been assessed by [Malik and Anderson \(1991\)](#), who showed that non-planar effects can be fairly significant, especially if the cone angle is small. For instance, they found that, compared to a planar boundary layer, flow divergence and curvature decreased the 2nd mode growth rate by about 10% for a 10° half-angle cone and by about 33% for a 2° cone at a Reynolds number of $R = 1000$. In this work, we focus mainly on flat plates so this is not a concern. However, in a few instances comparisons are made with experimental data involving cones and the assumption of a planar boundary layer is invoked. While this assumption is commonly used within the boundary layer transition community, the shortcomings described above must be appreciated.

Although the Mangler transform has been used quite successfully for modeling calorically perfect gases, its applicability to nonequilibrium flows is unclear. It is not immediately obvious whether a nonequilibrium axisymmetric boundary layer can be related to an equivalent flow over a flat plate, or whether the simple relations given in Equation 3.17 can be used for nonequilibrium flows. In this section, these questions are answered by applying the Mangler transformation to the nonequilibrium boundary layer equations (3.1).

Suppose that the flow past an axisymmetric body is described by the flow variables \tilde{U} , \tilde{V} , \tilde{T} , and \tilde{T}_v , which are functions of the independent variables \tilde{x} and \tilde{y} . In this section the tilde is used to designate variables relevant to an axisymmetric flow, and all variables are nondimensionalized using the scheme in Equations 2.13. Suppose also that the radius of the axisymmetric body is $\tilde{r}(\tilde{x})$. If one neglects the transverse curvature (assuming $\delta \ll \tilde{r}$), then the nonequilibrium equivalents of the axisymmetric boundary layer equations (Schlichting and Gersten, 2000) are

$$\frac{\partial}{\partial \tilde{x}} \left(\tilde{r}(\tilde{x}) \tilde{\rho} \tilde{U} \right) + \tilde{r}(\tilde{x}) \frac{\partial}{\partial \tilde{y}} \left(\tilde{\rho} \tilde{V} \right) = 0 \quad (3.18a)$$

$$\tilde{\rho} \tilde{U} \frac{\partial \tilde{U}}{\partial \tilde{x}} + \tilde{\rho} \tilde{V} \frac{\partial \tilde{U}}{\partial \tilde{y}} = \frac{1}{Re_L} \frac{\partial}{\partial \tilde{y}} \left(\tilde{\mu} \frac{\partial \tilde{U}}{\partial \tilde{y}} \right) \quad (3.18b)$$

$$\begin{aligned} \tilde{\rho} \left(\tilde{U} \frac{\partial \tilde{T}}{\partial \tilde{x}} + \tilde{V} \frac{\partial \tilde{T}}{\partial \tilde{y}} \right) &= \frac{1}{Re_L \sigma_e} \frac{\partial}{\partial \tilde{y}} \left(\tilde{k} \frac{\partial \tilde{T}}{\partial \tilde{y}} \right) \\ &+ \frac{(\gamma_e - 1) M^2}{Re_L} \tilde{\mu} \left(\frac{\partial \tilde{U}}{\partial \tilde{y}} \right)^2 - Re_L \tilde{Q} \end{aligned} \quad (3.18c)$$

$$\tilde{\rho} \tilde{c}_{v,v} \left(\tilde{U} \frac{\partial \tilde{T}_v}{\partial \tilde{x}} + \tilde{V} \frac{\partial \tilde{T}_v}{\partial \tilde{y}} \right) = \frac{1}{Re_L \sigma_e} \frac{\partial}{\partial \tilde{y}} \left(\tilde{k}_v \frac{\partial \tilde{T}_v}{\partial \tilde{y}} \right) + Re_L \tilde{Q} \quad (3.18d)$$

Other than notational differences, the equations of x momentum, energy, and vibrational energy are unchanged from those given for a plate in Equation 3.1.

Generalizing the approach of White (1974), the Mangler transform is applied by introducing a new set of scaled variables:

$$\begin{aligned} x &= \int_0^{\tilde{x}} \tilde{r}^2(\tilde{x}) d\tilde{x} & y &= \tilde{r} \tilde{y} \\ \bar{U}(x) &= \tilde{U}(\tilde{x}) & \bar{V}(x) &= \frac{1}{\tilde{r}} \left(\tilde{V} + \frac{\tilde{y} \tilde{U}}{\tilde{r}} \frac{d\tilde{r}}{d\tilde{x}} \right) \\ \bar{T}(x) &= \tilde{T}(\tilde{x}) & \bar{T}_v(x) &= \tilde{T}_v(\tilde{x}) \\ \bar{\rho}(x) &= \tilde{\rho}(\tilde{x}) \end{aligned} \quad (3.19)$$

As will be seen, the variables on the LHS correspond to an equivalent flow over a flat plate. On the basis of this transformation, the derivatives map according to the

relations:

$$\frac{\partial}{\partial \tilde{x}} = \tilde{r}^2 \frac{\partial}{\partial x} + \frac{y}{\tilde{r}} \frac{\partial \tilde{r}}{\partial \tilde{x}} \frac{\partial}{\partial y} \quad (3.20a)$$

$$\frac{\partial}{\partial \tilde{y}} = \tilde{r} \frac{\partial}{\partial y} \quad (3.20b)$$

When the change of variables (3.19) is applied to the axisymmetric boundary layer equations (3.18), the result is:

$$\frac{\partial}{\partial x} (\bar{\rho} \bar{U}) + \frac{\partial}{\partial y} (\bar{\rho} \bar{V}) = 0 \quad (3.21a)$$

$$\bar{\rho} \left(\bar{U} \frac{\partial \bar{U}}{\partial x} + \bar{V} \frac{\partial \bar{U}}{\partial y} \right) = \frac{1}{Re_L} \frac{\partial}{\partial y} \left(\bar{\mu} \frac{\partial \bar{U}}{\partial y} \right) \quad (3.21b)$$

$$\begin{aligned} \bar{\rho} \left(\bar{U} \frac{\partial \bar{T}}{\partial x} + \bar{V} \frac{\partial \bar{T}}{\partial y} \right) &= \frac{1}{\sigma_e Re_L} \frac{\partial}{\partial y} \left(\bar{k} \frac{\partial \bar{T}}{\partial y} \right) \\ &+ \frac{(\gamma_e - 1) M^2}{Re_L} \bar{\mu} \left(\frac{\partial \bar{U}}{\partial y} \right)^2 - \frac{Re_L \bar{Q}}{\tilde{r}^2} \end{aligned} \quad (3.21c)$$

$$\bar{\rho} \bar{c}_{v,v} \left(\bar{U} \frac{\partial \bar{T}_v}{\partial x} + \bar{V} \frac{\partial \bar{T}_v}{\partial y} \right) = \frac{1}{\sigma_e Re_L} \frac{\partial}{\partial y} \left(\bar{k}_v \frac{\partial \bar{T}_v}{\partial y} \right) + \frac{Re_L \bar{Q}}{\tilde{r}^2} \quad (3.21d)$$

These equations are identical to those for a flat-plate boundary layer (3.1) with the exception that the vibrational source terms are divided by a factor of \tilde{r}^2 . These equations can be solved using exactly the same technique as in Section 3.3, provided that at each marching step the vibrational source terms \bar{Q} are divided by the local radius squared.

The above result applies to a general axisymmetric body. For the special case of a cone with a half-angle of χ , the cone radius is given by:

$$\tilde{r}(\tilde{x}) = \tilde{x} \sin(\chi) \quad (\text{Cone}) \quad (3.22)$$

One can then use the expressions in Equation 3.19 to find explicit relations between

the cone coordinates (\tilde{x}, \tilde{y}) and those of an equivalent flat plate (x, y) :

$$\tilde{x} = [3x/\sin^2(\chi)]^{1/3} \quad (3.23a)$$

$$\tilde{y} = \frac{y}{\tilde{x} \sin(\chi)} = \frac{y}{[3x \sin(\chi)]^{1/3}} \quad (3.23b)$$

After solving the equivalent flat plate problem in the (x, y) plane, these relations can be used to return to the (\tilde{x}, \tilde{y}) plane associated with a cone.

As described in Section 3.3, it is often convenient to compute the boundary layer profiles in terms of the Blasius similarity variable $\eta = y/\sqrt{\nu_e^* x/U_e}$, even when the flow is not self-similar. Using Equations 3.23, it can easily be shown that the Blasius variables for the flat plate (η) and the cone ($\tilde{\eta}$) are related by:

$$\tilde{\eta} = \frac{\tilde{y}}{\sqrt{\nu_e^* \tilde{x}/U_e}} = \frac{y}{\sqrt{\nu_e^*(3x)/U_e}} = \frac{\eta}{\sqrt{3}} \quad (3.24)$$

If the flow is self-similar, then the velocity and temperature profiles are only a function of η . Hence the solutions for the flat plate and the cone are identical when their vertical scales coincide: $\tilde{\eta} = \eta$. This implies that $\tilde{x} = 3x$, $\tilde{R} = \sqrt{3}R$, and $\tilde{\delta} = \sqrt{3}\delta$, as explained in the introduction to this section. For a non-similar flow the relationship between the cone and flat plate solutions is more complicated, as the velocity and temperature profiles are functions of both η and x . However, there is still a one-to-one mapping between the solutions on a flat plate and on a cone; for a general flow variable f the relation is:

$$\tilde{f}(\tilde{x}, \tilde{\eta}) = f\left([3x/\sin^2(\chi)]^{1/3}, \frac{\eta}{\sqrt{3}}\right) \quad (3.25)$$

where \tilde{f} is the solution on a cone and f is the solution on a flat plate.

Chapter 4

Modal Stability Analysis

This chapter describes several methods that can be used to conduct modal stability analysis of high enthalpy boundary layers. In modal analysis one calculates the eigenmodes of a linearized flow field and searches for unstable, exponentially growing solutions. This is in contrast to non-modal stability analysis (also known as transient growth), which is the subject of Chapter 6. In this chapter, two different methods for computing the eigenvalues of the linearized Navier-Stokes system are described, and their various advantages and disadvantages are discussed. Both methods have been widely used in the literature for analyzing flows of perfect gases, but here they are extended for gases that are out of thermal equilibrium. Results obtained using these methods are presented in Chapter 5.

The growth or decay of small disturbances in the laminar boundary layer is studied by linearizing the compressible Navier-Stokes equations and computing the eigenvalues and eigenvectors of the resulting linear system. The linearization is accomplished by decomposing the flow variables into mean and fluctuating parts of the form:

$$\mathbf{q} = \bar{\mathbf{q}}(y) + \Re \{ \hat{\mathbf{q}}(y) \times e^{i(\alpha x + \beta z - \omega t)} \} \quad (4.1)$$

where \Re designates the real part of a complex variable and \mathbf{q} is the vector of flow variables:

$$\mathbf{q} = (u, v, w, p, T, T_v)^T$$

Here over-bars designate the base flow and hats designate the complex amplitude coefficients of the fluctuations. The streamwise and spanwise wavenumbers α and β are nondimensionalized using the local Blasius boundary layer thickness $\delta = \sqrt{\nu_e^* x^* / U_e^*}$, and the frequency ω is nondimensionalized using the timescale δ / U_e^* . In this decomposition, the flow is assumed to be locally parallel, meaning that three types of terms are neglected:

1. Terms involving x derivatives of the mean flow variables
2. Terms involving the mean vertical velocity \bar{V}
3. Terms involving x derivatives of the amplitude coefficients of the disturbances (designated by hats)

The neglect of these terms can be justified using multiple-scales analysis (Nayfeh, 1980, Fedorov and Khokhlov, 2001), in which flow variables are taken as a perturbation expansion in powers of the parameter $\epsilon = \delta_L / L$, where δ_L is the Blasius boundary layer thickness at the end of the plate or cone and L is its length. Using the Blasius boundary layer scaling arguments (Schlichting and Gersten, 2000), it can be shown that the mean vertical velocity \bar{V} is a factor of ϵ smaller than the stream-wise velocity \bar{U} . Likewise, derivatives with respect to x are a factor of ϵ smaller than derivatives with respect to y . Because the boundary layer equations scale in this way, the locally-parallel flow assumed here corresponds to the lowest order of the multiple-scales expansion (ϵ^0), with non-parallel effects entering at order ϵ^1 . The accuracy of the parallel flow assumption improves as the Reynolds number $R_L = \delta_L U_e^* / \nu_e^*$ increases, since $\epsilon = \delta_L / L = 1 / R_L$.

The majority of the simulations performed in this work are spatial analyses in which the frequency ω is assumed to be real and the streamwise wavenumber α is determined as the eigenvalue. Eigenvalues having negative imaginary part α_i are then unstable. The alternative is temporal analysis, in which the wavenumber α is assumed to be real and the frequency ω is the eigenvalue, with positive ω_i indicating instability. The spatial framework is generally considered to better represent convectively unstable flows like the boundary-layer than the temporal framework.

Two different methods are available for computing the eigenvalues of the linearized Navier-Stokes equations. The first method is called the “global” method in the literature. In this method the linearized equations are cast in the form of a large matrix eigenvalue problem and all the eigenvalues of the matrix are determined using standard linear algebra algorithms. This method requires no *a priori* knowledge of the eigenvalues and returns both the discrete modes and discrete approximations to the continuous spectra. However, the global method is rather computationally expensive since the computational effort scales with the cube of the matrix dimension.

The second method is called the “local” method in the literature: in this method a single discrete eigenvalue is determined rapidly and with high accuracy, but a close initial guess of the eigenvalue is needed. The local method has an additional advantage that the freestream boundary conditions (discussed in Section 4.3) can be treated exactly, whereas the global method can employ only approximate boundary conditions. In practice, a poorly-resolved eigenvalue search with the global method is often used to provide initial guesses for the more accurate local method. Each of these two methods is described in the sections that follow.

4.1 Global Method

The fluctuations given in Equation 4.1 are substituted into the Navier-Stokes equations (2.14) and linearized. As detailed in Appendix A, the resulting linearized equations can be rearranged in the form of six second order differential equations:

$$\left(\mathbf{A} \frac{\partial^2}{\partial y^2} + \mathbf{B} \frac{\partial}{\partial y} + \mathbf{C} \right) \hat{\mathbf{q}} = 0 \quad (4.2)$$

where \mathbf{A} , \mathbf{B} , and \mathbf{C} are 6×6 matrices whose coefficients are given in Appendix A, and $\hat{\mathbf{q}}$ is the column vector of disturbance amplitudes:

$$\hat{\mathbf{q}} = \left(\hat{u}, \hat{v}, \hat{p}, \hat{\theta}, \hat{w}, \hat{\theta}_v \right)^T \quad (4.3)$$

Here \hat{u} , \hat{v} , and \hat{w} are the fluctuations in streamwise, vertical, and spanwise velocities, \hat{p} is the pressure fluctuation, and $\hat{\theta}$ and $\hat{\theta}_v$ are the fluctuations in translational and vibrational temperatures. The boundary conditions imposed here are the Dirichlet conditions:

$$\hat{u} = \hat{v} = \hat{w} = \hat{\theta} = \hat{\theta}_v = 0 \quad y = 0 \quad (4.4a)$$

$$\hat{u} = \hat{v} = \hat{w} = \hat{\theta} = \hat{\theta}_v = 0 \quad y = y_{max} \quad (4.4b)$$

At the wall, the velocity boundary conditions $\hat{u} = \hat{v} = \hat{w} = 0$ follow from the no-slip condition and the temperature boundary conditions $\hat{\theta} = \hat{\theta}_v = 0$ are based on the assumption that the thermal inertial of the wall is large, which is true for the high frequency (kHz-MHz) fluctuations experienced in high enthalpy boundary layers. In the freestream, the Dirichlet boundary conditions (4.4b) are an overly-restrictive approximation; the correct boundary condition is that the disturbances must remain bounded as $y \rightarrow \infty$. This correct boundary condition is implemented for the local analysis (Section 4.2), but cannot be easily employed for the global eigenvalue calculation. The only recourse is to use a very large domain ($y_{max} = 10 - 20\delta_{99}$) for which the Dirichlet approximation is nearly correct. Further analysis of the freestream boundary conditions is given in Section 4.3.

In Equation 4.2, derivatives with respect to y are evaluated using differentiation matrices that are based on the Chebyshev polynomials collocated at the Gauss-Lobatto points (Canuto et al., 1988). After discretizing the system using N wall-normal points, the elements of the matrices in Equation 4.2 can be factored according to the terms which have α , α^2 , and ω as coefficients. The resulting discretized system takes the form:

$$(\mathbb{A}_o + \mathbb{A}_\omega \omega + \mathbb{A}_\alpha \alpha + \mathbb{A}_{\alpha^2} \alpha^2) \mathbf{Q} = 0 \quad (4.5)$$

where \mathbb{A}_o , \mathbb{A}_ω , \mathbb{A}_α , and \mathbb{A}_{α^2} are all $6N \times 6N$ matrices and \mathbf{Q} is a $6N$ column vector that contains the discretized flow variables. For a temporal analysis in which α is

prescribed and ω is the desired eigenvalue, the matrices \mathbb{A}_o , $\alpha\mathbb{A}_\alpha$, and $\alpha^2\mathbb{A}_{\alpha^2}$ are combined, leaving a $6N \times 6N$ generalized eigenvalue problem for ω , which is solved using the LAPACK implementation of the QZ algorithm.

For spatial analysis in which ω is prescribed and α is sought, one is confronted with a quadratic eigenvalue problem in Equation 4.5. This can be dealt with in one of two ways. First, one can simply linearize the eigenvalue problem and neglect the α^2 term. For boundary layers over flat plates and cones, this often works well, especially at high Reynolds numbers, since the terms involving α^2 are of viscous origin and hence are inversely proportional to the Reynolds number R . The eigenvalues determined from the linearized eigenvalue problem are generally close enough to the true eigenvalue that they are acceptable initial guesses for the more accurate local analysis. It is also demonstrated in Chapter 6 that linearization of the eigenvalue problem works quite well for spatial transient growth calculations.

The second approach is to solve the full, quadratic eigenvalue problem for α in Equation 4.5, which also enables the quantification of errors introduced by the linearization described above. Extending the method described by Malik (1990), this is accomplished by introducing the additional variables $\alpha\hat{u}$, $\alpha\hat{v}$, $\alpha\hat{\theta}$, $\alpha\hat{w}$, and $\alpha\hat{\theta}_v$. The addition of these five variables is supplemented by adding ten more boundary conditions:

$$\alpha\hat{u}, \alpha\hat{v}, \alpha\hat{w}, \alpha\hat{\theta}, \alpha\hat{\theta}_v = 0 \qquad y = 0 \qquad (4.6a)$$

$$\alpha\hat{u}, \alpha\hat{v}, \alpha\hat{w}, \alpha\hat{\theta}, \alpha\hat{\theta}_v = 0 \qquad y = y_{max} \qquad (4.6b)$$

With the aid of these additional variables, one can rearrange Equation 4.5 to construct an $11N \times 11N$ eigenvalue problem that is linear in α , which can then be solved using the QZ algorithm. Since the computational effort of the eigenvalue search increases with the cube of the matrix dimension, the computational expense is about 6 times greater for the full, quadratic ($11N \times 11N$) eigenvalue problem compared to the linearized version ($6N \times 6N$).

Examples of spatial and temporal eigenvalue spectra from the global method are

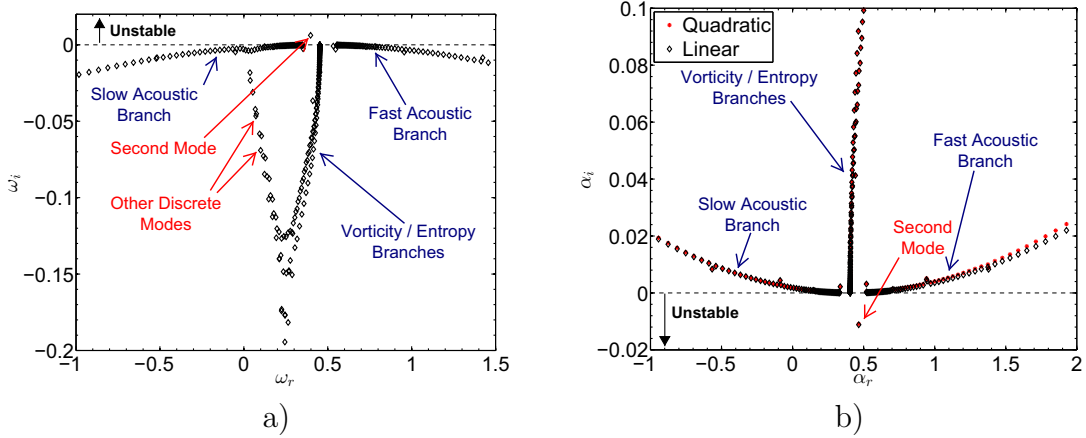


Figure 4.1: Global eigenvalue spectra for 2D waves ($\beta = 0$) in air at $R = 2000$, $P_e^* = 10$ kPa, $M_e = 4.5$, $T_e^* = T_{v,e}^* = 1500$ K, $T_w^* = 300$ K. a) Temporal analysis with $\alpha = 0.45$. b) Spatial analysis with $\omega = 0.41$.

given in Figure 4.1. The flow is air at $M = 5$ in a high enthalpy boundary layer with a cold wall. For both the spatial and temporal results, the spectrum shown corresponds to the most unstable second mode disturbance, with $\alpha = 0.45$ for the temporal analysis and $\omega = 0.41$ for the spatial analysis. For the spatial case, results from both the quadratic and linear eigenvalue problems are given: these two methods produce nearly identical eigenvalues except at large values of α_r , where slight differences are seen.

The eigenvalue spectra in Figure 4.1 consist of several discrete modes as well as discrete approximations to the continuous spectra. For temporal analysis, there are four branches of continuous spectrum which are indicated in Figure 4.1a. The continuous spectra correspond to waves that are non-decaying in the freestream. By examining the behavior in the freestream of the eigenfunctions corresponding to these branches, one finds that they propagate as plane waves and hence can be identified by their correspondence to the plane wave solutions of 1D compressible flow. The two branches extending to the left and right in Figure 4.1a propagate as acoustic waves, whereas two overlapping vertical branches propagate as vorticity and entropy waves.

The situation is similar for spatial analysis as shown in Figure 4.1b, but there are three additional branches of continuous spectrum (Balakumar and Malik, 1992) which are not visible in the figure; however, these additional branches correspond to

highly-damped, upstream-propagating waves which are not important in the context of boundary layer stability analysis (Tumin, 2007).

4.2 Local Method

The second method of computing the eigenvalues of the linearized Navier-Stokes equations is called the “local” method, meaning that only a single mode of the eigenvalue spectrum is computed rather than an approximation to the entire spectrum, as in the “global” method described previously. The local method is sometimes called the “Mack method,” since Mack was the first to develop and implement this procedure for compressible flows. The method described here closely follows his work (Mack, 1965), but is generalized to include the effects of vibrational nonequilibrium.

For the local analysis, it is convenient to cast the linearized Navier-Stokes equations in the form of 10 first-order differential equations:

$$\frac{d\hat{\mathbf{q}}}{dy} = \mathbf{a}\hat{\mathbf{q}} \quad (4.7)$$

where \mathbf{a} is an 10×10 matrix whose coefficients are derived in Appendix A, and $\hat{\mathbf{q}}$ is the column vector of disturbance variables and their wall-normal gradients:

$$\hat{\mathbf{q}} = \left(\hat{u}, \frac{\partial \hat{u}}{\partial y}, \hat{v}, \hat{p}, \hat{\theta}, \frac{\partial \hat{\theta}}{\partial y}, \hat{w}, \frac{\partial \hat{w}}{\partial y}, \hat{\theta}_v, \frac{\partial \hat{\theta}_v}{\partial y} \right)^T \quad (4.8)$$

The boundary conditions are:

$$\hat{u} = \hat{v} = \hat{w} = \hat{\theta} = \hat{\theta}_v = 0 \quad y = 0 \quad (4.9a)$$

$$\hat{u}, \hat{v}, \hat{w}, \hat{\theta}, \hat{\theta}_v, \hat{p} < \infty \quad y \rightarrow \infty \quad (4.9b)$$

Unlike the global method (Section 4.1), in which Dirichlet boundary conditions were used in the freestream, here a less restrictive and more physically meaningful boundary condition is applied in which the disturbances are required only to remain

bounded as $y \rightarrow \infty$.

4.2.1 Fundamental Solutions

The general solution of Equation 4.7 consists of a linear combination of ten fundamental solutions $\phi_k(y)$, for $k = 1..10$. Each fundamental solution is a 10 element column vector that is a function of y . The fundamental matrix $\Phi(y)$, which has the solutions $\phi_k(y)$ as its columns, then satisfies the differential equation

$$\frac{d\Phi}{dy} = \mathbf{a}\Phi \quad (4.10)$$

The asymptotic behavior of the fundamental solutions as $y \rightarrow \infty$ can be readily determined, since for a planar boundary layer the matrix \mathbf{a} in Equation 4.7 becomes a constant matrix \mathbf{a}_∞ in the freestream. At this condition, Equation 4.7 admits solutions of the form $\exp(i\lambda y)$, where λ is the wall-normal wavenumber, which satisfies the eigenvalue relation

$$(\mathbf{a}_\infty - i\lambda) \phi_\infty = 0 \quad (4.11)$$

The ten eigenvalues λ_k and eigenvectors $\phi_{\infty,k}$ that satisfy this equation then determine the asymptotic behavior of the fundamental solutions ϕ_k as $y \rightarrow \infty$.

The ten fundamental solutions remain linearly independent only if the Wronskian of the system (4.10) is nonzero. Using Abel's identity (Bender and Orszag, 1987), one finds that the Wronskian W obeys the differential equation

$$\frac{dW}{dy} = \text{tr}(\mathbf{a})W \quad (4.12)$$

where the operator $\text{tr}()$ designates the trace of a matrix. This ordinary differential equation has the solution:

$$W(y) = C \exp\left(\int_{y_1}^y \text{tr}(\mathbf{a})dy'\right) \quad (4.13)$$

where C is some constant. Unless one of the diagonal elements of \mathbf{a} is singular, the exponential remains nonzero and the Wronskian is either zero everywhere (i.e., $C = 0$) or it is nonzero everywhere. By inspection of the matrix coefficients listed in Appendix A, it is found that only one coefficient can ever be singular. Specifically, the coefficient a_{44} is singular if the parameter χ given in Equation A.20 is zero. The condition $\chi = 0$ is equivalent to the following:

$$\alpha = \frac{\omega}{\bar{U}} + \frac{iR}{\bar{U}\bar{\mu}\gamma_e M^2(2+r)} \quad (4.14)$$

where r is the ratio of the second viscosity to the shear viscosity (assumed to be constant). The criterion (4.14) can only be satisfied by highly damped modes which are of little practical interest: for spatial analysis α_i must be large (order of R) and positive, while for temporal analysis ω_i must be large and negative. Both of these situations correspond to extremely highly-damped modes. It is difficult to conceive of a meaningful scenario in which Equation 4.14 is true. This being the case, it can be concluded that all diagonal elements of \mathbf{a} are nonsingular, and hence the Wronskian is either zero everywhere or nowhere. The value of the Wronskian can be easily evaluated in the freestream:

$$W_\infty = \det |\Phi_\infty| = \prod_{k=1}^{10} \lambda_k \quad (4.15)$$

This second equality follows from the fact that the determinant of a matrix is equal to the product of its eigenvalues. Unless one of the eigenvalues λ is zero, the Wronskian is nonzero in the freestream and hence, on the basis of the arguments above, nonzero everywhere. This establishes the linear independence of the fundamental solutions $\phi_k(y)$ throughout the entirety of the boundary layer. Cases for which one of the eigenvalues λ is zero are not a concern because modes having this property belong to the continuous spectrum (and thus are damped), whereas in this analysis we are only interested in the discrete modes.

Having determined the asymptotic behavior of the fundamental solutions (Equa-

tion 4.11) and established their linear independence, each of the fundamental solutions can now be numerically computed. This is done by numerically integrating Equation 4.7 from the freestream to the wall, using the vectors $\phi_{\infty,k}$ as the initial conditions in the freestream. The numerical integration is carried out using a fourth order Runge-Kutta routine. For all simulations the number of grid points in the boundary layer is at least 1000. This number has been found to produce grid independent results for Reynolds numbers up to about $R = 6000$, where $R = U_e^* \delta / \nu_e^* = \sqrt{Re_x}$ is the Reynolds number based on boundary layer thickness. The size of the domain used depends on the Mach number, and is selected to be a factor of 1.5-5 larger than δ_{99} . The results obtained are unchanged if the domain is made larger than this, even when the eigenfunctions are slowly decaying outside of the boundary layer.

After integrating the fundamental solutions from the freestream to the wall, the total solution is determined from their linear combination:

$$\hat{\mathbf{q}}(y) = \sum_{k=1}^{10} C_k \phi_k(y) \quad (4.16)$$

Five of the coefficients C_k are immediately determined by requiring that the solutions be bounded as $y \rightarrow \infty$. Since the eigenvalues λ_k in Equation 4.11 appear in pairs having opposite signs, half of the eigenvalues are decaying in the freestream and half are growing. The coefficients C_k belonging to the growing solutions are set to zero.

The remaining linear combination coefficients C_k are determined by applying the boundary conditions from Equation 4.9 at the wall. These boundary conditions are homogeneous and can be satisfied only when an eigenvalue has been found. In order to determine the eigenvalue, the boundary condition $\hat{\theta}(0) = 0$ is replaced by the normalization condition $\hat{p}(0) = 1$. The linear combination coefficients C_k are then

determined by solving the linear system:

$$\begin{bmatrix} \hat{u}_1(0) & \hat{u}_2(0) & \hat{u}_3(0) & \hat{u}_4(0) & \hat{u}_5(0) \\ \hat{v}_1(0) & \hat{v}_2(0) & \hat{v}_3(0) & \hat{v}_4(0) & \hat{v}_5(0) \\ \hat{w}_1(0) & \hat{w}_2(0) & \hat{w}_3(0) & \hat{w}_4(0) & \hat{w}_5(0) \\ \hat{\theta}_{v,1}(0) & \hat{\theta}_{v,2}(0) & \hat{\theta}_{v,3}(0) & \hat{\theta}_{v,4}(0) & \hat{\theta}_{v,5}(0) \\ \hat{p}_1(0) & \hat{p}_2(0) & (0)\hat{p}_3(0) & \hat{p}_4(0) & \hat{p}_5(0) \end{bmatrix} \begin{pmatrix} C_1 \\ C_2 \\ C_3 \\ C_4 \\ C_5 \end{pmatrix} = \begin{pmatrix} 0 \\ 0 \\ 0 \\ 0 \\ 1 \end{pmatrix} \quad (4.17)$$

After solving this system, the temperature fluctuation at the wall is not in general equal to zero, and only reaches zero when an eigenvalue has been found. Therefore vanishing of the wall temperature $|\hat{\theta}(0)|$ is the criterion used to determine when an eigenvalue has been found. The eigenvalue search in the complex plane is accomplished using the secant method. For instance, during a spatial analysis the current guess α_n of the eigenvalue is updated using the formula

$$\alpha_{n+1} = \alpha_n - \hat{\theta}_n(0) \frac{\alpha_n - \alpha_{n-1}}{\hat{\theta}_n(0) - \hat{\theta}_{n-1}(0)} \quad (4.18)$$

These iterations are repeated until $|\hat{\theta}_n(0)|$ falls below a tolerance of 10^{-7} , which indicates that an eigenvalue has been successfully found.

4.2.2 Orthonormalization

An additional difficulty in solving the Equation 4.7 is that the eigenvalues of the matrix \mathbf{a} are widely separated. As a consequence, during the Runge-Kutta integration from the freestream to the wall, errors associated with truncation and finite precision arithmetic cause the fundamental solutions ϕ_k to become linearly dependent in spite of their mathematical independence discussed above. As a result, the matrix in Equation 4.17 becomes ill-conditioned, the linear combination coefficients C_k determined from this equation become inaccurate, and the search for eigenvalues fails to converge or converges to an incorrect value.

Numerous techniques for overcoming this difficulty have been proposed, and one of

the simplest is to conduct orthonormalization at various intervals as the Runge-Kutta integration proceeds (Conte, 1966, Garg, 1980, Davey, 1983). This orthonormalization involves projecting the solutions ϕ_k onto a new, orthonormal basis, which can be easily accomplished using the Gram-Schmidt process. However, in practice one occasionally wishes to reconstruct the eigenfunctions corresponding to a particular eigenvalue. To do so, one must be able to reverse the orthonormalization procedure and revert the solutions back to their original basis.

The procedure used is as follows. As the integration of Equation 4.10 from the freestream to the wall proceeds, the L2 norm $\|\Phi\|$ is monitored. When this norm exceeds a chosen tolerance, usually $10^3 - 10^6$, Φ is projected onto a new orthonormal basis Φ' :

$$\Phi' = \Phi \mathbf{P} \quad (4.19)$$

where \mathbf{P} is an upper triangular matrix whose coefficients are determined using the Gram-Schmidt process. The matrix \mathbf{P} is upper-triangular and invertible, with inverse $\mathbf{R} = \mathbf{P}^{-1}$, a matrix which can be used to return to the original basis. Every time an orthonormalization is carried out, the matrix \mathbf{R} is stored, as is the wall-normal location at which the orthonormalization was performed. Upon completing the eigenvalue search, the eigenfunctions are reconstructed by marching from the wall to the freestream and inverting the orthonormalization, $\Phi = \Phi' \mathbf{R}$ at each location at which orthonormalization was carried out.

The success of this approach can be evaluated by comparing the eigenfunctions computed using the local and global methods. Since these two methods are implemented completely independently, this is a useful means of verifying the analysis. Figure 4.2 compares the eigenfunctions determined by these two approaches, with lines corresponding to the local analysis and symbols coming from the global analysis. The flow is a high enthalpy flow at Mach 4.5, with a freestream temperature of $T_e^* = 1500 \text{ K}$ and a cold wall at $T_w^* = 300 \text{ K}$. The eigenfunctions shown in the figure correspond to the most unstable 2nd mode disturbance, which has a frequency

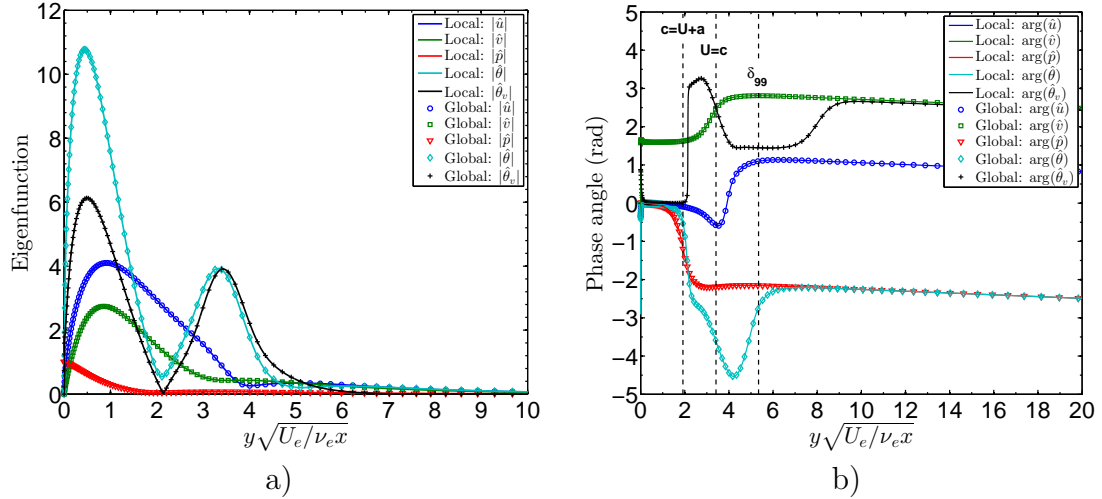


Figure 4.2: Comparison of eigenfunctions calculated using local method (solid lines) and global method (symbols). a) Eigenfunction amplitude; b) Eigenfunction phase angle. Flow is air at $M = 4.5$, $T_e^* = T_{v,e}^* = 1500$ K, $P_e^* = 10$ kPa, $R = 2000$, and $T_w^* = 300$ K.

of $\omega = 0.405$. For both solution techniques, the disturbance eigenfunctions are normalized such that the pressure at the wall is 1.0. For all disturbance components, excellent agreement between the global and local methods is found. This confirms that the technique described above successfully reverses the orthonormalization.

4.3 Freestream Boundary Conditions

The use of the asymptotic boundary condition (4.9) provides a significant advantage over the Dirichlet approximation (4.4) that is used in the global method; if Dirichlet boundary conditions are used then the domain must be much larger than the boundary layer thickness in order to capture the asymptotic behavior of the eigenfunctions in the freestream. Because of this large domain, a highly stretched grid is needed to achieve sufficient resolution of the instability within the boundary layer and near the wall. In contrast, if the asymptotic boundary condition is used then the domain need only be slightly larger than the boundary layer thickness, and hence the grid points are used more efficiently. This feature is especially useful when simulating hypersonic boundary layers with very cold walls; at these conditions the unstable

disturbances can travel supersonically relative to the exterior flow and their eigenfunctions are nearly non-decaying in the freestream (see Section 5.3 for more details). This non-decaying behavior can be captured only by using the asymptotic boundary conditions or a very large domain, and the eigenvalues can be affected if Dirichlet boundary conditions are used with too small a domain.

To demonstrate this phenomenon, Figure 4.3 plots the spatial growth rate as a function of frequency for a high enthalpy boundary layer at Mach 5. The solid line indicates the spatial growth rate from the local stability solver with a domain height of $y_{max}/\delta_{99} = 2.5$ and asymptotic boundary conditions in the freestream. Lines with symbols show the spatial growth rates obtained from the global method using several different domain heights and Dirichlet boundary conditions in the freestream. In each case, 120 wall-normal points are used in the global analysis and the grid points are clustered such that half the points are concentrated below δ_{99} . For this analysis, the full nonlinear spatial eigenvalue problem is solved rather than using the linearized version (Section 4.1).

For low frequencies, $\omega < 0.4$, the global analysis agrees well with the local analysis. However, for larger frequencies, $\omega > 0.4$, the global analysis predicts unphysical oscillations of the growth rate. These oscillations are larger for small domain sizes; they are caused by the Dirichlet boundary conditions forcing the disturbance waves to reach zero at the edge of the domain. As shown in Section 5.3, for $\omega > 0.4$ the unstable disturbances travel supersonically with respect to the freestream and radiate energy outward into the freestream, a process which cannot be captured when Dirichlet boundary conditions are imposed.

Figure 4.4 shows the eigenfunctions determined for two frequencies, $\omega = 0.35$ and 0.45. Results are compared from the global analysis (symbols) and the local analysis (lines). In both cases the domain is small ($y_{max}/\delta_{99} = 2.5$). For the low frequency case, $\omega = 0.35$, the eigenfunctions decay quite rapidly in the freestream. As a consequence, the errors caused by the Dirichlet boundary conditions in the global method are not serious and the agreement between the two methods is reasonably good.

For the higher frequency case, $\omega = 0.45$, the eigenfunctions decay very slowly in

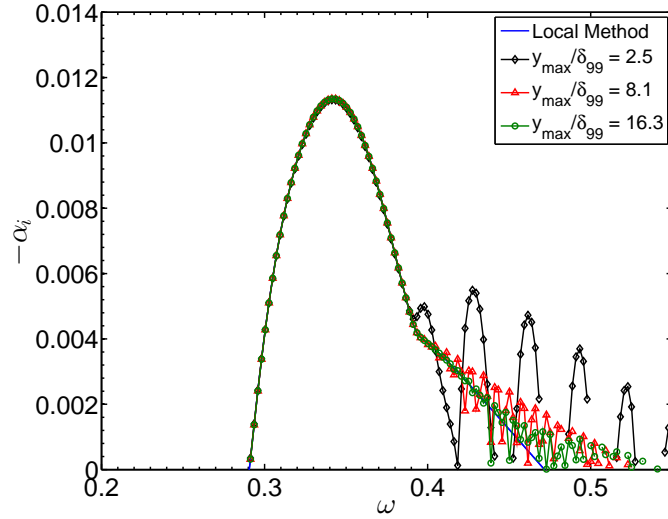


Figure 4.3: Spatial growth rates computed using various domain sizes. Flow is air at $M = 5$, $T_e^* = T_{v,e}^* = 1000$ K, $P_e^* = 10$ kPa, $R = 2000$. Solid line: local method with asymptotic boundary conditions, $y_{max}/\delta_{99} = 2.5$. Symbols: global method with Dirichlet boundary conditions.

the freestream. Although the local and global methods agree reasonably well within the interior of the boundary layer, the freestream behavior from the global method is completely incorrect. This is seen more clearly in Figure 4.5, which magnifies the streamwise velocity eigenfunction. This figure shows that by forcing the disturbances to reach zero at the edge of the domain, spurious waves are introduced in the freestream which influence the eigenvalues obtained. Note that the sharp change in slope at about $y\sqrt{U_e/\nu_e x} = 3$ is located at the critical layer where streamwise velocity \bar{U} and the real part of the phase speed c_r are equal. Although the eigenfunction changes slope abruptly near this point, these results are grid-converged, and the local analysis includes a large number of points in this region so that the numerical solution is smooth.

In many linear stability codes, Dirichlet boundary conditions are applied in both the global analysis and the local eigenvalue refinement. The findings above indicate that care must be taken in interpreting the results obtained, especially when the modes involved travel supersonically with respect to the freestream, since unphysical oscillations of the growth rate can be produced by the Dirichlet conditions.

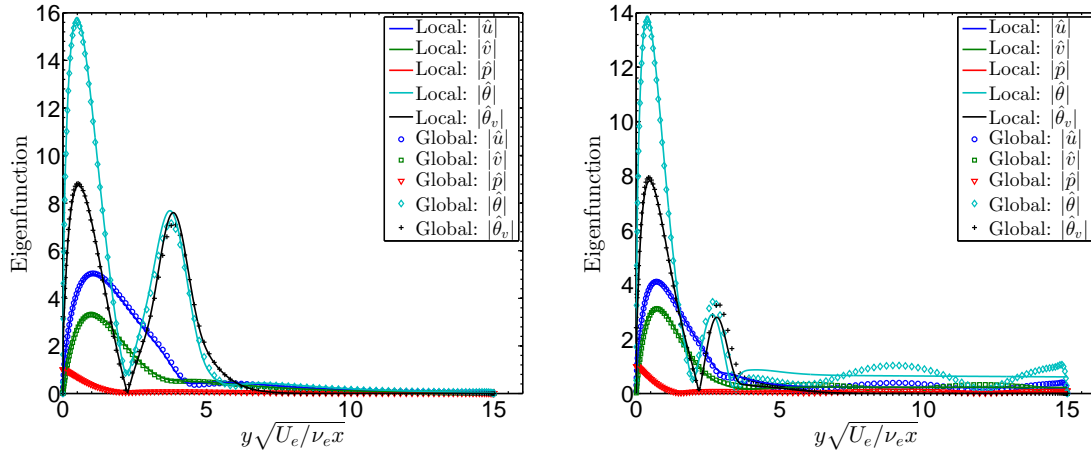


Figure 4.4: Comparison of eigenfunctions from local solver with asymptotic boundary conditions (lines) and global solver with Dirichlet boundary conditions (symbols). Left: $\omega = 0.35$. Right: $\omega = 0.45$. Flow conditions are the same as in Figure 4.3.

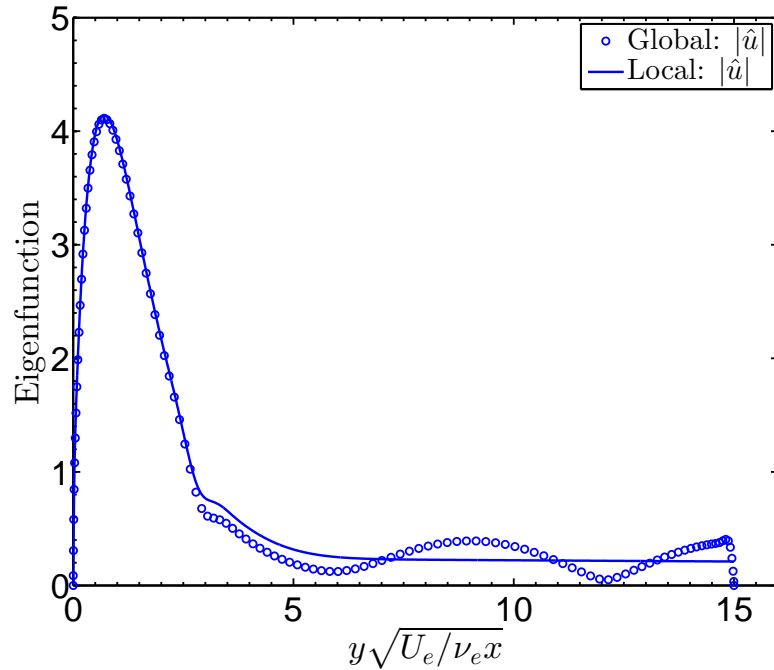


Figure 4.5: Same as RHS of Figure 4.4, but showing only the streamwise velocity eigenfunction $|\hat{u}|$.

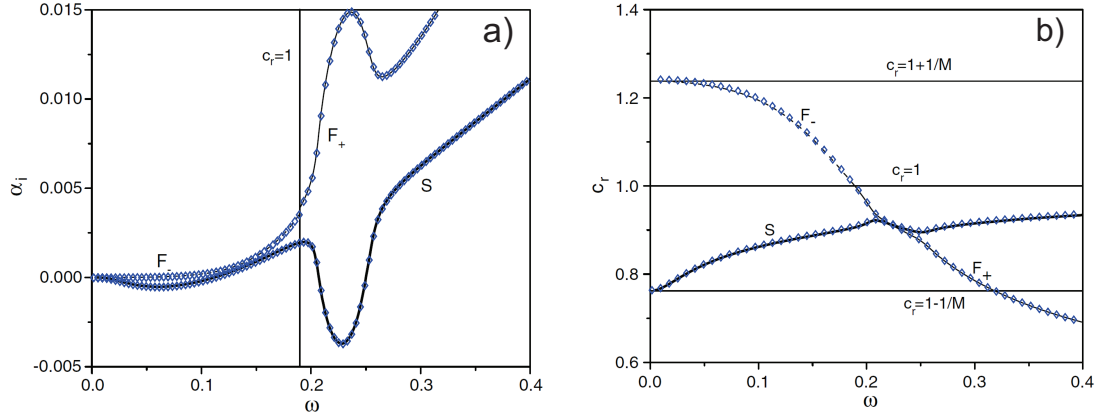


Figure 4.6: Comparison of present stability results (symbols) with those of Fedorov and Tumin (2011). Flow is calorically perfect air with $M = 4.2$, $T_o^* = 300$ K, $R = 2000$, and $T_w^* = T_{ad}^*$. Figure is adapted with permission from Fedorov and Tumin (2011).

4.4 Model Verification

4.4.1 Low enthalpy flow

The present linear stability analysis was verified through comparisons with established results from the literature. The first verification case is flow of a calorically perfect gas over an adiabatic flat plate, which was simulated by Fedorov and Tumin (2011). The flow is at Mach 4.2 with a stagnation temperature of 300 K, Reynolds number of $R = 2000$, Prandtl number of 0.72, and a Sutherland constant of 110.4 K. Figure 4.6 overlays the results from the present stability analysis (symbols) against the results of Fedorov and Tumin (2011) (lines). Excellent agreement is found for both the growth rates (left) and phase speeds (right).

4.4.2 High enthalpy flow

Model verification for higher enthalpy cases was accomplished through comparisons with the predictions of the STABL stability software suite developed at the University of Minnesota (Johnson et al., 1998, Wright et al., 1998, Johnson, 2000). This software conducts linear stability analysis for chemically reacting, nonequilibrium flows, and is also able to integrate the downstream development of unstable modes by solving

the Parabolized Stability Equations (PSE). However, in the following comparisons with the present LST analysis, the PSE integration step is not performed in order to make as direct a comparison as possible. For the sake of comparison, non-parallel terms (those involving derivatives of mean flow variables with respect to x) were also eliminated from the STABL analysis, since these terms are not included in the current LST model. However, all effects of vibrational and chemical nonequilibrium were retained in the STABL calculations.

Examples of stability diagrams from STABL and from the present LST analysis are given in Figure 4.7. The corresponding base flows were plotted previously in Figure 3.3. Figure 4.7a is a fairly low enthalpy flow which is representative of free flight of a slender body at $M = 5$. At the edge of the boundary layer, both the translational and vibrational temperatures are equal to 300 K. Figure 4.7b is a higher enthalpy flow with $T_e^* = T_{v,e}^* = 1500$ K, which is representative of flow in a shock tunnel.

For both cases, close agreement between the LST analysis and the prediction of STABL is observed, although the agreement is slightly poorer for low Reynolds numbers where the present LST analysis predicts slightly larger growth rates. These differences may be caused by the viscous-inviscid interaction at the leading edge of the plate, in which the displacement caused by growth of the boundary layer induces a weak oblique shock. The shock is included in the STABL analysis, but is excluded from our analysis since our base flow is determined from the boundary layer equations rather than the full Navier-Stokes equations. This explanation is consistent with the findings of Chang et al. (1990), who showed that when a shock wave is close to the edge of the boundary layer there is a slight stabilization of the second mode instability. Differences in transport properties also likely contribute to the observed discrepancies: the differences in transport properties are more important at low Reynolds numbers, where viscous effects are greater.

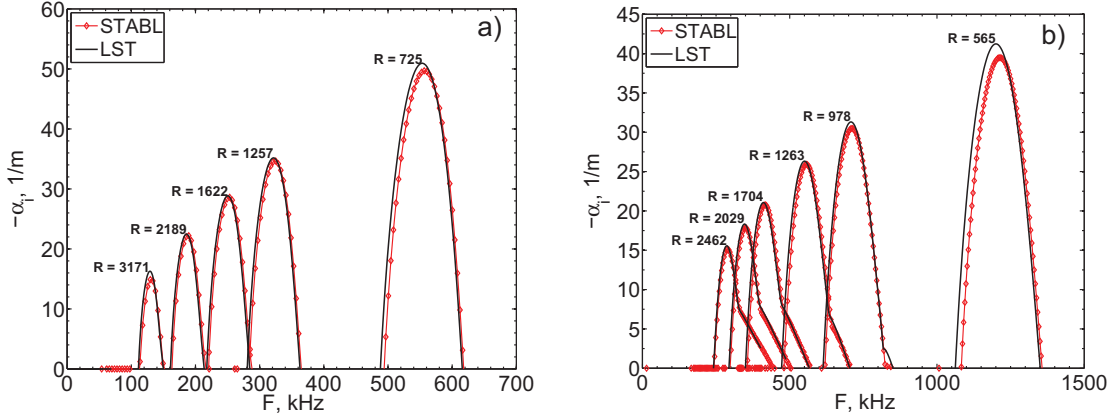


Figure 4.7: Comparisons of spatial growth rates from STABL PSE-Chem ($-\diamond-$) and present LST analysis ($-$). a) Low enthalpy air, $P_e^* = 5$ kPa, $M = 5$, $T_e^* = 300$ K, $T_e^* = T_{v,e}^* = 300$ K; b) High enthalpy air, $P_e^* = 20$ kPa, $M = 5$, $T_e^* = 400$ K, $T_e^* = T_{v,e}^* = 1500$ K.

4.4.3 Chemical Reactions

The present chemically frozen stability analysis might be expected to perform poorly for high enthalpy flows where the temperature in the interior of the boundary layer is large enough to significantly dissociate the gas. For example, it was shown in Figure 2.1 that the enthalpy error of chemically frozen flow starts to become significant at about 2400 K, and this temperature can be significantly exceeded in high enthalpy shock tunnels. However, we have found that for slender bodies in air, the stability characteristics at these conditions can still be predicted reasonably well under the assumption of a chemically inert gas.

Figure 4.8 shows mean boundary layer profiles and stability calculations for a high enthalpy boundary layer with an edge temperature of 2500 K and Mach number of $M = 5$. This corresponds to a stagnation enthalpy of about 15 MJ/kg, which is close to the maximum stagnation enthalpy achievable in reflected shock tunnel facilities like the T5 facility at Caltech. For this case, the peak temperature within the boundary layer exceeds 3500 K, which is well above the limit at which dissociation of O_2 becomes significant. The chemically reacting Navier-Stokes simulations reveal that at $R = 1500$ the mass fraction of atomic oxygen reaches a peak value of 0.72% in the interior of the boundary layer. The mean boundary layer profiles (Figure 4.8a) are in reasonable

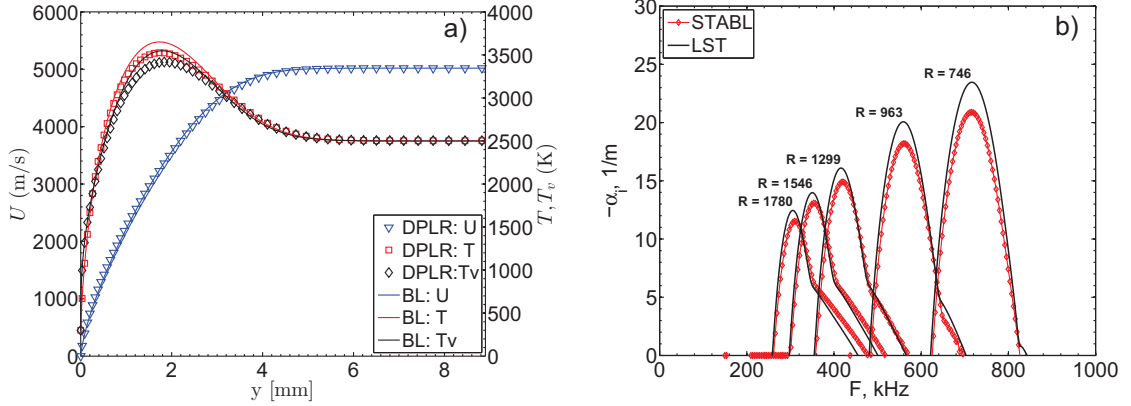


Figure 4.8: High enthalpy comparison between current method and STABL software. Air, $P_e^* = 20$ kPa, $M = 5$, $T_w^* = 300$ K, $T_e^* = T_{v,e}^* = 2500$ K. a) Comparison of boundary layer profiles at $R = 1500$ from STABL Navier-Stokes solver (symbols) and boundary layer code (solid lines). Profiles are velocity (∇), translational/rotational temperature (\square), and vibrational temperature (\diamond). b) Comparison of spatial growth rates from STABL PSE-Chem (symbols) and present LST analysis (solid lines). Only 2D waves are included.

agreement with the Navier-Stokes simulations from STABL, although the boundary layer code produces noticeably greater temperatures by neglecting chemistry. The difference in peak temperature is large at the high Reynolds number shown, but is much smaller at lower Reynolds numbers, where the chemical reactions have not progressed as far towards equilibrium.

In Figure 4.8b, the chemically frozen stability predictions from the present method are compared with the chemically reacting results from STABL. The agreement is reasonably good, especially considering that we have neglected chemical reactions and are using different transport property models. The discrepancy is largest near the leading edge of the plate and may again be the result of the viscous-inviscid interaction and transport properties. These results suggest that despite the high temperatures in the interior of the boundary layer, the present chemically frozen analysis can be used to study the stability of flows of air over slender bodies in high enthalpy shock tunnels without incurring serious errors. This finding can be explained in part by the analysis of [Fujii and Hornung \(2003\)](#), which showed that in air at 1000-3000 K, the absorption of sound waves caused by thermochemical nonequilibrium occurs at frequencies

much lower than those of second mode disturbances in hypervelocity boundary layers. That is, the instability waves are of such high frequency that thermochemical energy transfer is negligible.

It must be emphasized that the conclusions stated above regarding the relative unimportance of chemical reactions are only valid for flows of air over slender bodies. For other gases having different dissociation energies and different reaction rates, the situation may be different. Also for blunt bodies, the low flow velocities and extremely high temperatures that exist behind the bow shock may lead to more significant chemical effects and the frozen analysis may no longer be adequate.

Chapter 5

Modal Stability Results ¹

This chapter describes the results of modal stability calculations for high enthalpy boundary layers. These results are based primarily on the “local” method of stability analysis described in Chapter 4. In the first section of this chapter, the basic stability characteristics of hypersonic boundary layers are reviewed. Then in Sections 5.2-5.4, the stability properties of high enthalpy flows of air are reported. Finally, Sections 5.5-5.6 investigate the influence of vibrational relaxation on the stability behavior for flows of air and carbon dioxide.

5.1 Stability Characteristics

5.1.1 Dispersion curves

We begin by introducing and reviewing the basic stability characteristics of hypersonic boundary layers. An example of a typical dispersion curve is given in Figure 5.1, which shows the spatial growth rates $-\alpha_i$ and phase speeds c_r as a function of frequency ω for flow over a flat plate at $M = 5$, $R = 2000$. Here $R = U_e^* \delta / \nu_e^* = \sqrt{Re_x}$ is the Reynolds number based on boundary layer thickness. This example is a low enthalpy flow with a cold freestream (65.15 K) and an adiabatic wall, which models the wind tunnel experiments of Kendall (1975). The same flow conditions were considered by Ma and Zhong (2003a) and the results shown here are identical to theirs to within

¹Much of the material presented in this chapter is taken from Bitter and Shepherd (2015).

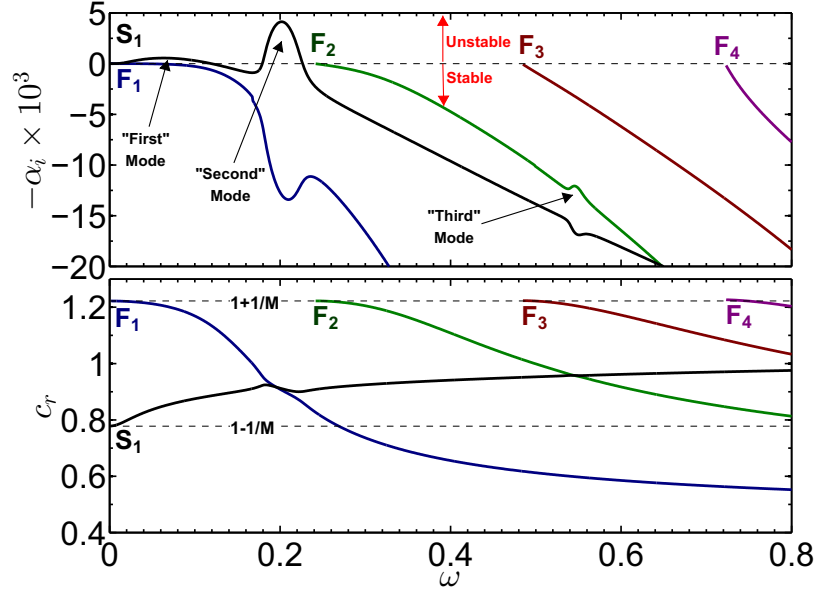


Figure 5.1: Spatial growth rates (top) and phase speeds (bottom) for low enthalpy flow of air with $M = 4.5$, $R = 2000$, $T_e^* = 65.15$ K, $P_e^* = 727$ Pa, adiabatic wall. Flow conditions are modeled after [Ma and Zhong \(2003a\)](#).

plotting accuracy.

The phase speed diagram in [Figure 5.1](#) features an infinite sequence of modes labeled F_n which “cut in” as the frequency increases. By “cut in” it is meant that these modes transition from the continuous spectrum to the discrete spectrum. For instance, the mode F_2 does not exist as a discrete mode until $\omega > 0.24$. Each of these modes cuts in with a dimensionless phase speed of $c_r = 1 + 1/M$, which is the speed of fast acoustic waves in the freestream, and hence these modes are termed “fast modes” and designated F_1 , F_2 , etc. in order of increasing frequency. Each additional mode that cuts in is characterized by an additional zero in the real part of the pressure eigenfunction, with mode F_n having $n - 1$ zeros. There is an additional mode labeled S_1 which tends to a phase speed of $1 - 1/M$ as $\omega \rightarrow 0$. This mode is termed the slow mode.

As the frequency increases, the phase speed of the slow mode sequentially crosses that of each of the fast modes. At these crossing points, the phase speeds and eigenfunctions of the slow and fast modes are nearly identical, which leads to a “synchronism” between the modes, as is extensively discussed by [Fedorov and Khokhlov](#)

(2001). Near the synchronism, one of the two modes experiences amplification and the other attenuation; for example, when the phase speeds of modes F_1 and S_1 cross, S_1 becomes unstable and F_1 becomes highly damped. This gives rise to instabilities known as the “second” and “third” mode instabilities as indicated in the figure, as well as higher modes at higher frequencies. As discussed by Fedorov and Tumin (2011), this terminology can be misleading since the “first mode”, “second mode”, and higher modes are not modes in the mathematical sense, i.e., they are not eigenmodes of the linearized Navier-Stokes equations (modes F_n and S_1 are true eigenmodes). However, the terms “first mode” and “second mode” have become established in the literature and will be used here as well.

The stability diagram shown in Figure 5.1 was constructed for a fixed Reynolds number of $R = 2000$ and a variable frequency ω . However, it is often more useful to consider the downstream propagation of a disturbance having a fixed frequency and a varying Reynolds number. The frequency of such a disturbance is usually described by the nondimensional frequency parameter F , which is defined as:

$$F = \frac{\omega}{R} = \frac{2\pi f^* U_e^{*2}}{\nu_e^*} \quad (5.1)$$

where f^* is the dimensional circular frequency in Hz. The difference between the frequencies ω and F is that ω is nondimensionalized by the freestream velocity and the local boundary layer thickness, whereas F is normalized by the freestream velocity and the viscous length ν_e^*/U_e^* . Examples of dispersion curves presented in this manner are given in Figure 5.2. As this figure shows, each frequency is unstable at a different location in the boundary layer, with lower frequencies being unstable at higher Reynolds numbers. For these flow conditions the instability is predominantly second mode, although for $F = 1 \times 10^{-4}$ there is a slight first mode instability for about $500 < R < 1000$.

The stability characteristics are more easily visualized on a contour plot in which the spatial growth rate $-\alpha_i$ is parameterized by the Reynolds number R and the frequency F . Such a diagram is given in Figure 5.3, with only contour levels greater

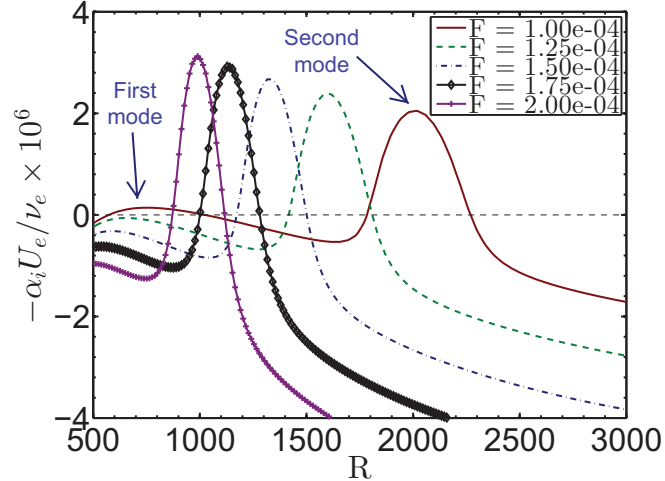


Figure 5.2: Spatial growth rates as a function of Reynolds number for several frequencies F . The flow is air with $M = 4.5$, $T_e^* = 65.15$ K, $P_e^* = 727$ Pa, adiabatic wall. Flow conditions are modeled after [Ma and Zhong \(2003a\)](#).

than zero shown. There are two regions of instability. The lower region of instability is the first mode, which is only unstable at low frequencies and whose unstable frequency band decreases in width as the Reynolds number increases. The upper region of instability is the second mode, which is unstable only for a narrow band of frequencies or Reynolds numbers. The most unstable second mode frequency is strongly dependent on the Reynolds number and is proportional to $1/R$.

5.1.2 The N Factor

For a particular frequency and Reynolds number, the locally-parallel stability analysis presented above yields only the local growth rate, $-\alpha_i$. However, in predicting boundary layer transition one is less interested in the local growth rate and more interested in the net amplification that a disturbance experiences as it travels downstream. An intuitive method of predicting this net growth is to simply integrate the spatial growth rate as a function of downstream distance. The amplitude A of the disturbance relative to its initial amplitude A_o at some point x_o is then

$$\frac{A(x)}{A_o} = \exp \left(\int_{x_o}^x -\alpha_i(x') dx' \right) \quad (5.2)$$

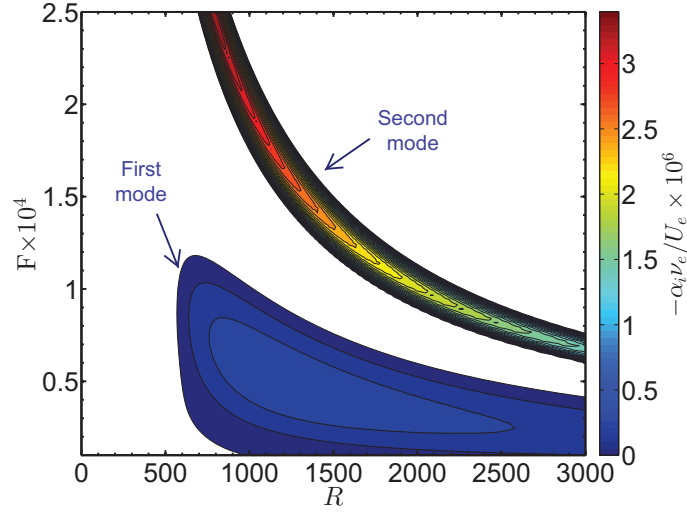


Figure 5.3: Stability diagram for a flow of air with $M = 4.5$, $T_e^* = 65.15$ K, $P_e^* = 727$ Pa, adiabatic wall.

This procedure is also motivated by the method of multiple scales (Nayfeh, 1980) in which the disturbances are described by a rapidly-varying length scale x and a slowly-varying scale $X = \epsilon x$, where $\epsilon = \delta_L/L$ is the ratio of the Blasius boundary layer thickness to the length L of the plate or cone. According to the method of multiple scales, the disturbance vector $\hat{\mathbf{q}}$ is decomposed into a slowly-varying amplitude coefficient $C(X)$ multiplied by a shape function $\hat{\mathbf{Q}}$ and a rapidly-varying exponential using an expansion in powers of ϵ :

$$\hat{\mathbf{q}} = C(X) \left[\hat{\mathbf{Q}}_0(X, y) + \epsilon \hat{\mathbf{Q}}_1(X, y) + \dots \right] \exp \left(\int i\alpha(x) dx + i\beta z - i\omega t \right) \quad (5.3)$$

At order ϵ^0 , the amplitude coefficient $C(X)$ is arbitrary and the variation in amplitude of the disturbance depends solely on the exponential, which leads to the relation (5.2). Thus Equation 5.2, in addition to having intuitive appeal, derives from the lowest order approximation of a non-parallel multiple-scales analysis. At higher orders of approximation, the variation of the amplitude coefficient $\partial C/\partial X$ also contributes to the disturbance growth and hence constitutes a nonparallel correction.

Given the large levels of amplification that can occur in a boundary layer, it is often convenient to describe the amplification in terms of the “N factor”, which is

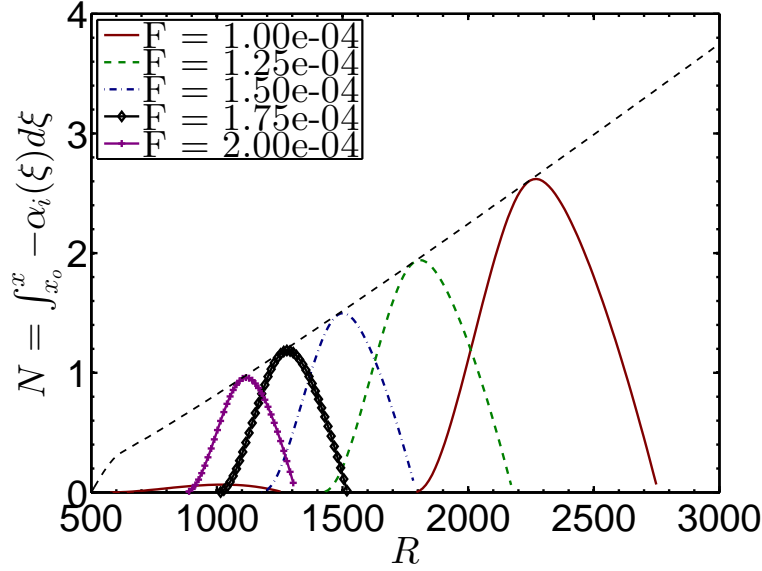


Figure 5.4: N Factor integrals for several frequencies F . The flow is air with $M = 4.5$, $T_e^* = 65.15$ K, $P_e^* = 727$ Pa, adiabatic wall.

just the natural logarithm of the amplification:

$$N(x) \equiv \ln \left(\frac{A(x)}{A_o} \right) = \int_{x_o}^x -\alpha_i(x') dx' \quad (5.4)$$

Examples of N factors corresponding to Figure 5.2 are given in Figure 5.4. In this figure the N factors for each frequency have been scaled such that $N = 0$ (or equivalently, $A = A_o$) when the that frequency first becomes unstable. The envelope of all the curves in Figure 5.4 is called the “maximum N factor” and indicates the maximum possible amplification of any discrete mode in the flow, according to the linear, spatial, locally-parallel theory. The maximum N factor scales approximately linearly with the Reynolds number except for a small deviation at low Reynolds numbers.

The maximum N factor (maximized over all frequencies) is often used to correlate experimental measurements of the transition distance with stability calculations, an approach which was pioneered by [Smith and Gamberoni \(1956\)](#). For example, boundary layer transition in conventional wind tunnels is usually observed at the Reynolds number for which $N = 5-10$, which corresponds to a disturbance amplification of 150-22,000. Therefore it is often assumed that transition will occur at some “critical

N factor of transition” in the range of 5-10, where the precise value of the critical N factor is calibrated using experimental data. This method of estimating transition is known in the literature as the e^N method.

Of course, the reality is that transition occurs when the disturbances reach a large enough amplitude that nonlinear interactions become important, so the actual amplitude A is more relevant to transition than the amplification ratio A/A_o or N . An ideal transition prediction method would therefore couple the amplifications predicted here with initial amplitudes obtained from receptivity calculations based on known disturbance sources in the flow. Unfortunately, theories of receptivity have not yet been developed to the point where this is feasible, and the idea of a “critical N factor” for transition is used instead. But because this method does not account for the initial disturbance amplitudes, the precise value of N at which transition occurs is different for each flow geometry and wind tunnel facility. However, there is some evidence that the e^N method described above has predictive value once calibrated to a particular flow configuration (Schneider, 2015).

5.2 High and low enthalpy flows

Many of the differences between high and low enthalpy flows can be illustrated by comparing the low enthalpy dispersion curve of Figure 5.1 with that of a higher enthalpy flow in Figure 5.5. The flow conditions in these two figures are identical except for the ratio of wall temperature to edge temperature: Figure 5.1 has an adiabatic wall ($T_w^*/T_e^* = 4.4$) and a cold freestream of $T_e^* = 65$ K, whereas Figure 5.5 has a cold wall at $T_w^* = 300$ K relative to the edge temperature of $T_e^* = 1500$ K. Figures 5.1 and 5.5 are representative of flow conditions in a continuous-run hypersonic wind tunnel and a reflected shock tunnel, respectively. By comparing Figures 5.1 and 5.5, several differences are notable:

1. The frequency of the second mode instability is roughly a factor of two larger for the high enthalpy flow. This illustrates that the second mode frequency is

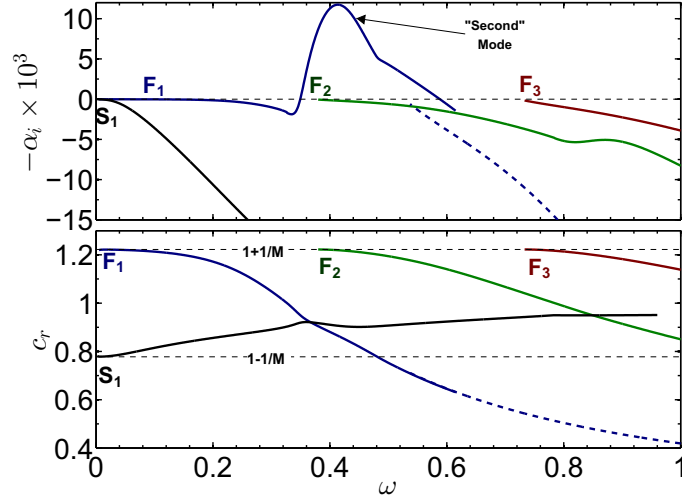


Figure 5.5: Spatial growth rates (top) and phase speeds (bottom) for high enthalpy flow of air with $M = 4.5$, $R = 2000$, $T_e^* = T_{v,e}^* = 1500$ K, $T_w^* = 300$ K, $P_e^* = 10$ Pa.

tuned to the boundary layer thickness, which is a factor of 2.5 thinner for the high enthalpy case.

2. The maximum spatial growth rate is a factor of 2.9 larger for the high enthalpy case. It is well known that the second mode instability is destabilized by cooling of the wall. It will be seen in Section 5.4.2 that, like the frequency, the spatial growth rate scales approximately inversely with the boundary layer thickness.
3. There is no first mode instability for the high enthalpy case. It is well known that the first mode is stable when the wall temperature is significantly smaller than the adiabatic wall temperature.
4. For the low enthalpy case, mode S_1 is unstable while for the high enthalpy case, mode F_1 is unstable. This behavior has also been observed by Fedorov and Tumin (2011), who determined that the second and higher mode instabilities are associated with pairs of branch points in the complex ω plane. The locations of these branch points are functions of Mach number, Reynolds number, wall temperature, and other parameters. As the real frequency ω increases, either mode F_1 or S_1 can be unstable depending on whether the dispersion curve passes above or below these branch points. Although the identity of the unstable mode

is different, the instability behavior does not depend on which of the two modes is unstable.

5. In the high enthalpy case, there is an abrupt change in slope of the second mode unstable region at about $\omega = 0.5$ which leads to a wider range of unstable frequencies compared to the low enthalpy case.
6. In Figure 5.5, the mode labeled F_1 ceases to exist for frequencies greater than about $\omega = 0.62$ and a new, related mode (dashed line) appears at $\omega = 0.54$. These two modes have nearly the same phase speed over the frequency range $0.54 < \omega < 0.62$ for which they both exist.

The first four differences between Figures 5.1-5.5 are well-known, but the last two differences have not been widely reported in the literature. Although a similar kink in the dispersion curve (#5 above) is visible in the results of Klentzman and Tumin (2013) for high enthalpy flows of oxygen, the causes or implications of this phenomenon were not investigated. Analogous behavior has also been observed in the context of boundary layers with injection (Fedorov et al., 2014) and with porous walls (Fedorov et al., 2011, Bres et al., 2013). As will be seen in the sections that follow, differences 5-6 between high and low enthalpy flow that were mentioned above are caused by unstable disturbances propagating supersonically with respect to the freestream fluid.

5.3 Supersonic Unstable Modes

5.3.1 Shape of Dispersion Curve

We first investigate the sharp change in slope of the dispersion curve observed in Figure 5.5. Figure 5.6 shows the growth rates and phase speeds for flow at $M = 5$ and $R = 2000$. Three cases are shown with freestream temperatures of 300, 1000, and 1500 K and with the wall temperature fixed at 300 K in all cases. As the ratio T_w^*/T_e^* decreases, a kink appears in the high-frequency end of the growth rate curve

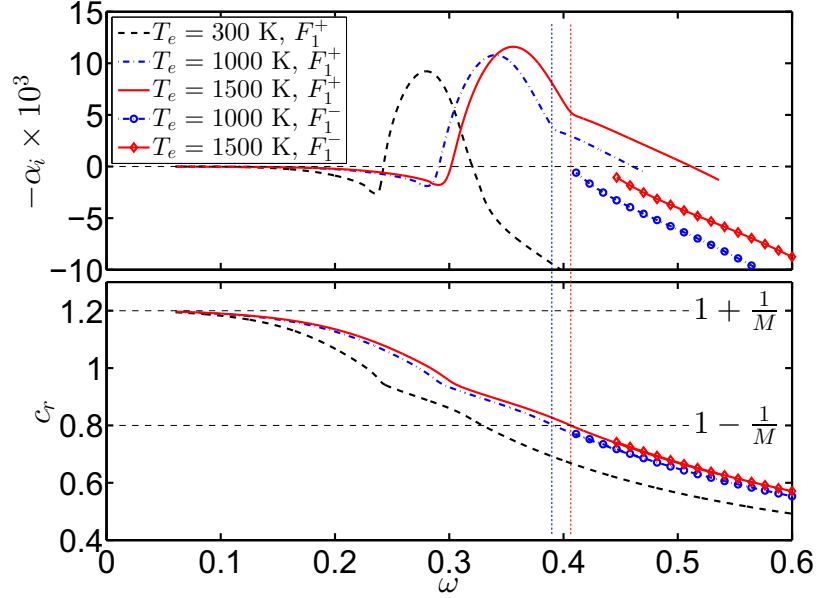
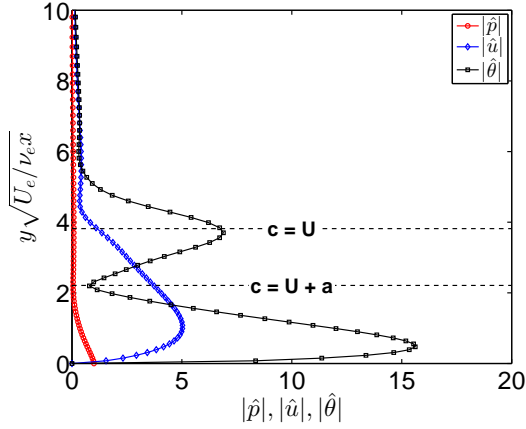


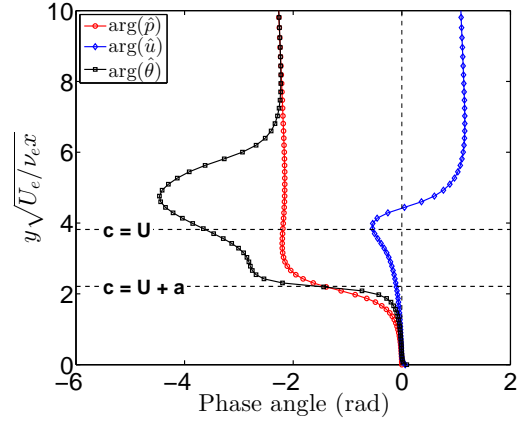
Figure 5.6: Effect of wall cooling on the spatial growth rate (top) and phase speed (bottom). For all cases, the gas is air, $M = 5.0$, $R = 2000$, $T_w^* = 300$ K, $P_e^* = 10$ kPa. Lines with symbols designate an additional mode that appears when $T_w^* \ll T_e^*$.

and the width of the unstable region increases. For each case, the frequency at which the kink occurs is marked by a vertical dashed line. From the intersection between these vertical lines and the phase speed diagram below, one can see that the change in slope of the growth rate curve occurs precisely when the dimensionless phase speed falls below $1 - 1/M$. That is, the change in shape of the dispersion curve occurs when the unstable modes travel supersonically relative to the freestream. Supersonic modes can exist for all wall temperature conditions, but they only become unstable when the wall is highly cooled, usually (but not necessarily) below the freestream temperature. This behavior was also encountered by [Chang et al. \(1997\)](#) in their study of chemically reacting, high enthalpy flow over a wedge, and the existence of supersonic, unstable modes was also briefly mentioned by [Mack \(1969, 1987\)](#) for the inviscid case.

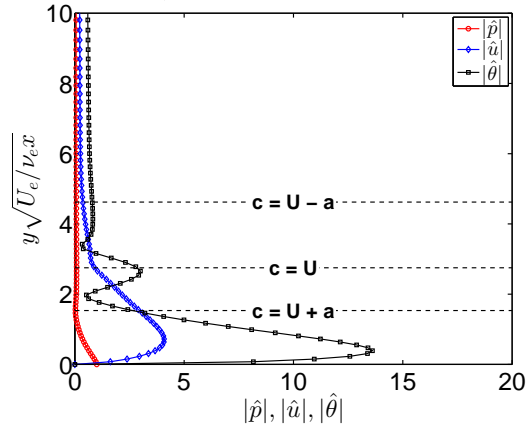
The eigenfunctions corresponding to two values of ω from Figure 5.6 are shown in Figure 5.7 with $T_e^* = 1500$ K. In each case, the locations of the critical layer ($c_r = \bar{U}$) and the sonic lines $c_r = \bar{U} \pm \bar{a}$ are indicated by horizontal dashed lines. For $\omega = 0.35$ (just before the kink in the dispersion curve), the phase speed is above $c_r > 1 - 1/M$



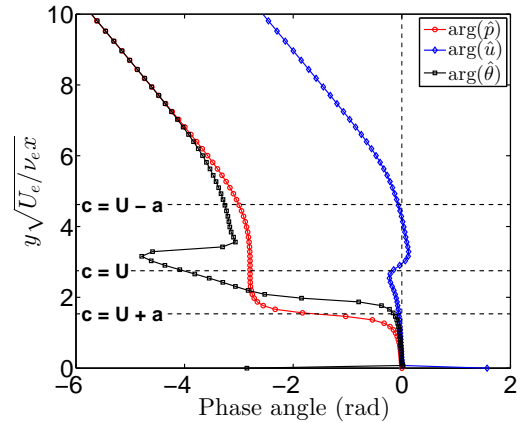
a) Eigenfunction amplitude for subsonic mode, $\omega = 0.35$



b) Eigenfunction phase angle for subsonic mode, $\omega = 0.35$



c) Eigenfunction amplitude for supersonic mode, $\omega = 0.45$



d) Eigenfunction phase angle for supersonic mode, $\omega = 0.45$

Figure 5.7: Eigenfunction amplitude and phase at two points along the dispersion curve in Figure 5.6. Air, $R = 2000$, $T_e^* = 1500$ K, $T_w^* = 300$ K, $M = 5.0$.

and only one sonic line exists, but for $\omega = 0.45$ (just after the kink) there are two sonic lines because $c_r < 1 - 1/M$. Between these two lines the disturbance is traveling subsonically relative to the fluid, but outside of these lines the disturbance travels supersonically.

From Figure 5.7 one can see that for $\omega = 0.45$ the eigenfunctions decay very slowly in the freestream. This is highlighted by the contours of the temperature disturbance given in Figure 5.8. In the interior of the boundary layer, the structure is similar for $\omega = 0.35$ and 0.45 , and a large peak in temperature is visible at the critical layer. For $\omega = 0.35$, the waves decay rapidly in the freestream, but for $\omega = 0.45$ the second

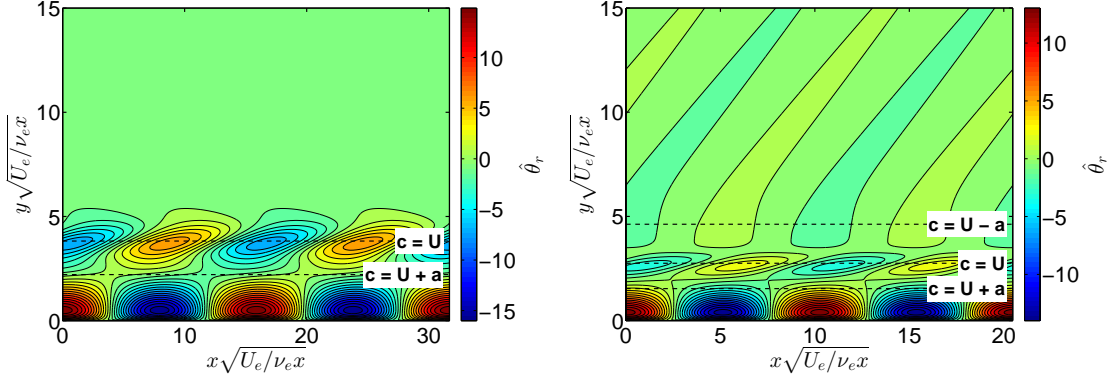


Figure 5.8: Contours of temperature fluctuations at two points along the dispersion curve in Figure 5.6. Air, $R = 2000$, $T_e^* = 1500$ K, $T_w^* = 300$ K, $M = 5.0$. Left: $\omega = 0.35$, subsonic mode. Right: $\omega = 0.45$, supersonic mode.

sonic line acts as a turning point, leading to oscillatory waves that are radiated into the freestream. The same behavior in the freestream is also observed in the pressure and velocity (not shown).

This non-decaying behavior can be anticipated from the compressible Rayleigh equation for the pressure (see Mack (1969), Lees and Lin (1946), or Lees and Reshotko (1962)), which describes the wall-normal variation of pressure disturbances for an inviscid flow:

$$\frac{d^2 \hat{p}}{dy^2} - \left(\frac{2\bar{U}'}{\bar{U} - c} - \frac{\bar{T}'}{\bar{T}} \right) \frac{d\hat{p}}{dy} - \alpha^2 \left(1 - \frac{M^2(\bar{U} - c)^2}{\bar{T}} \right) \hat{p} = 0 \quad (5.5)$$

Here \bar{U}' and \bar{T}' are the wall-normal gradients of the mean velocity and temperature and $c = \omega/\alpha$ is the complex phase speed. In the freestream, where there are no gradients and $\bar{U} = \bar{T} = 1$, the Rayleigh equation reduces to

$$\frac{d^2 \hat{p}}{dy^2} - \alpha^2 \left[1 - M^2(1 - c)^2 \right] \hat{p} = 0 \quad (5.6)$$

which has the solution

$$\hat{p} = \exp \left(\alpha \sqrt{1 - M^2(1 - c)^2} y \right) \quad (5.7)$$

In evaluating the solution, the branch of the square root must be chosen such that the

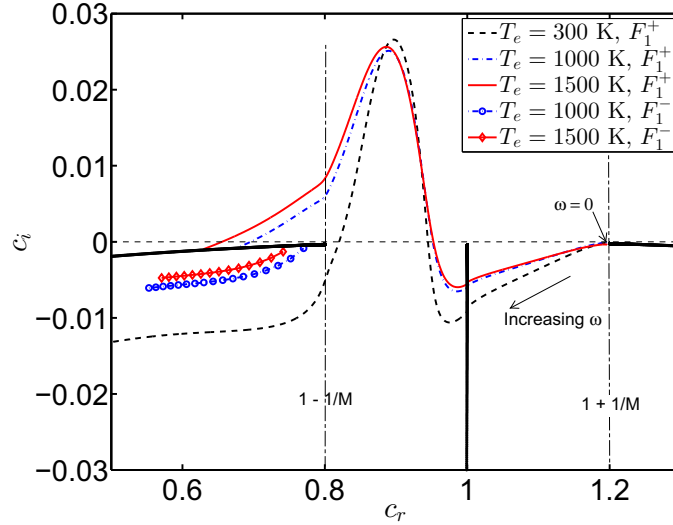


Figure 5.9: Map of real and imaginary parts of phase speed in the complex plane. Then flow is air at $M = 5.0$ and $R = 2000$. Solid black lines correspond to the continuous spectra evaluated at $\omega = 0.4$. Lines with symbols designate an additional mode that appears when $T_w^* \ll T_e^*$.

real part of the exponential's argument is negative so that the pressure is bounded. In a typical boundary layer flow, $|c_i| \ll |c_r|$ and $|\alpha_i| \ll |\alpha_r|$. Consequently, the pressure is mainly exponentially decaying if $c_r > 1 - 1/M$ with slight oscillations arising from the imaginary parts of α and c . Conversely, for supersonic modes (having $c_r < 1 - 1/M$) the solution is mainly oscillatory, with slight damping caused by the imaginary parts of α and c . Therefore slowly-decaying eigenfunctions can always be expected for supersonic modes at high Reynolds numbers.

Figure 5.6 showed that cases which develop a supersonic unstable mode also experience a discontinuity in the dispersion curve. As the frequency increases, the fast mode (labeled F_1^+ in the figure) disappears and a new mode (labeled F_1^-) appears. To further investigate this effect, the real and imaginary parts of the complex phase velocity are plotted for mode F_1 in Figure 5.9. The data are exactly the same as in Figure 5.6, except that now the real and imaginary parts of the phase speed are plotted with ω as a parameter along the curves. Also shown in the figure are three thick black lines which mark the branch cuts corresponding to the continuous spectra; the two nearly horizontal branches are the acoustic branch cuts, while the vertical

branch near $c_r = 1$ (which is actually two overlapping branches) corresponds to vorticity and entropy waves. Further discussion about the location of these branch cuts and methods for their computation are available from [Balakumar and Malik \(1992\)](#). It should be noted that the continuous spectrum is a (weak) function of ω , and the spectra plotted in [Figure 5.9](#) are evaluated at a single value of $\omega = 0.4$.

At $\omega = 0$, the mode F_1^+ is a neutral wave with phase speed $c_r = 1 + 1/M$ which originates at the branch point of the fast acoustic branch cut. As indicated by the arrow in [Figure 5.9](#), as the frequency increases the mode's phase speed reduces and it becomes damped. As the mode crosses the branch cut at $c_r \sim 1$, the growth rate suffers a small jump while real part of α remains nearly continuous. This phenomenon is discussed further by [Fedorov and Khokhlov \(2001\)](#), who showed that the synchronism between the eigenvalue and the vorticity/entropy waves of the continuous spectrum causes the mode F_1 to be especially receptive to entropy spots and vortical freestream disturbances at this condition.

As the frequency is increased further, the mode becomes unstable. For the case with $T_e^* = 300$ K, the mode becomes stable again before the phase speed falls below $1 - 1/M$, so the mode passes below the slow acoustic branch point in the complex plane. This is typical of boundary layers that are adiabatic or have wall temperatures greater than the freestream temperature. In contrast, for the cases with $T_e^* = 1000$ and 1500 K, the mode remains unstable for $c_r < 1 - 1/M$ and therefore passes above the branch point of the slow acoustic waves.

Because the mode with $T_e^* = 1000$ or 1500 K passes above the branch point, it must eventually cross the slow acoustic branch cut. When this happens, the mode coalesces with the branch cut and ceases to be a discrete mode; however, a new mode emerges from the other side of the branch cut. This new mode emerges from the branch cut at a slightly lower frequency than the one at which coalescing mode disappears. The modes on the top and bottom of the branch cut are distinguished by the labels F_1^+ and F_1^- , similar to the notation used by [Fedorov and Tumin \(2011\)](#) to describe modes crossing the branch cut at $c_r \sim 1$.

This crossing of the branch cut results in a synchronism between the instability

mode and acoustic disturbances in the freestream. This is similar to the synchronism with vorticity/entropy waves that occurs when the branch cut at $c_r = 1$ is crossed (Fedorov et al., 2013, Fedorov and Khokhlov, 2001), which has been found to produce increased receptivity to vorticity and entropy spottiness. The synchronism identified here is expected to cause a similar effect, but with enhanced receptivity to acoustic disturbances in the freestream rather than vorticity/entropy disturbances. However, unlike the vorticity/entropy synchronism which occurs upstream of the lower neutral branch, the synchronism with freestream acoustic waves takes place downstream of the upper neutral branch. As a result, modes excited in this manner by freestream acoustic waves are unlikely to experience amplification. Nevertheless, the synchronism can still affect the downstream development of amplified waves, which may be important during the nonlinear stages of transition.

5.3.2 Effect of Reynolds and Mach Numbers

In Figure 5.6, it was shown that the supersonic, unstable modes only appear when the wall is sufficiently cold. In this section we investigate also how the Reynolds number and Mach number influence these supersonic modes. Figure 5.10a compares the spatial growth rates for a high enthalpy boundary layer at several different Reynolds numbers. For low enough Reynolds numbers, the mode remains subsonic throughout the entire unstable region, but for higher R the “tail” on the dispersion curve appears and grows considerably larger as the Reynolds number is further increased.

As can be noted from Figure 5.10a, at higher Reynolds numbers the supersonic modes contribute significantly to the area under the dispersion curve, which is related to the N factor distribution. This brings into question whether the supersonic modes significantly influence the N factors. Figure 5.10b shows the N factor envelope curves for a cold wall case with $M = 5$, $T_e^* = 1500$ K. Two envelope curves are included in this figure: the dashed red line excludes growth rates having frequencies above $\omega = 0.4$, while the solid black line is the full N factor curve. The difference between the two curves then indicates the contribution of supersonic modes. Clearly the supersonic

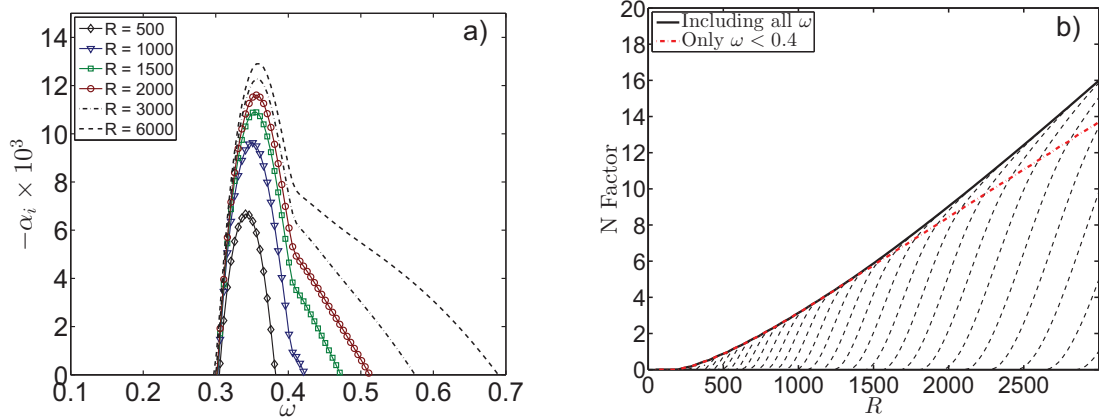


Figure 5.10: a) Effect of Reynolds number on the shape of the dispersion curve for a cold-wall case in air: $M = 5.0$, $T_e^* = 1500 \text{ K}$, $T_w^* = 300 \text{ K}$, $P_e^* = 20 \text{ kPa}$. b) N factor curve corresponding to a). Heavy black line is the complete N factor curve. Dot-dashed red line includes only values of $\omega < 0.4$.

modes do not contribute much to the N factor until the Reynolds number exceeds about 1500. However, at this point the N factor is already fairly high, reaching the level of 5-10 at which transition is typically observed experimentally. This suggests that the supersonic modes do not significantly increase the level of amplification, despite their influence on the shape and behavior of the dispersion curve.

Lastly, the effect of the Mach number on the stability of highly-cooled flows is considered. Figure 5.11 shows dispersion curves for several Mach numbers with $T_e^* = 1500 \text{ K}$ and $T_w^* = 300 \text{ K}$. The left figure is for a lower Reynolds number of $R = 1000$, while the right figure is $R = 2000$. These plots reveal that the supersonic unstable modes are most prominent for $M = 5$. At $R = 1000$, the supersonic mode is only slightly visible for $M = 5$, but at higher R it is present over a wide range of Mach numbers and is most significant for $M = 5$.

5.4 Stability Trends in Air

This section summarizes the effects of wall temperature and Mach number on the stability characteristics of slender bodies in air. Although the results of numerous stability calculations for flat plates and cones in air have been reported in the liter-

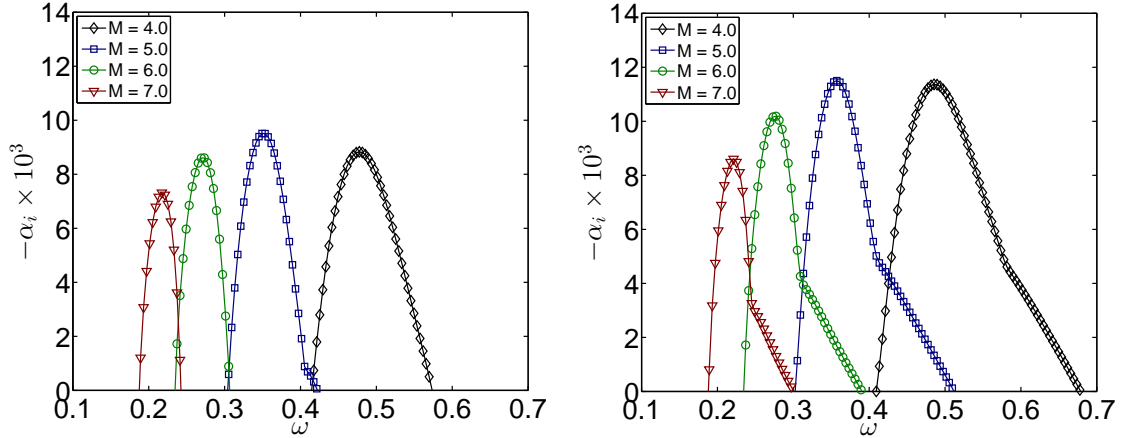


Figure 5.11: Dispersion curves for cold-wall flows of air ($T_w^*/T_e^* = 0.2$) for various Mach numbers. Left: $R = 1000$. Right: $R = 2000$.

ature, most of them focus on a few specific flow conditions and hence consider only a small parameter space. A few researchers have performed more systematic investigations involving a range of Mach numbers and wall temperature conditions (Mack, 1969, 1984, Masad et al., 1992, Malik, 1989), but these studies have targeted low enthalpy conditions, whereas the present results are relevant to high enthalpy flows. Past systematic studies have also, for the most part, excluded the very high levels of wall cooling ($T_w/T_e \ll 1$) that are relevant to hypervelocity impulse facilities.

5.4.1 Growth Rates

A sequence of simulations was conducted in which the wall temperature was fixed at 300 K while the freestream temperature was incrementally raised from 70 K to 2000 K. Although wall temperature effects are often spoken of in terms of “wall cooling”, we choose here to keep the wall temperature fixed and adjust the freestream temperature so that comparisons with experiments in both high and low enthalpy impulse facilities can be made more easily. However, it should be recognized that in terms of the stability behavior, raising the freestream temperature is nearly equivalent to cooling the wall, with differences being caused only by the temperature dependence of transport properties and specific heats, as well as non-equilibrium effects. Accordingly, we refer to cooling of the wall and heating of the freestream interchangeably.

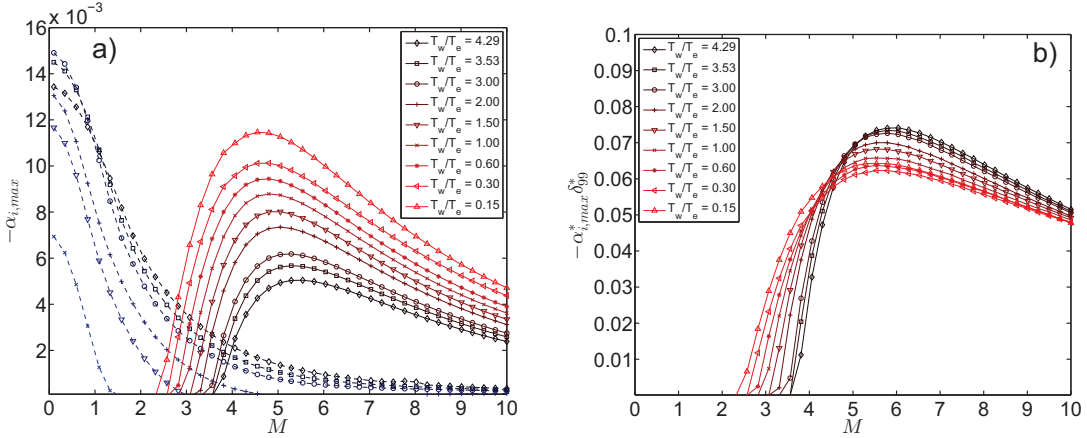


Figure 5.12: Effect of wall cooling on the maximum spatial growth rates of the first and second modes for $R = 1500$, $T_w^* = 300$ K, $T_e^* = 70 - 2000$ K, $P_e^* = 10$ kPa. a) Maximum growth rates for first and second modes. b) Maximum growth rate of second mode normalized by δ_{99} .

These results are also presented in terms of T_w^*/T_e^* rather than the customary T_w^*/T_{ad}^* because the adiabatic wall temperature depends on one's assumptions about specific heats, chemistry, and transport models, and must in general be simulated. Thus it can be difficult to reproduce results that are reported in terms of T_{ad}^* .

Figure 5.12a shows the maximum spatial growth rate as a function of Mach number for several values of the ratio T_w^*/T_e^* . Two sets of curves are shown: the dashed lines correspond to the first mode instability and the solid lines to the second mode. For each curve, the spatial growth rate has been maximized over all frequencies ω and all spanwise wavenumbers β . These curves are very similar to those of Mack (1984) and Masad et al. (1992), except that we consider a wider range of wall temperature conditions and hold T_w^*/T_e^* fixed along each curve rather than T_w^*/T_{ad}^* . Note that in this figure and the ones that follow, the neglect of chemistry may not be valid for some of the high Mach number cases, but these results are included anyways for completeness.

For the first mode, no instability was found for some of the cases having $T_w^*/T_e^* < 1$, so the corresponding lines are not included on the figure. For the second mode, a monotonic increase in growth rate is observed as the wall is cooled. Additionally, the second mode becomes unstable at lower Mach numbers as the wall is cooled, with

instability occurring at Mach numbers as low as 2.5. Although it is commonly stated that the second mode becomes dominant above about $M = 4$, this statement is true only when the wall is nearly adiabatic. The second mode instability also exhibits a large degree of sensitivity to the Mach number and wall temperature for $3 < M < 5$, which means that small changes in experimental conditions can potentially lead to correspondingly larger changes in stability behavior. For example, streamwise variation in the wall temperature (which occurs in real flight and in continuous-flow test facilities) could cause significant changes to the stability properties if the Mach number is between 3 and 5.

5.4.2 Scaling of instability parameters

The destabilizing influence of wall cooling appears to be caused mainly by thinning of the boundary layer. This is illustrated in Figure 5.12b in which the spatial growth rate of the second mode is normalized by the δ_{99} boundary layer thickness rather than the Blasius thickness $\delta = \sqrt{\nu_e^* x^* / U_e^*}$. The maximum second mode growth rates normalized in this way experience much less variation with both Mach number and wall temperature than in Figure 5.12a, indicating that the spatial growth rate is nearly inversely proportional to δ_{99} . Although it is well-known that the frequency and wavenumber of the second mode scale inversely with the boundary layer thickness (Stetson et al., 1983, Demetriades, 1977), the correlation of growth rate with boundary layer thickness has been less widely recognized.

The relationship between the frequency of second mode disturbances and the boundary layer thickness was first examined experimentally by Stetson et al. (1983) and Demetriades (1977), who both made hot wire measurements of disturbance fluctuations in the same Mach 8 wind tunnel. Their results showed that the nondimensional frequency $2f^* \delta_{99} / U_e^*$ is nearly constant, decreasing only slightly with Reynolds number and with increased wall cooling. Figure 5.13 shows the variation of dimensionless frequency with Mach number and wall temperature ratio at $R = 1000$. For Figure 5.13a, the plotted frequency is the most amplified one, i.e., the frequency for

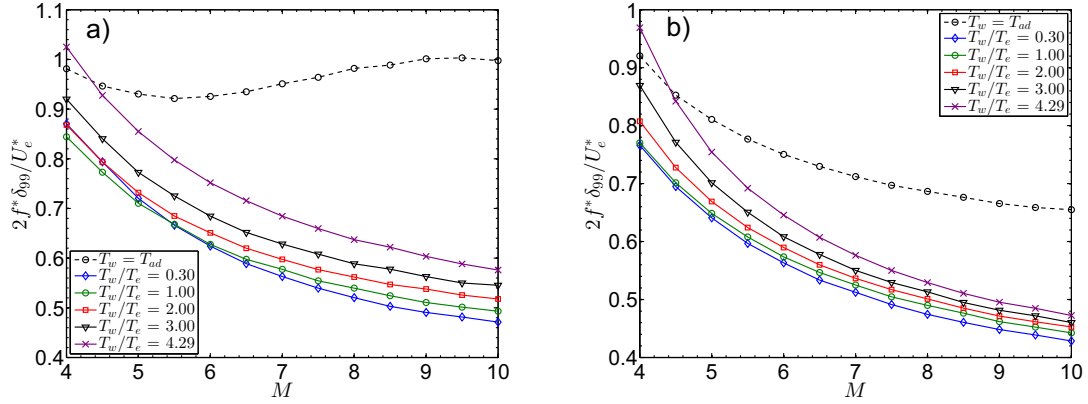


Figure 5.13: Variation of second mode frequencies with Mach number and wall temperature at $R = 1000$. For $T_w^* = T_{ad}^*$, the edge temperature is $T_e^* = 70$ K; for all other cases, $T_w^* = 300$ K. a) Most amplified frequency (max N factor). b) Most unstable frequency (max $-\alpha_i$).

which the N factor is largest. This is the frequency that is measured most often in experiments. Figure 5.13b shows the most unstable frequency, that is, the frequency which has the largest spatial growth rate $-\alpha_i$. For flows with a cold wall, the most unstable and most amplified frequencies follow similar trends, and the most unstable frequency is slightly smaller. This is consistent with the results of [Marineau et al. \(2014\)](#), who measured both the most unstable and the most amplified frequencies for flow over a sharp cone. However, for an adiabatic wall the most unstable and most amplified frequencies exhibit very different variations with Mach number.

For flows with highly-cooled walls, Figures 5.12b and 5.13 reveal that the effect of the wall temperature can be nearly scaled out of the problem by normalizing both the frequency and the growth rate by δ_{99} . This length scale is preferable to the Blasius boundary layer thickness $\delta = \sqrt{\nu_e^* x^* / U_e^*}$, which only takes into account the freestream conditions, whereas the δ_{99} length scale includes the physical structure of the boundary layer and encapsulates the change in thickness that occurs when the wall is cooled. These results suggest that by scaling the growth rate and frequency with δ_{99} one can generate a single dispersion curve that, to a good approximation, describes a range of wall temperature conditions. An example of such a dispersion curve is given in Figure 5.14. In the left figure the growth rate and frequency are

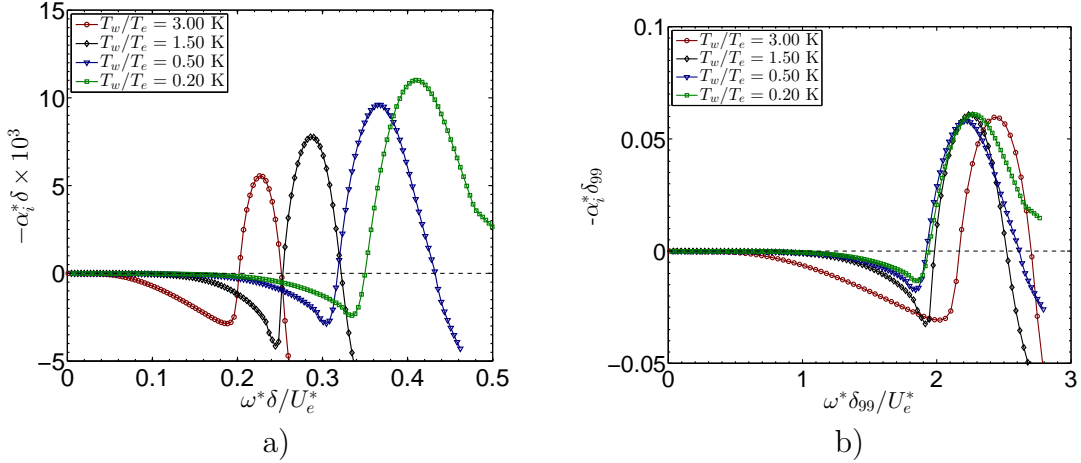


Figure 5.14: Spatial growth rates for several different wall temperature conditions. $M = 4.5$, $T_w^* = 300$ K, $R = 1500$, $P_e^* = 10$ kPa. Only 2D waves ($\beta = 0$) are included. a) Normalized using Blasius thickness $\delta = \sqrt{\nu_e^* x^* / U_e^*}$. b) Normalized using δ_{99} boundary layer thickness.

scaled by the usual Blasius boundary layer thickness δ , whereas in the right figure they are scaled by δ_{99} . The latter scaling nearly collapses the dispersion curves onto one another, though for the case with large T_w/T_e the collapse is not as good. For the cases with smaller T_w/T_e , however, the collapse is excellent, especially along the lower neutral branch, which contributes most significantly to the N factor.

The collapse of the scaled dispersion curves in Figure 5.14b suggests that one might be able to collapse the N factors in a similar fashion. To achieve this, it is assumed that for a given Mach number the dispersion curves for all wall temperatures are well-approximated by a two-parameter function \mathcal{F} of the form

$$-\alpha_i^* \delta_{99} = \mathcal{F} \left(R, \frac{\omega^* \delta_{99}}{U_e^*} \right) \quad (5.8)$$

This functional dependence follows from the collapsed dispersion curves in Figure 5.14b and the fact that the dispersion curve is also a function of the Reynolds number.

One can show that the following definitions of the N factor are equivalent:

$$N(F) = \int_{x_o^*}^{x^*} -\alpha_i^*(F, x^*) dx^* = \int_{R_o}^R -2\alpha_i(F, R) dR \quad (5.9)$$

where $R_o = \sqrt{U_e^* x_\delta^* / \nu_e^*}$ is the Reynolds number at which the frequency F first becomes unstable, α_i^* is the dimensional spatial growth rate, and α_i is the nondimensional growth rate normalized by the Blasius thickness δ . In Equation 5.9, F is the frequency parameter defined by

$$F = \frac{2\pi f^* \nu_e^*}{U_e^{*2}} \quad (5.10)$$

where $f^* = \omega^*/2\pi$ is the dimensional circular frequency in Hz. Making use of these definitions, one can re-write the dispersion relation (5.8) in the form:

$$\alpha_i \frac{\delta_{99}}{\delta} = \mathcal{F} \left(R, F \frac{\delta_{99}}{\delta} \right) \quad (5.11)$$

By substituting this result into Equation 5.9, one arrives at the functional dependence:

$$N \delta_{99} / \delta = \mathcal{F} (R, F \delta_{99} / \delta) \quad (5.12)$$

The ratio δ_{99}/δ is constant for a given Mach number and usually falls between about 3 and 20, increasing with both Mach number and wall temperature. The functional form of Equation 5.12 suggests that if one makes measurements of maximum N factors N_1 and N_2 for two different wall temperatures, then the maximum N factors and the corresponding most amplified frequencies F_1 and F_2 are related by

$$N_2 = N_1 \frac{\delta_{99,1}/\delta_1}{\delta_{99,2}/\delta_2} \quad F_2 = F_1 \frac{\delta_{99,1}/\delta_1}{\delta_{99,2}/\delta_2} \quad (5.13)$$

The effectiveness of this scaling is demonstrated by several examples given in Figure 5.15. Figure 5.15a shows the maximum N factors for several different wall temperature conditions, as well as individual N factor curves for the frequency $F = 4 \times 10^{-4}$. The N factor at $R = 1500$ is about 2.6 times greater for the cold wall than for $T_w/T_e = 3$, and the frequency $F = 4 \times 10^{-4}$ is amplified at different locations for each wall temperature condition.

Figure 5.15b shows the same N factor curves, but scaled by the ratio δ_{99}/δ , which

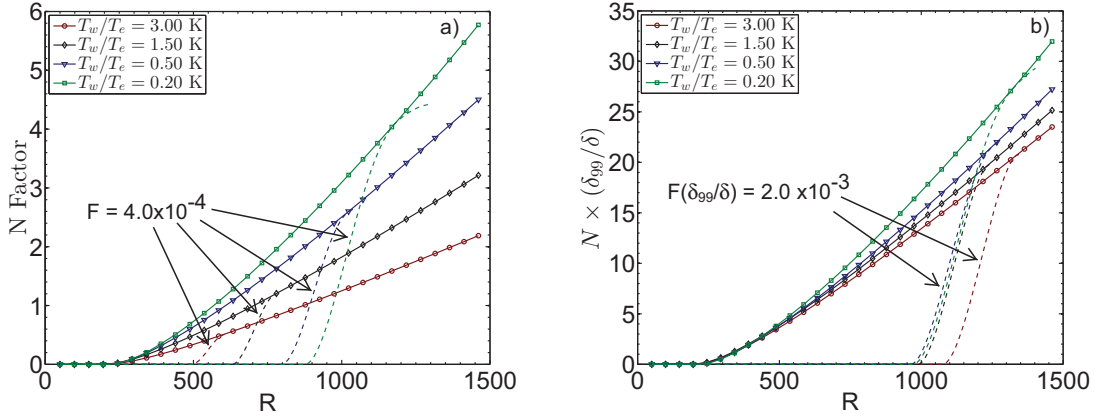


Figure 5.15: Maximum N factors for several different wall temperature conditions. $M = 4.5$, $T_w^* = 300$ K, $R = 1500$, $P_e^* = 10$ kPa. Only 2D waves ($\beta = 0$) are included. a) Maximum N factors and individual N factor curves for $F = 4 \times 10^{-4}$; b) Maximum N factors scaled by δ_{99}/δ and individual N factor curves corresponding to $F(\delta_{99}/\delta) = 3 \times 10^{-3}$.

significantly reduces the spread between the curves. Also shown in Figure 5.15b are the N factors for the frequencies satisfying $F(\delta_{99}/\delta) = 2 \times 10^{-3}$. All of the frequencies scaled in this way are amplified at nearly the same Reynolds number. For both the frequencies and the N factors, the collapse is poorer for large T_w/T_e . The poorer collapse for large T_w/T_e may in part be associated with the much smaller freestream temperature used in this case, since the viscosity varies more rapidly at low temperatures.

This manner of collapsing the N factors has been applied over a wide range of wall temperatures and Mach numbers. The result is shown in Figure 5.16. Figure 5.16a reports the maximum N factors at $R = 1500$ without using the scaling of (5.12). This plot includes results only for two dimensional waves ($\beta = 0$) since these are most amplified for the second mode, but it should be noted that three dimensional first mode waves can produce larger N factors for some of the cases with lower Mach numbers and large values of T_w/T_e . The maximum N factors shown in the figure exhibit the same trends as the growth rates from Figure 5.12, namely, maximum amplification at about $M = 5$, a systematic increase in growth as the wall is cooled, and reduction in the most amplified Mach number as the wall is cooled. This indicates that although the influence of Mach number and wall temperature have historically

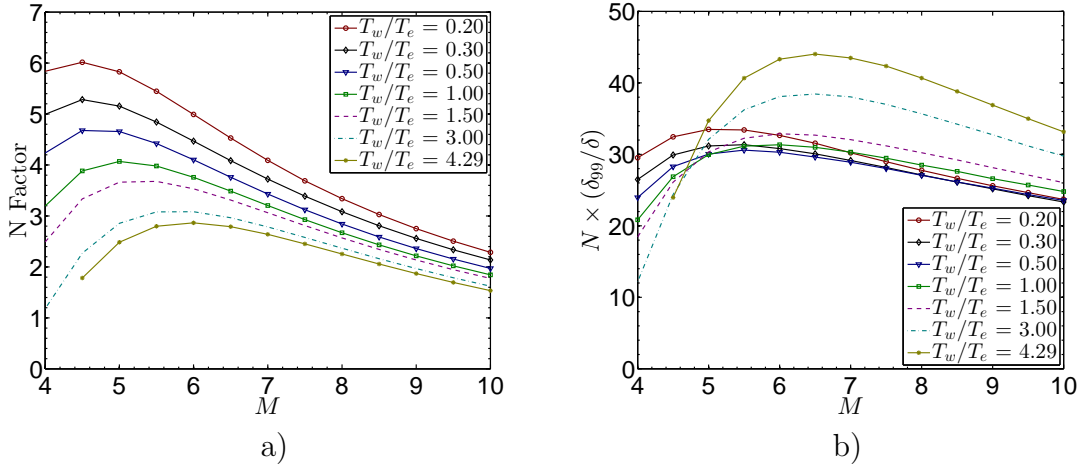


Figure 5.16: Effect of Mach number and wall cooling on the maximum N factors for the second mode. Only 2D waves ($\beta = 0$) are considered. In all cases, $R = 1500$, $T_w^* = 300$ K, and $P_e^* = 10$ kPa. a) Maximum N factors. b) Maximum N factors scaled by δ_{99}/δ .

been characterized mainly using the maximum spatial growth rates, the N factors behave similarly.

Figure 5.16b attempts to collapse the maximum N factors for different wall temperatures by scaling the N factor by δ_{99}/δ . This scaling is quite successful for the cases with $0.2 \leq T_w/T_e \leq 1.5$, but performs poorly for the cases with large T_w/T_e . In spite of the imperfect collapse of the data, the scaling arguments demonstrated here may be useful for estimating how a change in the wall temperature or stagnation temperature might affect the stability characteristics and transition location in an experiment.

5.4.3 Comparison with experiments

Comparisons between measured and predicted second mode frequencies for several different Mach numbers and wall temperatures are given in Table 5.1. Measurements in the AEDC Tunnel 9 (T9 in the table) were made by [Marineau et al. \(2014\)](#) using PCB pressure transducer arrays. Measurements in Caltech's T5 reflected shock tunnel were made by [Parziale \(2013\)](#) using focused laser differential interferometry (FLDI). The FLDI technique was also used by [Heitmann et al. \(2015\)](#) in the Hypersonic Ludwig

Table 5.1: Comparison of most amplified frequencies from computation and experiment. M is the post-shock Mach number. R is the Reynolds number for flow over a cone, equal to $\sqrt{3}$ times the value for a plate. s is the streamwise distance. For AEDC Tunnel B, the wall temperature is nearly adiabatic. For all other cases, the wall temperature is ambient.

Tunnel	Shot	M	T_w/T_e	s (m)	R	δ_{99} (mm)	f_{expt} (kHz)	f_{sim} (kHz)	$2f_{sim}\delta_{99}/U_e^*$
T9	3745	7.76	3.86	0.40	1090	3.5	122.8	122.9	0.62
T9	3745	7.76	3.86	0.65	1390	4.5	97.8	96.9	0.63
HEG	“A”	6.41	0.85	0.73	1660	2.1	300.9	345.2	0.61
HEG	“B”	6.41	0.86	0.63	1900	1.6	397	456.6	0.61
HEG	“D”	5.42	0.18	0.83	1350	2.1	615	688	0.67
T5	2789	4.55	0.14	0.63	1730	1.2	1200	1507	0.82
HLB		5.28	4.2	0.34	1270	2.2	158.7	165	0.81
HLB		5.28	4.2	0.34	1530	1.8	192.9	204	0.81
TB	Run 32	6.8	9.0	0.54	1670	4.4	127.4	123.9	0.95
TB	Run 30	6.8	9.0	0.59	1732	4.6	119.0	119.8	0.96

tube at Braunschweig (HLB). Measurements in the High Enthalpy shock tunnel at Göttingen (HEG) were made by [Laurence et al. \(2014\)](#) using Schlieren deflectometry and full-field pulsed-laser Schlieren photography. Measurements in AEDC Tunnel B (TB in the table) were made using hot wires by [Stetson et al. \(1983\)](#); these data were more recently re-plotted and analyzed by [Schneider \(2006\)](#). For both experiments and computations, the frequency given is the most amplified one.

All of the measured frequencies agree well with the simulated ones, although the agreement is slightly poorer for the reflected shock tunnels (T5 and HEG), where the freestream conditions are known with less certainty. In all cases except HEG, the cones are nominally sharp, and the reported nose radii are small enough that the measurement stations are far downstream of the entropy swallowing length. For the HEG data, the cone is slightly blunted with a nose radius of $R_n = 2.5$ mm. According to the swallowing length correlations reported by [Stetson \(1980\)](#), the measurement station is at about twice the swallowing length, but the local boundary layer thickness may still be influenced by the nose bluntness ([Stetson et al., 1984](#)). This may in part explain why the measured frequencies are slightly larger than the sharp cone predictions. This may also be a factor in the T5 data, where the ratio of the

streamwise distance s to the nose radius of $R_n \approx 0.5$ mm is about $s/R_n = 1260$ and the measured frequencies are again somewhat greater than the sharp-cone prediction. The experiments tabulated here employ an array of different measurement techniques and span a wide range of flow conditions, from low enthalpy adiabatic flow (AEDC Tunnel B) to high enthalpy reflected shock tunnels (T5 and HEG condition “D”). Although the Reynolds numbers of the measurements are slightly different from the value $R = 1000$ used in Figure 5.13, the measured data confirm the major features of the trends shown in the figure.

5.4.4 Stability map

A final illustration of the effects of Mach number and wall temperature on the stability behavior is given in Figure 5.17. This plot contains the same data from Figure 5.12, but is organized in contour form to better portray the stability boundaries. The contour levels indicate the spatial growth rate, which is optimized over all values of the frequency ω and spanwise wavenumber β . For reference, a line (symbols) corresponding to the adiabatic wall condition is also included. Most practical conditions would fall below this line, as the points above it correspond to a heated wall. There is a clear region at low Mach numbers and small values of T_w^*/T_e^* for which no modal instabilities are found. Although this region shrinks slightly as the Reynolds number is increased, it is still present even at rather high Reynolds numbers, $R > 4000$. Since no modal instabilities are found at these conditions, one might conclude that large amplitude (nonlinear) disturbances are needed to cause transition when the Mach number is low and the wall is cold. However, the transient growth calculations described in Chapter 6 report elevated levels of non-modal amplification at these conditions, which offers an alternative transition mechanism for infinitesimal disturbances.

5.5 Effects of Vibrational Nonequilibrium

In this section, the influence of thermal nonequilibrium on the growth of disturbances is examined. Although these effects were included in all the preceding results, we

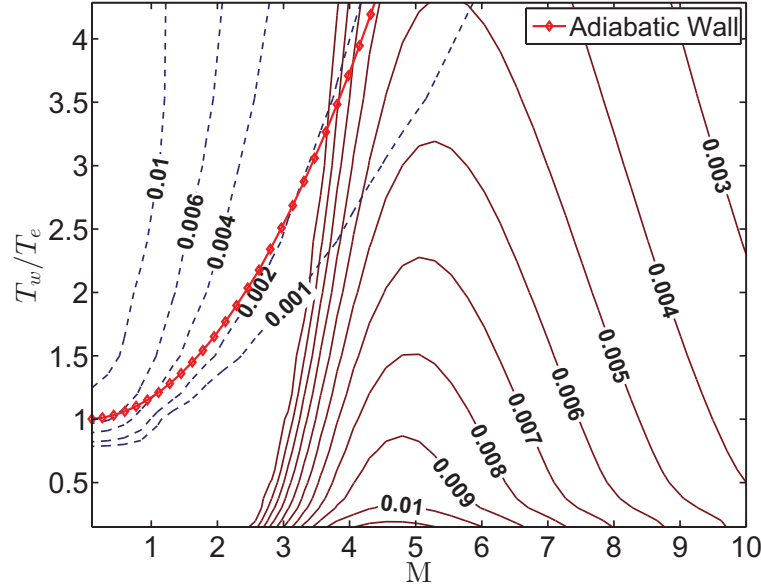


Figure 5.17: Map of unstable regions for first and second modes. $R = 1500$, $T_w^* = 300$ K, $T_e^* = 70 - 2000$ K, $P_e^* = 10$ kPa. Contour levels are spatial growth rates maximized over all values of ω and β for the first mode (--) and second mode (-).

now investigate their importance and discuss the mechanisms involved. The effects of vibrational relaxation are investigated first for air, where they are rather small, and then for CO_2 , where they are considerably more important.

Vibrational nonequilibrium primarily enters the stability analysis in two ways. First, the mean profiles of temperature, density, and (to a smaller extent) velocity are influenced by the exchange of energy between the translational and vibrational modes. This indirectly affects the disturbances through changes to the mean flow profile. The second effect of vibrational nonequilibrium is the attenuation of sound waves caused by the phase lag between the kinetic energy of molecules and their internal energy modes (Clarke and McChesney, 1964, Lighthill, 1956, Vincenti and Kruger, 1967, Fujii and Hornung, 2003). Further discussion regarding these processes and their timescales is given in Section 5.6.

5.5.1 Vibrational Relaxation in Air

The first effect of vibrational nonequilibrium involves changes to the mean flow profiles. These changes are illustrated in Figure 5.18, where the temperature profiles at

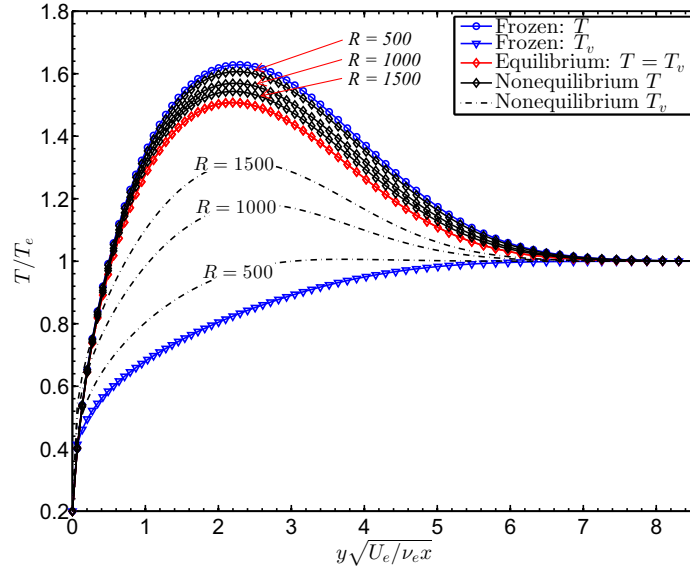


Figure 5.18: Temperature profiles for air at $M = 5$, $T_e^* = 1500$ K, $T_w^* = 300$ K.

various Reynolds numbers are compared. The blue lines show the frozen translational (-o-) and vibrational (-▽-) temperature profiles, whereas the red lines (-◇-) show the equilibrium temperature profile. The nonequilibrium profiles of translational temperature (-◇-) and vibrational temperature (---) are given in black for three Reynolds numbers of $R = 500$, 1000 , and 1500 . As the Reynolds number increases, there is a 7% decrease in translational temperature and an increase in density. The corresponding velocity profiles are not shown since they are nearly unaffected by the vibrational energy transfer.

The effect of these changes to the mean temperature profiles can be assessed by conducting stability analysis for three different base flows: a frozen flow with vibrational energy neglected, a non-equilibrium flow with finite rates of vibrational energy transfer, and an equilibrium flow in which vibrational energy is assumed to be exchanged at an infinite rate. In computing the stability of these three base flows, fully nonequilibrium disturbances are modeled. The resulting stability diagram is shown in Figure 5.19a. As could be expected, the nonequilibrium solution agrees best with the frozen solution for small Reynolds numbers, and tends to the equilibrium solution for large R . The nonequilibrium base flow is destabilized in comparison to the frozen case. The corresponding N factors shown in Figure 5.19b reveal that the equilibrium

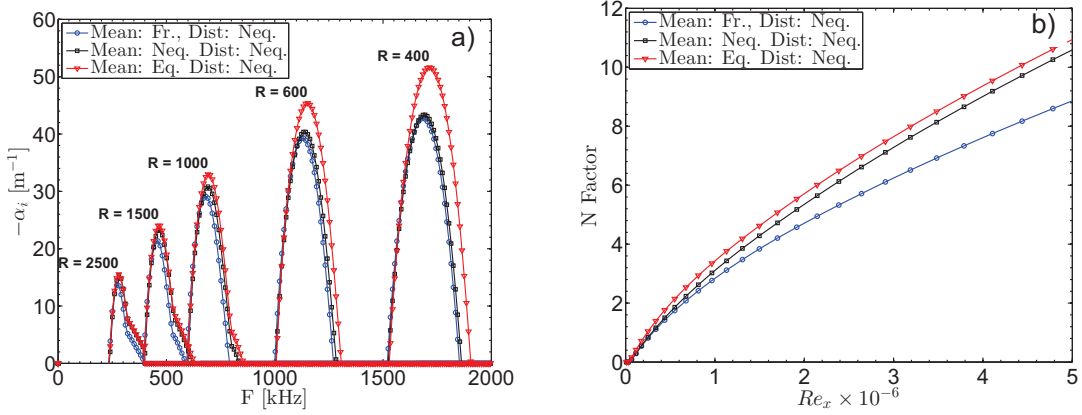


Figure 5.19: a) Stability diagrams for air, $M = 5$, $T_e^* = T_{v,e}^* = 1500$ K, $P_e^* = 20$ kPa. Three different models of the mean flow: frozen, nonequilibrium, and equilibrium. Disturbances are nonequilibrium. b) N factor diagram corresponding to a).

model lies closest to the nonequilibrium one, but there is a noticeable discrepancy between them. This suggests that for transition prediction in high enthalpy air one should make use of a non-equilibrium mean flow solution, although the equilibrium approximation performs reasonably well. The frozen base flow is a rather poor approximation, since if one assumes a transition N factor of about 8 the transition Reynolds number from the frozen flow is in error by about 30%.

The influence of acoustic absorption on the disturbance growth rates can be investigated in a similar manner. In this case three different disturbance models are applied to a single, fully nonequilibrium base flow. The three disturbance models are frozen, thermal equilibrium, and full thermal nonequilibrium. The growth rates are compared in Figure 5.20a and the N factors in Figure 5.20b. In this case, the frozen disturbance model is nearly indistinguishable from the nonequilibrium one. This is consistent with the findings of Fujii and Hornung (2003), who showed that for air at temperatures below about 3000 K, the frequency of maximum acoustic absorption is several orders of magnitude lower than the frequency (\sim MHz) of second mode disturbances in hypervelocity boundary layers.

Similar calculations to Figures 5.19-5.20 have been carried out for a wide range of Mach numbers and wall temperature conditions relevant to shock tunnel experi-

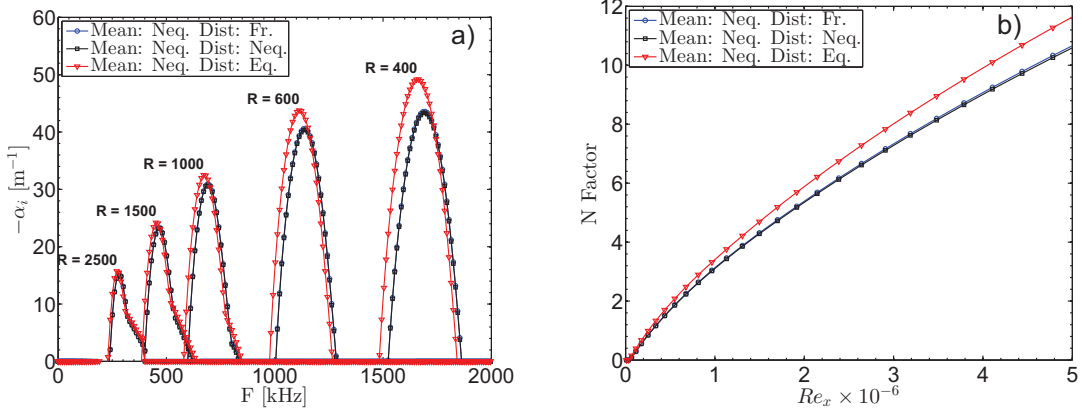


Figure 5.20: a) Stability diagrams for air, $M = 5$, $T_e^* = T_{v,e}^* = 1500$ K, $P_e^* = 20$ kPa. Three different models of the disturbances: frozen, nonequilibrium, and equilibrium. Mean flow is nonequilibrium. b) N factor diagram corresponding to a).

ments. In all cases, it was found that the influence of vibrational relaxation is quite small. This conclusion is demonstrated in Figure 5.21, which shows the maximum spatial growth rate as a function of Mach number and wall temperature, similar to Figure 5.12. In Figure 5.21, the symbols correspond to a fully nonequilibrium calculation (identical to Figure 5.12), while the solid lines correspond to a simplified model in which the base flow is in vibrational equilibrium and the disturbances are vibrationally frozen. As can be seen, this is a reasonably good approximation. There are slight differences for $T_w^*/T_e^* < 1$, which are caused by the nonequilibrium base flow profiles. The discrepancy is largest (about 8%) for $T_w^*/T_e^* = 0.3$ (or $T_e^* = 1000$); below this temperature the vibrational energy of the flow is too small to produce a significant effect and above this temperature, the vibrational relaxation is fast enough that the equilibrium model is quite good.

These findings are independent of the mean pressure of the flow, so the results given above in terms of the Reynolds number, dimensionless wavenumber, and dimensionless frequency apply for any pressure. This is because both the viscous timescale and the timescale of vibrational relaxation are inversely proportional to the pressure, meaning that the effects of vibrational nonequilibrium are always the same at a given Reynolds number. The pressure-independence of the results can also be deduced from

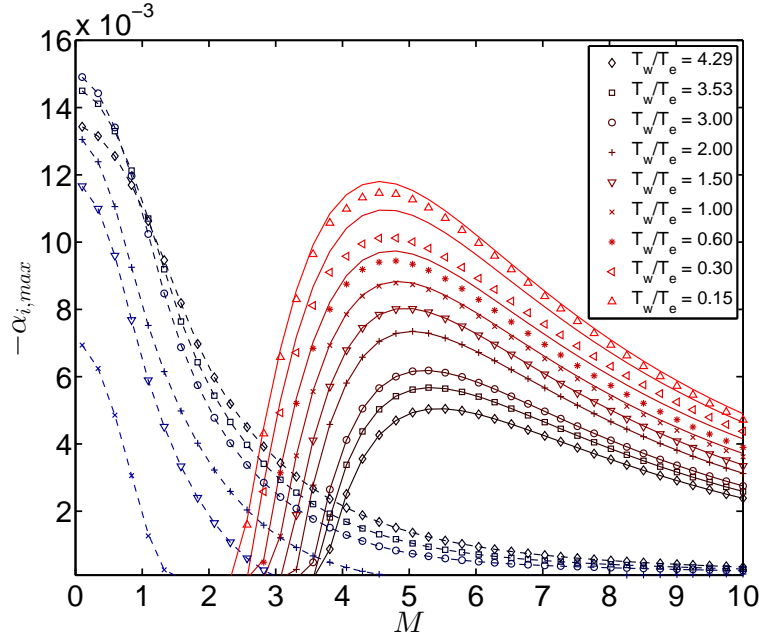


Figure 5.21: Effect of wall cooling on the maximum spatial growth rates of the first and second modes for air, $R = 1500$, $T_w^* = 300 \text{ K}$, $T_e^* = 70 - 2000 \text{ K}$, $P_e^* = 10 \text{ kPa}$. Solid lines: equilibrium base flow, frozen disturbances. Symbols: Nonequilibrium base flow and disturbances.

the dimensionless governing equations (2.14), in which none of the parameters except the Reynolds number depend on the mean pressure.

5.5.2 Vibrational Relaxation in CO₂

In this section, the influence of vibrational relaxation on the stability properties of carbon dioxide flows is investigated. Nonequilibrium flow effects in CO₂ are considerably more important than in air, because CO₂ exhibits a faster vibrational relaxation time and stores a larger fraction of its total internal energy within vibrational modes. This enables both a tuning of the relaxation time to the disturbance frequency and a large damping rate of acoustic waves.

Following the same procedure used for air in the preceding section, we first investigate the effect of the base flow calculation on the stability results. This is done by performing a nonequilibrium stability analysis on three different base flows obtained using frozen, equilibrium, and nonequilibrium models. The resulting growth rates are

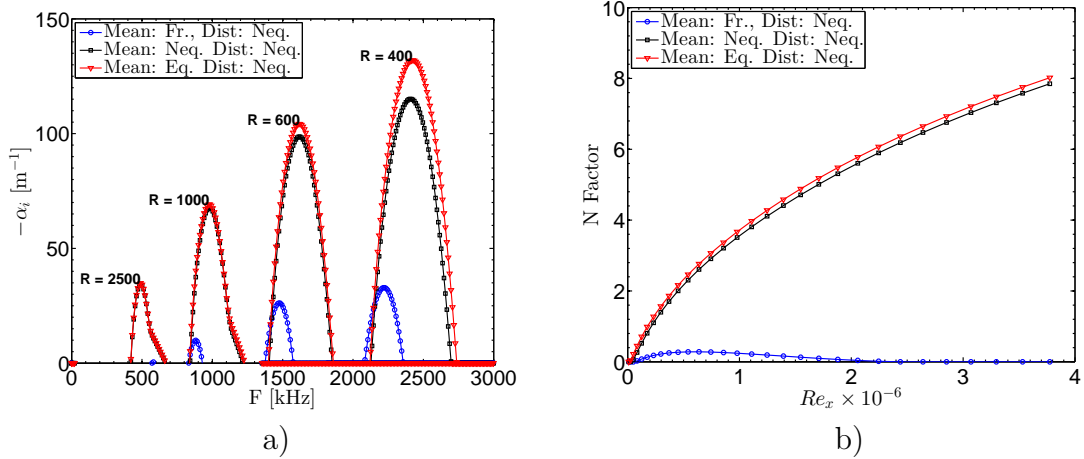


Figure 5.22: a) Stability diagrams for CO_2 , $M = 5$, $T_e^* = T_{v,e}^* = 1000$ K, $P_e^* = 20$ kPa. Three different models of the mean flow: frozen, nonequilibrium, and equilibrium. Disturbances are nonequilibrium. b) N factor diagram corresponding to a).

given in Figure 5.22a and the N factors in Figure 5.22b.

The results show that, as one might expect, the nonequilibrium base flow solution with finite rates of energy transfer yields results that are very close to the equilibrium solution, except near the leading edge. This indicates that the base flow is close to equilibrium, which is confirmed by looking at the base flow profiles that were shown already in Figure 3.5. That figure showed that the nonequilibrium profiles are very close to the equilibrium one downstream of about $R = 600$. The N factors in Figure 5.22b also show good agreement between the equilibrium and nonequilibrium results.

Interestingly, stability analysis of the frozen base flow yields an enormous damping of the disturbances and complete stabilization of the boundary layer as one moves downstream. The same result was observed by Johnson et al. (1998), who applied a chemically reacting stability analysis to a non-reacting base flow of CO_2 and also found complete stabilization. The reason for this behavior is that the vibrationally frozen base flow profiles, which resemble Figure 3.5a at all R , feature a large, artificial separation between the mean vibrational and translational temperatures since vibrational energy transfer was eliminated. Such a separation is non-physical, since the high rate of vibrational energy exchange in reality would rapidly bring the mean

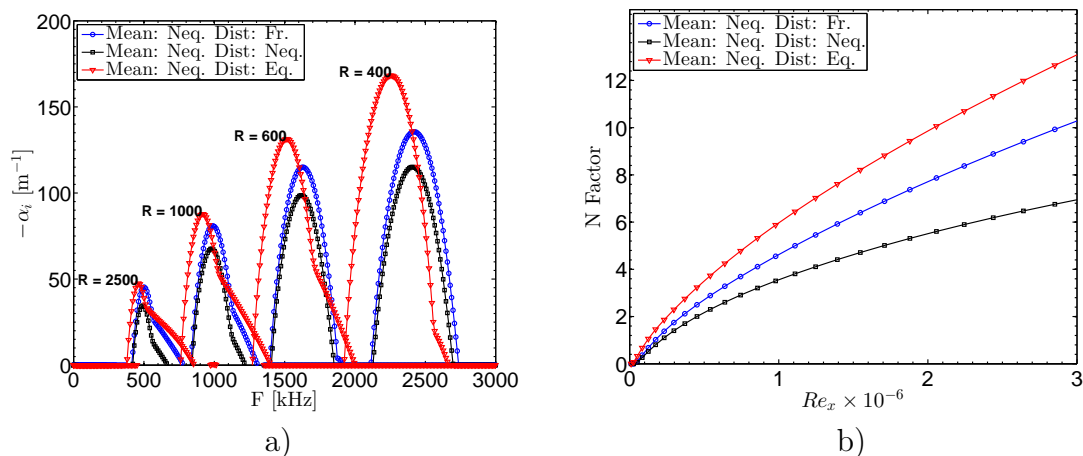


Figure 5.23: a) Stability diagrams for CO_2 , $M = 5$, $T_e^* = T_{v,e}^* = 1000$ K, $P_e^* = 20$ kPa. Three different models of the disturbances: frozen, nonequilibrium, and equilibrium. Mean flow is nonequilibrium. b) N factor diagram corresponding to a).

temperature distributions together. By artificially freezing the base flow but allowing vibrational energy exchange in the stability analysis, one produces an enormous stabilizing source term in the linearized stability equations.

The influence of vibrational relaxation in the disturbance modeling can be assessed by calculating a fully nonequilibrium base flow (See Figure 3.5 for the profiles) and running three different stability analyses on the same base flow. The three stability analyses employ nonequilibrium, equilibrium, and frozen disturbance models. The resulting growth rates and N factor distributions are given in Figure 5.23.

In this figure, one observes that the disturbances are highly stabilized by vibrational nonequilibrium. Stabilization is only achieved in the nonequilibrium situation; if the vibrational relaxation time is too small (approaching the equilibrium result) then the relaxation time and the inverse frequency of disturbances are no longer comparable, and damping does not occur. It is interesting to note that for high Reynolds numbers, the “tail” on the RHS of the growth rate curve is much larger when the disturbances are in equilibrium. As discussed in Section 5.3, this feature exists when unstable modes travel supersonically with respect to the freestream. It is well known that in a gas which has a single dominant vibrational relaxation timescale, the sound speed decreases monotonically as one moves from frozen to equilibrium flow (See

Vincenti and Kruger (1967), Chapter VIII). Because of this reduction in sound speed at equilibrium conditions, the unstable disturbances are able to travel supersonically and hence develop the features mentioned above.

The results above have shown that vibrational nonequilibrium affects the stability characteristics in two ways. First, vibrational relaxation leads to a change in the mean temperature profile, which generally has a destabilizing effect relative to the frozen base flow. Second, acoustic absorption of the second mode waves reduces the growth rate, an effect which is quite small for air but can be significant for carbon dioxide. The net result of these two phenomena can be either stabilizing or destabilizing compared to a completely frozen flow, depending on the flow conditions. The relative importance of these two processes will be investigated further in the sections that follow.

5.6 Vibrational Nonequilibrium Estimates

The preceding sections have shown that thermal nonequilibrium processes are relatively unimportant for flows of air over slender bodies, but for carbon dioxide the influence of vibrational nonequilibrium is quite significant. It is highly desirable to be capable of estimating this behavior using simple methods prior to resorting to a fully nonequilibrium stability calculation. Such estimates also lead to an enhanced understanding of the underlying nonequilibrium flow phenomena.

Estimates regarding the influence and importance of vibrational relaxation can be obtained by considering an inviscid gas consisting of a single species, and therefore featuring a single relaxation timescale (assuming that all vibrational energy states of the molecule are in equilibrium with one another). Although the inviscid results do not necessarily agree quantitatively with viscous calculations, the second mode instability is an inviscid one and its qualitative behavior is the same for both viscous and inviscid flow (Mack, 1984). Moreover, the growth rates from inviscid flow and viscous flow at $Re_x \sim 10^7$ typically differ by less than a factor of 2, so the inviscid limit is reasonable for estimating orders of magnitude. With these approximations,

the dimensionless governing equations (2.14) are reduced to the following:

$$\frac{\partial \rho}{\partial t} + \nabla \cdot (\rho \mathbf{u}) = 0 \quad (5.14a)$$

$$\rho \frac{D\mathbf{u}}{Dt} + \nabla p = 0 \quad (5.14b)$$

$$c_{v,v} \frac{DT_v}{Dt} = Re_L \frac{e_v(T) - e_v(T_v)}{\tau} \quad (5.14c)$$

$$\rho \frac{DT}{Dt} + \rho c_{v,v} \frac{DT_v}{Dt} - M^2(\gamma_e - 1) \frac{Dp}{Dt} = 0 \quad (5.14d)$$

$$\gamma_e M^2 p = \rho T \quad (5.14e)$$

In these equations the nondimensional scalings presented in Equation 2.13 have been used. The nondimensional vibrational energy $e_v = e_v^*/c_{p,tr}^* T_e^*$ and the nondimensional relaxation time $\tau = \tau^* U_e^{2*}/\nu_e^*$ are also introduced.

5.6.1 Vibrational energy fluctuations

Following the procedure described in Chapter 4, one can substitute disturbances in the form of normal modes (Equation 4.1) into the inviscid flow equations (5.14) and linearize the perturbations. For a locally parallel flow, the vibrational and total energy equations (5.14c-5.14d) of the disturbances are reduced to:

$$\bar{c}_{v,v} \left[i(\alpha \bar{U} - \omega) \hat{\theta}_v + \hat{v} \frac{\partial \bar{T}_v}{\partial y} \right] = R \frac{\bar{c}_{v,v}(\bar{T}) \hat{\theta} - \bar{c}_{v,v}(\bar{T}_v) \hat{\theta}_v}{\bar{\tau}} \quad (5.15a)$$

$$\bar{\rho} i(\alpha \bar{U} - \omega) \left[\hat{\theta} + \bar{c}_{v,v} \hat{\theta}_v \right] + \bar{\rho} \hat{v} \left[\frac{\partial \bar{T}}{\partial y} + \bar{c}_{v,v} \frac{\partial \bar{T}_v}{\partial y} \right] = i(\alpha \bar{U} - \omega) M^2 (\gamma_e - 1) \hat{p} \quad (5.15b)$$

where over-bars designate base flow variables and hats signify the complex amplitude coefficients of the normal modes. Here the local Blasius boundary layer thickness $\delta = \sqrt{\nu_e^* x^*/U_e^*}$ has been chosen as the length scale, such that the Reynolds number becomes $R = U_e^* \delta / \nu_e^*$. Equation 5.15a can be solved for the vibrational temperature

fluctuation $\hat{\theta}_v$:

$$\bar{c}_{v,v}(\bar{T}_v)\hat{\theta}_v = \frac{\bar{c}_{v,v}(\bar{T})\hat{\theta} - \hat{v}\bar{c}_{v,v}(\bar{T}_v)\frac{\partial\bar{T}_v}{\partial y}\frac{\bar{\tau}}{R}}{\left[1 + i\left(\frac{\bar{U}}{c} - 1\right)F\bar{\tau}\right]} \quad (5.16)$$

In obtaining this result the frequency parameter $F = \omega/R$ was introduced, where F is related to the dimensional frequency by Equation 5.1. This result shows that fluctuations in vibrational energy are produced by two sources. First, if there is a positive fluctuation in translational temperature $\hat{\theta}$, a positive fluctuation in $\hat{\theta}_v$ will follow, according to the Landau-Teller mechanism. Secondly, a positive vertical velocity fluctuation \hat{v} acting against a positive mean gradient in vibrational energy $\partial\bar{T}_v/\partial y$ results in a decrease of $\hat{\theta}_v$, since the vertical velocity fluctuation is pulling fluid with lower vibrational energy upward.

Both of these mechanisms of energy transfer are modulated by the denominator of Equation 5.16, which can be represented as an amplitude and a phase shift:

$$\frac{1}{1 + i\left(\frac{\bar{U}}{c} - 1\right)F\bar{\tau}} = \frac{\exp\left\{-i \tan^{-1}\left[F\bar{\tau}\left(\frac{\bar{U}}{c} - 1\right)\right]\right\}}{\sqrt{1 + \left(\frac{\bar{U}}{c} - 1\right)^2 F^2\bar{\tau}^2}} \quad (5.17)$$

When the product $F\bar{\tau}$ is large, then the denominator tends to ∞ and the phase angle is $\pi/2$. According to Equation 5.16, this means that the vibrational temperature $\hat{\theta}_v$ does not respond to fluctuations in temperature $\hat{\theta}$ or vertical velocity \hat{v} and is out of phase with these variables. In such cases the disturbances in $\hat{\theta}$ and \hat{v} oscillate too rapidly for the vibrational energy to keep pace. At the other extreme, $F\bar{\tau} \ll 1$, the denominator tends to 1 and the phase angle to zero. This means that the vibrational energy responds instantaneously to fluctuations in $\hat{\theta}$ and \hat{v} .

Between these limits, where $F\bar{\tau}$ is $O(1)$, the amplitude of $\hat{\theta}_v$ decreases monotonically as $F\bar{\tau}$ increases, and the phase angle of $\hat{\theta}_v$ relative to \hat{v} or $\hat{\theta}$ increases. Interestingly, near the critical layer where $\bar{U} = c$, the phase lag is always zero and the vibrational temperature responds instantaneously and completely to fluctuations in $\hat{\theta}$ and \hat{v} . This is because the particle velocity and the disturbance phase velocity are

equal, meaning that the fluid particle itself experiences no fluctuations and quickly reaches vibrational equilibrium. The phase lag of the vibrational temperature always changes sign at the critical layer, with the vibrational energy experiencing a phase lead below the critical layer and a phase lag above it.

5.6.2 Effective vibrational specific heat

The expression (5.16) for $\hat{\theta}_v$ can be substituted into the energy equation (5.15b) and re-arranged to yield:

$$\begin{aligned} \bar{\rho}i(\alpha\bar{U} - \omega) \left[1 + \frac{\bar{c}_{v,v}(\bar{T})}{\left[1 + i \left(\frac{\bar{U}}{c} - 1 \right) F\bar{\tau} \right]} \right] \hat{\theta} \\ + \bar{\rho}\hat{v} \left[\frac{\partial\bar{T}}{\partial y} + \frac{\bar{c}_{v,v}(\bar{T}_v)}{\left[1 + i \left(\frac{\bar{U}}{c} - 1 \right) F\bar{\tau} \right]} \frac{\partial\bar{T}_v}{\partial y} \right] = i(\alpha\bar{U} - \omega)M^2(\gamma_e - 1)\hat{p} \end{aligned} \quad (5.18)$$

For the special case in which the base flow is close to equilibrium, $\bar{T} \approx \bar{T}_v$, this reduces further to

$$\left[1 + \frac{\bar{c}_{v,v}(\bar{T})}{\left[1 + i \left(\frac{\bar{U}}{c} - 1 \right) F\bar{\tau} \right]} \right] \left(i(\alpha\bar{U} - \omega)\hat{\theta} + \hat{v} \frac{\partial\bar{T}}{\partial y} \right) = i(\alpha\bar{U} - \omega)M^2(\gamma_e - 1)\hat{p}/\bar{\rho} \quad (5.19)$$

The only difference between Equation 5.19 and the energy equation for a vibrationally frozen flow is the term in brackets, which is equal to 1.0 for the frozen case. Therefore for inviscid flow the influence of vibrational energy transfer is entirely encapsulated in the quantity

$$c_{v,eff} \equiv \frac{\bar{c}_{v,v}}{1 + i \left(\frac{\bar{U}}{c} - 1 \right) F\bar{\tau}} \quad (5.20)$$

which acts as an effective, frequency-dependent vibrational specific heat and varies between $0 < c_{v,eff} < \bar{c}_{v,v}$. For the more general case in which $\bar{T} \neq \bar{T}_v$, the same

expression appears twice in Equation 5.18, but the numerator must be evaluated at either \bar{T} or \bar{T}_v , depending on which term in Equation 5.18 is being computed.

When $c_{v,eff}$ tends to zero, the entire system of inviscid stability equations reduces exactly to that of a frozen flow with constant specific heats. Likewise, when $c_{v,eff} = \bar{c}_{v,v}$, then the entire system of inviscid equations reduces to the equilibrium flow result. Therefore $c_{v,eff}$ provides a figure of merit through which the action of vibrational nonequilibrium can be assessed. For low temperatures, $\bar{c}_{v,v}$ approaches zero and indeed frozen flow is recovered. For very high frequency disturbances the flow again becomes vibrationally frozen, and for low frequency disturbances thermal equilibrium is achieved.

However, Equation 5.20 reveals that the product $F\tau$ itself is not the most important parameter, rather, the relevant quantity is

$$\left(\frac{\bar{U}}{c} - 1\right) F\bar{\tau} \equiv F_{rel}\bar{\tau} \quad (5.21)$$

where F_{rel} is the frequency of disturbances when measured in the frame of reference of a fluid particle. The factor $F_{rel}\bar{\tau}$ is a function of wallnormal height in the boundary layer, and at the critical layer where $\bar{U} = c$, the relative frequency is zero because the fluid particles are traveling at the same speed as the disturbance wave. Thus even for very high frequency disturbances, vibrational energy transfer may still be significant at the critical layer. Previous simplified estimates of vibrational relaxation have not included the possibility of a non-uniform base flow (Fujii and Hornung, 2001, Vincenti and Kruger, 1967, Clarke and McChesney, 1964), but as discussed above this feature can be important in the context of boundary layers.

5.6.3 Second Mode Frequency Estimates

For a particular boundary layer flow, the size of the relative frequency F_{rel} for second mode waves can be estimated, since the most unstable frequency scales inversely with the boundary layer thickness. As was demonstrated in Section 5.4.2, the most unstable frequency of the second mode instability follows the scaling $f^* = CU_e^*/2\delta_{99}$,

where f^* is the dimensional frequency in Hz, δ_{99} is the boundary layer thickness, and C is a constant that falls in the range $0.4 < C < 1$. The δ_{99} boundary layer thickness can be related to the Blasius boundary layer thickness $\delta = \sqrt{\nu_e^* x^* / U_e^*}$ by a proportionality of the form $\delta_{99} = K\delta$, where K is a constant that depends on the Mach number and the ratio T_w^*/T_{ad}^* . For hypersonic boundary layers K typically falls in the range $2 < K < 20$ and takes on larger values for higher Mach numbers and lower levels of wall cooling. [White \(1974\)](#) provides the estimate:

$$K = \sqrt{\frac{\rho_w \mu_w}{\rho_e \mu_e}} \left[5 + \left(0.2 + \frac{0.9 T_w}{T_{ad}} \right) (\gamma_e - 1) M^2 \right] \quad (5.22)$$

where μ_w and ρ_w are the viscosity and density at the wall. For low Mach numbers and adiabatic flow, the constant reduces to $K = 5.0$ from classic boundary layer theory ([Schlichting and Gersten, 2000](#)). Making use of the above approximation for the disturbance frequency, one finds the relative frequency

$$F_{rel} \bar{\tau} = \left(\frac{\bar{U}}{c} - 1 \right) \frac{\pi C}{K \sqrt{Re_x}} \frac{\tau^* U_e^{*2}}{\nu_e^*} \quad (5.23)$$

The most important observation is that the factor $F_{rel} \bar{\tau}$ is inversely proportional to the square root of the Reynolds number. At the leading edge of the plate, second mode disturbances are of such high frequency that they are vibrationally frozen. As one moves downstream, a nonequilibrium flow is encountered, and eventually the disturbances reach equilibrium far downstream. In the next section, the relative frequency derived here is used to estimate the importance of vibrational nonequilibrium in various flows.

5.6.4 Damköhler numbers

In Section [3.1.4](#) it was found that the effects of vibrational nonequilibrium on the mean flow can be assessed by comparing the quantity $U_e^* \tau^* / x^*$ to 1.0. Then in Section [5.6.3](#) it was found that for linear stability analysis the relative frequency $F_{rel} \tau$ is the controlling parameter. Using these two parameters, one can define Damköhler

Table 5.2: Typical Damköhler numbers for mean flow and disturbances in air at $Re_x = 2.25 \times 10^6$, $M = 5$, and $P_e^* = 10$ kPa.

Gas	T_e^* (K)	U_e^* (m/s)	τ^* (ms)	$\tau^* U_e^{*2} / \nu_e^*$	K	Da_{mean}	Da_{dist}
Air	300	1738	891	1.7×10^{10}	7.35	7.43×10^3	3.71×10^5
Air	1000	3098	3.56	2.8×10^7	6.0	12.3	751
Air	1500	3759	0.80	4.7×10^6	5.7	2.07	133
CO2	300	1351	0.048	1.0×10^6	7.50	0.45	22.2
CO2	1000	2362	7.9×10^{-3}	5.7×10^4	5.5	0.025	1.68
CO2	1500	2875	5.0×10^{-3}	2.6×10^4	5.22	0.019	0.83

numbers for the base flow and for the disturbances:

$$Da_{mean} = \frac{U_e^* \tau^*}{x^*} = \frac{1}{Re_x} \frac{U_e^{*2} \tau^*}{\nu_e^*} \quad (\text{Base Flow}) \quad (5.24a)$$

$$Da_{dist} = F_{rel} \tau = \left(\frac{\bar{U}}{c} - 1 \right) \frac{\pi C}{K} \frac{1}{\sqrt{Re_x}} \frac{U_e^{*2} \tau^*}{\nu_e^*} \quad (\text{Disturbances}) \quad (5.24b)$$

Comparison of these Damköhler numbers to 1.0 indicates whether or not the influence of vibrational nonequilibrium is important in either the base flow or the stability calculations. Damköhler numbers have been calculated for several representative flow conditions and are tabulated in Table 5.2. The flow conditions are $M = 5$, $Re_x = 2.25 \times 10^6$, and $P_e^* = 10$ kPa, although the pressure only affects the dimensional relaxation time τ^* and not the Damköhler numbers. In this calculation the phase speed was assumed to be $c = 0.9U_e^*$, which is an excellent approximation for unstable second mode waves. The constant C was assumed to be 0.7 on the basis of Figure 5.13, and the factor $K = \delta_{99} \sqrt{U_e^* / \nu_e^* x^*}$ was taken from computed boundary layer profiles rather than using the correlation of Equation 5.22.

The Damköhler numbers in Table 5.2 exactly confirm the trends observed in the full stability calculations of Section 5.5. For air, the Damköhler number of the mean flow is very large for $T_e^* = 300$ K and is $O(1)$ at 1500 K, indicating a completely frozen base flow at 300 K and a highly nonequilibrium base flow at 1500 K. This is exactly the behavior observed in the base flow profiles of Figure 3.3. For disturbances in air, the Damköhler numbers Da_{dist} are all much larger than 1.0, indicating

that the disturbances are essentially vibrationally frozen, which was demonstrated in Figure 5.20.

For CO₂, the Damköhler number of the base flow is much less than 1.0, indicating that the base flow reaches vibrational equilibrium almost immediately. This was confirmed in the base flow profiles of Figure 3.5. The disturbance Damköhler numbers for CO₂ in Table 5.2 are $O(1)$, which means that the inverse frequency of disturbances and the vibrational relaxation time are comparable. Consequently, neither frozen nor equilibrium stability calculations will suffice and one must resort to a fully nonequilibrium disturbance model. The same conclusion is drawn from the numerical results of Figure 5.23. Therefore the detailed numerical simulations of the base flow (Section 3.4) and stability behavior (Section 5.5) confirm that the simple Damköhler number estimates given in Equation 5.24 can be used to estimate whether or not vibrational relaxation will be important at a particular flow condition.

A final observation can be made regarding the x dependence of the Damköhler numbers in Equation 5.24. In this equation, the only parameter that varies significantly in the x direction is the Reynolds number. The Damköhler number of the base flow is inversely proportional to the Reynolds number, whereas the Damköhler number of the disturbances is inversely proportional to its square root. This indicates that near the leading edge of the plate, both Damköhler numbers will be very large and both the mean flow and the second mode disturbances will be vibrationally frozen. Likewise, if one travels far enough downstream both Damköhler numbers tend to zero and both the mean flow and the disturbances will be in vibrational equilibrium. In between these two extremes, however, the Damköhler number of the mean flow decreases much more rapidly than that of the disturbances. Specifically, Da_{mean} decreases a factor of $\sqrt{Re_x}$ faster than Da_{dist} .

This situation is shown schematically in Figure 5.24 in which the boundary layer is divided up into frozen, nonequilibrium, and equilibrium zones for both the base flow and the disturbances. The zones are not the same for the base flow and the disturbances, and there can be a considerable amount of overlap between them. The configuration shown in the figure applies to the flows of both high enthalpy air and

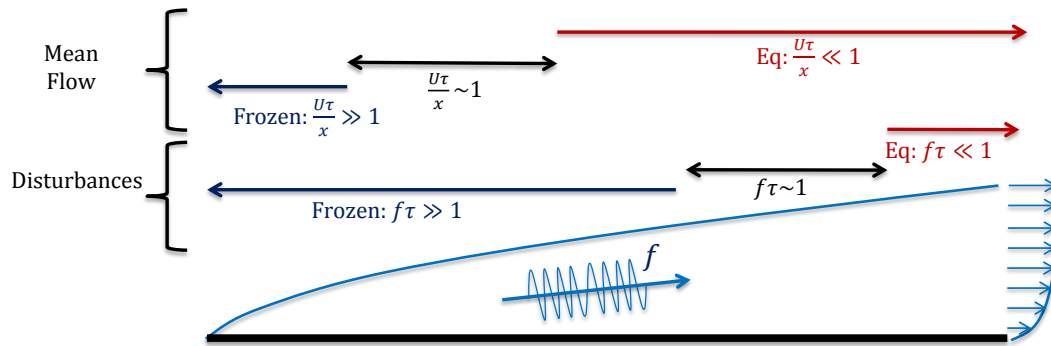


Figure 5.24: Schematic of relaxation times in a boundary layer.

CO₂ discussed previously and tabulated in Table 5.2. For air, the base flow passes through frozen, nonequilibrium, and equilibrium states before vibrational energy exchange starts to become important in the disturbances. For the CO₂ cases, the base flow is essentially in equilibrium while the disturbances experience vibrational nonequilibrium.

Chapter 6

Transient Growth¹

6.1 Introduction

Most of the early analyses of hypersonic boundary layer stability emphasized the exponential growth of perturbations corresponding to unstable discrete eigenvalues (Mack, 1965, 1969, 1984, Reshotko, 1976), as detailed in Chapters 4-5. More recently, however, it has been recognized that disturbances can experience a large amount of amplification even in the absence of unstable modes. This mechanism of disturbance amplification is called non-modal growth, or transient growth. It has been hypothesized that disturbances undergoing transient growth may reach sufficient amplitudes to trigger nonlinear interactions which ultimately cause the breakdown into turbulent motion (Andersson et al., 1999, Trefethen et al., 1993). This chapter develops a compressible transient growth analysis, systematically explores the transient growth behavior over a wide parameter space, and makes direct comparisons between transient growth and modal growth in hypersonic boundary layers.

6.2 Background

Non-modal growth first received a great deal of attention in the incompressible flow regime (Hultgren and Gustavsson, 1981, Butler and Farrell, 1992, Andersson et al.,

¹Much of the material presented in this chapter was reported in a paper by Bitter and Shepherd (2014).

1999, Luchini, 1996, 2000, Tempelmann et al., 2010) since it provides a plausible explanation for the experimentally observed transition of flows like Couette and pipe flow that have no unstable eigenvalues (Schmid and Henningson, 2001, Reddy and Henningson, 1993). The first transient growth analysis of compressible boundary layers was conducted by Hanifi et al. (1996) using the temporal framework. They found that the optimal disturbances in compressible boundary layers share many features with those in incompressible ones; for instance, optimal perturbations take the form of streamwise vortices, energy growth scales with the Reynolds number based on x , and the amplification is driven by Landahl's "lift-up" effect (Landahl, 1977, 1980). Subsequent compressible transient-growth analyses have employed the spatial framework (Tumin and Reshotko, 2001) and focused on the inclusion of nonparallel flow effects (Tumin and Reshotko, 2003, Zuccher et al., 2006, Tempelmann et al., 2012).

As discussed by Corbett and Bottaro (2000) for the incompressible case, flows experience a competition between modal and non-modal growth mechanisms. At low enough Reynolds numbers, the flow is generally modally stable and the only possible growth mechanism is transient growth, which may or may not produce large amounts of amplification depending on the flow conditions. At higher Reynolds numbers, both modal and non-modal growth mechanisms may be active, and one must determine whether the short-time dynamics of transient growth are able to surpass the exponential amplification of unstable modes. In the literature, very few direct comparisons between modal growth and transient growth have been made, especially for compressible boundary layers. Moreover, the few comparisons that are available do not account for the fact that second mode waves of a given frequency are only unstable over a short range of Reynolds numbers (c.f. Figure 5.3) rather than experiencing continued exponential growth for all time. Therefore one goal of this chapter is to make a meaningful comparison between modal and non-modal growth that takes these factors into account.

In comparing the amplification caused by modal and non-modal mechanisms, the wall temperature condition and Mach number are of great importance. As was

demonstrated in Chapter 5, the growth rates of both the first and second mode instabilities are quite sensitive to these parameters, the first mode being stabilized by wall cooling and the second and higher modes being destabilized. Although the influence of wall cooling is well-known for modal instabilities, with regard to transient growth the effects of wall cooling are not so simple and have not been studied in such great detail. [Tumin and Reshotko \(2001, 2003\)](#) did investigate the effects of wall cooling for relatively low Mach numbers of 0.5 and 3.0 as well as modest wall temperature ratios ($T_w/T_{ad} = 0.25-1.0$), and they observed a reduction in transient growth with wall cooling for $M = 3$ and an increase for $M = 0.5$. [Tempelmann et al. \(2012\)](#) also investigated the effect of wall cooling for a swept flat-plate boundary layer at $M = 0.75$ and found wall cooling to increase the level of transient growth, which is consistent Tumin's subsonic result. [Reshotko and Tumin \(2004\)](#) reported a wider range of wall temperatures and Mach numbers and demonstrated that the wall temperature effect is strongly dependent on the Mach number. In this chapter, a systematic study of the effects of Mach number and wall temperature is undertaken to further clarify the roles of these parameters in transient growth and provide results for flow conditions that are relevant to high enthalpy impulse experiments.

As was pointed out in Chapter 5 there are no modal instabilities for flows with a cold wall and $M < 2.5$. At these conditions, the first mode is stable because of the high level of wall cooling and the second mode is stable because of the low Mach number. For high levels of wall cooling, the absence of modal instabilities at $M < 2.5$ raises the question of whether or not such boundary layers are completely stable to infinitesimal perturbations, with transition to turbulence being caused only by nonlinear interactions between finite amplitude disturbances. In this chapter we also investigate whether transient growth produces sufficient amplification to plausibly lead to transition in such flows.

The transient growth calculations reported in this chapter are conducted mainly in the temporal framework, but we also report several cases using the spatial framework as well. Although previous research has been done in both the temporal ([Hanifi et al., 1996](#), [Hanifi and Henningson, 1998](#)) and spatial ([Tumin and Reshotko, 2001, 2003](#),

(Tempelmann et al., 2012) cases, the connection between the two frameworks remains unclear and few direct comparisons between the two methods are available. Several authors (Criminale et al., 1997, Lasseigne et al., 1999) have reported promising results in which spatial results are nearly reproduced from the temporal ones by a simple re-scaling of variables; however, an analogue to Gaster’s transform (Gaster, 1962) that might facilitate the comparison between spatial and temporal results has not yet been proposed. Nevertheless, by comparing the results of the references above it is clear that the spatial and temporal calculations have the same qualitative behavior, including the form of the optimal perturbations, the magnitude of energy growth achieved, the scaling of results with Reynolds and Mach numbers, and the effects of wall-cooling. In this study, we make both spatial and temporal transient growth calculations for selected cases that are otherwise identical in order to clarify the similarities and differences between the two methods.

6.3 Simple Transient Growth Example

Before describing the details of the transient growth analysis, it is useful to introduce the differences between modal and non-modal amplification by means of a simple example. First we consider a simple linear system of two ordinary differential equations which exhibits only the traditional modal growth:

$$\frac{d}{dt} \begin{pmatrix} X \\ Y \end{pmatrix} = \begin{bmatrix} 0.1 & 0 \\ 0 & -1 \end{bmatrix} \begin{pmatrix} X \\ Y \end{pmatrix} \quad (6.1)$$

In this example, the behavior is very simple since the system matrix is diagonal, and therefore the equations are uncoupled. It is then easily seen that the two eigenvalues are $\lambda_1 = 0.1$, $\lambda_2 = -1$ and the right eigenvectors (scaled arbitrarily) are:

$$\xi_1 = \begin{pmatrix} 0.1 \\ 0 \end{pmatrix} \quad \xi_2 = \begin{pmatrix} 0 \\ 1 \end{pmatrix} \quad (6.2)$$

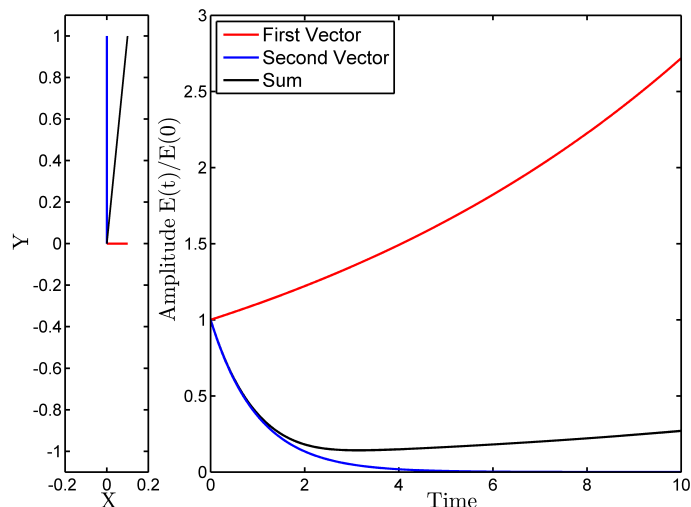


Figure 6.1: Left: Eigenvectors ξ_1 (red), ξ_2 (blue), and linear combination $\xi_1 + \xi_2$ (black) corresponding to system in Equation 6.1. Right: Length of the three vectors as a function of time, relative to initial length. E is the Euclidean norm of the vector.

which are clearly orthogonal. One can then construct the solution for any initial condition using a linear combination of these eigenvectors and their known exponential variation with time.

The results of such a calculation are shown in Figure 6.1. The left portion of this plot shows the two eigenvectors ξ_1 and ξ_2 in red and blue, as well as their linear combination $\xi_1 + \xi_2$ in black, at the initial instant $t = 0$. The right portion of the figure shows the length of these three vectors as functions of time, relative to their initial length. The behavior is very simple: the vector ξ_1 grows exponentially because of its positive eigenvalue, ξ_2 decays exponentially, and the linear combination initially decays but then grows exponentially as $t \rightarrow \infty$, following the dominant mode ξ_1 . Any initial condition will eventually experience this exponential growth unless it is exactly orthogonal to ξ_1 .

A second example illustrates non-modal or transient growth of disturbances. The system matrix of Equation 6.1 is now modified slightly by adding a large off-diagonal term and changing the sign of one of the diagonal elements:

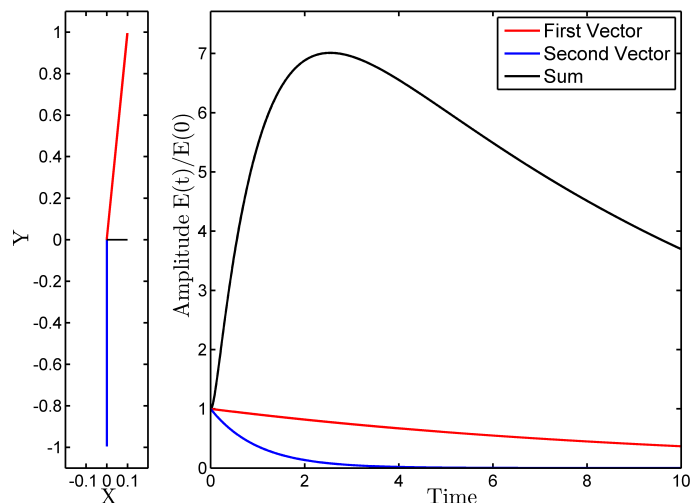


Figure 6.2: Left: Eigenvectors ξ_1 (red), ξ_2 (blue), and linear combination $\xi_1 + \xi_2$ (black) corresponding to system in Equation 6.3. Right: Length of the three vectors as a function of time, relative to initial length. E is the Euclidean norm of the vector.

$$\frac{d}{dt} \begin{pmatrix} X \\ Y \end{pmatrix} = \begin{bmatrix} -0.1 & 0 \\ 9 & -1 \end{bmatrix} \begin{pmatrix} X \\ Y \end{pmatrix} \quad (6.3)$$

In this case the eigenvalues are $\lambda_1 = -0.1$ and $\lambda_2 = -1$, and the eigenvectors are

$$\xi_1 = \begin{pmatrix} 0.1 \\ 1 \end{pmatrix} \quad \xi_2 = \begin{pmatrix} 0 \\ -1 \end{pmatrix} \quad (6.4)$$

Both eigenvalues are now negative, so any initial condition applied to this system will eventually decay away. However, in this case the eigenvectors are no longer orthogonal; in fact, they are nearly parallel.

Figure 6.2 plots the eigenvectors of Equation 6.3 as well as their change in length as a function of time. As expected, both eigenvectors and their linear combination decay as $t \rightarrow \infty$. However, the linear combination shown in black experiences a large amount of growth before finally decaying away. This behavior is easily explained by observing that at time $t = 0$ the two vectors ξ_1 and ξ_2 almost cancel one another out, but as time progresses ξ_2 decays much more rapidly than ξ_1 , thus destroying the

near cancellation of these two vectors. The amount of transient growth can be made arbitrarily large by increasing the size of the off-diagonal term in Equation 6.3, which causes the eigenvectors to become closer to parallel.

The transient growth behavior observed in this simple example occurs for any linear system that has widely-separated eigenvalues and non-orthogonal eigenvectors. Such a linear system is called non-normal. The linearized Navier-Stokes equations are in fact non-normal (Trefethen et al., 1993) and hence do support transient growth. The method for calculating transient growth is conceptually similar to the simple examples described above. The discretized, linearized Navier-Stokes equations are represented as a matrix eigenvalue problem and the eigenvalues and eigenvectors are computed. If the eigenvalues are unstable, then modal growth ensues. If all of the eigenmodes are damped, then transient growth is computed by seeking the linear combination of the eigenvectors that leads to the largest possible growth of disturbance energy.

6.4 Methodology

The first step in the transient growth analysis is to calculate the global eigenvalue spectrum. This is done using exactly the same procedures that were described in Section 4.1. As described in Chapter 4, the flow is assumed to be locally parallel, meaning that the x derivatives of mean flow variables are neglected, as is the mean vertical velocity. While these approximations are quite good for the unstable modes described in Chapter 5, they are somewhat poorer for transient growth. As will be seen, the optimal disturbances associated with transient growth are elongated in the streamwise direction and evolve over large streamwise distances. In contrast, unstable modes such as the second mode instability have short streamwise wavelengths over which the variation in boundary layer thickness is usually negligible. The validity of the parallel flow assumption for transient growth analysis has been evaluated by Tumin and Reshotko (2003), who demonstrated that the inclusion of non-parallel effects leads to some quantitative differences in the maximum transient growth but

little qualitative change in the behavior; they concluded that “nonparallel effects probably are not significant for estimates of transient growth.” Since in this chapter we are interested mainly in qualitative trends and orders of magnitude associated with transient growth, the slight numerical errors introduced by the locally parallel flow assumption are deemed acceptable.

6.4.1 Energy Norm

After calculating the global eigenvalue spectrum, the next step in the transient growth analysis is to determine the linear combination of eigenvectors that leads to the largest amount of disturbance growth in the downstream direction. However, this step requires a meaningful measure of the size of the disturbance. Unlike modal analysis in which the disturbance velocity, pressure, and temperature amplify in proportion to one another, for transient growth one must make use of a metric that includes all of these variables. A common approach is to use the disturbance energy as a measure of the size of the disturbance. Although the disturbance energy has been derived for perfect gases in various ways by others (Chu, 1965, Mack, 1969, Hanifi et al., 1996), in this section we add vibrational energy to the energy norm.

The energy of a disturbance can be characterized by considering an inviscid plane wave of small amplitude traveling in a uniform medium. Even though the boundary layer itself is not a uniform flow, the energy contained in a uniform medium provides a useful measure of the disturbance energy. Since the wave is traveling in a uniform flow, one can always translate the frame of reference such that the medium becomes stationary. In that case, the equations of continuity, momentum, energy,

and vibrational energy can be linearized and written:

$$\frac{\partial \tilde{\rho}}{\partial t} + \bar{\rho} \nabla \cdot \tilde{\mathbf{u}} = 0 \quad (6.5a)$$

$$\bar{\rho} \frac{\partial \tilde{\mathbf{u}}}{\partial t} + \nabla \tilde{p} = 0 \quad (6.5b)$$

$$\bar{\rho} \bar{c}_v \frac{\partial \tilde{\theta}}{\partial t} + \bar{\rho} \bar{c}_{v,v} \frac{\partial \tilde{\theta}_v}{\partial t} + \bar{p} \nabla \cdot \tilde{\mathbf{u}} = 0 \quad (6.5c)$$

$$\bar{c}_{v,v} \frac{\partial \hat{\theta}_v}{\partial t} = \tilde{Q} \quad (6.5d)$$

where the tilde indicates fluctuations and overbars signify mean flow quantities. The translational specific heat is \bar{c}_v , the vibrational specific heat is $\bar{c}_{v,v}$, and \tilde{Q} is the rate of energy transfer between fluctuations in vibrational and translational energy. Although this term is usually modeled using the method of Landau and Teller (c.f. Equation 2.6), there is no need to specify a model for \tilde{Q} in the present analysis. Following the method of [Chu \(1965\)](#) and extending it for vibrational energy, one can multiply Equation 6.5a by $(\bar{a}^2/\gamma\bar{\rho})\tilde{\rho}$, (6.5b) by \tilde{u} , (6.5c) by $\tilde{\theta}/\bar{T}$, and (6.5d) by $\bar{\rho}\tilde{\theta}_v/\bar{T}$. After doing so, the equations are summed to obtain the result:

$$\frac{1}{2} \frac{\partial}{\partial t} \left(\bar{\rho} |\tilde{\mathbf{u}}|^2 + \frac{\bar{a}^2}{\gamma\bar{\rho}} \tilde{\rho}^2 + \frac{\bar{\rho}\bar{c}_v}{\bar{T}} \tilde{\theta}^2 + \frac{\bar{\rho}\bar{c}_{v,v}}{\bar{T}} \tilde{\theta}_v^2 \right) = -\nabla \cdot (\tilde{p}\tilde{\mathbf{u}}) - \frac{\bar{\rho}\bar{c}_{v,v}}{\bar{T}} \tilde{\theta} \frac{\partial \tilde{\theta}_v}{\partial t} + \frac{\bar{\rho}\tilde{Q}\tilde{\theta}_v}{\bar{T}} \quad (6.6)$$

The second term on the RHS can be replaced using the vibrational energy equation (6.5d), which leads to:

$$\frac{1}{2} \frac{\partial}{\partial t} \left(\bar{\rho} |\tilde{\mathbf{u}}|^2 + \frac{\bar{a}^2}{\gamma\bar{\rho}} \tilde{\rho}^2 + \frac{\bar{\rho}\bar{c}_v}{\bar{T}} \tilde{\theta}^2 + \frac{\bar{\rho}\bar{c}_{v,v}}{\bar{T}} \tilde{\theta}_v^2 \right) = -\nabla \cdot (\tilde{p}\tilde{\mathbf{u}}) + \frac{\bar{\rho}}{\bar{T}} \tilde{Q} (\tilde{\theta}_v - \tilde{\theta}) \quad (6.7)$$

One can now integrate this equation over some region of space Ω . By virtue of the divergence theorem, the first term on the RHS integrates to zero if the disturbances satisfy one of the following properties:

1. The disturbances are periodic in space
2. The domain boundary is at ∞ and the disturbances decay to zero there

3. The velocity normal to the boundary is zero

For boundary layers, the disturbances are generally considered to be periodic in x and decaying as $y \rightarrow \infty$, and they exhibit zero normal velocity at the wall. Therefore, in integrating over the domain the pressure work term on the RHS is zero. As a result, the integral becomes

$$\frac{\partial E}{\partial t} \equiv \frac{1}{2} \frac{\partial}{\partial t} \int_{\Omega} \left(\bar{\rho} |\tilde{\mathbf{u}}|^2 + \frac{\bar{a}^2}{\gamma \bar{\rho}} \tilde{\rho}^2 + \frac{\bar{\rho} \bar{c}_v}{\bar{T}} \tilde{\theta}^2 + \frac{\bar{\rho} \bar{c}_{v,v}}{\bar{T}} \tilde{\theta}_v^2 \right) d\Omega = \int_{\Omega} \frac{\bar{\rho}}{\bar{T}} \tilde{Q} (\tilde{\theta}_v - \tilde{\theta}) d\Omega \quad (6.8)$$

The terms on the LHS represent the time rate of change of the disturbance energy, and its variation with time is (in the absence of viscous effects) caused solely by the vibration-translation energy exchange. In the absence of vibrational energy, the energy integral on the LHS reduces to an energy norm that is widely used in the literature (Chu, 1965, Mack, 1969, Hanifi et al., 1996).

For application to the specific context of boundary layers, the integral above is rewritten in terms of the dimensionless variables defined in Equation 2.13, and the energy is scaled by $\rho_e^* U_e^{*2}$. The result is then

$$2E \equiv \int_0^{y_{max}} \left(\bar{\rho} (|\hat{u}|^2 + |\hat{v}|^2 + |\hat{w}|^2) + \frac{\bar{T}}{M^2 \gamma \bar{\rho}} \hat{\rho}^2 + \frac{\bar{\rho}}{\gamma(\gamma-1)M^2 \bar{T}} \hat{\theta}^2 + \frac{\bar{\rho} \bar{c}_{v,v}}{(\gamma-1)\bar{T}M^2} \hat{\theta}_v^2 \right) dy \quad (6.9)$$

Vibrational energy has been included in this norm for completeness, but in Section 6.5.7 its effect is shown to be rather small. Therefore in the results that follow, the vibrational energy of the disturbances is neglected unless indicated otherwise.

Although the energy norm used here follows intuitively from the equations of motion, it is not the only choice. For example, the observation that optimal disturbances take the form of stream-wise streaks has motivated some researchers to use $|\hat{u}^2|$ alone as the energy norm. Zuccher and Tumin (2005) compared results using the full energy norm from Equation 6.9 (but without $\hat{\theta}_v$) with a partial norm involving only $|\hat{u}|^2$ and $|\hat{\theta}|^2$. They found that the differences in energy growth between these two cases could be as high as 62% at $M = 3$. This indicates that the choice of energy norm can have

a significant effect on the results obtained. Further discussion regarding the choice of energy norm is given in Section 6.5.6.

6.4.2 Transient growth calculation

The transient growth calculation used in this work closely follows the method of Hanifi et al. (1996) and Tumin and Reshotko (2001). Both spatial and temporal calculations are carried out. First, the eigenvalues and eigenvectors of Equation 4.2 are calculated using the methods of Section 4.1. The disturbance vector $\hat{\mathbf{q}} = (\hat{u}, \hat{v}, \hat{p}, \hat{\theta}, \hat{w}, \hat{\theta}_v)^T$ is then projected onto the truncated eigenvector basis as follows:

$$\hat{\mathbf{q}}(x, y) = \sum_{k=1}^N \kappa_k \tilde{\mathbf{q}}_k(y) e^{i\alpha_k x} \quad (6.10)$$

In this equation, the vectors $\tilde{\mathbf{q}}_k$ are the spatial eigenvectors and κ_k are expansion coefficients which are as yet unknown. For temporal analysis, the exponential is replaced by $\exp(-i\omega t)$ and the temporal eigenfunctions are used. This eigenvector decomposition may be represented compactly in vector notation by the relation

$$\hat{\mathbf{q}} = \mathbf{Q}\mathbf{\Lambda}\boldsymbol{\kappa} \quad (6.11)$$

where \mathbf{Q} is a matrix containing the eigenvectors $\tilde{\mathbf{q}}_k$ as its columns, $\mathbf{\Lambda}$ is the diagonal matrix having diagonal elements $\exp(-i\omega_k t)$ or $\exp(i\alpha_k x)$, and $\boldsymbol{\kappa}$ is the column vector of expansion coefficients.

The disturbance energy norm from Equation 6.9 can be written in terms of the eigenvector expansion (6.11) as follows:

$$2E = (\mathbf{\Lambda}\boldsymbol{\kappa})^H \left[\int_0^{y_{\max}} \mathbf{Q}^H \mathbf{M} \mathbf{Q} dy \right] \mathbf{\Lambda}\boldsymbol{\kappa} \quad (6.12)$$

where superscript H designates the Hermitian transpose and \mathbf{M} is a 6×6 matrix containing the coefficients of the disturbance quantities in (6.9). The integral in brackets is a positive-definite matrix, and thus it may be factored as the product of

a matrix \mathbf{F} and its Hermitian transpose (Schmid and Henningson, 1994):

$$\mathbf{F}^H \mathbf{F} \equiv \int_0^{y_{\max}} \mathbf{Q}^H \mathbf{M} \mathbf{Q} dy \quad (6.13)$$

The matrix \mathbf{F} can be calculated using the Cholesky decomposition; this matrix does not depend on x or t or on the eigenvector expansion coefficients $\boldsymbol{\kappa}$, so it can be immediately computed once the eigenvector basis is known. By combining the definition in (6.13) with (6.12), the energy norm can be written as a weighted 2-norm of the expansion coefficients $\boldsymbol{\kappa}$:

$$2E = (\mathbf{F} \boldsymbol{\Lambda} \boldsymbol{\kappa})^H (\mathbf{F} \boldsymbol{\Lambda} \boldsymbol{\kappa}) = \|\mathbf{F} \boldsymbol{\Lambda} \boldsymbol{\kappa}\|_2^2 \quad (6.14)$$

Using this expression for the disturbance energy, one can calculate the ratio of the energy at some downstream location x to the energy at the initial location and seek to maximize this ratio over all possible initial conditions. The maximized energy ratio is denoted G :

$$G(x) \equiv \max \frac{E(x)}{E(0)} = \max \frac{\|\mathbf{F} \boldsymbol{\Lambda} \boldsymbol{\kappa}\|_2^2}{\|\mathbf{F} \boldsymbol{\kappa}\|_2^2} = \max \frac{\|\mathbf{F} \boldsymbol{\Lambda} \mathbf{F}^{-1} \mathbf{F} \boldsymbol{\kappa}\|_2^2}{\|\mathbf{F} \boldsymbol{\kappa}\|_2^2} = \|\mathbf{F} \boldsymbol{\Lambda} \mathbf{F}^{-1}\|_2^2 \quad (6.15)$$

The 2-norm of this matrix is calculated using the singular value decomposition, and the eigenvector expansion coefficients $\boldsymbol{\kappa}$ of the optimal perturbation are extracted from right singular vector corresponding to the largest singular value (Schmid and Henningson, 1994).

For spatial analysis, $G(\omega, \beta, x)$ is the maximum possible amplification that can occur a distance x downstream from the initial station. Analogously, for temporal analysis $G(\alpha, \beta, t)$ is the maximum amplification that can occur at time t . Following the notation of Hanifi et al. (1996), the maximum value of G over all t (temporal case) or x (spatial case) will be denoted G_{\max} , and the value of G_{\max} that is optimized over all β and ω (or α for temporal analysis) will be referred to as G_{opt} . This quantity can be regarded as a property of the boundary layer. The time or distance at which the optimal amplification is achieved is denoted t_{opt} or x_{opt} , and the optimal spanwise

wavenumber is denoted β_{opt} .

The numerical implementation of the transient growth calculation is as follows. For a chosen pair of wavenumbers (α, β) or (ω, β) , the global eigenvalue spectrum is computed as described in Section 4.1. In all calculations, the number of grid points is 150, the height of the domain is $y_{max} = 100$, and half of the grid points are clustered below $y = 10$ using the algebraic grid stretching suggested by Malik (1990). Pointwise checks have been performed at a large number of different conditions using 100 or 200 grid points as well as domain heights of 100, 200, or 300; these checks have shown that values of G_{max} are affected less than 0.5% by these changes, which confirms that the transient growth calculation is converged.

If any unstable modes are found in the global eigenvalue calculation, they are refined using a local stability solver described in Section 4.2. If unstable modes are present, the calculation is terminated since the maximum energy growth is then infinite. If no unstable modes are found by the global eigenvalue calculation, then the matrix \mathbf{F} defined in (6.13) is constructed from the eigenvector basis. The numerical integration involved in (6.13) is carried out using the spectrally accurate method reported by Hanifi et al. (1996). Having constructed the matrix \mathbf{F} and its inverse, the product $\mathbf{F}\mathbf{\Lambda}\mathbf{F}^{-1}$ is formed for different values of time x (or t for temporal analysis) and for each value of x the singular value decomposition is employed to obtain G . This procedure is repeated until the downstream distance x is found that maximizes G .

The transient growth calculation described here has been validated by reproducing both the temporal results of Hanifi et al. (1996) and the spatial results of Tumin and Reshotko (2001). An example of the comparison with Tumin's work is shown in Figure 6.3, where good agreement is seen over a wide range of Mach numbers.

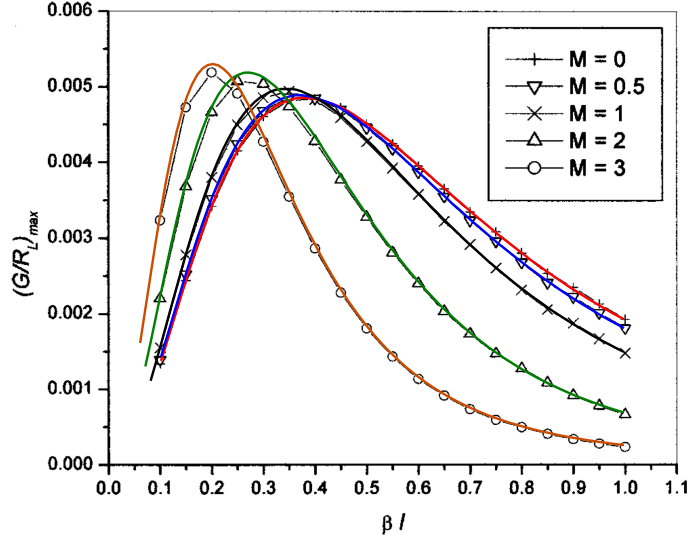


Figure 6.3: Comparison of present results (thick solid lines) with those of [Tumin and Reshotko \(2001\)](#) (markers). Adiabatic wall, spatial analysis, $T_o = 333$ K, $\omega = 0$, $R = \sqrt{U_e x / \nu_e} = 300$.

6.5 Results

6.5.1 Optimal Perturbations

Figure 6.4 shows contour plots of the maximum temporal energy amplification, G_{\max} , as a function of streamwise and spanwise wavenumber. Each plot is constructed on a grid of 150 values each of α and β . The Mach numbers are 2.5 (left) and 5.0 (right), the wall is adiabatic, and the Reynolds number based on boundary layer thickness is $R \equiv \sqrt{U_e x / \nu_e} = \sqrt{Re_x} = 300$. The colored contours represent $G_{\max}(\alpha, \beta)$, but the white regions contain unstable modes and hence the maximum possible energy amplification in these zones is infinite. Contour lines in these regions instead indicate the temporal growth rate, ω_i , with contour lines equally spaced between zero and the maximum value, which is reported in Table 6.1. The unstable regions that are visible in Figure 6.4 correspond to the first mode instability and have their maximum growth rate for $\beta > 0$, indicating that oblique disturbances are most unstable. The second mode is also unstable at this Reynolds number for $M = 5$, but the instability region is located at $\alpha > 0.1$ and is not visible on the plot.

For both Mach numbers, the energy amplification G_{\max} features a local maxi-

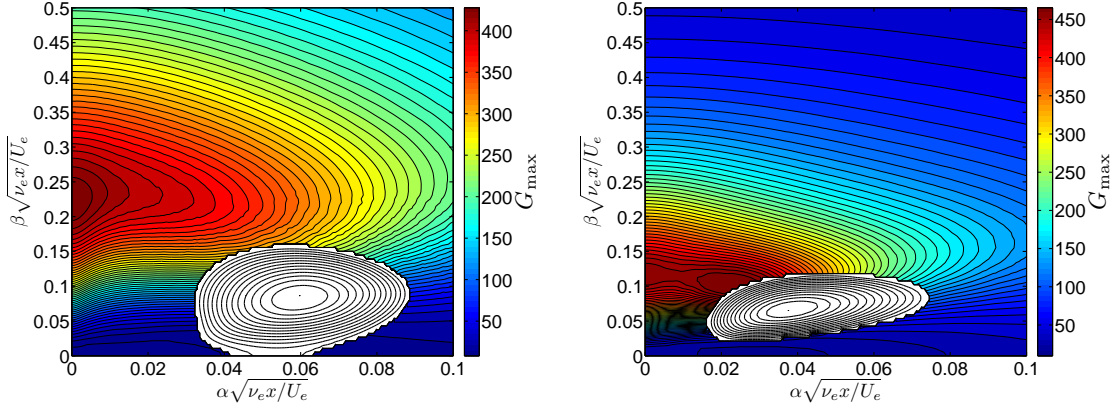


Figure 6.4: Contours of maximum (temporal) energy amplification G_{\max} vs. streamwise and spanwise wavenumbers. Mach number is 2.5 (left) and 5.0 (right), and $T_w = T_{ad}$, $R = 300$, $T_e = 70$ K. Colored contours indicate maximum energy amplification, while black contours indicate the growth rate ω_i in regions that are modally unstable. Maximum growth rates in the unstable region are $\omega_i = 9.2 \times 10^{-4}$ for $M = 2.5$ and $\omega_i = 5.1 \times 10^{-4}$ for $M = 5.0$.

imum for an oblique wave having $\alpha = 0$. This condition corresponds to a streamwise vortex, as is verified by the shape of the optimal disturbance shown in Figure 6.5. The disturbance is comprised mainly of vertical and spanwise velocities, with the temperature fluctuation being substantially smaller and the pressure and streamwise velocity negligible. This form of optimal disturbance has been widely demonstrated for incompressible (Butler and Farrell, 1992, Andersson et al., 1999) and compressible (Tumin and Reshotko, 2001, 2003) flows alike. By comparison of the two cases in Figure 6.5, it is apparent that the shape of the optimal velocity distribution is insensitive to the Mach number. Although the optimal disturbance does contain a noticeable temperature perturbation for the $M = 5$ case, the energy of the disturbance is mostly kinetic: 99.4% of the initial energy is contained in the first three terms of (6.9).

Figure 6.6 shows the shape of the optimal perturbation after it has grown to its maximum amplification ($t = t_{opt}$). The amplified disturbance consists mainly of temperature and streamwise velocity, which is consistent with the findings of Hanifi et al. (1996). These amplified disturbances take the form of streamwise streaks of alternating high and low velocity and temperature. The physical interpretation of this amplification is the well-known lift-up effect (Landahl, 1977, 1980) in which the

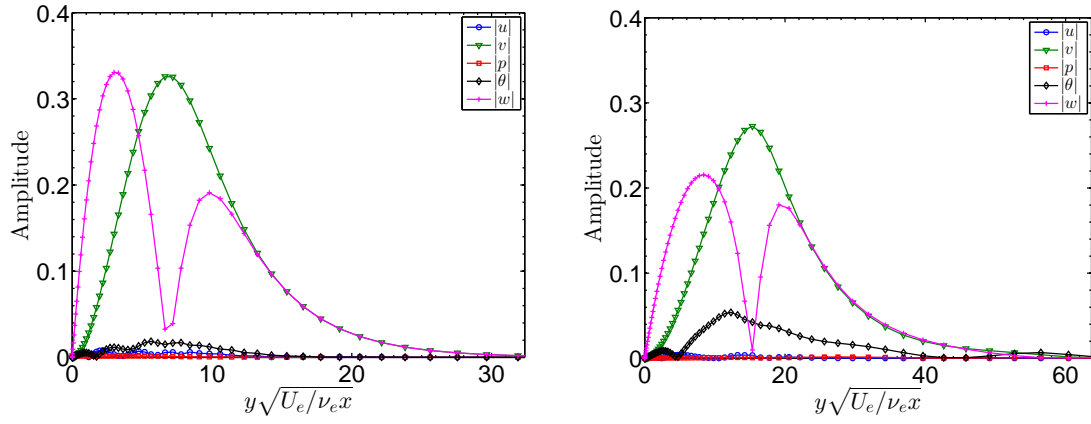


Figure 6.5: Optimal disturbances corresponding to Figure 6.4, $R = 300$, $T_e = 70$ K, $T_w = T_{ad}$. Left: $M = 2.5$, $\alpha = 0$, $\beta = 0.22$. Right: $M = 5.0$, $\alpha = 0$, $\beta = 0.12$.

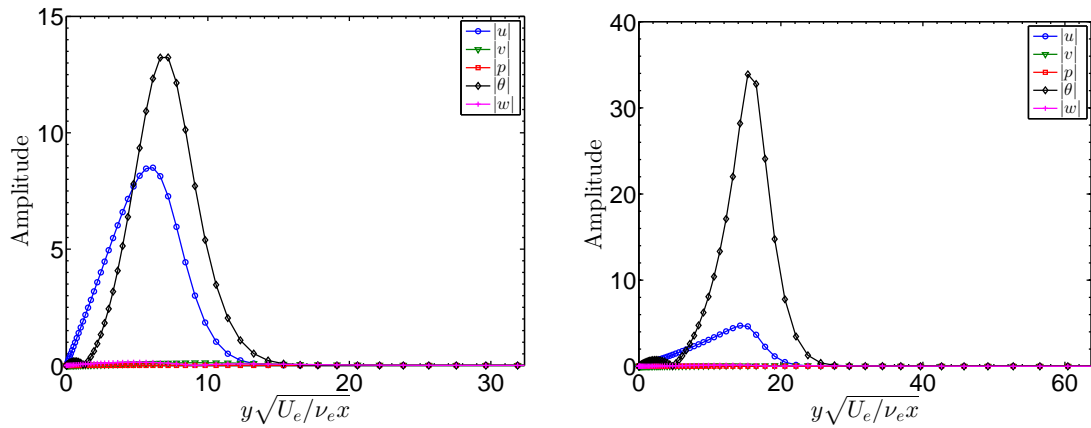


Figure 6.6: Optimal disturbances after amplification, $t = t_{opt}$, corresponding to Figure 6.4. $R = 300$, $T_e = 70$ K, $T_w = T_{ad}$. Left: $M = 2.5$, $\alpha = 0$, $\beta = 0.22$. Right: $M = 5.0$, $\alpha = 0$, $\beta = 0.12$.

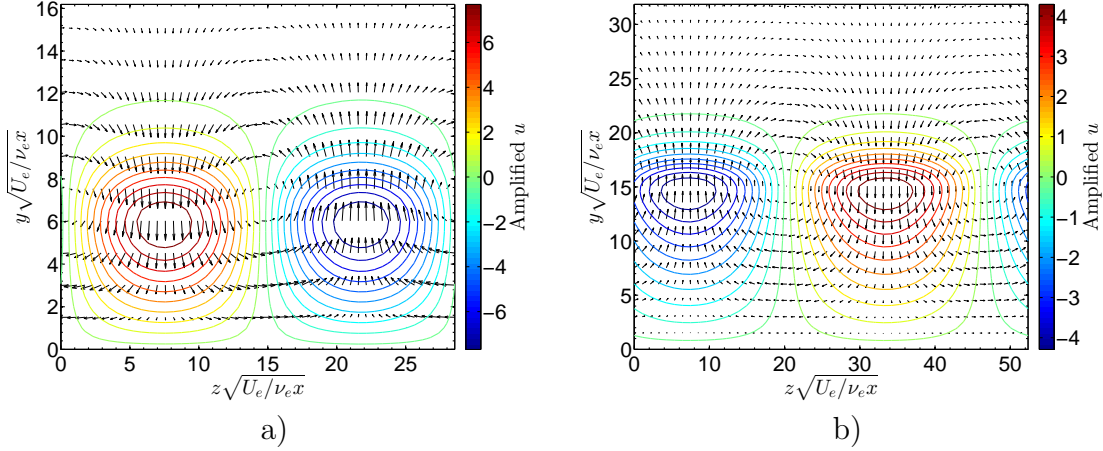


Figure 6.7: Velocity vectors of optimal input disturbance at $t = 0$ and contours amplified streamwise velocity at $t = t_{opt}$. a) $M = 2.5$, $\alpha = 0$, $\beta = 0.22$; b) $M = 5.0$, $\alpha = 0$, $\beta = 0.12$.

streamwise vortices transport low velocity and high temperature (for an adiabatic wall) fluid from the wall towards the outer edge of the boundary layer and vice versa. Although the input disturbances were composed mainly of kinetic energy, after amplification the kinetic energy makes up only 55% (for $M = 2.5$) and 20% (for $M = 5.0$) of the total energy. This demonstrates that the inclusion of the terms involving $\hat{\theta}$ and $\hat{\rho}$ has a significant impact on the computed energy growth. A similar distribution of energy amongst its various components was observed by [Tempelmann et al. \(2012\)](#).

The lift-up effect described above is illustrated more clearly in Figure 6.7, where contours of the amplified streamwise velocity distribution u at $t = t_{opt}$ (colored contours) are superimposed over the velocity vectors of the optimal disturbance at $t = 0$. In this figure, the downstream direction points into the page. The velocity vectors

Table 6.1: Summary of temporal transient growth characteristics for $R = 300$.

M_e	T_w/T_e	G_{opt}	T_{opt}	β_{opt}	$\omega_{i,\max}(1^{st} \text{ mode})$
2.5	2.1 (adiabatic)	437	1030	0.22	9.2×10^{-4}
5.0	5.3 (adiabatic)	483	1150	0.10	5.1×10^{-4}
2.5	1.0	337	750	0.33	0
5.0	1.0	251	897	0.25	0
2.5	0.3	390	602	0.44	0
5.0	0.3	239	770	0.31	0

consist of a row of counter-rotating vortices, and the resulting high velocity streak is located at the point where the vortices are pulling high momentum fluid downward from the top of the boundary layer, and vice versa for the low velocity streak. Temperature streaks can be produced by the same mechanism when the streamwise vortices are acting against gradients in the mean temperature profile. The same behavior is observed at both Mach numbers shown in the figure.

The preceding discussion has focused on disturbances having $\alpha = 0$, but at $M = 5.0$, Figure 6.4 features a second local maximum that borders the first mode instability region, and the energy amplification at this local maximum is slightly larger than at $\alpha = 0$. The optimal disturbance at this condition is composed of the (slightly) damped Tollmien-Schlichting (TS) wave combined with several other more highly damped discrete modes as well as modes from the continuous spectra. This is demonstrated in Figure 6.8 where the global eigenvalue spectrum is plotted and the 10 modes that contribute most significantly to the optimal disturbance are marked with red boxes. Because of the non-normality of the Navier-Stokes operator, the TS mode and the modes from the vorticity branch interfere destructively such that the initial energy is 1.0 despite the large amplitudes of the modes involved. As time progresses, the modes belonging to the vorticity branch rapidly decay leaving a large-amplitude, slowly-decaying Tollmien-Schlichting mode behind. This process results in a large transient increase in energy. A similar process is always involved in transient growth (Schmid, 2007), but this instance is somewhat unique because discrete modes contribute significantly to the transient amplification, rather than modes from the continuous spectrum alone. Interactions of this sort have not been reported in most prior compressible transient growth studies because the perturbations are usually assumed to have $\alpha = 0$ for temporal analyses and $\omega = 0$ for spatial ones. However, there is some similarity between the present result and the “optimally-perturbed TS mode” considered by Farrell (1988) and Corbett and Bottaro (2000), who sought the initial conditions that produce the largest possible amplitude of Tollmien-Schlichting wave at a later time.

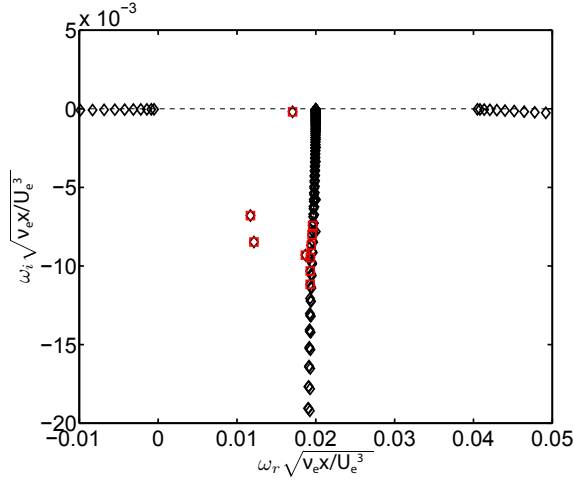


Figure 6.8: Discrete modes and the discrete approximation to the continuous spectra. $M = 5.0$, $T_w = T_{ad}$, $R = 300$, $\alpha = 0.02$, $\beta = 0.10$. Red squares designate the 10 modes that make the largest contribution to the optimal disturbance.

6.5.2 Wall Cooling

Figure 6.9 provides contour plots of maximum amplification for a cooled wall with temperature ratio $T_w/T_e = 1.0$; this condition was achieved by setting both the freestream temperature and wall temperature to 300 K. Again, the Mach numbers are 2.5 and 5 and the Reynolds number is $R = 300$. Owing to the reduction in T_w/T_e relative to the adiabatic case, the first mode instability region is no longer present. There is still a second mode unstable region for $M = 5$, but it is again located at $\alpha > 0.1$ and is not visible in the contour plots. The optimal amplification G_{opt} is somewhat reduced compared to the adiabatic case shown in Figure 6.4. Also the optimal spanwise wavenumber β_{opt} is increased for $T_w/T_e = 1$, which is a consequence of the thinner boundary layer. By comparison of Figs. 6.4 and 6.9, it appears that as the Mach number or level of wall cooling is increased, the transient growth drops off more rapidly away from the optimal condition. That is, near-optimal disturbances cause less amplification for high Mach numbers and cooled walls.

Figure 6.10 shows amplification contours for a further reduction in wall temperature relative to the freestream value, $T_w/T_e = 0.3$. In this case the wall temperature is held at 300 K and the freestream temperature is 1000 K, which is representative of a low or moderate enthalpy conditions in a reflected shock facility ($H_o = 2.3$ MJ/kg

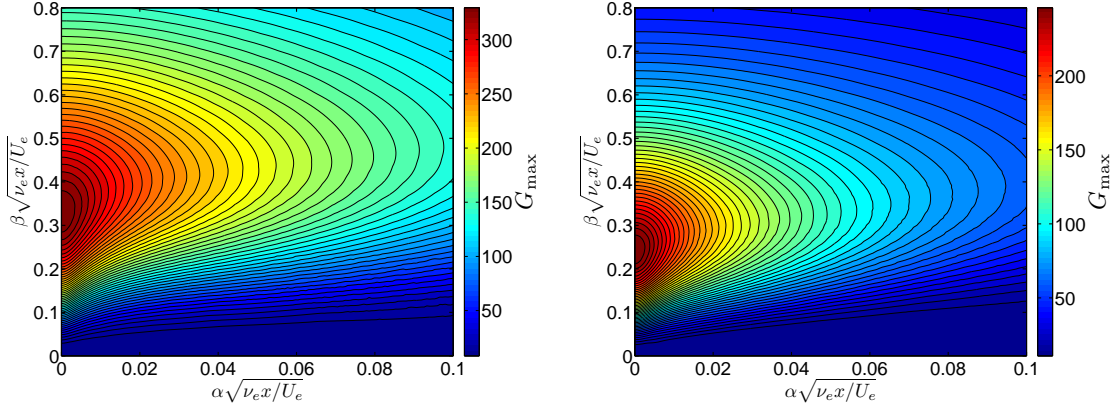


Figure 6.9: Contours of maximum energy amplification G_{\max} vs. streamwise and spanwise wavenumbers. Mach number is 2.5 (left) and 5.0 (right), and $T_w/T_e = 1.0$, $R = 300$, $T_e = 300$ K.

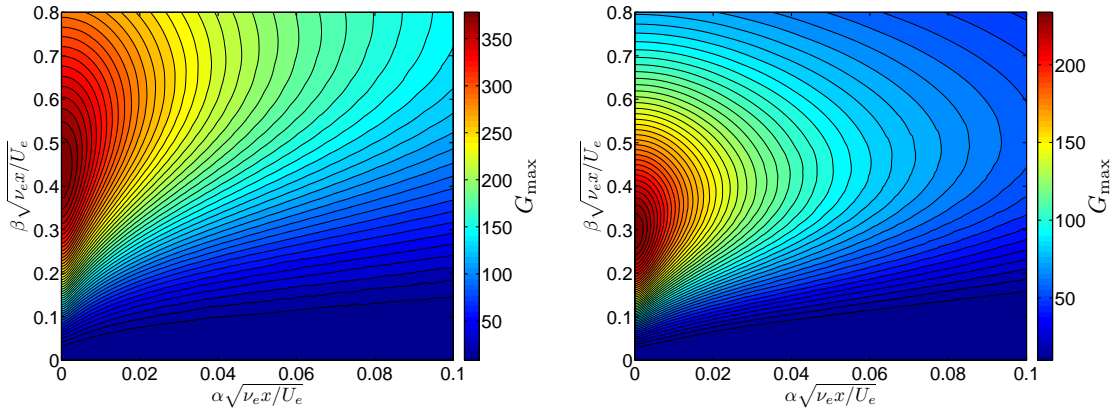


Figure 6.10: Contours of maximum energy amplification G_{\max} vs. streamwise and spanwise wavenumbers. Mach number is 2.5 (left) and 5.0 (right), and $T_w/T_e = 0.3$, $R = 300$, $T_e = 1000$ K.

for $M = 2.5$, 6 MJ/kg for $M = 5$). We have chosen to investigate the effects of wall cooling by raising the freestream temperature rather than by cooling the wall in order to match the conditions found in blow-down facilities and shock tunnels, where the wall temperature is usually ambient. Comparison of Figure 6.10 to Figure 6.9 reveals a further increase in β_{opt} because of the decreased boundary layer thickness caused by wall cooling, but for $M = 5$ there is a slight increase in G_{opt} relative to the case $T_w/T_e = 1$. This suggests that transient growth is minimized for a particular wall temperature condition, as will be verified in the next section.

6.5.3 Effects of Mach Number and Wall Temperature

The effects of Mach number and wall temperature ratio on the optimal growth were assessed by assembling values of G_{opt} for a large number of different conditions. Different wall temperature ratios were achieved by fixing the wall temperature at 300 K and varying the freestream temperature; as discussed in Section 6.5.1, this method was selected in order to match the experimental conditions in impulse facilities. Because of the considerable computational expense of the transient growth calculation, the search for G_{opt} was performed only for $\alpha = 0$, which, as discussed above, is normally where the optimal growth is found. Figure 6.11 reports values of G_{opt}/R^2 that are optimized over all time, α , and β . This scaling between energy growth and Reynolds number is chosen on the basis of the work by Hanifi and Henningson (1998), who showed that G_{opt}/R^2 approaches a constant as the Reynolds number increases. The red line with markers indicates the adiabatic wall temperature. Most experimental and flight conditions would fall below this line, but it is possible to conceive of situations in which the wall temperature would be hotter than adiabatic; for instance, a re-entry vehicle that is decelerating from high to low Mach number could experience elevated wall temperatures of this sort.

Figure 6.11 reveals that the adiabatic line is nearly tangent to an isoline of energy amplification, so if only adiabatic conditions are considered one finds only a slight increase in transient growth as the Mach number is increased, as was seen in Figure 6.3. If the wall is cooled below the adiabatic temperature, however, reductions in amplification can be achieved at high Mach numbers. In particular, as the Mach number is increased there is locus of wall temperature ratios slightly less than 1.0 along which the transient growth is minimized. This minimum in G_{opt}/R^2 is also visible in the results of Tumin and Reshotko (2003) and Reshotko and Tumin (2004), and the results of the present study are in good agreement with theirs. The agreement is excellent for low Mach numbers, but small numerical differences are found at higher Mach numbers and high levels of wall cooling because of our high stagnation temperature and the variable specific heats, which are included in our mean flow

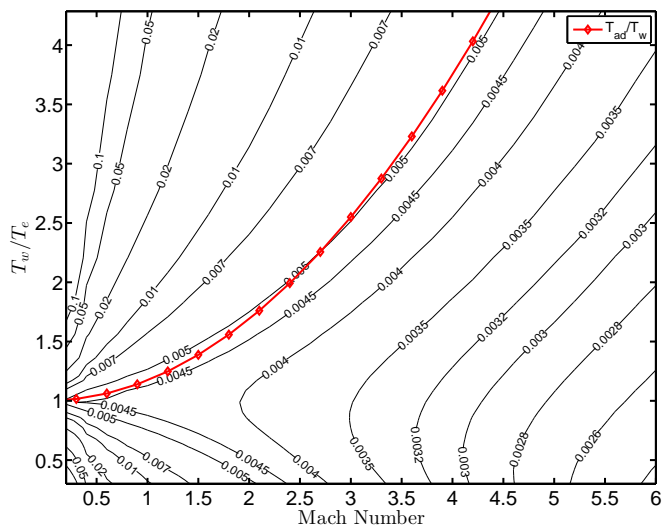


Figure 6.11: Contours of the maximum possible transient growth vs Mach number and wall temperature ratio. Contour levels represent G_{opt}/R^2 and are optimized over all values of time, α , and β . Red line with markers designates the adiabatic wall temperature. Results were calculated at $R = 300$.

calculation.

For low Mach numbers, the influence of wall cooling on the transient growth is substantial. Cooling or heating the wall by a factor of 2.0 results in more than an order of magnitude increase in energy amplification. As noted Chapter 5, when the wall is highly cooled there are no modal instabilities for low supersonic Mach numbers, and even for $M < 1$ the instabilities can be delayed to arbitrarily high Reynolds numbers, which brings into question the route to turbulence at such conditions. The results of Figure 6.11 suggests that transition to turbulence may still be initiated by infinitesimal perturbations since the large density gradients introduced by wall cooling result in high levels of non-modal amplification.

6.5.4 Temporal vs. Spatial

For convective flows like the boundary layer, the spatial framework is often preferred over the temporal one since it is easier to interpret experimentally. Figure 6.12 reports transient growth contours for the same conditions as Figure 6.4 except that here the spatial framework is used. Both plots in this figure have been generated using the full

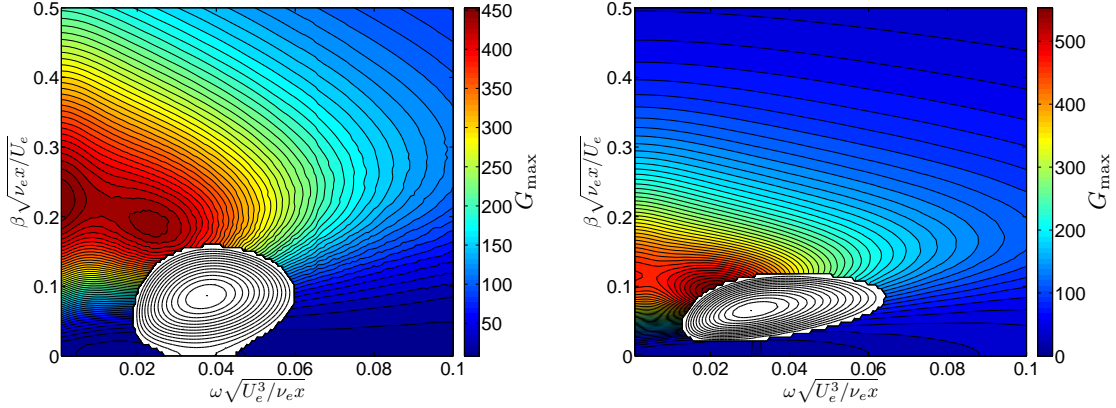


Figure 6.12: Contours of maximum (spatial) energy amplification G_{\max} vs. streamwise and spanwise wavenumbers. Mach number is 2.5 (left) and 5.0 (right). $T_w = T_{ad}$, $R = 300$, $T_e = 70$ K. Conditions are the same as in Figure 6.4 except that the spatial analysis is used here. The distance x_{opt} at which optimal growth is reached is 790 for $M = 2.5$ and 1150 for $M = 5.0$. For $M = 2.5$, the maximum modal growth rate is $-\alpha_i = 1.3 \times 10^{-3}$ (first mode). For $M = 5$, the maximum growth rates are 5.9×10^{-4} (first mode) and 1.2×10^{-3} (second mode).

quadratic eigenvalue problem described in Section 4.1. The same contour plots were also generated using the linearized eigenvalue problem, but these results are not shown because they are visually indistinguishable from those given in Figure 6.12. Because of the close agreement between the quadratic and linearized eigenvalue problems, all subsequent results are computed using the linearized version.

Despite the fact that the independent variable is the frequency rather than the wavenumber, the qualitative behavior in the spatial case (Figure 6.12) is quite similar to that of the temporal case (Fig 6.4). Specifically, the energy amplification features a local maximum for an oblique disturbance at $\alpha = 0$ or $\omega = 0$, and the values of G_{opt} and β_{opt} at these conditions are nearly the same. This similarity between the spatial and temporal cases arises from the fact that most of the modes involved in the optimal disturbance belong to the vorticity and entropy branches of the continuous spectrum (c.f. Figure 6.8), for which the phase speed is very nearly 1.0, meaning that the values of α and ω are nearly identical along these branch cuts.

For $M = 2.5$ there is one noticeable difference between the spatial and temporal results, namely, the appearance of a second local maximum in the energy amplification

for $\omega > 0$ that is not present in the temporal case. This second peak at $\omega = 0.022$ has a slightly lower amplification than the one at $\omega = 0$ but develops more rapidly, reaching maximum energy growth at $x = 400$. The optimal disturbance at $\omega = 0$, on the other hand, is maximized at $x = 790$. This demonstrates the fact that slightly sub-optimal disturbances can grow more rapidly than the optimal ones, as will be discussed in the next section.

6.5.5 Optimization for prescribed downstream distance

As was pointed out by [Butler and Farrell \(1992\)](#) and [Corbett and Bottaro \(2000\)](#) for incompressible flows, the optimal disturbances take a rather long time to develop. For instance, in [Figure 6.12](#) the distance x_{opt} at which the energy is maximized is 790 and 1150 for the respective Mach numbers of 2.5 and 5.0. Recalling that x is normalized by the boundary layer thickness δ , this suggests that the optimal disturbance requires $O(1000\delta)$ to develop. From a modeling standpoint, this fact makes the locally parallel assumption questionable; however, it may be noted that large values of x_{opt} relative to the boundary layer thickness are found in non-parallel simulations as well ([Tumin and Reshotko, 2003](#), [Andersson et al., 1999](#)). From a practical standpoint, if x_{opt} is $O(1000\delta)$ it may be unlikely that this distance is reached in a typical laboratory experiment: disturbances initiated near the nose of the body where δ is small will reach G_{opt} , but disturbances initiated farther downstream may not achieve their maximum amplification before the end of the test article is reached. This suggests that it may be preferable to maximize the amplification G at a particular distance or time that is relevant to the streamwise length scale of interest rather than optimizing over all possible distances.

[Figure 6.13](#) provides contours of spatial energy growth G at six fixed distances downstream of the initial disturbance. For each pair of values (ω, β) , the energy growth G from [\(6.15\)](#) is calculated at a single, fixed value of x rather than optimizing over all values of x as was done in [Figure 6.12](#). Although the basic features of the plots in [Figure 6.13](#) are similar to those at x_{opt} ([Figure 6.12](#)), the level of amplification

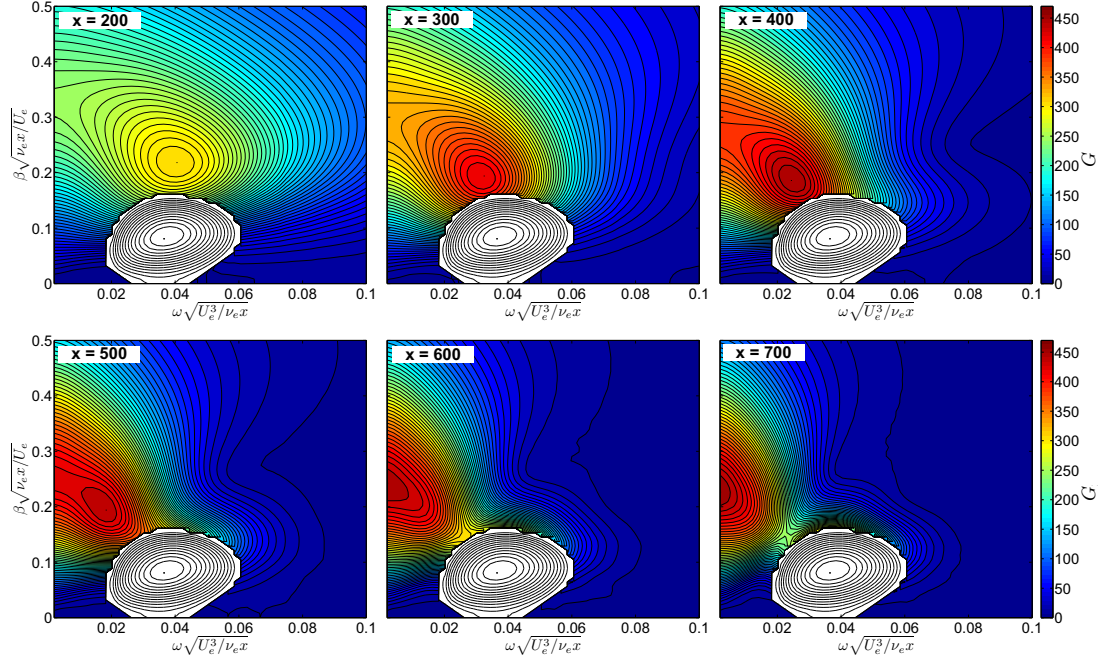


Figure 6.13: Contours of maximum (spatial) energy amplification G vs. streamwise and spanwise wavenumbers at six different streamwise distances. Mach number is 2.5, adiabatic wall, $R = 300$, $T_e = 70$ K. Optimal growth is found at $x_{opt} = 790$, $\omega = 0$, $\beta = 0.22$.

is somewhat lower and the optimal disturbance is no longer found at $\omega = 0$. This is consistent with the (temporal) observation of [Butler and Farrell \(1992\)](#) that disturbances having smaller streamwise wavelengths reach their maximum amplitude more rapidly. Although the level of amplification has been reduced relative to the optimal value, the reduction is not always so great as to render the non-modal amplification negligible. For example, at $M = 2.5$ the energy amplification reaches about 2/3 of its optimal value at $x/x_{opt} = 0.25$, which demonstrates that near-optimal amplification can be achieved at distances much less than x_{opt} .

The topology of Figure 6.13 is the same as that observed by [Corbett and Bottaro \(2000\)](#) for incompressible flow. An isolated peak in G is seen which increases in strength as x is increased. For small x the peak is located at a larger value of ω and approaches $\omega = 0$ as x increases. When x reaches x_{opt} (about 790 for these conditions), the peak value of G is located at $\omega = 0$ and the disturbance takes the form of the optimal streamwise vortex noted in Figure 6.5.

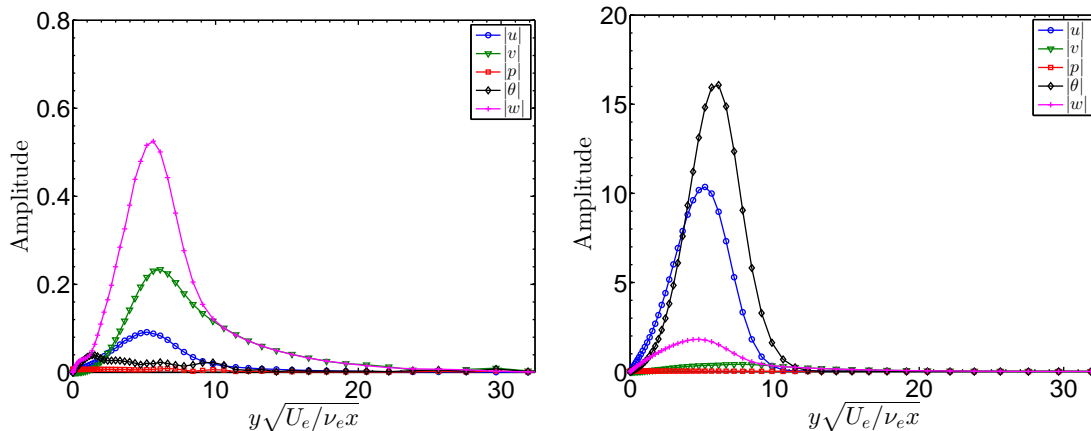


Figure 6.14: Optimal disturbance for a prescribed downstream distance of $x = 400$. $M = 2.5$, $R = 300$, $\omega = 0.025$, $\beta = 0.186$. Left: Optimal disturbance at $x = 0$. Right: Amplified disturbance at $x = 400$.

For $x < x_{opt}$, the optimal disturbance is no longer a streamwise vortex. This is shown in Figure 6.14 (left) which plots the optimal disturbance that produces the peak amplification at $x = 400$ in Figure 6.13. These results show that all three velocity components u , v , and w participate in the optimal disturbance, in contrast to the streamwise vortices observed previously. This initial perturbation evolves into the amplified disturbance shown in Figure 6.14 (right) at $x = 400$, and velocity vectors of the optimal disturbance at $x = 0$ superimposed on streamwise velocity contours of the amplified disturbance are given in Figure 6.15. These results show that the amplified disturbance still consists of streaks of velocity and temperature, which suggests that the lift-up effect is again responsible for the transient growth.

6.5.6 Effect of Energy Norm

A source of uncertainty in the transient growth analysis is the choice of energy norm (Section 6.4.1), which is not unique. However, there are some constraints that must be met in choosing a norm. One of these is that all disturbance variables must take part in the norm.

To see why this is so, consider an energy norm that consists only of the kinetic energy. One might be tempted to use such a norm since both the optimal and

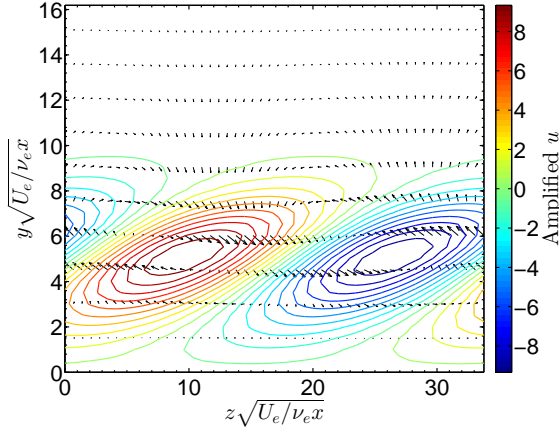


Figure 6.15: Velocity vectors of optimal input disturbance at $x = 0$ and contours of amplified streamwise velocity at $x = 400$. $M = 2.5$, $R = 300$, $\omega = 0.025$, $\beta = 0.186$.

amplified disturbances shown previously consist mainly of kinetic energy. However, this is not a meaningful choice of norm since one can easily achieve infinite transient growth by using kinetic energy alone to describe the disturbance. This would happen if the initial condition consists only of temperature and pressure fluctuations, and hence has zero initial kinetic energy. Some of the acoustic and thermal energy of the initial disturbance would then be converted into kinetic energy by the flow, resulting in a finite kinetic energy at some location downstream. Consequently, such an initial condition would produce infinite energy growth according to the kinetic energy norm. Clearly, one must include all disturbance variables in the energy norm in order to avoid this situation.

To investigate the sensitivity of results to the choice of energy norm, we arbitrarily penalized some of the terms in Equation 6.9 in comparison with others. An example of the result is given in Figure 6.16, where the temporal energy growth G for a high enthalpy Mach 5 flow is given as a function of spanwise wavenumber β for several different energy norms. In all cases vibrational energy of the disturbances is neglected. Blue diamonds represent the full energy norm involving all terms in Equation 6.9 except $\hat{\theta}_v$. For the case shown with green circles, the thermal energy (TE) is penalized by multiplying the terms involving $\hat{\rho}$ and $\hat{\theta}$ by a factor of 0.1 in Equation 6.9. Note that although these terms are here called the “thermal energy,”

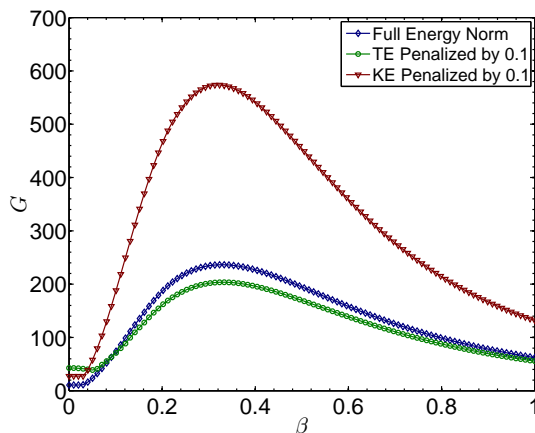


Figure 6.16: Energy growth G vs spanwise wavenumber for several different energy norms. TE is thermal energy and KE is kinetic energy. $M = 5$, $T_e = 1500$ K, $P_e = 10$ kPa, $R = 300$, $\alpha = 0$.

they actually contain the acoustic potential energy as well. For the case shown with red triangles, the kinetic energy (KE) is similarly penalized by a factor of 0.1.

When the thermal energy is penalized, the results do not differ appreciably from the full energy norm, though there is a slight reduction in G . The effect is small because the thermal energy already plays only a small role in the full energy norm for these conditions. Figure 6.17 shows the optimal disturbances at $t = 0$ and the amplified disturbances at $t = t_{opt}$. The optimal and amplified disturbances are almost identical for the full norm and the norm with penalized thermal energy. The slight reduction in G observed in Figure 6.16 occurs because the contribution of the amplified temperature disturbance to the energy is reduced.

For the case in which the kinetic energy is penalized, the behavior is quite different. As seen in Figure 6.17a, the penalization of kinetic energy enables a much larger initial streamwise vortex while maintaining unit energy of the initial condition. The stronger initial vortex then produces a larger amplified disturbance at $t = t_{opt}$. Although the streamwise velocity u of the amplified disturbance is penalized, the thermal energy is not, and this leads to the large increase in G observed for this case in Figure 6.16. It is interesting to note that these changes to the energy norm merely re-scale the optimal and amplified disturbances in Figure 6.17 without significantly changing their shape.

These results demonstrate that although the qualitative behavior appears to be

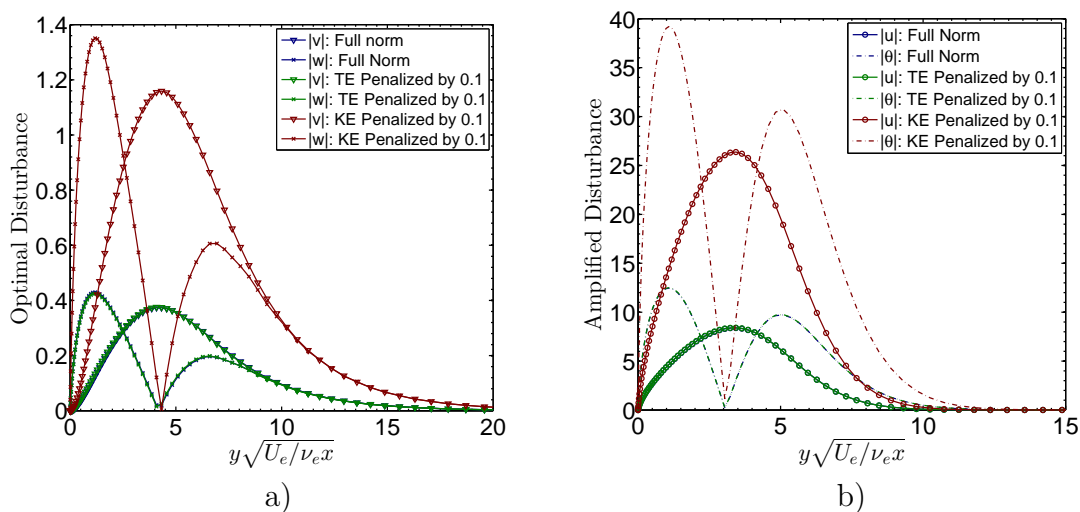


Figure 6.17: a) Optimal disturbances at $t = 0$. b) Amplified disturbances at $t = t_{opt}$. Each case corresponds to the most amplified spanwise wavenumber β in Figure 6.16. Disturbance variables not shown are an order of magnitude smaller than the ones plotted.

insensitive to the choice of norm, the level of amplification observed can be affected significantly. One can think of many different ways the norm could be altered, and each choice will affect the energy growth computed. Ultimately, the “best” choice for predicting boundary layer transition might take into account the manner in which disturbances interact nonlinearly, and could be tailored to the types of disturbances that most effectively generate harmonics and mean flow distortion. For example, since the Navier-Stokes equations are quadratic in velocity, one might expect large velocity disturbances to be more effective in triggering transition than large temperature disturbances, so one might choose a norm that is biased towards velocity disturbances. Lacking detailed studies of this nature, the energy norm used in Equation 6.9 appears to be a good choice since it derives naturally from the equations of motion for plane waves.

6.5.7 Effect of Vibrational Nonequilibrium

The preceding sections have assumed that the base flow is in a state of thermal equilibrium and the disturbances are vibrationally frozen, which are reasonable ap-

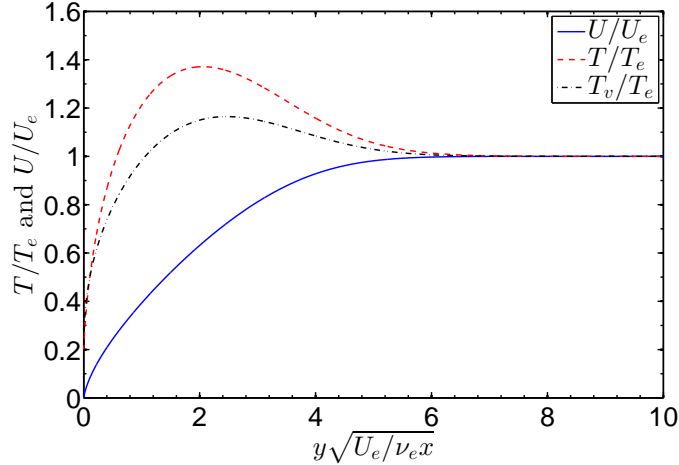


Figure 6.18: Base flow profiles for flow of CO_2 over a flat plate. Gas is CO_2 , $M = 5$, $T_e^* = 1000$ K, $T_w^* = 300$ K, $R = 300$.

proximations for flows of air. In this section, we briefly consider the influence of vibrational nonequilibrium on the non-modal disturbance amplification. To investigate these effects, this section analyses a highly nonequilibrium flow of carbon dioxide at $M = 5$ with an edge temperature of 1000 K and a wall temperature of 300 K. A fairly low Reynolds number of $R = 300$ is considered, where the base flow is out of equilibrium. The base flow at this Reynolds number is shown in Figure 6.18.

Using the mean profiles shown in Figure 6.18, transient growth calculations were conducted both with and without vibrational energy transfer included in the fluctuations. The resulting temporal profiles of G as a function of spanwise wavenumber are shown in Figure 6.19 for $\alpha = 0$. A slight increase in transient growth is observed when vibrational energy is included in the analysis. The transient growth mechanism observed here is the lift-up effect described previously, in which the initial streamwise vortices act against the gradients in mean velocity and temperature, thereby generating streamwise streaks of temperature and velocity. In the nonequilibrium case, there is a mean gradient in vibrational energy as well, and the action of the streamwise vortices generates vibrational temperature streaks in addition to the velocity and temperature streaks discussed previously. The increased energy growth observed in the non-equilibrium flow is the result of the vibrational energy streaks that develop.

These observations are demonstrated in Figure 6.20, which plots the optimal dis-

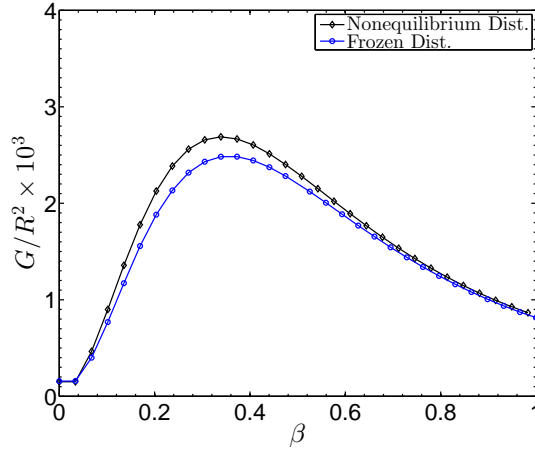


Figure 6.19: Energy growth for disturbances with and without vibrational energy transfer. Gas is CO_2 , $M = 5$, $T_e^* = 1000$ K, $T_w^* = 300$ K, $R = 300$.

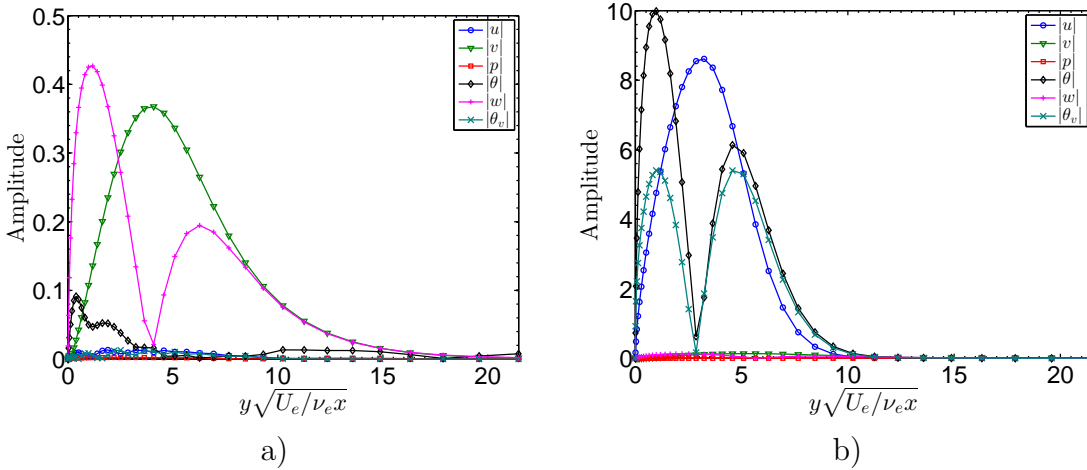


Figure 6.20: a) Optimal disturbances at $t = 0$. b) Amplified disturbances at $t = t_{opt}$. Flow is CO_2 , $M = 5$, $T_e^* = 1000$ K, $T_w^* = 300$ K, $R = 300$, $\alpha = 0$, $\beta = 0.36$

turbances (left) at $t = 0$ and the amplified disturbances (right) at $t = t_{opt}$. As has been observed in previous sections, the optimal disturbance consists mainly of vertical and spanwise velocities, \hat{v} and \hat{w} , in the form of a streamwise vortex. The amplified disturbance at $t = t_{opt}$ consists of streaks of streamwise velocity \hat{u} , temperature $\hat{\theta}$, and vibrational temperature $\hat{\theta}_v$.

Although the amplified disturbance contains a single velocity streak, the amplified temperatures $\hat{\theta}$ and $\hat{\theta}_v$ both consist of a pair of two streaks. The reason is that the mean temperature profiles of T and T_v contain a maximum (Figure 6.18), and the upward vertical velocity induced by a streamwise vortex produces a positive temper-

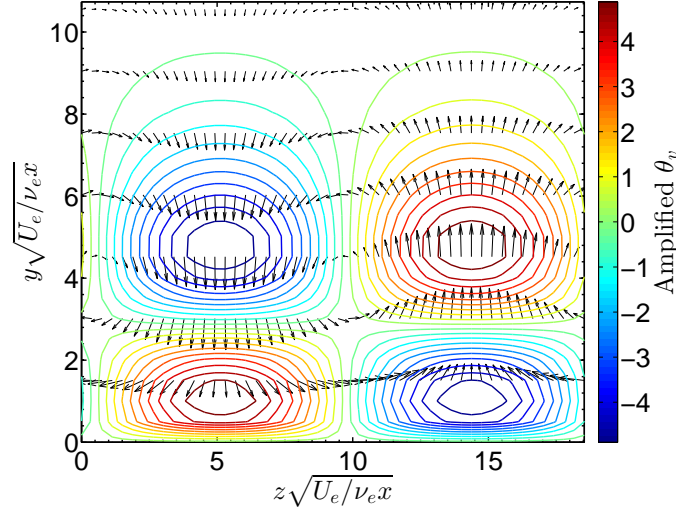


Figure 6.21: Velocity vectors of optimal input disturbance at $t = 0$ and contours amplified vibrational temperature at $t = t_{opt}$. $M = 5.0$, $\alpha = 0$, $\beta = 0.36$, $R = 300$.

ature streak above the maximum and a negative temperature streak below. This is in contrast to the mean velocity profile, which is monotonic, and hence a single velocity streak is produced. This explanation is confirmed by Figure 6.21, where contours of amplified vibrational temperature $\hat{\theta}_v$ are overlaid against the optimal velocity vectors.

Although the energy growth appears to be larger for nonequilibrium situations, this does not necessarily imply that transition onset will occur sooner. Compared with velocity or density streaks, the vibrational temperature streaks that develop may be less likely to participate in secondary instabilities and nonlinear interactions that ultimately lead to turbulence. In some circumstances (for example, if the vibrational energy exchange rate is slow), the vibrational energy may behave as a passive scalar, in which case its amplification would be largely irrelevant for transition prediction. In such a scenario it might be preferable to exclude the vibrational temperature from the energy norm in Equation 6.9. In general, the decision to include or exclude vibrational energy will ultimately depend on the rate of energy transfer between $\hat{\theta}$ and $\hat{\theta}_v$ and the manner in which this energy exchange participates in the nonlinear breakdown process.

6.5.8 Modal vs. Non-modal

Our final consideration is a direct comparison between modal and non-modal energy amplification. The transient growth calculations are conducted in the spatial framework with disturbances having $\omega = 0$, since such conditions usually produce the largest energy amplification according to the preceding results. Spatial transient growth calculations are carried out for several initial Reynolds numbers, and the downstream evolution of energy for each Reynolds number is compared with the energy growth arising from modal instabilities.

Recall from Section 5.1.2 that for a particular frequency F the N factor for modal instabilities is defined by:

$$N_{modal}(F, \beta) = \int_{x_o}^x -\alpha_i(x, F, \beta) dx \quad (6.16)$$

where x_o is the location at which disturbances of frequency F first become unstable. This N factor describes the logarithm of the downstream growth of a fixed-frequency disturbance. An analogous N factor for non-modal growth can be defined by the relation

$$N_{opt}(x) \equiv \frac{1}{2} \ln(G(x)) \quad (6.17)$$

The factor of 1/2 arises from the fact that the energy amplification G scales quadratically with the disturbance amplitude, so to make a meaningful comparison with the amplitude growth of a single discrete mode one must take the square root. The definition (6.17) is chosen such that N_{opt} and N_{modal} are identical when the disturbance consists of a single discrete mode.

A comparison between the modal and non-modal N factors is shown in Figure 6.22. Here the Mach number is 2.5 and the wall temperature is adiabatic. The N factors involving transient growth are labeled N_{opt} , and the ten curves correspond to ten different initial Reynolds numbers Re_x between 10^4 and 10^6 . Separate curves for each initial Reynolds number are required since each value of Re_x yields a slightly

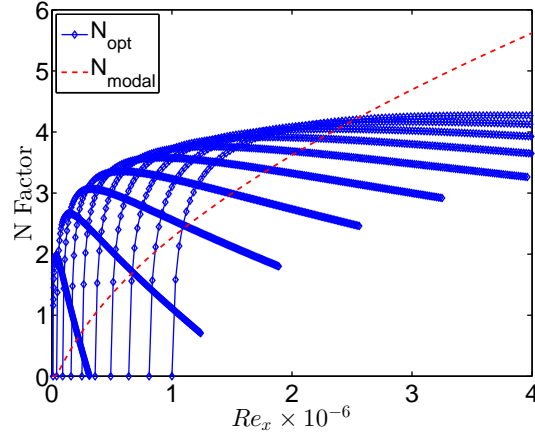


Figure 6.22: Comparison of N factors from modal and non-modal stability calculations for $M = 2.5$, $T_w = T_{ad}$, $T_e = 70$ K. N_{opt} is the N factor corresponding to non-modal disturbances, and N_{modal} is the modal N factor envelope over all values of ω and β .

different optimal disturbance that evolves differently as it travels downstream. For each initial Reynolds number, the optimal disturbance corresponding to the maximum of Figure 6.12 ($\omega = 0$, $\beta = 0.22$) is selected and its downstream amplification is calculated. The envelope of these curves marks the maximum level of transient growth that is plausible at each location. The dashed red line represents the envelope of all possible N factor curves corresponding to modal instabilities; this envelope curve is optimized over all frequencies and contains both 2D and 3D disturbances for both the first and second mode instabilities.

It must be emphasized that this downstream development of optimal disturbances is based on the locally parallel calculation and neglects boundary layer growth. However, by comparing the nonparallel results of Tumin and Reshotko (2003) with the parallel results of Tumin and Reshotko (2001), it is observed that both the optimization distance x_{opt} and the energy growth G are in reasonable agreement. The energy growth G can differ by a factor of 2-3, but for the purposes of making comparisons with modal analysis this difference is acceptable since the corresponding error in N_{opt} is only about 0.4-0.5.

For the adiabatic condition shown in Figure 6.22, modal growth surpasses non-modal growth at a Reynolds number of about $Re_x = 2.9 \times 10^6$. The N factor at this location is 4.2, which corresponds to an increase in modal amplitude of about 67 and

an energy amplification of 4400. This level of amplification is not large, suggesting that under these conditions transition via transient growth might be expected only in a noisy environment where disturbance amplitudes are high, or in situations involving discrete surface roughness elements where strong streamwise, vortical disturbances are likely (Reshotko and Tumin, 2004). However, the level of N at which nonlinear breakdown begins is open to question and may be different for modal and non-modal instabilities, given the differences in the disturbance shapes. The value of N at which transition occurs is also expected to depend on the strength of disturbance sources and the boundary layer's receptivity to them.

Two additional examples of N factor distributions are shown in Figure 6.23 which demonstrate the effects of wall cooling. The first example (left) is flow at Mach 5 with a cold wall, $T_w/T_e = 0.3$. This condition might be encountered in a shock tunnel operating at a moderate enthalpy of $H_o = 6$ MJ/kg. In comparison to the low Mach number, adiabatic case shown in Figure 6.22, the modal instability overtakes the non-modal one much more rapidly. This is caused by both lower levels of non-modal energy amplification and the larger growth rate of the second mode instability. The modal instability overtakes the transient growth at $Re_x = 1.2 \times 10^6$ where the N factor is 3.7 and the energy amplification is only 1600. Experiments conducted at similar conditions (Adam and Hornung, 1997) have reported transition at Reynolds numbers of 2 – 3 million; at this point modal instabilities have undergone more than an order of magnitude larger amplification than non-modal ones, which suggests that transition to turbulence is caused by modal mechanisms at these conditions.

The last example, Figure 6.23 (right), is flow at Mach 0.5 with a cold wall, $T_w/T_e = 0.3$. As discussed in the introduction, there are no modal instabilities for these conditions, so the modal N factor is zero. At a Reynolds number of 2.0×10^6 , N_{opt} is about 5.3 which corresponds to $G = 40000$. Moreover, given the well-known (Hanifi and Henningson, 1998) scaling $G_{opt} \propto Re_x$, much larger amplification is possible as the Reynolds number is increased. On the basis of this result, it seems reasonable to conclude that flows at low Mach numbers with wall cooling may transition to turbulence from infinitesimal perturbations despite the absence of modal instabilities. In

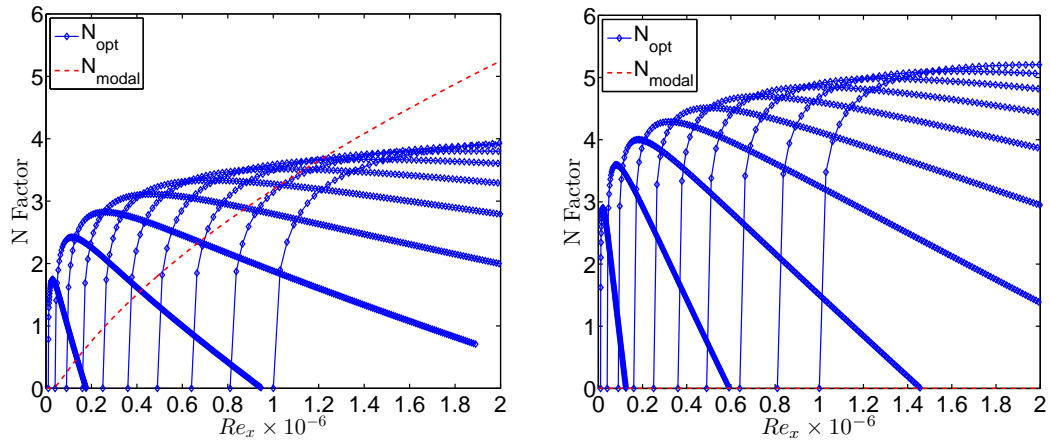


Figure 6.23: Comparison of N factors from modal and non-modal stability calculations. Left: $M = 5.0$, $T_w/T_e = 0.3$, $T_e = 1000$ K. Right: $M = 0.5$, $T_w/T_e = 0.3$, $T_e = 1000$ K.

contrast, high Mach number flows with cold wall conditions seem likely to transition by modal mechanisms alone.

Chapter 7

Linearized DNS Calculations

7.1 Introduction

The linear stability calculations presented in the preceding chapters made use of either the spatial or the temporal approximations, in which either the frequency ω or the wavenumber α is assumed to be a constant. At a particular location along the boundary layer, these two methods are roughly equivalent and can locally be related to one another using Gaster's transform (Gaster, 1962). The advantage of the spatial method, which has become the state of the art for boundary layer stability analysis, is that the downstream propagation of a disturbance in a non-parallel boundary layer can be described by a succession of locally-parallel analyses. The change in amplitude A of a disturbance as it propagates downstream is then obtained by integrating the local growth rate

$$\frac{A(x)}{A(x_o)} = e^{N(x)} = \exp\left(\int_{x_o}^x -\alpha_i(x')dx'\right) \quad (7.1)$$

where N is the N factor discussed in Section 5.1.2 and α_i is the spatial growth rate. In using this method, the frequency of the disturbance is assumed to remain fixed as it propagates downstream. Such an assumption is motivated by the so-called signaling problem (Ashpis and Reshotko, 1990), in which a fixed-frequency disturbance source such as a vibrating ribbon or a pulsating jet is placed in the boundary layer at a particular location. The disturbances then propagate downstream with a well-defined,

fixed frequency and a periodic steady-state is reached. Such an arrangement was used in the famous experiments of [Schubauer and Skramstad \(1947\)](#) and provides a means of examining the frequency response of a boundary layer.

In most experiments and in actual flight, the disturbances are not generated in such a well-controlled and precise manner. For instance, in most hypersonic wind tunnels the boundary layer is irradiated with acoustic waves generated by turbulent boundary layers on the nozzle and tunnel wall, and these waves contain a wide range of length and time scales ([Laufer, 1964](#)). Since acoustic waves are generated by vortical structures within the turbulent boundary layer on the tunnel wall through eddy-Mach wave radiation ([Laufer et al., 1964](#)), the length and time scales of the acoustic radiation into the test section are strongly correlated with the properties of the boundary layer from which they originate. Direct numerical simulations by [Duan and Choudhari \(2013, 2014\)](#) revealed that for conventional wind tunnels, the de-correlation length of acoustic waves in the freestream is only several times the thickness of the boundary layer from which they emerge. This means that the freestream disturbances take the form of packets that are localized in space and time. When such localized, intermittent wave packets impinge on the boundary layer, they may excite packets of instability waves that are also localized in space and time. This is demonstrated by experimental measurements of second mode waves within the boundary layer, which usually appear as wave packets consisting of 5-20 waves. Two examples of such experimental measurements from the literature are reproduced in [Figure 7.1](#).

When a packet of second mode waves is excited in this manner, the boundary layer serves as a filter that selectively damps some frequencies or wavenumbers and amplifies others. The scales that are damped or amplified depend on the streamwise location, with small length and time scales being amplified at low Reynolds numbers where the boundary layer thickness is small and large length and time scales being amplified at large Reynolds numbers. As was shown in [Chapter 5](#), the frequency selectivity of the boundary layer is especially strong for second mode waves, which are amplified only over a very narrow band of frequencies, and the unstable frequency band is a strong function of downstream distance (c.f. [Figure 5.3](#)).

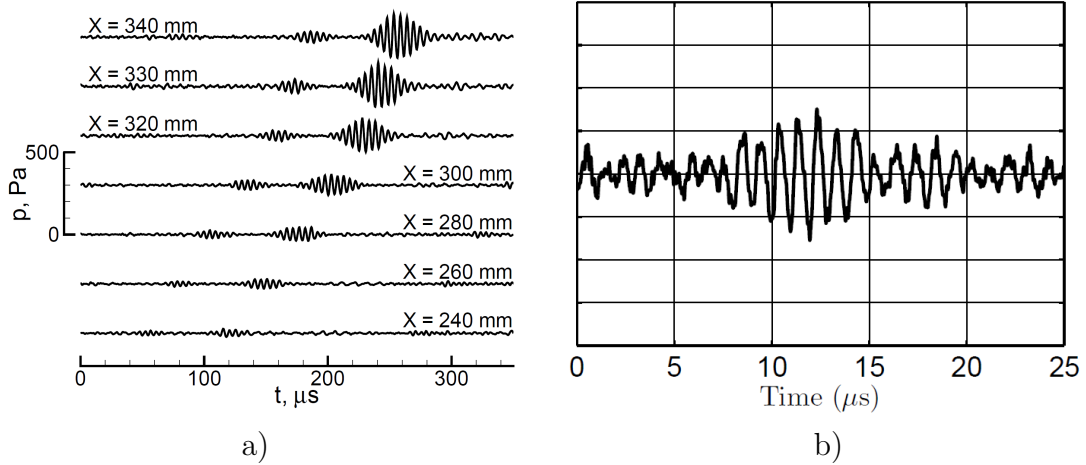


Figure 7.1: a) Wall pressure traces recorded by Heitmann et al. (2011) in a Mach 6 Ludwig tube (reproduced with permission). b) Focused Laser Differential Interferometer time traces in a high enthalpy boundary layer in T5 recored by Parziale (2013) (reproduced with permission). Ordinate is relative density fluctuation $\tilde{\rho}/\bar{\rho}$ with grid spacing of 2.5×10^{-3} .

Packets of instability waves that are localized in space and time, such as those observed in Figure 7.1, contain a spectrum of frequencies and wavenumbers. As the packet travels down the boundary layer, the frequency and wavenumber content of the packet evolve in response to the local amplification or damping properties. A precise description of how such a wavepacket evolves has not previously been given, yet it is highly relevant for predictions of boundary layer transition. In this chapter, linearized DNS is used to investigate the downstream evolution of such instability wavepackets. Three different types of simulations are conducted, which are illustrated in Figure 7.2. The three types of simulations proceed from the most idealized configuration to the most physically realistic one.

1. **Spatial DNS:** In this type of simulation, a second mode wave of a fixed frequency is imposed at the inlet of the computational domain and the simulation is run until a periodic steady-state is reached. An example of the periodic steady-state pressure distribution that is obtained is given in Figure 7.2a. Note that the waves imposed at the inlet are not visible because their amplitude is much smaller than those of the more highly amplified waves downstream. The

periodic flow profiles obtained from this type of simulation describe the amplification of a single frequency or Fourier mode of second mode waves. This calculation is analogous to the spatial linear stability theory of Chapter 5, but fully takes into account all non-parallel effects. This type of analysis, and its computationally efficient alternative based on the Parabolized Stability Equations (PSE), are presently the state of the art for boundary layer transition prediction.

2. **Second Mode Wavepackets:** In this type of simulation, a second mode instability wave packet of finite width is directly placed into the boundary layer slightly upstream of the upper neutral branch. The initial properties of this wave packet are determined from the linear stability analysis of Chapter 5. An example of the initial pressure field for this type of simulation is given in Figure 7.2b. The initial condition consists of periodic, second-mode eigenfunctions modulated by a Gaussian envelope in the streamwise direction. This initial wave packet then travels downstream and its amplitude and frequency spectrum are monitored. This type of analysis relaxes the assumption of a fixed frequency wave, but intentionally ignores the question of how the instability wave originates; that is, receptivity is bypassed by placing the disturbance directly into the boundary layer as an initial condition. The advantage is that the complications of receptivity are eliminated from the problem so that the downstream evolution of the wavepacket as it passes through the instability region can be isolated and studied.
3. **Incoming Acoustic Wavepackets:** In this type of simulation, a Gaussian-shaped packet of planar acoustic waves is generated in the freestream above the boundary layer. An example of the initial condition for this type of simulation is shown in Figure 7.2c. This packet of waves then impinges at an angle on the boundary layer and excites second mode waves, and the downstream development of these waves is monitored. This method of exciting disturbances in the boundary layer is motivated by the wind tunnel experiments discussed above,

in which packets of acoustic radiation in the freestream impinge on the boundary layer. In this configuration both the receptivity and downstream growth of second mode waves are included in the analysis, hence it constitutes the most realistic model of boundary layer transition considered in this chapter.

In all of the cases shown in Figure 7.2, the wavelength of the disturbances is much smaller than the local boundary layer thickness, which is marked by the thick black lines on the figures. This feature motivates the locally parallel analysis reported in Chapter 5, in which boundary layer growth is ignored over the small length scale associated with the wavelength of the disturbances. It also causes the DNS to be expensive, since one must resolve the small scales of the disturbances while at the same time using a large domain that captures the full extent of the boundary layer.

7.2 Previous Work

Several experimental and computational studies of wavepacket evolution have been carried out in the past, mostly involving incompressible flows and Tollmien-Schlichting type disturbances. Gaster and Grant (1975) were among the first to study this problem experimentally; they developed an experiment in which wavepackets were generated by a loudspeaker projecting through a hole in a flat plate, and the downstream development of these waves was measured using hot wire probes. They noted that the frequency content of the disturbances shifted to lower frequencies as the packet traveled downstream, and also that the increase in wavepacket amplitude was substantially less than the prediction of linear stability theory. They concluded that the wavepacket amplitude consists of a sum of many modes having different frequencies, each evolving in a different manner as the wavepacket travels downstream.

In coordination with this experimental study, Gaster (1975) developed a theoretical model in which the wavepacket was represented as a summation over the normal modes corresponding to 128 different frequencies. Using this method he was able to reproduce the measured downstream evolution of the wavepacket, although *ad hoc* phase shifting of the individual Fourier modes was needed to match the experimental

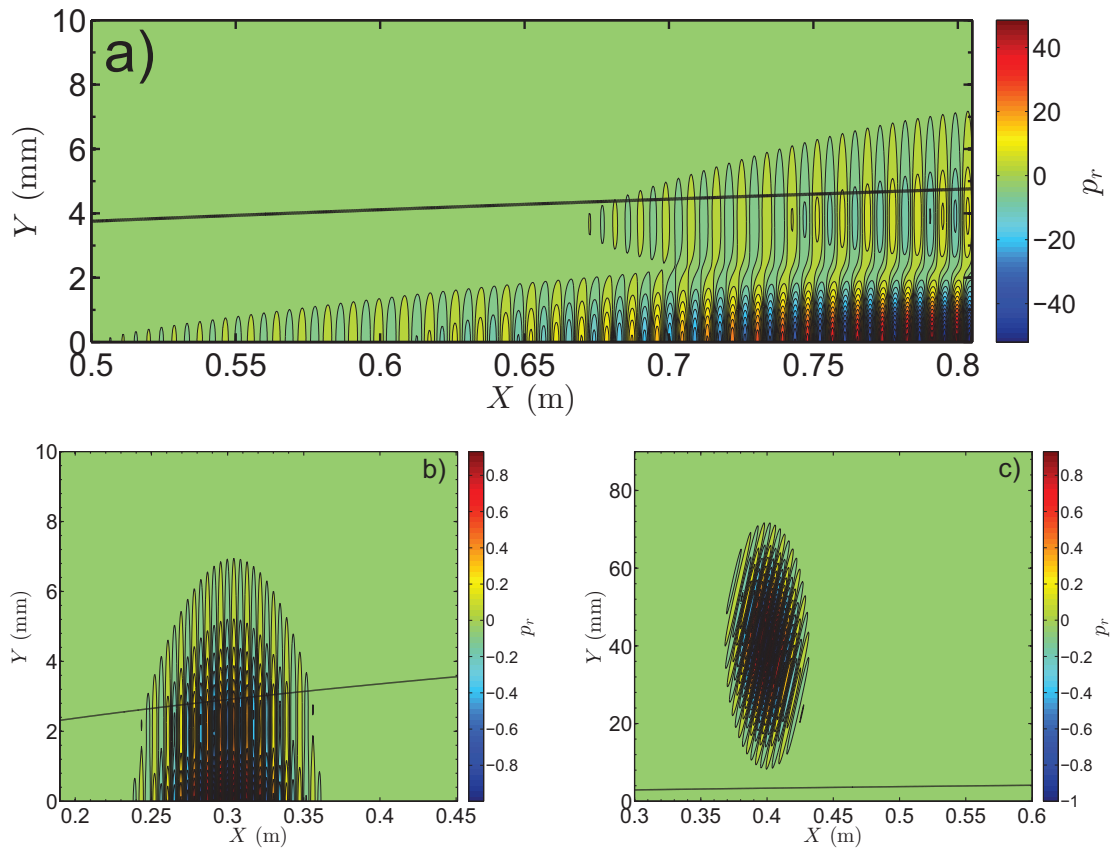


Figure 7.2: Examples of pressure fields from three types of simulations. Thick, black line indicates δ_{99} . a) Final, periodic steady-state pressure field from spatial DNS. b) Initial pressure field for a packet of second mode waves placed within the boundary layer. c) Initial pressure field for an incoming wave packet impinging on the boundary layer from the freestream.

data. Gaster also assumed that all Fourier modes were excited to the same amplitude by the disturbance source. In later work, [Gaster \(1982a,b\)](#) employed the method of steepest descents and several other simple approximations to evaluate the wave packet shape at distances far downstream from its source. However, in these analyses simplified models of the dispersion relation were used and certain terms involving the eigenfunction shape of the disturbance were neglected, meaning that only qualitative results could be obtained.

[Cohen et al. \(1991\)](#) used a pulsed air jet to generate instability wave packets in an incompressible boundary layer and recorded their downstream evolution using hot wire probes. Although the disturbance velocity profiles agreed well with the eigenfunctions of Tollmien-Schlichting waves, the downstream progression of the wavepacket amplitude and frequency content were not reported or compared with linear stability theory. Instead the study focused on nonlinear interactions between various instability wave modes. Similarly, later studies by [Cohen \(1994\)](#) and [Medeiros and Gaster \(1999\)](#) focused on secondary instabilities and nonlinearity rather than on the linear wave packet amplitude development.

Only a few authors have investigated the evolution of wave packets in compressible boundary layers. Notable examples are the DNSs of [Mayer et al. \(2011\)](#) and [Sivasubramanian and Fasel \(2014\)](#), in which boundary layers at Mach 3.5 and 6 were perturbed by a velocity pulse through a hole in the surface of a sharp cone. These studies used Fourier transforms to extract specific frequencies from the simulations and analyze the downstream propagation and nonlinear interaction of the various Fourier modes; however, they did not report on the downstream amplification of the wavepacket itself.

[Forgoston and Tumin \(2006\)](#) conducted a theoretical study in which the downstream evolution of a wave packet in a perfectly parallel boundary layer was computed. This is the first and only compressible stability analysis in which the Fourier and Laplace transforms with respect to space and time (duals to α and ω) were inverted to compute the propagation of a wave in physical space. Their analysis captured the growth and spreading of a second mode wave packet and showed that the method of

steepest descents can successfully determine the wave packet shape at distances far downstream from its source. Nevertheless, since this analysis was restricted to a perfectly parallel boundary layer, the influence of the increasing boundary layer thickness and the accompanying changes in dispersive behavior were not taken into account. These properties must be included in order to assess the wavepacket behavior over distances that are more than a few boundary layer thicknesses long.

A few experimental studies have also been carried out in which wave packets were excited using impulsive disturbances in a hypersonic boundary layer. [Heitmann et al. \(2011\)](#) focused a pulsed laser to a point outside of the boundary layer and generated a spherical blast wave that then impinged on the boundary layer and excited second mode waves. Surface pressure measurements were then used to study the response of the boundary layer. Although instability waves were successfully excited, these waves were measured only over a short distance (about 40 mm) and hence the growth and dispersion of these waves could not be examined. [Casper et al. \(2012a,b, 2014\)](#) generated disturbances on the nozzle wall of Purdue's Mach 6 quiet tunnel using electrical discharges and then measured the pressure fluctuations downstream of this point; however, the properties of the laminar boundary layer on the nozzle wall were not reported, so it is difficult to relate the measured disturbances to the boundary layer modes. Recently [Casper et al. \(2013a,b\)](#) have recorded simultaneous pressure measurements and schlieren images of second mode wave packets at Mach 5, 8, and 14 and their results appear promising, but most of the measurements were made over a short distance (about 40 mm) over which little dispersion occurs.

In spite of these few computational and experimental studies of wave packet propagation in compressible boundary layers, the amplification of such wave packets and its relation to linear stability theory remain completely unknown. However, numerous experiments such as those shown in [Figure 7.1](#) have shown that the second mode instability usually consists of intermittent bursts of finite-width wave packets, rather than long wave trains of a single frequency (as is assumed in conventional stability analysis). Therefore it is important to analyze the influence of a finite wave packet width on its amplification and take this into account in predicting boundary layer

transition.

7.3 Governing Equations

For the sake of simplicity, the simulations carried out in this chapter are restricted to 2D flows of calorically perfect ideal gases. We are interested mainly in the second mode instability, since this instability is most important for high Mach number flows (Section 5.4). Because 2D second mode waves are more unstable than 3D waves, it suffices to perform 2D simulations as a first approximation, although three dimensionality may be important for disturbances that are localized in the spanwise direction (Sivasubramanian and Fasel, 2014). In this chapter, the flow conditions are representative of a low enthalpy wind tunnel, so simulations involving a calorically perfect ideal gas are quite reasonable.

The DNSs are carried out using the linearized Navier-Stokes equations, rather than the full nonlinear equations. There are several reasons for this:

1. We are interested in the growth of small disturbances and in making comparisons with the linearized theory, so we plan to investigate only situations in which nonlinear interactions are negligible. In that case it makes sense to use a linearized method.
2. To perform nonlinear simulations one must use either shock capturing or shock fitting to model the weak shock wave that is produced by viscous-inviscid interaction at the leading edge. By using a linearized method, the flow is decomposed into a mean part and a fluctuating part, and the mean part can be assumed to be a self-similar, shock-free laminar boundary layer, thus avoiding the complexity of capturing the shock. Of course, the simulations will then exclude interactions between the shock wave and the disturbances, but these are only important near the very leading edge of the plate and far outside the boundary layer.

The shock-disturbance interactions in the nose region are likely to be important,

since many authors have shown that receptivity to acoustic waves is strongest near the leading edge of a plate or cone (Fedorov and Khokhlov, 1993, Fedorov, 2003, Balakumar, 2009, Malik and Balakumar, 2007, Balakumar, 2007, Ma and Zhong, 2003b). However, in this work we are interested in the excitation of waves downstream of this point as well as their downstream evolution, and the presence of the shock wave has little influence on either of these processes. Away from the leading edge, the interaction of freestream waves with the shock can be treated separately from the DNS using the methods of McKenzie and Westphal (1968), which have been shown to agree well with DNS results (Ma and Zhong, 2003b).

3. Solving the linearized Navier-Stokes equations enables the use of complex-value disturbances. While this increases the computational cost, it also increases the amount of information available in the solutions and facilitates the extraction of quantities like frequency, phase, growth rate, and eigenfunction from the solutions and enables close comparisons with linear stability results.

After applying the assumption of a calorically perfect ideal gas, the nondimensional Navier-Stokes equations from Equation 2.14 are simplified and re-arranged in the following form:

$$\frac{D\rho}{Dt} + \rho \nabla \cdot \mathbf{u} = 0 \quad (7.2a)$$

$$\rho \frac{D\mathbf{u}}{Dt} + \nabla p = \frac{1}{Re_L} \nabla \cdot \boldsymbol{\tau} \quad (7.2b)$$

$$\rho \frac{DT}{Dt} + M^2 \gamma (\gamma - 1) p \nabla \cdot \mathbf{u} = \frac{\gamma (\gamma - 1) M^2}{Re_L} \nabla \mathbf{u} : \boldsymbol{\tau} - \frac{\gamma}{\sigma Re_L} \nabla \cdot \mathbf{q} \quad (7.2c)$$

$$\gamma M^2 p = \rho T \quad (7.2d)$$

where σ is the Prandtl number, γ is the ratio of specific heats, and Re_L is the Reynolds number based on the plate length L . The elements of the heat flux vector

\mathbf{q} and the viscous stress tensor $\boldsymbol{\tau}$ are

$$q_i = -k \frac{\partial T}{\partial x_i} \quad (7.3a)$$

$$\tau_{ij} = \mu \left(\frac{\partial u_i}{\partial x_j} + \frac{\partial u_j}{\partial x_i} - \frac{2}{3} \frac{\partial u_k}{\partial x_k} \delta_{ij} \right) \quad (7.3b)$$

In the viscous stress tensor, Stokes' assumption of zero bulk viscosity has been applied. Linearization of Equations 7.2 for 2D waves leads to the following system of equations:

Continuity:

$$\frac{\partial \tilde{\rho}}{\partial t} + \bar{U} \frac{\partial \tilde{\rho}}{\partial x} + \bar{V} \frac{\partial \tilde{\rho}}{\partial y} + \frac{1}{\bar{T}} \left(\frac{\partial \tilde{u}}{\partial x} + \frac{\partial \tilde{v}}{\partial y} \right) + \tilde{\rho} \nabla \cdot \bar{\mathbf{U}} - \frac{1}{\bar{T}^2} \left[\tilde{u} \frac{\partial \bar{T}}{\partial x} + \tilde{v} \frac{\partial \bar{T}}{\partial y} \right] = 0 \quad (7.4a)$$

X Momentum:

$$\begin{aligned} & \frac{\partial \tilde{u}}{\partial t} + \bar{U} \frac{\partial \tilde{u}}{\partial x} + \bar{V} \frac{\partial \tilde{u}}{\partial y} + \tilde{u} \frac{\partial \bar{U}}{\partial x} + \tilde{v} \frac{\partial \bar{U}}{\partial y} + \bar{T} \tilde{\rho} \left(\bar{U} \frac{\partial \bar{U}}{\partial x} + \bar{V} \frac{\partial \bar{U}}{\partial y} \right) \\ & + \frac{1}{\gamma M^2} \left[\frac{\partial \tilde{\theta}}{\partial x} + \bar{T}^2 \frac{\partial \tilde{\rho}}{\partial x} + \left(\tilde{\rho} \bar{T} - \frac{\tilde{\theta}}{\bar{T}} \right) \frac{\partial \bar{T}}{\partial x} \right] = \frac{\bar{T}}{Re_L} \left(\frac{\partial \tilde{\tau}_{xx}}{\partial x} + \frac{\partial \tilde{\tau}_{xy}}{\partial y} \right) \end{aligned} \quad (7.4b)$$

Y Momentum:

$$\begin{aligned} & \frac{\partial \tilde{v}}{\partial t} + \bar{U} \frac{\partial \tilde{v}}{\partial x} + \bar{V} \frac{\partial \tilde{v}}{\partial y} + \tilde{u} \frac{\partial \bar{V}}{\partial x} + \tilde{v} \frac{\partial \bar{V}}{\partial y} + \bar{T} \tilde{\rho} \left(\bar{U} \frac{\partial \bar{V}}{\partial x} + \bar{V} \frac{\partial \bar{V}}{\partial y} \right) \\ & + \frac{1}{\gamma M^2} \left[\frac{\partial \tilde{\theta}}{\partial y} + \bar{T}^2 \frac{\partial \tilde{\rho}}{\partial y} + \left(\tilde{\rho} \bar{T} - \frac{\tilde{\theta}}{\bar{T}} \right) \frac{\partial \bar{T}}{\partial y} \right] = \frac{\bar{T}}{Re_L} \left(\frac{\partial \tilde{\tau}_{yx}}{\partial x} + \frac{\partial \tilde{\tau}_{yy}}{\partial y} \right) \end{aligned} \quad (7.4c)$$

Energy:

$$\begin{aligned}
& \frac{\partial \tilde{\theta}}{\partial t} + \bar{U} \frac{\partial \tilde{\theta}}{\partial x} + \bar{V} \frac{\partial \tilde{\theta}}{\partial y} + \tilde{u} \frac{\partial \bar{T}}{\partial x} + \tilde{v} \frac{\partial \bar{T}}{\partial y} + \tilde{\rho} \bar{T} \left(\bar{U} \frac{\partial \bar{T}}{\partial x} + \bar{V} \frac{\partial \bar{T}}{\partial y} \right) \\
& + (\gamma - 1) \bar{T} \left(\frac{\partial \tilde{u}}{\partial x} + \frac{\partial \tilde{v}}{\partial y} \right) + (\gamma - 1) \left(\tilde{\rho} \bar{T}^2 + \tilde{\theta} \right) \left(\frac{\partial \bar{U}}{\partial x} + \frac{\partial \bar{V}}{\partial y} \right) = \\
& \frac{\gamma(\gamma - 1) M^2 \bar{T}}{Re_l} \left(\tilde{\tau}_{ij} \frac{\partial \bar{U}_i}{\partial x_j} + \bar{\tau}_{ij} \frac{\partial \tilde{u}_i}{\partial x_j} \right) - \frac{\bar{T} \gamma}{\sigma Re_L} \frac{\partial \tilde{q}_i}{\partial x_i} \quad (7.4d)
\end{aligned}$$

where bars represent components of the mean laminar boundary layer, and tildes signify linear fluctuations. The disturbance variables are the streamwise and wall normal velocities \tilde{u} and \tilde{v} , the density $\tilde{\rho}$, and the temperature $\tilde{\theta}$. The components of the mean and fluctuating viscous stress tensors are

$$\begin{aligned}
\bar{\tau}_{ij} &= \bar{\mu} \left(\frac{\partial \bar{U}_i}{\partial x_j} + \frac{\partial \bar{U}_j}{\partial x_i} - \frac{2}{3} \delta_{ij} \frac{\partial \bar{U}_k}{\partial x_k} \right) \\
\tilde{\tau}_{ij} &= \bar{\mu} \left(\frac{\partial \tilde{u}_i}{\partial x_j} + \frac{\partial \tilde{u}_j}{\partial x_i} - \frac{2}{3} \delta_{ij} \frac{\partial \tilde{u}_k}{\partial x_k} \right) + \tilde{\mu} \left(\frac{\partial \bar{U}_i}{\partial x_j} + \frac{\partial \bar{U}_j}{\partial x_i} - \frac{2}{3} \delta_{ij} \frac{\partial \bar{U}_k}{\partial x_k} \right)
\end{aligned}$$

and the components of the fluctuating heat flux vector are

$$\tilde{q}_i = \bar{k} \frac{\partial \tilde{\theta}}{\partial x_i} + \tilde{k} \frac{\partial \bar{T}}{\partial x_i} \quad (7.5)$$

In deriving Equations 7.4, the mean density $\bar{\rho}$ was eliminated using the mean equation of state ($\bar{T} = 1/\bar{\rho}$) and the fluctuating equation of state was used to eliminate the pressure fluctuations:

$$\gamma M^2 \tilde{p} = \bar{\rho} \tilde{\theta} + \bar{T} \tilde{\rho} \quad (7.6)$$

The fluctuations in thermal conductivity \tilde{k} and viscosity $\tilde{\mu}$ are related to fluctuations in temperature by the formulas:

$$\tilde{k} = \frac{\partial \bar{k}}{\partial \bar{T}} \tilde{\theta} \quad \tilde{\mu} = \frac{\partial \bar{\mu}}{\partial \bar{T}} \tilde{\theta} \quad (7.7)$$

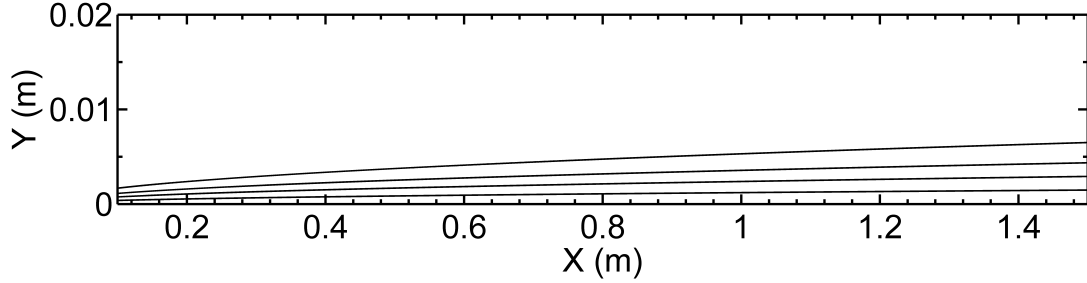


Figure 7.3: Example of flow domain. Contour lines are equally spaced between $\bar{U} = 0$ and $\bar{U} = 0.99$. $M = 4.5$, $T_e = 65$ K, adiabatic wall. Unit Reynolds number is $Re_u = 6.5$ million/m.

7.4 Numerical Methods

Equations 7.4 are discretized using fourth order, non-compact, central finite differences in space and then integrated using a fourth order Runge-Kutta scheme in time. In calculating derivatives of the viscous stress tensor $\tilde{\tau}_{ij}$ and the heat flux vector \tilde{q}_i , the derivatives are expressed analytically in terms of the primitive variables $\tilde{\rho}$, \tilde{u} , \tilde{v} , and $\tilde{\theta}$ and their derivatives, rather than computing the fields of $\tilde{\tau}_{ij}$ and \tilde{q}_i and subsequently differentiating these fields. At boundaries of the domain, the derivatives are reduced to second order accuracy since high order, biased derivatives are usually unstable (Zhong, 1998). Although the reduction to second order accuracy at the boundaries reduces the formal accuracy of the method to third order, our convergence studies indicate that near fourth-order convergence is still achieved (Section 7.4.3). Further information regarding the implementation of the boundary conditions is given in Section 7.4.2.

The flow domain begins slightly downstream of the leading edge of the flat plate. An example of a typical flow domain is given in Figure 7.3, where the contour lines indicate the mean horizontal velocity \bar{U} with contour levels equally spaced between 0 and 0.99. The domain is discretized using 4500-6000 equally-spaced points in x and 300-600 points in y . The large number of points in x is needed because the domain is much larger than the streamwise wavelength of the disturbances under consideration. In some simulations the grid points are stretched in y using the algebraic grid stretching described by Malik (1990) which maps a set of equally-spaced points $\xi \in [-1, 1]$

onto the interval $y \in [0, y_{\max}]$:

$$y = \frac{a(1 + \xi)}{b - \xi} \quad (7.8)$$

where

$$a = \frac{y_{\max} y_i}{y_{\max} - 2y_i} \quad b = 1 + \frac{2a}{y_{\max}}$$

With this grid stretching function, half of the grid points are clustered below the height y_i in the boundary layer. For a typical simulation, the domain height y_{\max} is selected to be a factor of 4-10 larger than the boundary layer thickness at the outlet of the domain, and y_i is chosen such that about half the points lie within the boundary layer.

When grid stretching is used, the finite differences are applied on the un-stretched domain $\xi \in [-1, 1]$ and the derivatives are then scaled to the physical domain using the relations

$$\frac{\partial}{\partial y} = \frac{\partial \xi}{\partial y} \frac{\partial}{\partial \xi} \quad \frac{\partial^2}{\partial y^2} = \frac{\partial^2 \xi}{\partial y^2} \frac{\partial}{\partial \xi} + \left(\frac{\partial \xi}{\partial y} \right)^2 \frac{\partial^2}{\partial \xi^2} \quad (7.9)$$

Using the mapping given in Equation 7.8, the metric coefficients needed in Equation 7.9 are determined to be:

$$\xi = \frac{yb - a}{a + y} \quad (7.10a)$$

$$\frac{\partial \xi}{\partial y} = \frac{a(1 + b)}{(a + y)^2} \quad (7.10b)$$

$$\frac{\partial^2 \xi}{\partial y^2} = -\frac{2a(1 + b)}{(a + y)^3} \quad (7.10c)$$

7.4.1 Base Flow Solution

Since the equations to be solved are linearized, a base flow must be chosen so that the interaction of disturbances with this base flow can be simulated. The base flow selected is a self-similar laminar boundary layer for a calorically perfect ideal gas,

which is computed using the similarity solutions described in Section 3.2. The method described in that section directly provides only the profiles of \bar{U} , \bar{V} , \bar{T} , $d\bar{U}/d\eta$, and $d\bar{T}/d\eta$, where $\eta = y\sqrt{U_e/\nu_e x}$ is the similarity variable. However, to evaluate certain terms in Equations 7.4, the first and second derivatives of \bar{U} , \bar{V} , and \bar{T} with respect to both x and y are also needed.

Second derivatives of \bar{U} and \bar{T} with respect to η can be immediately computed using the similarity equations (3.12) re-written in the form:

$$\frac{\partial^2 \bar{U}}{\partial \eta^2} = - \left(\frac{g}{\bar{\mu}} \frac{\partial \bar{U}}{\partial \eta} + \frac{1}{\bar{\mu}} \frac{\partial \bar{\mu}}{\partial \eta} \frac{\partial \bar{U}}{\partial \eta} \right) \quad (7.11a)$$

$$\frac{\partial^2 \bar{T}}{\partial \eta^2} = - \left[\frac{\sigma_e g}{\bar{k}} \frac{\partial \bar{T}}{\partial \eta} + \frac{1}{\bar{k}} \frac{\partial \bar{k}}{\partial \eta} + \frac{\sigma_e (\gamma - 1) M^2 \bar{\mu}}{\bar{k}} \left(\frac{\partial \bar{U}}{\partial \eta} \right)^2 \right] \quad (7.11b)$$

where g is known from Equation 3.10 and derivatives of the transport properties are known from the relations:

$$\frac{\partial \bar{k}}{\partial \eta} = \frac{\partial \bar{k}}{\partial \bar{T}} \frac{\partial \bar{T}}{\partial \eta} \quad \frac{\partial \bar{\mu}}{\partial \eta} = \frac{\partial \bar{\mu}}{\partial \bar{T}} \frac{\partial \bar{T}}{\partial \eta} \quad (7.12a)$$

The mean vertical velocity \bar{V} was given in Equation 3.9 and is reproduced here in the form:

$$\bar{V} = Re_x^{-1/2} \left[\frac{\bar{U}\eta}{2} - \frac{1}{2\bar{\rho}} \int_0^\eta \bar{\rho} \bar{U} d\eta' \right] \quad (7.13)$$

This equation can easily be differentiated twice to yield:

$$\frac{\partial \bar{V}}{\partial \eta} = Re_x^{-1/2} \frac{1}{2} \left[\eta \frac{\partial \bar{U}}{\partial \eta} - \frac{\partial \bar{T}}{\partial \eta} \int_0^\eta \bar{\rho} \bar{U} d\eta' \right] \quad (7.14a)$$

$$\frac{\partial^2 \bar{V}}{\partial \eta^2} = Re_x^{-1/2} \frac{1}{2} \left[\eta \frac{\partial^2 \bar{U}}{\partial \eta^2} + \frac{\partial \bar{U}}{\partial \eta} - \bar{\rho} \bar{U} \frac{\partial \bar{T}}{\partial \eta} - \frac{\partial^2 \bar{T}}{\partial \eta^2} \int_0^\eta \bar{\rho} \bar{U} d\eta' \right] \quad (7.14b)$$

Making use of the chain rule, one can show that derivatives with respect to x and y

are related to derivatives with respect to η by the formulas:

$$\frac{\partial}{\partial x} = -\frac{\eta}{2x} \frac{\partial}{\partial \eta} \quad (7.15a)$$

$$\frac{\partial^2}{\partial x^2} = \frac{\eta}{4x^2} \left(\eta \frac{\partial^2}{\partial \eta^2} + 3 \frac{\partial}{\partial \eta} \right) \quad (7.15b)$$

$$\frac{\partial}{\partial y} = \sqrt{\frac{U_e}{\nu_e x}} \frac{\partial}{\partial \eta} \quad (7.15c)$$

$$\frac{\partial^2}{\partial y^2} = \frac{U_e^2}{\nu_e x} \frac{\partial^2}{\partial \eta^2} \quad (7.15d)$$

Since \bar{U} and \bar{T} are functions only of η , Equations 7.15 are sufficient to calculate the desired first and second derivatives with respect to x and y . However, the vertical velocity \bar{V} (Equation 7.13) is a function of both x and η , so its derivatives are slightly more complicated. After some manipulation one can show that the x derivatives of the vertical velocity are

$$\frac{\partial \bar{V}}{\partial x} = -\frac{1}{2x} \left(\bar{V} + \eta \frac{\partial \bar{V}}{\partial \eta} \right) \quad (7.16a)$$

$$\frac{\partial^2 \bar{V}}{\partial x^2} = \frac{1}{4x^2} \left(3\bar{V} + 5\eta \frac{\partial \bar{V}}{\partial \eta} + \eta^2 \frac{\partial^2 \bar{V}}{\partial \eta^2} \right) \quad (7.16b)$$

where the derivatives of \bar{V} with respect to η were given in Equations 7.14. The collection of equations presented above determines all necessary derivatives of the mean flow variables. These relations have also been checked by computing self-similar boundary layer profiles as functions of η , converting the profiles and all derivatives into physical space using the formulas in this section, and then evaluating the boundary layer equations in physical space (3.1). After doing so, the RMS residuals of Equations 3.1 are found to be $O(10^{-7})$, which is the same order of magnitude as the tolerance used in the iterative solution of the self-similar profiles. This indicates that the flow variables and their derivatives have been determined correctly.

7.4.2 Boundary conditions

At the wall, Dirichlet boundary conditions are applied to the disturbances of velocity (\tilde{u} and \tilde{v}) and temperature ($\tilde{\theta}$). At the other three boundaries of the domain, however, either inlet or non-reflecting boundary conditions must be used (c.f. Figure 7.3). As discussed in Section 7.1, three types of simulations are conducted in this work. For spatial DNS, a fixed-frequency disturbance is imposed at the left side of the domain and the simulation is run until a periodic steady-state is reached (Figure 7.2a). In this case, Dirichlet boundary conditions are imposed at the inlet (left side of domain) and nonreflecting conditions are applied at the top and right surfaces. For simulations involving packets of second mode waves placed within the boundary layer or acoustic waves impinging on the boundary layer from the freestream (Figure 7.2b,c), nonreflecting boundary conditions are applied at the left, right, and top surfaces of the domain.

The nonreflecting boundary conditions are applied using the viscous extension of the Locally One-Dimensional Inviscid (LODI) relations described Poinot and Lele (1992), which are based on the inviscid method of Thompson (1987). These boundary conditions are only truly nonreflecting for inviscid waves traveling in a uniform flow and impinging exactly normally on the boundaries. Some spurious reflections will therefore occur if the wave impinges on the domain boundary at an angle or in a region of high shear. However, in the simulations considered in this work, the viscous extension of the LODI relations performs sufficiently well that there is no need for more advanced treatment (such as sponge layers) of the boundaries.

The 2D linearized Navier-Stokes equations (7.4) simulated in this work can be written in the form:

$$\frac{\partial \tilde{\mathbf{q}}}{\partial t} + \mathbf{A}_x \frac{\partial \tilde{\mathbf{q}}}{\partial x} + \mathbf{A}_y \frac{\partial \tilde{\mathbf{q}}}{\partial y} + \mathbf{A}_o \tilde{\mathbf{q}} = \mathbf{F}_{visc} \quad (7.17)$$

where $\tilde{\mathbf{q}} = (\tilde{\rho}, \tilde{u}, \tilde{v}, \tilde{\theta})^T$ is the vector of disturbance variables, the matrices \mathbf{A}_t , \mathbf{A}_x , and \mathbf{A}_y contain the coefficients of the 2D Euler equations, \mathbf{A}_o contains terms involving the gradients of the base flow, and \mathbf{F}_{visc} is the vector of viscous terms. Application of

the nonreflecting boundary conditions principally involves the matrices \mathbf{A}_x and \mathbf{A}_y , whose elements are

$$\mathbf{A}_x = \begin{bmatrix} \bar{U} & \frac{1}{\bar{T}} & 0 & 0 \\ \frac{\bar{T}^2}{\gamma M^2} & \bar{U} & 0 & \frac{1}{\gamma M^2} \\ 0 & 0 & \bar{U} & 0 \\ 0 & \bar{T}(\gamma - 1) & 0 & \bar{U} \end{bmatrix} \quad \mathbf{A}_y = \begin{bmatrix} \bar{V} & 0 & \frac{1}{\bar{T}} & 0 \\ 0 & \bar{V} & 0 & 0 \\ \frac{\bar{T}^2}{\gamma M^2} & 0 & \bar{V} & \frac{1}{\gamma M^2} \\ 0 & 0 & \bar{T}(\gamma - 1) & \bar{V} \end{bmatrix} \quad (7.18)$$

The matrices \mathbf{A}_x and \mathbf{A}_y can be diagonalized using the relations:

$$\mathbf{A}_x = \mathbf{R}_x \mathbf{\Lambda}_x \mathbf{L}_x \quad \mathbf{A}_y = \mathbf{R}_y \mathbf{\Lambda}_y \mathbf{L}_y \quad (7.19)$$

where \mathbf{R} is the matrix of right eigenvectors, $\mathbf{L} = \mathbf{R}^{-1}$ is the matrix of left eigenvectors, and $\mathbf{\Lambda}$ is the diagonal matrix of eigenvalues. The elements of these matrices are:

$$\mathbf{R}_x = \begin{bmatrix} \frac{1}{\bar{T}} & 0 & \frac{1}{\bar{T}^2} & \frac{1}{\bar{T}^2} \\ 0 & 0 & \frac{1}{M\sqrt{\bar{T}}} & \frac{-1}{M\sqrt{\bar{T}}} \\ 0 & 1 & 0 & 0 \\ -\bar{T} & 0 & (\gamma - 1) & (\gamma - 1) \end{bmatrix} \quad \mathbf{R}_y = \begin{bmatrix} \frac{1}{\bar{T}} & 0 & \frac{1}{\bar{T}^2} & \frac{1}{\bar{T}^2} \\ 0 & 1 & 0 & 0 \\ 0 & 0 & \frac{1}{M\sqrt{\bar{T}}} & \frac{-1}{M\sqrt{\bar{T}}} \\ -\bar{T} & 0 & (\gamma - 1) & (\gamma - 1) \end{bmatrix} \quad (7.20a)$$

$$\mathbf{L}_x = \begin{bmatrix} \frac{\bar{T}^{\gamma-1}}{\gamma} & 0 & 0 & \frac{-1}{\bar{T}\gamma} \\ 0 & 0 & 1 & 0 \\ \frac{\bar{T}^2}{2\gamma} & +\frac{M\sqrt{\bar{T}}}{2} & 0 & 1/2\gamma \\ \frac{\bar{T}^2}{2\gamma} & -\frac{M\sqrt{\bar{T}}}{2} & 0 & 1/2\gamma \end{bmatrix} \quad \mathbf{L}_y = \begin{bmatrix} \frac{\bar{T}^{\gamma-1}}{\gamma} & 0 & 0 & \frac{-1}{\bar{T}\gamma} \\ 0 & 1 & 0 & 0 \\ \frac{\bar{T}^2}{2\gamma} & 0 & +\frac{M\sqrt{\bar{T}}}{2} & 1/2\gamma \\ \frac{\bar{T}^2}{2\gamma} & 0 & -\frac{M\sqrt{\bar{T}}}{2} & 1/2\gamma \end{bmatrix} \quad (7.20b)$$

$$\mathbf{\Lambda}_x = \begin{bmatrix} \bar{U} & 0 & 0 & 0 \\ 0 & \bar{U} & 0 & 0 \\ 0 & 0 & \bar{U} + \frac{\sqrt{\bar{T}}}{M} & 0 \\ 0 & 0 & 0 & \bar{U} - \frac{\sqrt{\bar{T}}}{M} \end{bmatrix} \quad \mathbf{\Lambda}_y = \begin{bmatrix} \bar{V} & 0 & 0 & 0 \\ 0 & \bar{V} & 0 & 0 \\ 0 & 0 & \bar{V} + \frac{\sqrt{\bar{T}}}{M} & 0 \\ 0 & 0 & 0 & \bar{V} - \frac{\sqrt{\bar{T}}}{M} \end{bmatrix} \quad (7.20c)$$

In these results it can be noted that the quantity $\sqrt{\bar{T}}/M$ is the nondimensional mean sound speed, \bar{a} , which is made dimensionless using the freestream velocity U_e .

Following the notation of [Thompson \(1987\)](#), we define the wave amplitudes

$$\mathcal{L}_x = \mathbf{\Lambda}_x \mathbf{L}_x \frac{\partial \tilde{\mathbf{q}}}{\partial x} \quad \mathcal{L}_y = \mathbf{\Lambda}_y \mathbf{L}_y \frac{\partial \tilde{\mathbf{q}}}{\partial y} \quad (7.21)$$

which evaluate to:

$$\mathcal{L}_x = \begin{pmatrix} \bar{U} \left(\frac{\bar{T}^{\gamma-1}}{\gamma} \frac{\partial \bar{\rho}}{\partial x} - \frac{1}{T\gamma} \frac{\partial \bar{\theta}}{\partial x} \right) \\ \bar{U} \left(\frac{\partial \bar{v}}{\partial x} \right) \\ \left(\bar{U} + \frac{\sqrt{\bar{T}}}{M} \right) \left(\frac{\bar{T}^2}{2\gamma} \frac{\partial \bar{\rho}}{\partial x} + \frac{M\sqrt{\bar{T}}}{2} \frac{\partial \bar{u}}{\partial x} + \frac{1}{2\gamma} \frac{\partial \bar{\theta}}{\partial x} \right) \\ \left(\bar{U} - \frac{\sqrt{\bar{T}}}{M} \right) \left(\frac{\bar{T}^2}{2\gamma} \frac{\partial \bar{\rho}}{\partial x} - \frac{M\sqrt{\bar{T}}}{2} \frac{\partial \bar{u}}{\partial x} + \frac{1}{2\gamma} \frac{\partial \bar{\theta}}{\partial x} \right) \end{pmatrix} \quad (7.22a)$$

$$\mathcal{L}_y = \begin{pmatrix} \bar{V} \left(\frac{\bar{T}^{\gamma-1}}{\gamma} \frac{\partial \bar{\rho}}{\partial y} - \frac{1}{T\gamma} \frac{\partial \bar{\theta}}{\partial y} \right) \\ \bar{V} \left(\frac{\partial \bar{u}}{\partial y} \right) \\ \left(\bar{V} + \frac{\sqrt{\bar{T}}}{M} \right) \left(\frac{\bar{T}^2}{2\gamma} \frac{\partial \bar{\rho}}{\partial y} + \frac{M\sqrt{\bar{T}}}{2} \frac{\partial \bar{v}}{\partial y} + \frac{1}{2\gamma} \frac{\partial \bar{\theta}}{\partial y} \right) \\ \left(\bar{V} - \frac{\sqrt{\bar{T}}}{M} \right) \left(\frac{\bar{T}^2}{2\gamma} \frac{\partial \bar{\rho}}{\partial y} - \frac{M\sqrt{\bar{T}}}{2} \frac{\partial \bar{v}}{\partial y} + \frac{1}{2\gamma} \frac{\partial \bar{\theta}}{\partial y} \right) \end{pmatrix} \quad (7.22b)$$

These wave amplitudes (to be discussed further below) are the one dimensional Riemann invariants propagating along the four characteristic lines corresponding to entropy, vorticity, fast acoustic waves, and slow acoustic waves. Using these definitions, the linearized Navier-Stokes equations (7.17) can be written in the form:

$$\frac{\partial \tilde{\mathbf{q}}}{\partial t} + \mathbf{R}_x \mathcal{L}_x + \mathbf{R}_y \mathcal{L}_y + \mathbf{A}_o \tilde{\mathbf{q}} = \mathbf{F}_{visc} \quad (7.23)$$

The first three terms in this equation are hyperbolic terms describing the inviscid wave motion of the disturbances. The terms involving \mathbf{A}_o and \mathbf{F}_{visc} account for the non-uniformity of the base flow and viscous forces, respectively. The hyperbolic terms are seen to consist of linear combinations of the one dimensional Riemann invariants contained in \mathcal{L}_x and \mathcal{L}_y , where the linear combination coefficients are the elements of the matrices \mathbf{R}_x and \mathbf{R}_y . The physical meaning of this equation can be clarified by considering the special case of one dimensional, uniform, inviscid flow in the x direction, in which case \mathcal{L}_y , \mathbf{A}_o , and \mathbf{F}_{visc} are all equal to zero. One can then left-

multiply Equation 7.23 by the left eigenvector matrix \mathbf{L}_x to obtain:

$$\frac{\partial}{\partial t} (\mathbf{L}_x \tilde{\mathbf{q}}) + \mathcal{L}_x = 0 \quad (7.24)$$

which, after some manipulation, evaluates to

$$\left(\frac{\partial}{\partial t} + \bar{U} \frac{\partial}{\partial x} \right) \tilde{s} = 0 \quad (7.25a)$$

$$\left(\frac{\partial}{\partial t} + \bar{U} \frac{\partial}{\partial x} \right) \tilde{v} = 0 \quad (7.25b)$$

$$\left(\frac{\partial}{\partial t} + (\bar{U} + \bar{a}) \frac{\partial}{\partial x} \right) (\tilde{p} + \bar{\rho} \bar{a} \tilde{u}) = 0 \quad (7.25c)$$

$$\left(\frac{\partial}{\partial t} + (\bar{U} - \bar{a}) \frac{\partial}{\partial x} \right) (\tilde{p} - \bar{\rho} \bar{a} \tilde{u}) = 0 \quad (7.25d)$$

In obtaining this result, the equation of state has been used to replace fluctuations in density and temperature by fluctuations in pressure and entropy, where the fluctuating entropy \tilde{s} (made nondimensional using the gas constant) is

$$\tilde{s} = \frac{1}{\gamma - 1} \frac{\tilde{\theta}}{\bar{T}} - \bar{T} \tilde{\rho} \quad (7.26)$$

By comparing Equation 7.24 with Equations 7.25, one sees that the components of the wave amplitude vector \mathcal{L}_x are simply the one dimensional Riemann invariants along the entropy, vorticity, and acoustic characteristic rays. The elements of \mathcal{L}_y have a similar interpretation in the y direction. The direction of wave propagation along each characteristic is given by the corresponding eigenvalue in $\mathbf{\Lambda}_x$ and $\mathbf{\Lambda}_y$. Therefore the nonreflecting boundary conditions are applied by setting equal to zero the Riemann invariants (elements of \mathcal{L}_x or \mathcal{L}_y) which correspond to incoming waves.

In practice, the nonreflecting boundary conditions are applied using the following procedure, in which the left and right domain boundaries are used as an example:

1. At each point along the boundary, use Equations 7.20 to calculate the matrix \mathbf{R}_x of right eigenvectors and the matrix $\mathbf{\Lambda}_x$ of eigenvalues.
2. Calculate the wave amplitudes \mathcal{L}_x from Equations 7.22.

3. Find the elements of $\mathbf{\Lambda}_x$ that correspond to incoming waves ($\Lambda_x > 0$ for left boundary, $\Lambda_x < 0$ for right boundary) and set the corresponding elements of the wave amplitude vector \mathcal{L}_x equal to zero.
4. After setting the incoming wave amplitudes to zero, left-multiply the wave amplitude vector \mathcal{L}_x by the right eigenvectors \mathbf{R}_x .
5. Replace the term $\mathbf{A}_x(\partial\tilde{\mathbf{q}}/\partial x)$ in Equation 7.17 with the product $\mathbf{R}_x\mathcal{L}_x$ just computed.
6. Use Equation 7.17 to integrate forward in time.

For a boundary at the top or bottom of the domain, the procedure is exactly the same, with ‘x’ replaced by ‘y’. In essence, the method outlined above eliminates incoming waves from the hyperbolic part of the linearized Navier-Stokes equations, but leaves the viscous terms intact. Thus the boundary conditions are not merely the inviscid nonreflecting conditions corresponding to the Euler equations, but have been corrected by the inclusion of viscous terms and the terms involving gradients of the base flow (matrix \mathbf{A}_o). Although these boundary conditions are not necessarily expected to produce good results in regions of high mean shear (i.e., within the boundary layer) or for waves impinging obliquely on the domain boundary, we have found the performance to be quite good for the wavepacket simulations presented here. For example, when instability waves in the boundary layer were allowed to propagate out the downstream end of the domain, we were either unable to detect any evidence of spurious reflections or saw slight reflected waves with reflection amplitudes of only a few percent that quickly died out. However, we do see spurious reflections off of the top boundary of the domain when waves impinge with high obliqueness. Therefore the height of the domain is made large enough to avoid such interactions.

7.4.3 Convergence Study

In order to establish that the numerical simulations are sufficiently resolved, a convergence study spanning a factor of 4 in grid resolution was conducted. The simulated

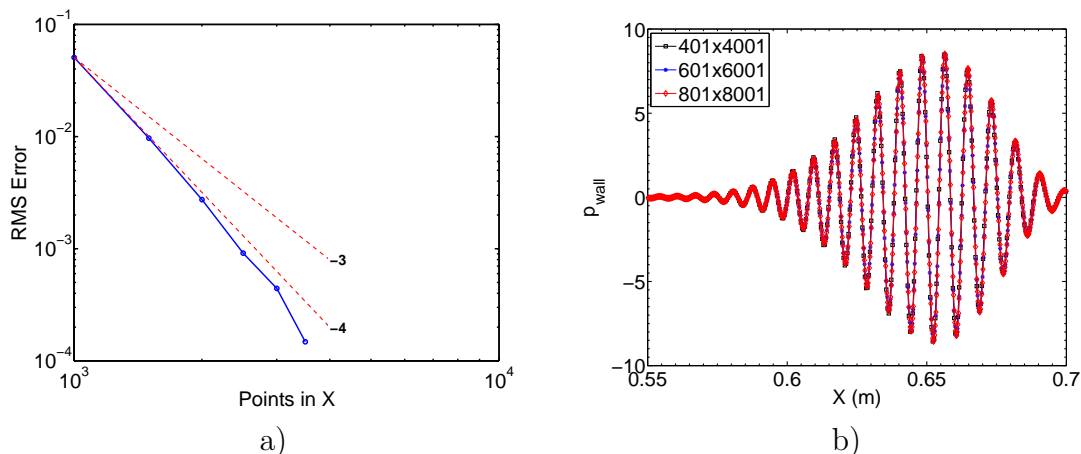


Figure 7.4: a) RMS error of pressure field as a function of grid resolution. RMS error is compared relative to the finest simulation with 8001 points in X . b) Example of wall pressure data at three different grid refinement levels ($Y \times X$).

flow field is described later in Section 7.8 and plotted in Figure 7.14. For all grid resolutions the time step was held fixed, using a Courant number of 0.9 based on the grid spacing of the finest mesh. The same initial condition was used in all cases, and was down-sampled from the finest mesh onto coarser ones. The simulation result at the finest grid level is used as the “true solution” against which the coarser solutions are compared.

To evaluate the convergence rate of the simulations, the pressure field from each simulation was down-sampled onto the coarsest grid. For each simulation, the down-sampled pressure field was compared with that of the finest grid, and the RMS error between these two fields was computed and normalized by the maximum pressure recorded on the finest grid. The resulting normalized RMS errors are reported in Figure 7.4a. This figure shows that close to fourth order convergence is achieved in spite of the second order boundary conditions.

As an alternative to the full-field RMS error plotted in Figure 7.4a, we also compute the infinity norm, or supremum norm, of the difference in pressure fields between each grid and the finest grid. That is, for each level of grid refinement we find the maximum point-wise error between the current grid and the finest grid, again normalizing the error by the maximum pressure simulated on the finest grid. The supremum

Table 7.1: Flow conditions for linearized direct numerical simulations, modeled after the experiments of [Kendall \(1975\)](#).

Condition	Units	Value
M	-	4.5
T_e	K	65
P_e	Pa	728
U_e	m/s	729
Re_u	1/m	6.5×10^6

norm exhibits the same near fourth order convergence seen in [Figure 7.4a](#). In all of the simulations reported in this chapter, the grid resolution used corresponds to the second last point on [Figure 7.4a](#), which employs 6001 grid points in the streamwise direction. For this grid resolution, the maximum point-wise error in the pressure field is about 1% compared to the finest grid. [Figure 7.4b](#) shows an example of the wall pressure from three different mesh refinement levels, demonstrating that the solution is unchanged by additional grid refinement. This pressure snapshot was taken about half way through the total duration of the simulation, at which point enough time had elapsed for any discretization errors to accumulate.

7.5 Flow Conditions and Linear Stability Analysis

The flow conditions considered in this chapter are taken from the work of [Ma and Zhong \(2003a\)](#) and are modeled after the experiments of [Kendall \(1975\)](#), which were conducted in a conventional, continuous-flow hypersonic wind tunnel. The relevant flow parameters are listed in [Table 7.1](#), and the wall is assumed to be adiabatic. The mean velocity and temperature profiles in terms of the similarity variable η are given in [Figure 7.5](#).

The linear stability characteristics of the selected flow condition are summarized in [Figure 7.6](#), where spatial growth rates (left) and N factors (right) are given for several frequencies F , where F is related to the dimensional frequency by [Equation 5.1](#). In this work we focus on waves having the frequency parameter $F = 10^{-4}$, which is the most unstable frequency at a Reynolds number of $R = 2000$, and this is the

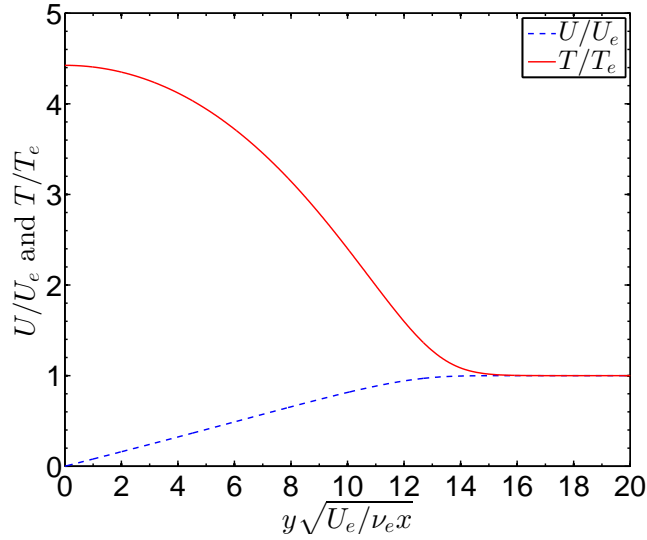


Figure 7.5: Base flow profiles for linearized DNS. Flow conditions are given in Table 7.1

frequency that we will attempt to excite in most of the the simulations. At this frequency, the flow is unstable between $x = 0.49$ and 0.8 m, with maximum growth rate at 0.62 m. According to the N factors in Figure 7.6b, an unstable disturbance of this frequency should decay back to its original amplitude by $x=1.2$ m, hence the length of the simulation domain is usually taken to be somewhat larger, about 2 m.

The linear stability results are presented on a stability diagram in Figure 7.7, where the point $R = 2000$ corresponds to the distance $x = 0.62$ m at which the frequency of interest $F = 10^{-4}$ is most unstable. The stability diagram shows a broad region of first mode instability at low frequencies, but these modes will not be excited in the numerical simulations. For each Reynolds number, the second mode is unstable only over a very narrow band of frequencies and this band varies strongly with the Reynolds number. Clearly the frequency-selectivity of the boundary layer is much stronger for second mode waves than for the first mode.

7.6 Validation

The first verification test is to ensure that the linearized DNS exactly reproduces the results of locally-parallel linear stability theory when the boundary layer is truly

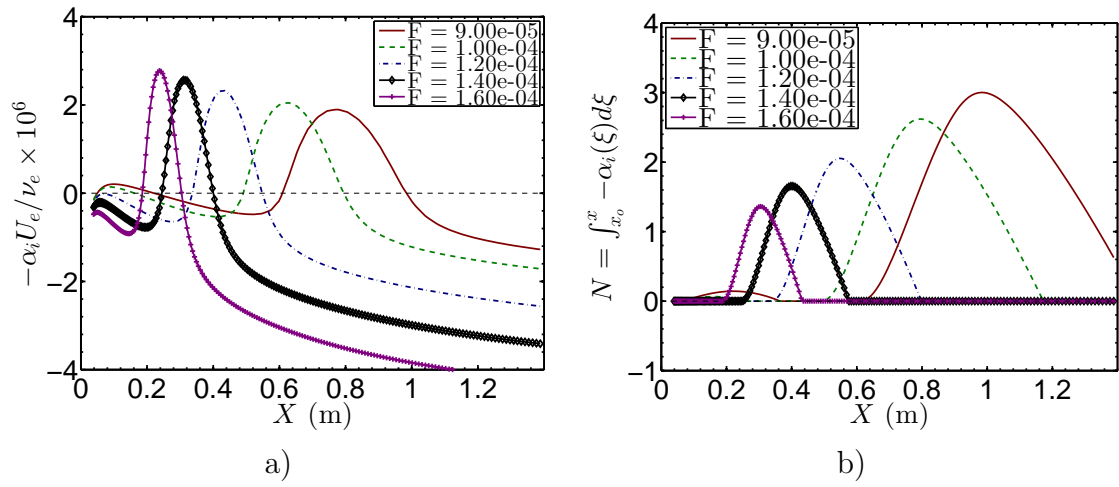


Figure 7.6: Locally-parallel stability characteristics for flow conditions of the linearized DNS. a) Growth rates; b) N factors

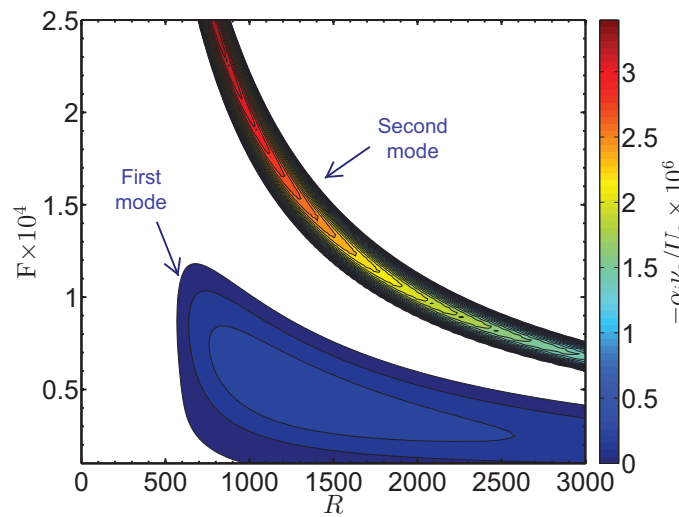


Figure 7.7: Stability diagram for flow conditions of the linearized DNS.

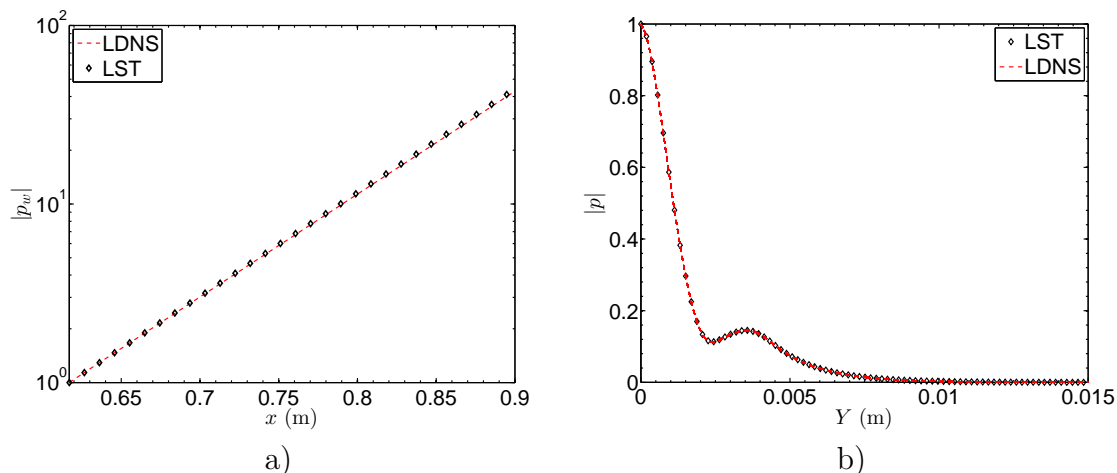


Figure 7.8: a) Comparison of amplification from linear stability theory (symbols) and linearized DNS (lines). b) Comparison of pressure eigenfunction from linear stability theory (symbols) and linearized DNS at 3000 locations between $x = 0.62$ and $x = 0.9$ m (lines). At each location, the pressure is normalized by the value at $y = 0$.

parallel. This was verified by computing boundary layer profiles at $x = 0.62$ m ($R = 2000$) and generating an exactly parallel boundary layer downstream from that point. This parallel boundary layer was then used as the base flow in the linearized DNS, the eigenfunctions from linear stability theory were imposed at the inlet of the domain, and the simulations were run until a periodic steady-state was reached.

Figure 7.8a shows the resulting pressure at the wall as a function of downstream distance. The simulations produce exponential growth that agrees exactly with the prediction of linear stability theory. This confirms that the numerical dissipation of the DNS is low enough to correctly capture the growth of disturbances with negligible artificial damping. Figure 7.8b shows the pressure eigenfunction from linear stability theory overlaid by pressure profiles from the DNS at 3000 different points along the parallel boundary layer. In each case the pressure profile from the DNS is normalized by the local pressure at the wall. The normalized pressure profiles from DNS collapse onto a single curve that matches the eigenfunction from linear stability theory, thus demonstrating that the disturbances keep exactly the same shape as they travel downstream and grow exponentially. The close agreement between the DNS and the linear stability eigenfunction verifies the implementation of the DNS, with

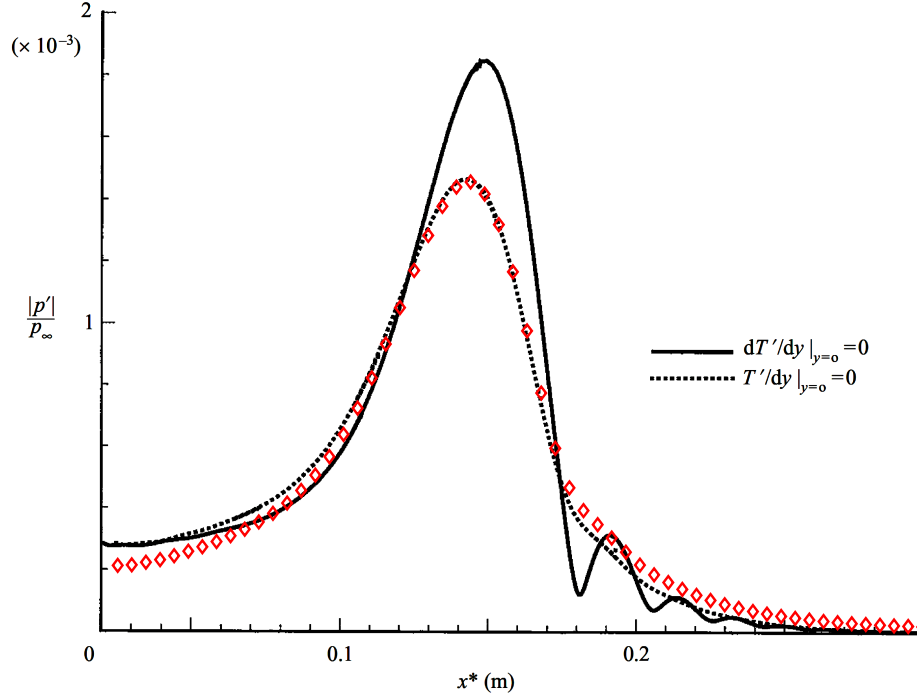


Figure 7.9: Comparison of wall pressure from [Ma and Zhong \(2003a\)](#) (lines) with present linearized DNS (markers). Frequency is 2.2×10^{-4} . Figure is adapted with permission from [Ma and Zhong \(2003a\)](#).

the exception of terms involving nonparallelism of the boundary layer.

As a second test, we compare the present spatial DNS with the results from [Ma and Zhong \(2003a\)](#). The flow conditions are the same as those described in Section 7.5. For comparison with the simulations of [Ma and Zhong \(2003a\)](#), the inlet of the domain is set to $x = 0.025$ m and a slow mode eigenfunction from locally parallel stability analysis is imposed at the inlet. The simulation is then run until a periodic steady-state is reached. The frequency of the imposed disturbance is $F = 2.2 \times 10^{-4}$, and the Reynolds number at the inlet is $R = 424$. The amplitude of the pressure at the wall resulting from this simulation is compared with the results of [Ma and Zhong \(2003a\)](#) in Figure 7.9. Note that in the figure, [Ma and Zhong \(2003a\)](#) considered both adiabatic and isothermal boundary conditions on the temperature fluctuations, but we only make comparisons for the isothermal case.¹

¹There is an error in the legend from [Ma and Zhong \(2003a\)](#), which is reproduced in Figure 7.9: the legend label for the dashed lines should read $T'|_{y=0} = 0$. In their notation, T' is the temperature fluctuation.

The agreement between the wall pressure amplitudes shown in this figure is quite good. The slight discrepancies can be attributed to two factors. First, the simulations of [Ma and Zhong \(2003a\)](#) use a shock-fitting method to include the viscous-inviscid interaction at the leading edge of the plate, and they show that this produces a significant pressure gradient near the leading edge. This is likely to influence the stability properties near the leading edge. Also, the eigenfunctions at the leading edge extend far outside the boundary layer and may interact with the shock wave, which is present in the simulations of [Ma and Zhong \(2003a\)](#) but not in our results. Secondly, [Ma and Zhong \(2003a\)](#) do not specify the parameters used in their Sutherland viscosity model; we have chosen parameters such that the present simulations have the same unit Reynolds number (7.2 million/m) as their work, but it is possible that the viscosity models are slightly different. Altogether, however, the agreement between the two simulations is quite good.

The results from the linearized DNS can also be compared with the predictions of linear stability theory. The frequency ω and wavenumber α are computed using the relations

$$\omega = \frac{i}{p} \frac{dp}{dt} \qquad \alpha = -\frac{i}{p} \frac{dp}{dx} \qquad (7.27)$$

which are evaluated along the wall at $y = 0$. These formulas assume that the instability waves locally take the form $p(x, t) = p_o \exp(i\alpha x - i\omega t)$, where p_o is a constant. The phase speed is then calculated as $c = \omega/\alpha$.

Since the simulation shown [Figure 7.11](#) has reached a periodic steady-state, the frequency is constant. The spatial growth rate $-\alpha_i$ and the real part of the phase speed c_r from the DNS are compared with those of the slow and fast modes (S and F) from linear stability theory in [Figure 7.10](#). The phase speeds from DNS and stability theory agree quite favorably, but poorer agreement is seen for the growth rates. Downstream of the point of maximum growth rate, there is reasonable agreement between the LST and the DNS, but upstream of the neutral point (where LST predicts $\alpha_i = 0$) the DNS predicts growth whereas the LST predicts that the flow is

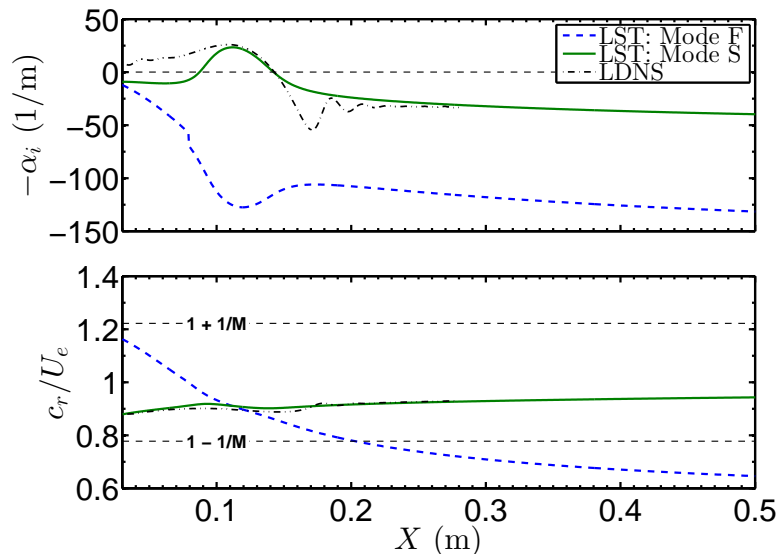


Figure 7.10: Growth rates (top) and phase speeds (bottom) from linear stability theory (LST) and linearized DNS (LDNS). Frequency is $F = 2.2 \times 10^{-4}$.

stable. The same discrepancy was observed for this case by [Ma and Zhong \(2003a\)](#) and is caused by non-parallel effects. Ma and Zhong also observed the same oscillations in the growth rate that are seen here downstream of the upper neutral branch ($x > 0.15$ m); these oscillations are physical and not artifacts of the differentiation involved in computing growth rates.

7.7 Results: Spatial DNS

As discussed in Section 7.1, we make use of three different simulation configurations in this work. The first type will be called “spatial DNS,” in which a second mode eigenfunction having a fixed frequency is imposed at the inlet of the domain and the simulation is run until a periodic steady-state is reached. This enables the response of the boundary layer to a particular frequency to be established. This is the conventional type of stability analysis that is currently the state of the art for predicting boundary layer transition, and hence serves as the baseline for comparison with subsequent simulations involving instability wave packets.

As mentioned previously, in this work we focus mainly on the frequency $F = 10^{-4}$,

so this is the frequency imposed at the inlet. The inlet is located at $x = 0.3$ m, which corresponds to a Reynolds number of $R = 1395$. The disturbance amplitude as a function of distance along the flat plate is shown in Figure 7.11. For nonparallel boundary layers, there is not a unique measure of the disturbance's downstream growth, since both the shape and amplitude of the disturbance change as it travels downstream. The distribution of energy amongst the mode's various components (velocity, temperature, etc.) also changes as it travels downstream. Three possible measures of amplification are compared in Figure 7.11: the absolute value of the wall pressure, the square root of the disturbance kinetic energy, and the square root of the total disturbance energy (c.f. Section 6.4.1). The kinetic and total energies are computed as

$$KE(x) = \frac{1}{2} \int_0^{y_{max}} \bar{\rho} (|\hat{u}|^2 + |\hat{v}|^2) dy \quad (7.28a)$$

$$E_{tot}(x) = \frac{1}{2} \int_0^{y_{max}} \left(\bar{\rho} (|\hat{u}|^2 + |\hat{v}|^2) + \frac{\bar{T}}{M^2 \gamma \bar{\rho}} |\hat{\rho}|^2 + \frac{\bar{\rho}}{\gamma(\gamma - 1)M^2 \bar{T}} |\hat{\theta}|^2 \right) dy \quad (7.28b)$$

In Figure 7.11 all quantities are plotted relative to their initial amplitudes at $x = 0.3$ m, and square roots of the energies are taken because the energy depends quadratically on the disturbance amplitude. The actual value of the total energy is always larger than the kinetic energy, but the amplification of the total energy relative to its initial value is in fact smaller than the amplification of kinetic energy. Substantial differences between these different energy measures are visible, which is similar to the observation made by Fasel and Konzelmann (1990) for incompressible flow. In the results that follow, we focus on the wall pressure as a disturbance measure since this quantity is most easily measured in experiments and most commonly reported in simulations. Also shown in Figure 7.11 is the predicted amplification from locally-parallel linear stability analysis, which is substantially smaller than the DNS result because of nonparallel effects.

Spatial growth rates $-\alpha_i$ and phase speeds are calculated from the DNS data using Equation 7.27 and are compared with linear stability analysis in Figure 7.12. The phase speeds from DNS and LST agree quite well, which suggests that the phase speed

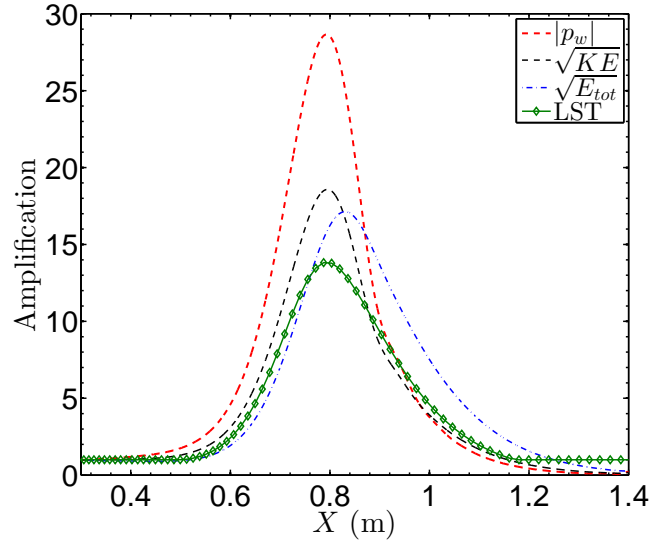


Figure 7.11: Amplification of disturbance pressure amplitude $|p_w|$, kinetic energy KE , and total energy E_{tot} relative to values at $x = 0.3$ m. Frequency is $F = 10^{-4}$.

is not strongly influenced by nonparallelism of the boundary layer. Even though the amplifications from LST and DNS agree poorly (Figure 7.11), the growth rates agree reasonably well, except upstream of the neutral branch, where LST predicts stability and the DNS predicts some growth. This disagreement is caused by the nonparallel boundary layer and is the source of much of the discrepancy in amplification.

7.8 Results: Second mode wave packets

The preceding section discussed the downstream propagation of disturbances that are continuously forced at a particular frequency at the inlet of the domain, which is the conventional type of stability analysis. We now relax the assumption of fixed-frequency disturbances and consider the downstream evolution of packets of second mode waves that are localized in both space and time. These wavepackets are directly placed into the boundary layer (e.g., Figure 7.2b) by specifying initial conditions of the following form:

$$\tilde{\mathbf{q}}(x, y, t = 0) = \mathbf{Q}(y) \exp \left(i\alpha_o x - 3.0 \frac{(x - x_o)^2}{R_x^2} \right) \quad (7.29)$$

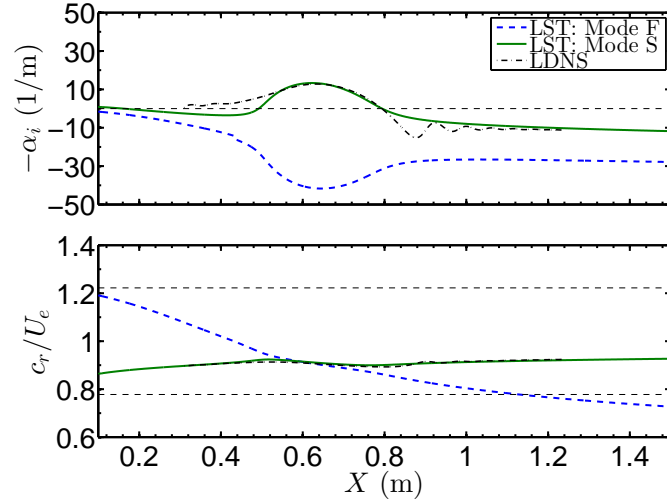


Figure 7.12: Growth rates (top) and phase speeds (bottom) from linear stability theory (LST) and linearized DNS (LDNS). Frequency is $F = 10^{-4}$.

In this equation $\mathbf{Q}(y)$ is a shape function that is determined from a spatial stability analysis at frequency F and streamwise location x_o ; it is a vector function that contains the velocity, density, and temperature eigenfunctions as its components. For a given frequency F and streamwise location x_o , the linear stability analysis also yields the central wavenumber α_o , which is the wavenumber at the center of the packet where $x = x_o$. This instability wave from linear stability analysis is modulated by a Gaussian envelope centered at x_o and having a radius of R_x , where R_x is the distance from x_o at which the Gaussian envelope decays to a value of 0.05. The initial condition (7.29) is therefore characterized by three free parameters: the frequency F , the initial location of the packet x_o , and the width of the packet R_x . The remaining parameters, $\mathbf{Q}(y)$ and α_o , are determined from linear stability analysis.

The first case we consider is a second mode wave packet with frequency $F = 10^{-4}$ initialized at $x_o = 0.3$ m. Recall that for $F = 10^{-4}$ the disturbance is unstable between $x = 0.49$ and 0.8 m, so this initial location x_o is slightly upstream of the lower neutral branch. At this location the second mode wavenumber is $\alpha_o = 724 \text{ m}^{-1}$, which corresponds to a wavelength of 8.7 mm. The radius of the Gaussian is chosen to be $R_x = 30$ mm, meaning that the wave packet contains about 7 periods of the instability wave. Figure 7.13 shows contours of the initial pressure distribution

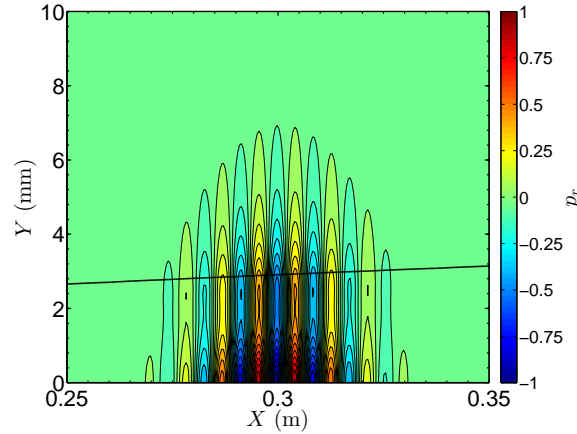


Figure 7.13: Initial pressure distribution corresponding to a packet of second mode waves. $F = 10^{-4}$, $x_o = 0.3$, $R_x = 30$ mm. Thick black line is δ_{99} .

corresponding to Equation 7.29.

Figure 7.14 shows contours of the disturbance pressure at several instants in time. Because of the many individual waves contained within the wave packet, individual contour levels are not visible, but the figure demonstrates the downstream evolution of the wave packet's structure. At $t = 0$ the maximum pressure amplitude is 1.0 and the wave is hardly visible in the contours, which have a maximum contour level of 10. As the wave packet propagates downstream, it amplifies by about a factor of 10 and then decays. As the wave packet travels downstream it spreads out considerably.

The propagation of the wave is more easily visualized using an x-t diagram, as shown in Figure 7.15. This enables the individual waves within the wave packet to be visualized. In the x-t diagram the vertical offset of each pressure trace is proportional to the time. Qualitatively, the amplitude of the wave packet follows the predictions from linear stability theory (Figure 7.12): growth between $x = 0.5 - 0.8$ m and decay downstream of 0.8 m. However, one can make a more quantitative comparison by tracking the maximum wall pressure of the wave packet at each x location along the boundary layer and then comparing this amplification with the predictions of LST as well as the spatial DNS that was carried out in Section 7.7. In what follows we will refer to the point of maximum wall pressure as the “center” of the packet, and the frequency and wavenumber at this point will be called the central frequency and

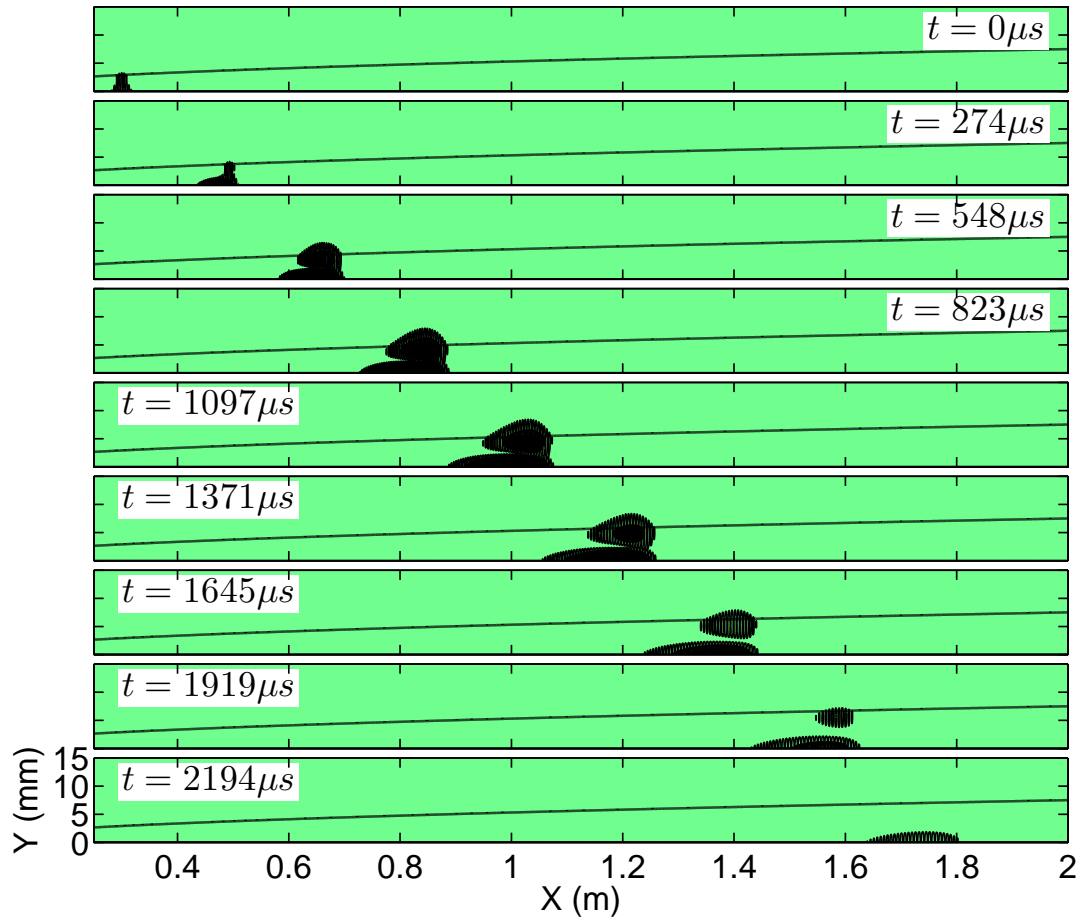


Figure 7.14: Contours of pressure at several time instants. $x_o = 0.3$ m, $F = 10^{-4}$, $R_x = 30$ mm. Heavy black line is the δ_{99} boundary layer thickness.

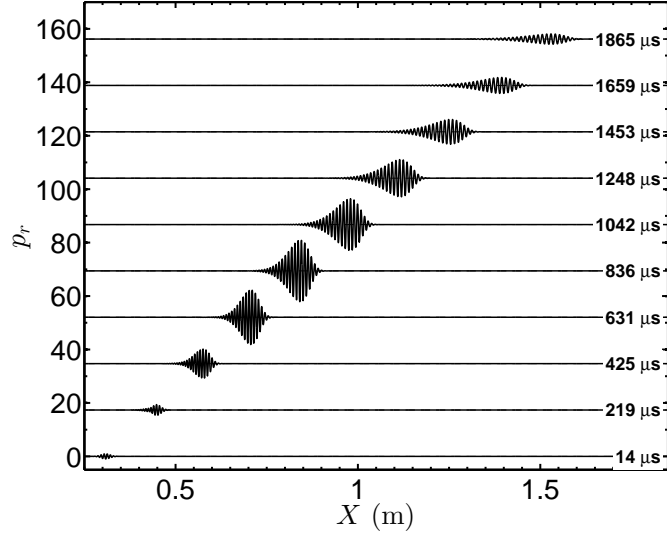


Figure 7.15: X-t diagram of the wall pressure for a second mode wave packet with $F = 10^{-4}$, $x_o = 0.3$ m, $R_x = 30$ mm. Vertical offset of the traces is proportional to time.

central wavenumber.

Figure 7.16a compares the maximum wall pressure of the wave packet with the predictions of LST and spatial DNS for $F = 10^{-4}$. For all three curves, the initial amplitudes at $x = 0.3$ m are set to the same value. The pressure at the center of the wave packet initially exceeds that of the LST and the spatial DNS, but the maximum pressure reached by the packet is substantially less than the prediction of the spatial DNS. The reason for this discrepancy is that the central frequency and wavenumber of the wave packet change as the packet propagates downstream, as shown in Figure 7.16b. Although the phase speed of the packet (the ratio of the frequency F to the nondimensional wavenumber $\alpha_r \nu_e / U_e$) is nearly constant, the frequency and wavenumber initially rise and then fall as the packet travels downstream. This is in contrast to the spatial DNS, in which the flow has reached a periodic steady state and hence contains only a single frequency of $F = 10^{-4}$, indicated by the dashed line on Figure 7.16b.

The change in central frequency and wavenumber of the wave packet can be appreciated by plotting the frequency on a stability diagram, as shown in Figure 7.17. The wave packet is initialized at $x_o = 0.3$ m and $F = 10^{-4}$. Since the wave packet is

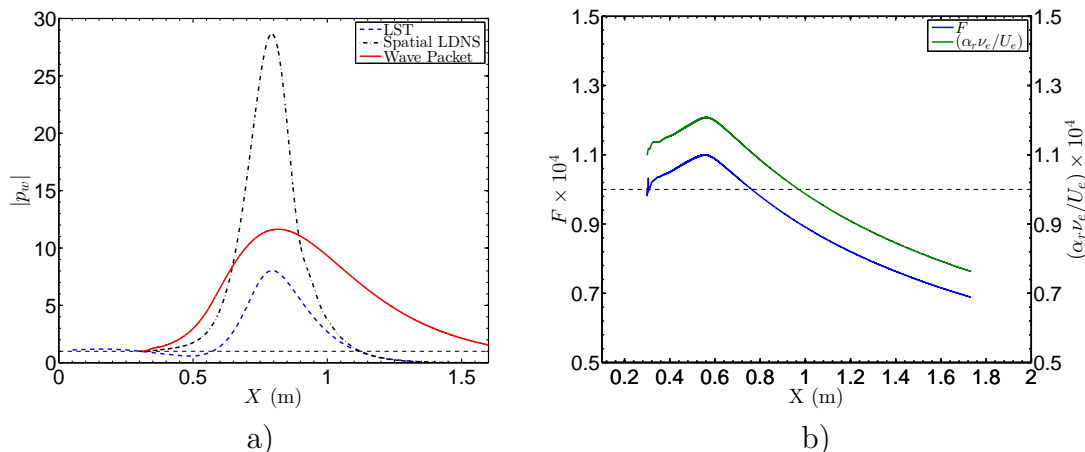


Figure 7.16: a) Comparison of wall pressure amplitudes from linear stability theory (LST), spatial DNS (LDNS), and center of wave packet. b) Frequency and wavenumber at center of wave packet. $F = 10^{-4}$, $x_o = 0.3$ m, $R_x = 30$ mm.

localized in space and time, it contains a spectrum of frequencies and wavenumbers; therefore when the packet approaches the instability region from below, higher frequencies are more unstable than lower frequencies, and hence the central frequency of the packet rises. Once the wave packet crosses the line of maximum growth rate on the stability diagram (the maximum contour level), lower frequencies become more unstable than higher frequencies. As a result, the central frequency of the wave packet drops. As the packet travels far downstream, its central frequency continues to fall since high frequency content is always more highly damped than low frequency content. As a result, the central frequency follows the upper neutral branch of the stability diagram. In contrast to the path taken by the wave packet on this diagram, a conventional linear stability analysis would assume that the frequency remains fixed and the disturbance propagates horizontally across the stability diagram (dashed line). This accounts for the difference in amplification observed in Figure 7.16a.

So far, we have discussed only the central frequency and wavenumber of the packet, that is, the frequency and wavenumber at the point where the wall pressure is a maximum. However, the wave packet actually contains a spectrum of frequencies and wavenumbers, and the evolution of these spectra play an important role in the wave packet's development. These spectra can be evaluated in the following way: for each

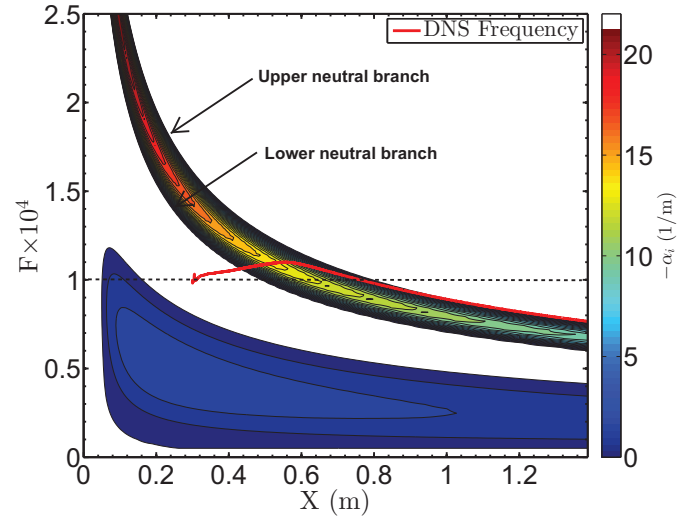


Figure 7.17: Central wave number of wave packet obtained from LDNS calculations and superimposed on a stability diagram.

time instant in the DNS, the wavenumber spectrum of the packet can be determined by taking Fourier transforms of the pressure data along the wall. Likewise, at each spatial location along the boundary layer the frequency spectrum can be determined using a temporal Fourier transform of the time series of the wall pressure at that location. Using this procedure, the frequency spectrum as a function of x and the wavenumber spectrum as a function of time are determined. The results of such a calculation are given in Figure 7.18.

Figure 7.18a shows the frequency spectrum of the wave packet as a function of x . The packet is initialized at $x_o = 0.3$ m and has a central frequency of $F = 10^{-4}$, but the Fourier amplitudes at the initial location are hardly visible in the contour plot because the disturbance initially has a small amplitude. As the wave packet travels downstream, its frequency spectrum follows the behavior of the central frequency, but also contains a narrow band of frequencies around the central value. Similar behavior is observed for the wavenumbers in Figure 7.18b as a function of time. It should be noted that the Fourier amplitudes increase as a result of both amplification and spreading of the wave packet, since a wide wave packet contains more spectral power than a narrow one, even if their amplitudes are the same.

The evolving frequency content of the wave packet is interpreted in terms of the

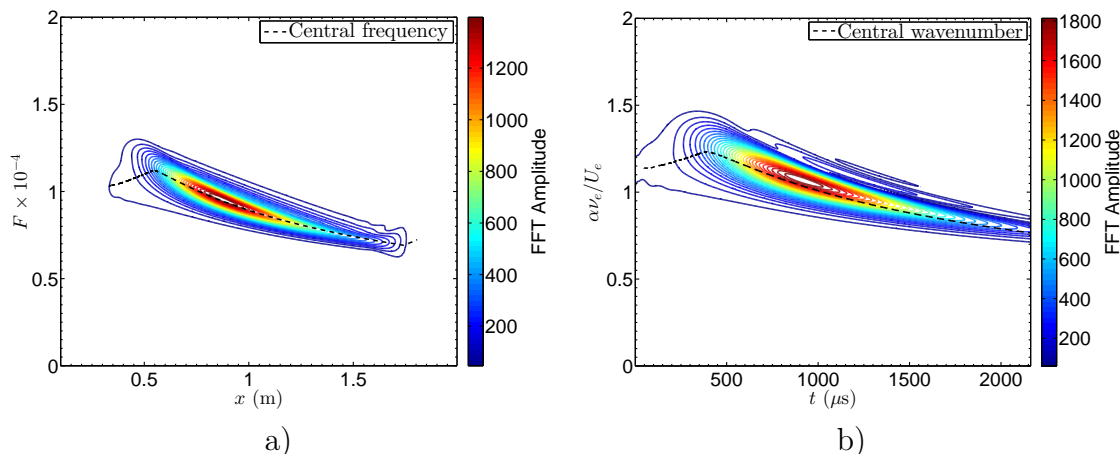


Figure 7.18: a) Temporal, and b) Spatial Fourier transforms of pressure data at the wall. Amplitudes are scaled arbitrarily.

stability diagram in Figure 7.19. Here the stability diagram is again taken from locally-parallel linear stability analysis. The red lines superimposed on the stability diagram indicate the boundaries between which the Fourier amplitude is greater than 10% of its local maximum value. That is, at each station x a temporal Fourier transform is computed, and the two frequencies at which the Fourier amplitude is 10% of the maximum are taken as points along the red boundary lines. Therefore, at each location x the red lines indicate the range of frequencies for which the wave packet has significant frequency content. The wave packet (which begins at $x_o = 0.3$ m) initially has a fairly wide band of frequency content, but this rapidly narrows as the wave packet travels downstream and many of the scales are damped. Further downstream, the frequency spectrum follows the stability diagram, with the lower bound of the frequency spectrum following the most unstable frequency and the upper bound of the frequency spectrum lying slightly above the upper neutral branch.

Having computed the Fourier amplitudes for each frequency F , we can compare the downstream propagation of each Fourier mode with the spatial DNS (Section 7.7). This differs from the wave packet amplitude discussed previously, which consists of a superposition over all the Fourier modes; here we filter out an individual Fourier mode and compare its amplification with predictions from spatial DNS. This comparison is made in Figure 7.20 for three different frequencies. In this figure the FFT amplitudes

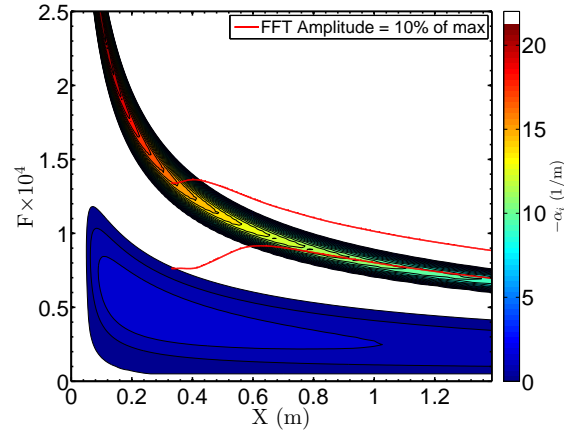


Figure 7.19: Contours: Stability diagram from locally-parallel linear stability analysis. Red lines: Boundaries between which the FFT amplitude is greater than 10% of its local maximum value.

in red are horizontal slices across Figure 7.18a, while the black dashed line is the spatial DNS from Figure 7.12 and similar results for the other frequencies. For the sake of comparison, the initial amplitudes from DNS and Fourier analysis are set to the same value. Excellent agreement is seen. This means that instead of performing an individual spatial DNS for each frequency of interest, one can run a single wave packet DNS containing a broad spectrum of frequencies. By performing FFT analysis of the data, one can then extract the downstream growth of each Fourier mode and produce the fully nonparallel growth rate curve for many different frequencies using a single simulation. This is a very computationally cheap way of executing spatial DNS for many different frequencies. This idea appears to have been conceived first by Herman Fasel's group at the University of Arizona (Mayer et al., 2011, Sivasubramanian and Fasel, 2014). They have conducted DNS of three dimensional wave packets, and using Fourier analysis in both the streamwise and spanwise directions they have been able to generate spatial growth rate curves for every combination of frequency and spanwise wavenumber using a single simulation.

The frequency spectrum of the second mode wave packet can be controlled by adjusting the width R_x of the initial condition (Equation 7.29), since waves that are wider in physical space are narrower in frequency space. One would then expect packets that are wider in physical space to more closely match the predictions of

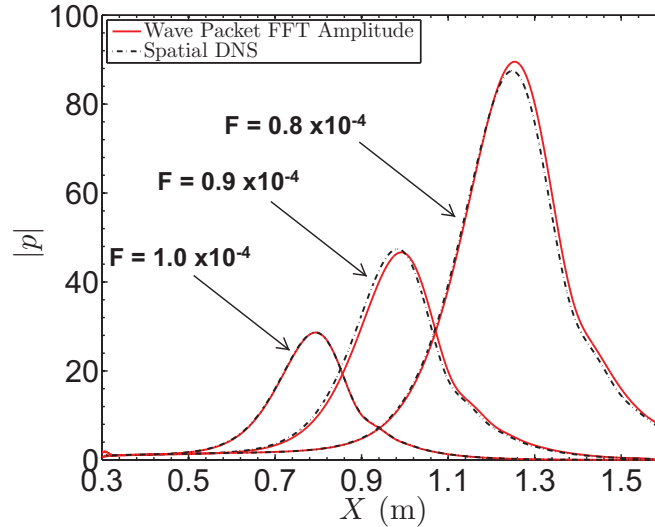


Figure 7.20: Comparison of wall pressure amplitude from spatial DNS with the Fourier amplitudes from a wave packet simulation. The Fourier amplitudes have been scaled to match the spatial DNS amplitude at the inlet, which is equal to 1.0 for all three frequencies.

spatial linear stability analysis because of their narrow band of frequency content. To test this theory, simulations are carried out with three other wave packet widths of $R_x = 15$, 60, and 120 mm, compared to the 30 mm packet shown previously. When $R_x = 15$ mm, the wave packet contains only about 3.5 complete waves; when $R_x = 120$ mm, it contains about 28 waves. Examples of pressure distributions for two other initial wave packet widths are shown in Figures 7.21 and 7.22. The wide wave packet ($R_x = 60$ mm) in Figure 7.21 grows rapidly and then decays rapidly, whereas the narrower wave packet ($R_x = 15$ mm) in Figure 7.22 continues to amplify as it travels across the entire domain.

To make these results quantitative, the maximum pressures at the center of the wave packet are compared in Figure 7.23. When the initial wave packet is very thin (small R_x), the maximum pressure is not very large but the wave persists for a very long distance downstream. This is because the initial condition contains a wide band of frequencies, and each of these frequencies amplifies at a different location along the boundary layer. Conversely, when the wave packet is wide, consisting of many cycles of instability waves, then the spatial DNS result (Section 7.7) is approached

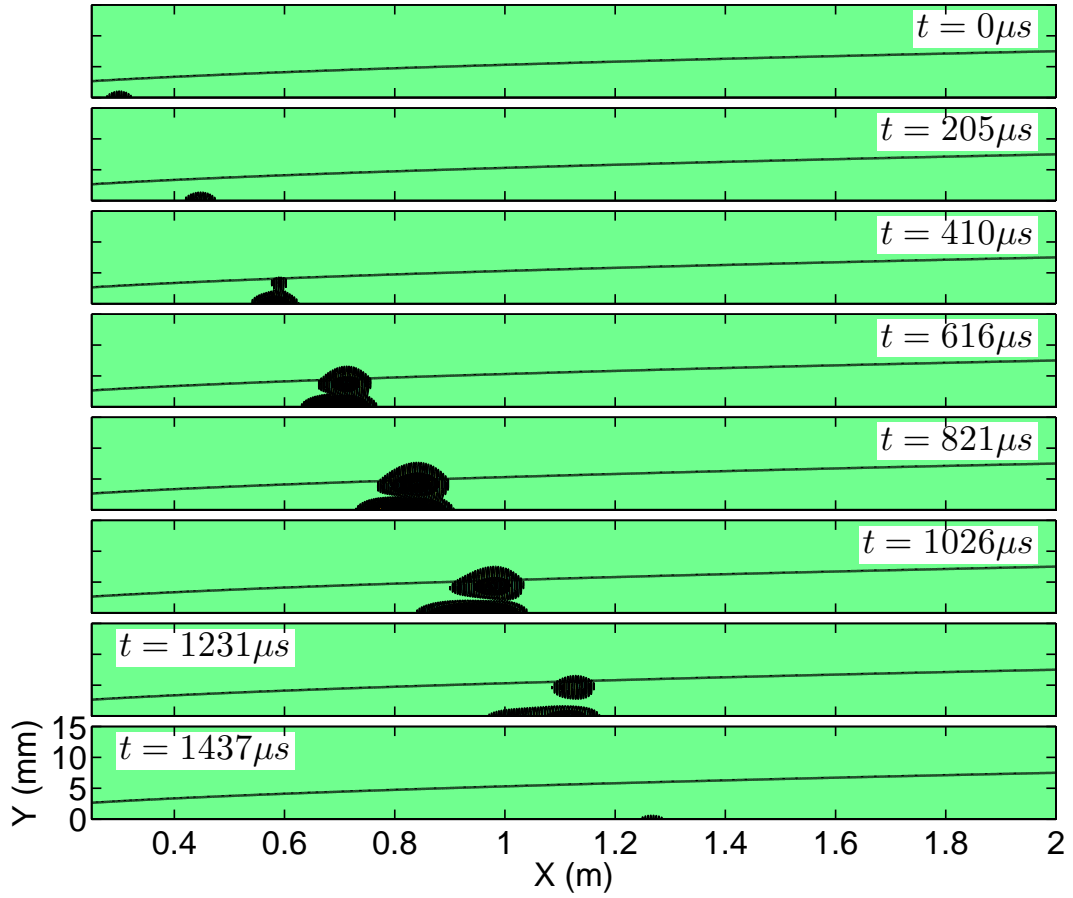


Figure 7.21: Contours of pressure at several time instants. $x_o = 0.3$ m, $F = 10^{-4}$, $R_x = 60$ mm. Heavy black line is the δ_{99} boundary layer thickness.

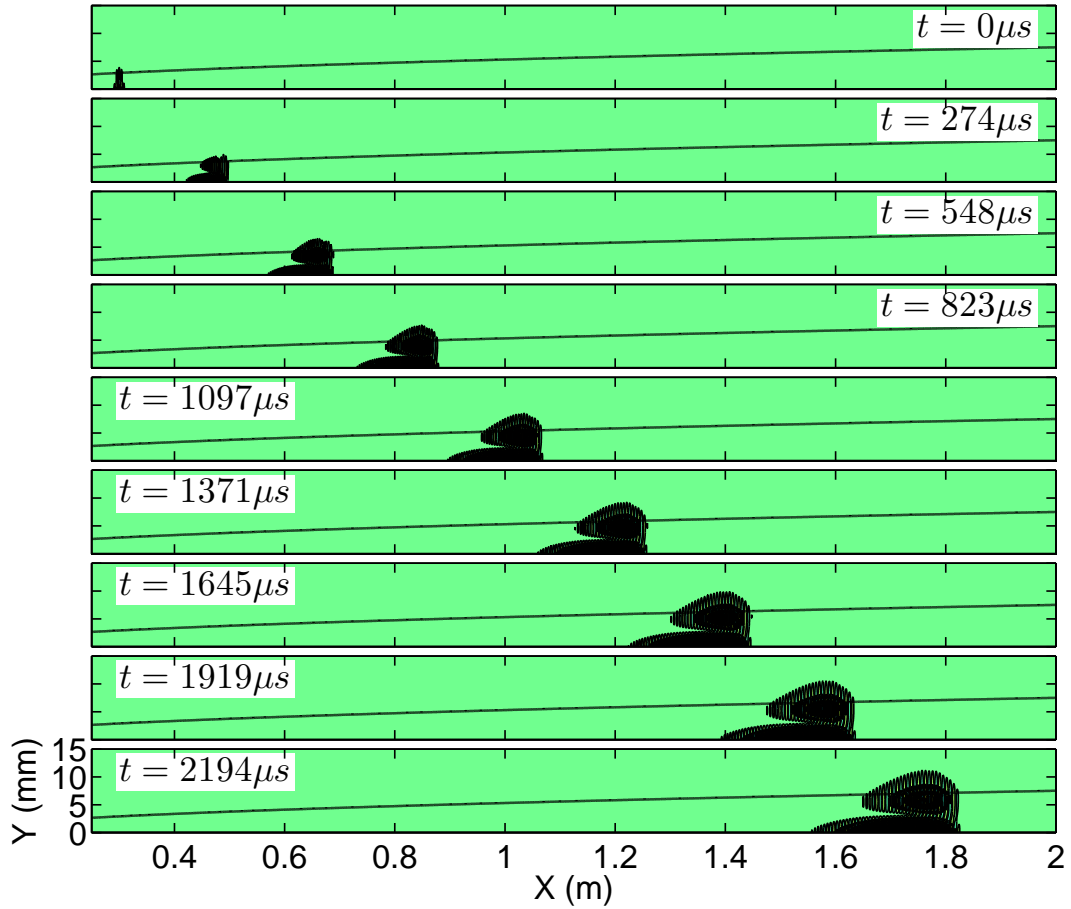


Figure 7.22: Contours of pressure at several time instants. $x_o = 0.3$ m, $F = 10^{-4}$, $R_x = 15$ mm. Heavy black line is the δ_{99} boundary layer thickness.

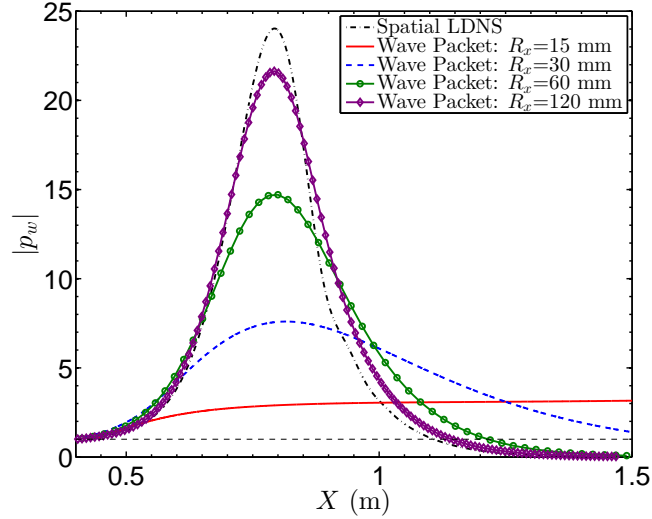


Figure 7.23: Comparison of maximum wave packet amplitude vs streamwise distance for wave packets of four different widths, as well as spatial DNS. $F = 10^{-4}$, $x_o = 0.3$ m.

and the disturbance reaches a large level of amplification but decays rapidly in the downstream direction.

These results demonstrate that in predicting the downstream growth of second mode instability waves it is essential that the width of the wave packet be taken into account. The amplification predicted by spatial stability analysis is only achieved when the wave packet contains many wavelengths. For a boundary layer that is artificially forced with harmonic disturbances, such as in the experiments of [Schubauer and Skramstad \(1947\)](#) or [Gaster and Grant \(1975\)](#) this is the case, but for a boundary layer undergoing “natural” transition in a wind tunnel the measured disturbances waves consist only of a few wavelengths (Figure 7.1) and hence the conventional spatial analysis is likely to over-predict the level of amplification.

7.9 Incoming Acoustic Wavepackets

Having explored the propagation of isolated second mode wave packets in a boundary layer, we now consider how these waves can be excited by incoming acoustic waves from the freestream. This is done by choosing a Gaussian-shaped packet of planar acoustic waves in the freestream as the initial condition and causing these waves to

impinge on the boundary layer and potentially excite the second mode instability. An example of such an initial condition was shown in Figure 7.2c.

7.9.1 Freestream waves

In order to specify incoming planar acoustic waves in the DNS, a model for plane wave propagation in the freestream must be derived. In the freestream, where the flow velocity is uniform, one can assume that the disturbances take the form of harmonic waves

$$\left(\tilde{\rho}, \tilde{u}, \tilde{v}, \tilde{\theta}\right)^T = \left(\hat{\rho}, \hat{u}, \hat{v}, \hat{\theta}\right)^T \times \exp(i\alpha x + i\lambda y - i\omega t) \quad (7.30)$$

where tildes signify the complex disturbances and hats signify the constant amplitudes of the harmonic waves. For solutions of this form, the equations of motion (7.4) reduce to

$$i(\alpha - \omega)\hat{\rho} + i\alpha\hat{u} + i\lambda\hat{v} = 0 \quad (7.31a)$$

$$i(\alpha - \omega)\hat{u} + \frac{i\alpha}{\gamma M^2}(\hat{\rho} + \hat{\theta}) + \frac{1}{R}[(\lambda^2 + \alpha^2(2+r))\hat{u} + \alpha\lambda(1+r)\hat{v}] = 0 \quad (7.31b)$$

$$i(\alpha - \omega)\hat{v} + \frac{i\lambda}{\gamma M^2}(\hat{\rho} + \hat{\theta}) + \frac{1}{R}[(\alpha^2 + (2+r)\lambda^2)\hat{v} + \alpha\lambda(1+r)\hat{u}] = 0 \quad (7.31c)$$

$$i(\alpha - \omega)\hat{\theta} + (\gamma - 1)(i\alpha\hat{u} + i\lambda\hat{v}) + \frac{\alpha^2 + \lambda^2}{R\sigma}\hat{\theta} = 0 \quad (7.31d)$$

For disturbances having sufficiently long wavelengths that $\alpha/R \ll 1$ and $\lambda/R \ll 1$ (which is the case for the simulations conducted here), Equations 7.31 are well approximated by their inviscid counterparts:

$$i(\alpha - \omega)\hat{\rho} + i\alpha\hat{u} + i\lambda\hat{v} = 0 \quad (7.32a)$$

$$i(\alpha - \omega)\hat{u} + \frac{i\alpha}{\gamma M^2}(\hat{\rho} + \hat{\theta}) = 0 \quad (7.32b)$$

$$i(\alpha - \omega)\hat{v} + \frac{i\lambda}{\gamma M^2}(\hat{\rho} + \hat{\theta}) = 0 \quad (7.32c)$$

$$i(\alpha - \omega)\hat{\theta} + (\gamma - 1)(i\alpha\hat{u} + i\lambda\hat{v}) = 0 \quad (7.32d)$$

which can be represented in matrix notation:

$$\begin{bmatrix} \alpha - \omega & \alpha & \lambda & 0 \\ \frac{\alpha}{\gamma M^2} & \alpha - \omega & 0 & \frac{\alpha}{\gamma M^2} \\ \frac{\lambda}{\gamma M^2} & 0 & \alpha - \omega & \frac{\lambda}{\gamma M^2} \\ 0 & \alpha(\gamma - 1) & \lambda(\gamma - 1) & \alpha - \omega \end{bmatrix} \begin{pmatrix} \hat{\rho} \\ \hat{u} \\ \hat{v} \\ \hat{\theta} \end{pmatrix} = 0 \quad (7.33)$$

The eigenvalues ω and right eigenvectors $\boldsymbol{\xi}$ of this matrix are:

$$\omega_1 = \alpha \quad \boldsymbol{\xi}_1 = \begin{pmatrix} 1 \\ 0 \\ 0 \\ -1 \end{pmatrix} \quad (7.34a)$$

$$\omega_2 = \alpha \quad \boldsymbol{\xi}_2 = \begin{pmatrix} 0 \\ \lambda \\ -\alpha \\ 0 \end{pmatrix} \quad (7.34b)$$

$$\omega_{3,4} = \alpha \pm \frac{\sqrt{\alpha^2 + \lambda^2}}{M} \quad \boldsymbol{\xi}_{3,4} = \begin{pmatrix} M\sqrt{\alpha^2 + \lambda^2} \\ \pm\alpha \\ \pm\lambda \\ (\gamma - 1)M\sqrt{\alpha^2 + \lambda^2} \end{pmatrix} \quad (7.34c)$$

The first two waves are called entropy and vorticity waves, as identified by the non-zero components of the right eigenvectors $\boldsymbol{\xi}_1$ and $\boldsymbol{\xi}_2$. The last two waves $\boldsymbol{\xi}_3$ and $\boldsymbol{\xi}_4$ are fast and slow acoustic waves. Any initial condition in the freestream can be represented as a linear combination of these four types of waves, but in this work we are principally interested in the acoustic waves. Therefore, the initial conditions used in this work are of the following form:

$$\mathbf{q}_o(x, y) = \boldsymbol{\xi}_{3,4} \exp \left[i\alpha_o x + i\lambda_o y - 3.0 \left(\frac{y - y_o}{R_y} \right)^2 - 3.0 \left(\frac{x - x_o}{R_x} \right)^2 \right] \quad (7.35)$$

This initial condition consists of an acoustic plane wave of streamwise wavenumber α_o and vertical wavenumber λ_o that is modulated by a Gaussian envelope in x and y . The angle of incidence of the wave is given by $\tan^{-1}(\lambda_o/\alpha_o)$. The size of the Gaussian envelope is specified by the radii R_x and R_y which are the distances from the center at which the Gaussian envelope reaches a value 5% (this is the reason for the factor of 3.0).

An initial disturbance of the form (7.35) contains central wavenumbers given by α_o and λ_o , and hence a central frequency ω_o determined by the dispersion relation of Equation 7.34c. However, because the Gaussian envelope limits the extent of the wave to a small region of space, the packet contains a continuum of different wavenumbers α and λ , and hence a continuum of frequencies. The spectrum of wavenumbers contained in the wave packet can be determined by computing Fourier transforms of Equation 7.35. After working out the two dimensional Fourier transform with respect to x and y (duals to α and λ), the initial wave packet from Equation 7.35 takes the following form in frequency space:

$$\mathbf{q}_{\alpha\lambda}(\alpha, \lambda) = \frac{\pi}{3} R_x R_y \boldsymbol{\xi}_{3,4} \exp\left(-\frac{R_x^2(\alpha - \alpha_o)^2}{12} - \frac{R_y^2(\lambda - \lambda_o)^2}{12}\right) \quad (7.36)$$

where $\mathbf{q}_{\alpha\lambda}(\alpha, \lambda)$ is the two dimensional Fourier transform of $\mathbf{q}_o(x, y)$. At each point in the (α, λ) wavenumber plane, one can compute a corresponding frequency through the dispersion relation (7.34c). An example of an initial pressure field in physical space is give in Figure 7.24a, and its corresponding wavenumber spectrum is shown in Figure 7.24b. The wavenumber spectrum (colored contour lines) is calculated using Equation 7.36 and normalized to have a maximum of one. The black contours show isolines of constant frequency F with values indicated on the plot; these are calculated by applying the dispersion relation (7.34) to the coordinates (α, λ) on the plot.

The key observation is that the incoming wave packet is sufficiently localized in space and time that it contains a fairly broad spectrum of wavenumbers and frequencies. Upon interacting with the boundary layer, all of these frequencies can participate in the excitation of modes within the boundary layer. This is in contrast

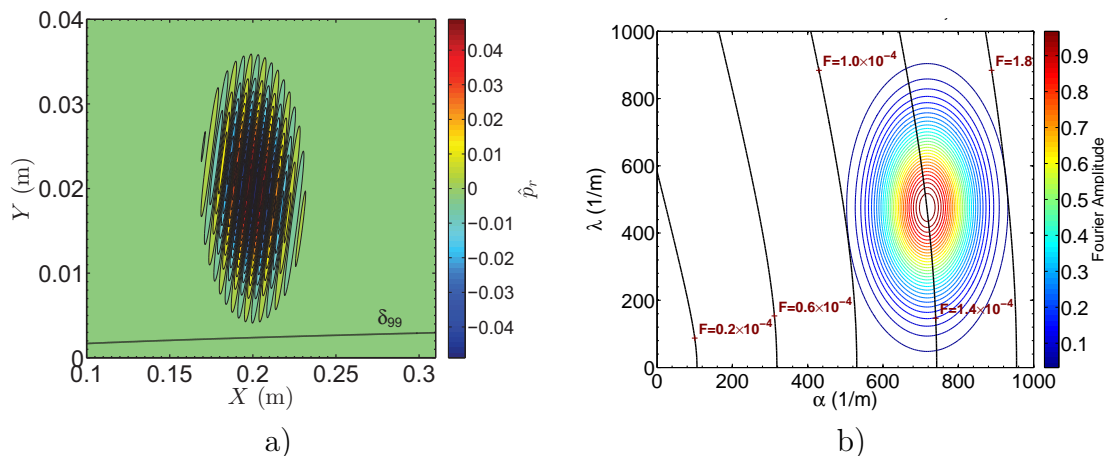


Figure 7.24: a) Wave packet initial condition in physical space. $\alpha_o = 717/\text{m}$, $\lambda_o = 476/\text{m}$, $R_x = 30 \text{ mm}$, $R_y = 15 \text{ mm}$; Fast mode. b) Wave packet in frequency space. Colored contours show two dimensional Fourier amplitudes. Black contours show iso-lines of frequency.

to conventional spatial receptivity calculations, which involve only a single frequency. One can of course perform individual spatial receptivity calculations for a wide variety of frequencies, but this does not capture the superposition of multiple frequencies that is experienced by wave packets in an actual boundary layer.

7.9.2 Receptivity considerations

The model for the incoming wave packet described by Equation 7.35 contains six free parameters: the streamwise and vertical wavenumbers α_o and λ_o , the initial coordinates of the center of the wavepacket (x_o, y_o) , and the width and height of the packet, R_x and R_y . The acoustic wave can also be either a fast wave or a slow wave. We seek to choose these parameters in such a way that the incoming wave packet excites unstable second mode waves as strongly as possible. However, since receptivity analysis of fixed-frequency disturbances is mainly limited to asymptotic theories near the leading edge (Fedorov and Khokhlov, 1993, Fedorov, 2003) and DNS (Ma and Zhong, 2003a,b, 2005, Balakumar, 2007, 2009), and no receptivity theory exists for wave packets consisting of more than one frequency, we attempt to choose initial conditions on the basis of the phase speeds from linear stability theory.

Figure 7.25 shows the growth rates and phase speeds for boundary layer modes with frequency $F = 10^{-4}$. As discussed in Section 5.1, there are several different boundary layer modes which are called the “fast modes” F_1 and F_2 (and higher modes), and the “slow mode” S_1 . For these flow conditions, the mode S_1 is the one that becomes unstable. In order for an incident acoustic wave striking the boundary layer to excite these waves, one would intuitively expect that the incoming wave should have the same phase speed and wavenumber as the second mode waves. When this happens, the freestream waves are said to be “synchronized” with the boundary layer modes. However, on the basis of the dispersion relation for acoustic waves given in Equation 7.34c, it is impossible for acoustic waves in the freestream to have a phase speed that falls within the shaded area in Figure 7.25, which is where the boundary layer modes exist. The only location at which the acoustic waves impinging on the boundary layer can have the same phase speed as the boundary layer modes is at $x = 0$, where both the boundary layer modes and the waves in the freestream can have the same phase speed of $1 \pm 1/M$ (the boundaries of the shaded region). Because of this, one expects receptivity to freestream acoustic waves to be largest at $x = 0$, and indeed this has been observed in DNS (Balakumar, 2007, 2009, Malik and Balakumar, 2007).

From Equation 7.34c, one also finds that the waves in the freestream have a phase speed of $c = \omega/\alpha = 1 \pm 1/M$ only when the vertical wavenumber λ is equal to zero. This means that waves in the freestream whose phase speed lies on the edge of the shaded region in Figure 7.25 are traveling parallel to the flat plate and have wavefronts that are perpendicular to the plate. Plane waves in the freestream that are propagating toward the plate at an angle have phase speeds that fall outside of the shaded region, with larger angles of incidence producing larger phase speeds. Therefore, waves that run parallel to the plate or impinge at a shallow angle are expected to be most effective in exciting modes within the boundary layer, while the boundary layer will be less receptive to waves impinging at a larger angle.

Guided by these observations, in the simulations that follow we choose an impinging wave packet represented by either of the black squares on Figure 7.25. These

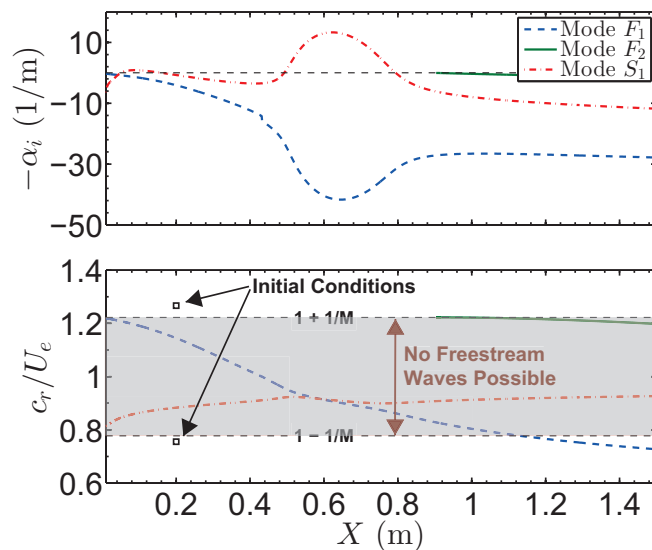


Figure 7.25: Spatial growth rates and phase speeds for $F = 10^{-4}$. Black squares show the streamwise location and phase speed of the simulation initial conditions. Shaded region is inaccessible to planar acoustic waves.

two conditions are chosen to excite either the fast mode or the slow mode. Since the slow mode is the one that becomes unstable, one would expect that the initial condition having a lower phase speed will be more effective in exciting unstable second mode waves, and indeed this will be demonstrated. For both of the initial conditions marked on the diagram, the wave in the freestream is a slightly incoming wave with a phase speed just outside of the limiting value of $c_r = 1 \pm 1/M$. This initial condition is an attempt to achieve realistic wave angles for the incoming waves while at the same time effectively exciting second mode waves.

7.9.3 Results

We consider first a fast acoustic wave impinging on the boundary layer. Figure 7.26 shows snapshots of the pressure contours at several instants in time. Because of the large number of individual waves inside the wave packet it is not possible to make out the actual contour levels, but the figure gives an indication of the progression of the wave structures. The initial condition consists of a Gaussian shaped packet of acoustic waves initialized slightly above the boundary layer. The wavenumbers of the

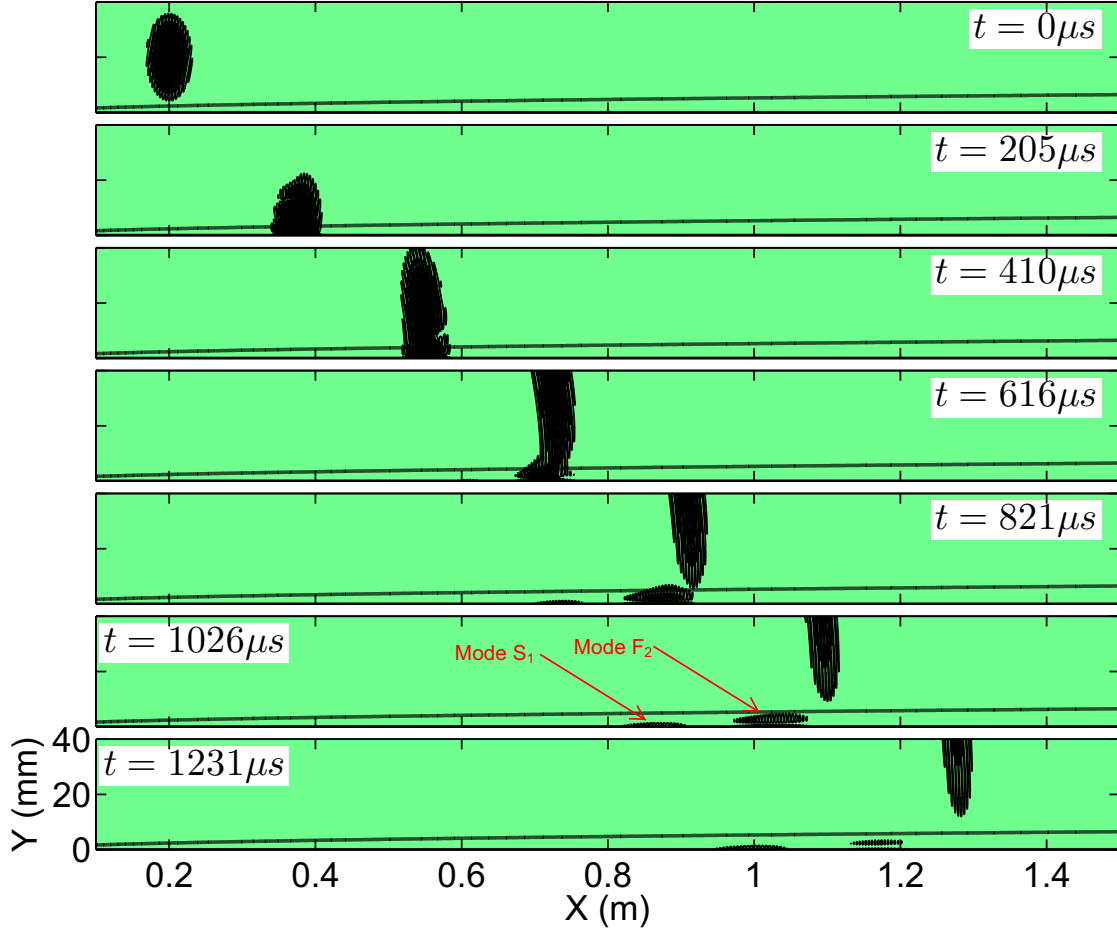


Figure 7.26: Pressure contours from an incident acoustic wave impinging on a boundary layer. Initial wave packet has $\alpha_o = 717 \text{ m}^{-1}$, $\lambda_o = -476 \text{ m}^{-1}$, $R_x = 30 \text{ mm}$, $R_y = 15 \text{ mm}$. Thick black line is δ_{99} .

individual waves inside the initial wave packet are $\alpha_o = 717 \text{ m}^{-1}$ in the streamwise direction and $\lambda_o = -476 \text{ m}^{-1}$ in the vertical direction, hence the wave is impinging at an angle of $\tan^{-1}(\lambda_o/\alpha_o) = -34$ degrees with respect to the horizontal axis. The chosen value of the streamwise wavenumber α_o has been selected to match that of unstable second mode waves at $x = 0.62 \text{ m}$ and $F = 10^{-4}$.

As shown in Figure 7.26, the packet of incident waves reflects off of the boundary layer and then propagates back into the freestream. Note that the simulation domain is much taller than that shown in the figure, so the reflected wave is not interacting with a computational boundary. As the waves from the freestream reflect off of the boundary layer, they excite two packets of boundary layer modes. Using Equa-

tion 7.27 to determine the frequency ω , wavenumber α , and phase speed $c = \omega/\alpha$, it has been found that the two packets of modes are the fast mode F_2 , which is stable, and the slow mode S_1 , which is unstable (Figure 7.25). Mode F_2 is excited to a high amplitude but decays downstream, whereas mode S_1 is excited to a low amplitude but grows somewhat as it travels downstream. In spite of the fact that the incoming acoustic wave was a fast wave with phase speed $c = 1 + 1.2/M$, it nevertheless successfully excited the unstable slow mode within the boundary layer. However, the amplitude of the second mode wave is quite small: the maximum amplitude of the wall pressure reached by the second mode wave packet is only about 6% of the peak pressure caused by the reflecting acoustic waves from the freestream.

Next we consider a packet of slow acoustic waves impinging on the boundary layer. Contours of the pressure at various instants of time are given in Figure 7.27. The wavenumbers in this simulation are $\alpha_o = 717 \text{ m}^{-1}$, $-\lambda_o = 230 \text{ m}^{-1}$, which imply an angle of incidence of 18 degrees. The radii of the Gaussian envelope describing the shape of the packet are $R_x = R_y = 30 \text{ mm}$. This time only the slow mode S_1 is excited; however, the second mode instability achieves a much larger amplitude compared to the excitation by fast acoustic waves above. In this case the maximum wall pressure of the second mode wave is about 4 times greater than that reached by the reflecting waves from the freestream.

Following the same procedure as in Section 7.8, the maximum wall pressure of the second mode waves excited by the reflecting acoustic radiation can be extracted as a function of distance along the plate. The corresponding frequencies and wavenumbers can be extracted using Equation 7.27. The results are shown in Figure 7.28 where they are compared with the predictions of a spatial stability analysis. The behavior is qualitatively similar to that of the isolated second mode waves in Figure 7.16: the wave packet experiences less amplification than predicted by spatial analysis and the central frequency and wavenumber of the packet decrease as it travels far downstream. The similarity with the results given previously for isolated second mode waves indicates that the approximation made in Section 7.8 of neglecting receptivity and directly placing the second mode waves within the boundary layer is a reasonable

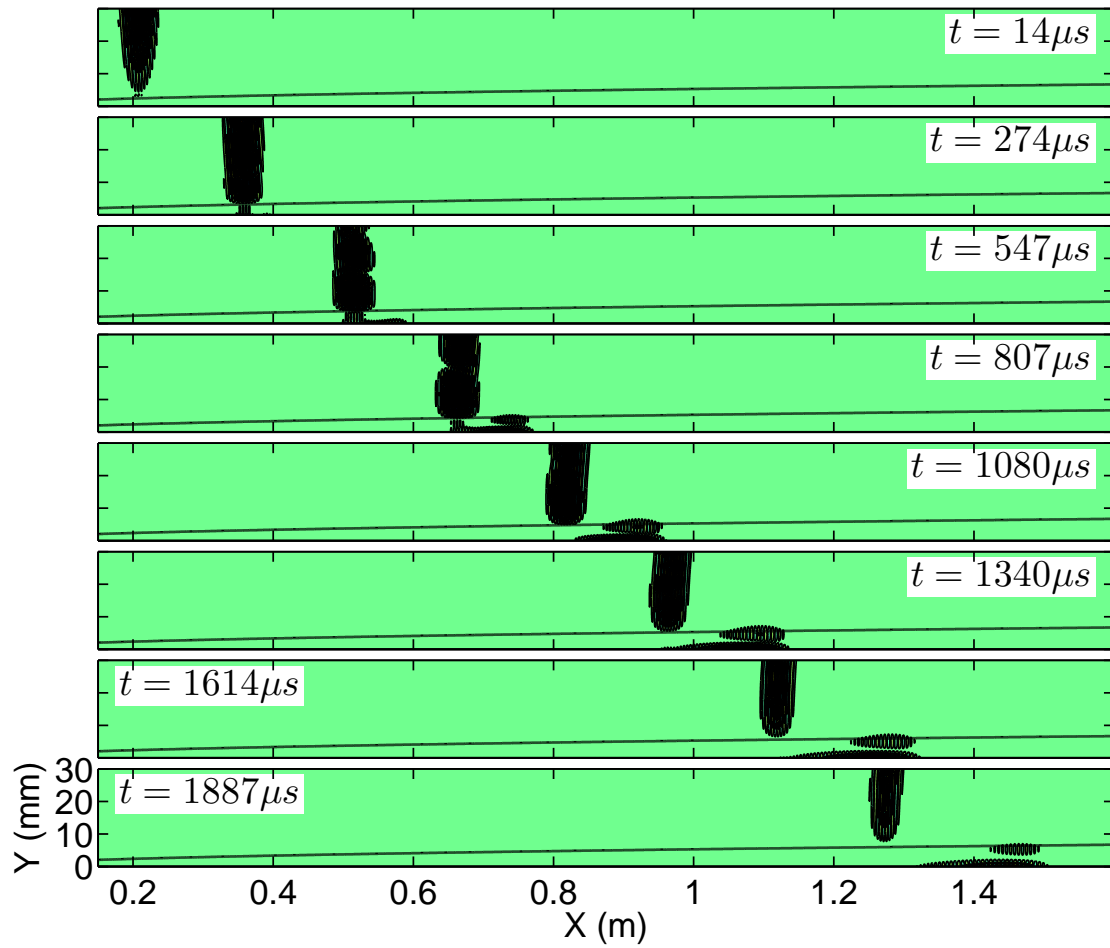


Figure 7.27: Pressure contours from an incident slow acoustic wave packet impinging on a boundary layer. Initial wave packet has $\alpha_o = 717 \text{ m}^{-1}$, $\lambda_o = 230 \text{ m}^{-1}$, $R_x = 30 \text{ mm}$, $R_y = 30 \text{ mm}$. Thick black line is δ_{99} .

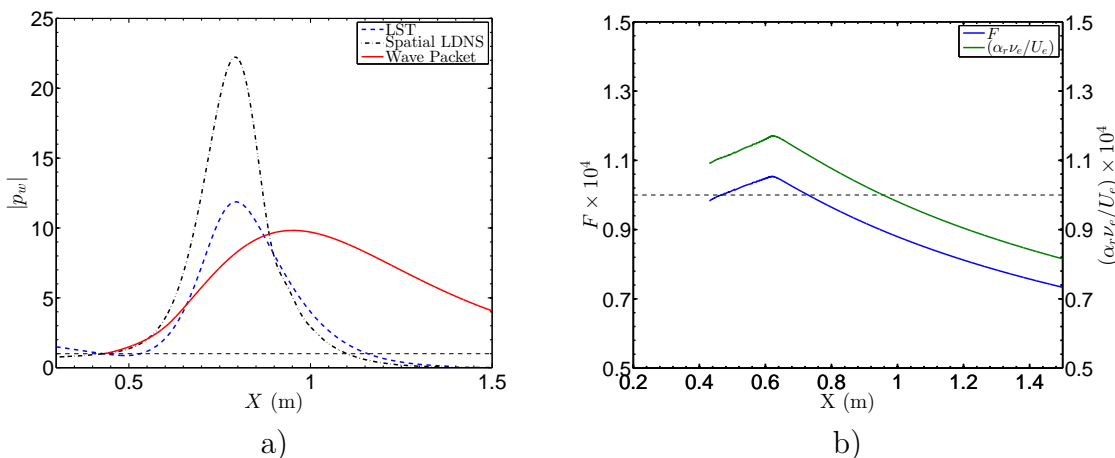


Figure 7.28: a) Comparison of wall pressure amplitudes from linear stability theory (LST), spatial DNS (LDNS), and center of wave a packet. b) Frequency and wavenumber at center of wave packet. Wave packet was generated by incoming slow acoustic waves with $\alpha_o = 717 \text{ m}^{-1}$, $R_x = 30 \text{ mm}$, $R_y = 15 \text{ mm}$, angle of incidence of 17 degrees.

one. However, the advantage of the receptivity calculation is that the absolute amplitude of the second mode wave can be determined if the amplitude of the freestream forcing is known.

Similar to the analysis used in Section 7.8, we can again investigate the influence of the wave packet width on the downstream development of second mode waves. This is done by adjusting the width R_x of the wave packet in the freestream (Equation 7.35), choosing the value $R_x = 60$ for comparison with the $R_x = 30 \text{ mm}$ case reported above. Examples of pressure contours from the simulation with $R_x = 60 \text{ mm}$ are given in Figure 7.29. Similar to the result of Section 7.8, this wave packet that is wide in physical space experiences more amplification than the narrower packet in Figure 7.27, but decays more rapidly as it moves downstream.

A quantitative comparison of the wave packet amplitudes is given in Figure 7.30, where all pressure amplitudes are normalized to 1.0 at about 0.61 m. The results are quite similar to those given previously in Figure 7.23 for second mode waves placed directly in the boundary layer (no receptivity). The wider wave packet in physical space experiences more amplification but decays more rapidly as it progress downstream. The narrower wave packet in physical space ($R_x = 30 \text{ mm}$) experiences less amplifi-

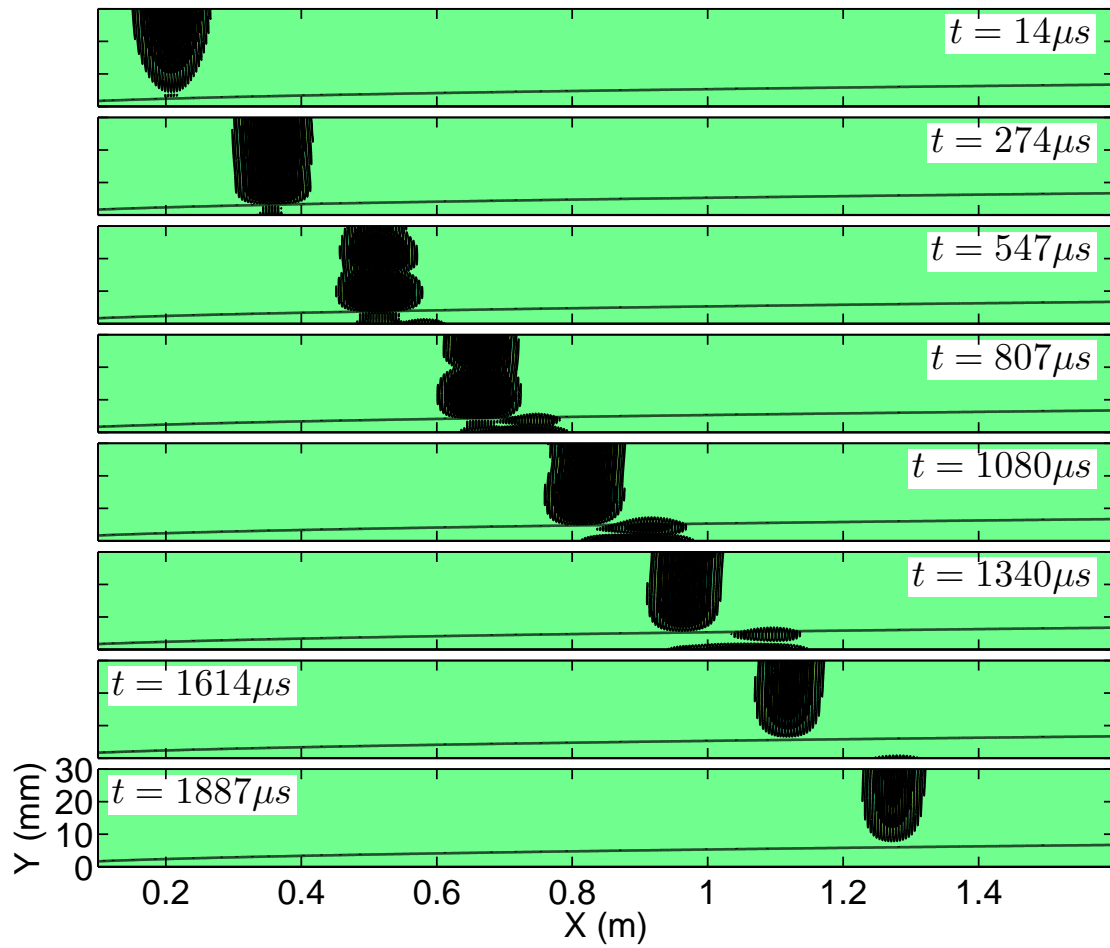


Figure 7.29: Pressure contours from an incident slow acoustic wave packet impinging on a boundary layer. Initial wave packet has $\alpha_o = 717 \text{ m}^{-1}$, $\lambda_o = 230 \text{ m}^{-1}$, $R_x = 60 \text{ mm}$, and $R_y = 30 \text{ mm}$. Thick black line is δ_{99} .

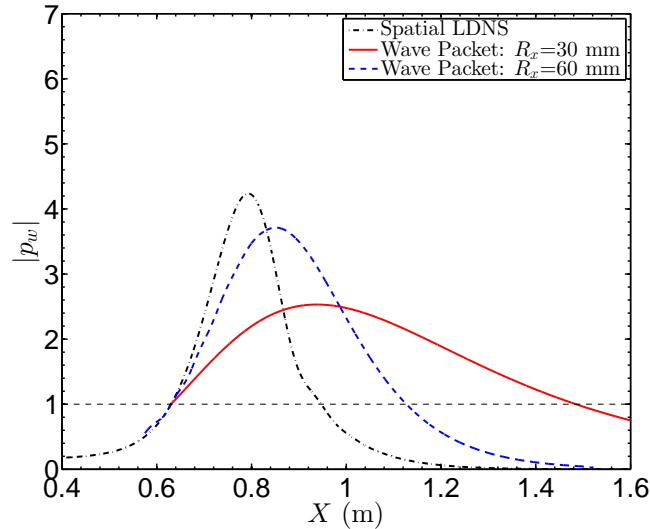


Figure 7.30: Comparison of maximum wave packet amplitude vs streamwise distance for wave packets of two different widths, as well as spatial DNS. $F = 10^{-4}$, $x_o = 0.3$ m.

cation but persists farther downstream. This result shows that regardless of whether second mode waves are placed directly in the boundary layer (Section 7.8) or forced naturally by planar acoustic waves, the qualitative result is the same: finite-width wave packets experience less amplification than the prediction of spatial stability analysis but decay more slowly as they move downstream.

7.10 Simple Wave Packet Model

The simulations reported in the preceding sections greatly clarify the downstream propagation of packets of second mode waves. However, the high computational expense of the simulations makes it difficult to cover a wide parameter space. The DNS results have thus considered only a few particular initial wave packet configurations which are parameterized by their initial streamwise location and their width in physical space (which implies a bandwidth in frequency space). However, to make predictions about transition one must consider all possible initial configurations that are likely to be excited in a particular experiment. In this section a simple wave packet model is developed using locally-parallel linear stability theory in order to capture the wave packet dynamics with modest computational expense. Using this model, a

method for predicting boundary layer transition is developed which successfully takes into account the finite width of the instability waves encountered in experiments.

7.10.1 Equations of motion

The problem of wave packet propagation in a boundary layer can be regarded as an initial boundary-value problem in which the shape of the wave packet is imposed as an initial condition. Similar to the DNS presented previously, this problem can be solved either by specifying an initial distribution of waves in the freestream that interacts with the boundary layer (the receptivity problem), or by specifying an initial packet of second mode waves that is already within the boundary layer (thus neglecting receptivity). The solutions that follow are sufficiently general to consider both methods, but numerical results will be computed only for the latter case of an initial second mode wave packet placed within the boundary layer, since this leads to some simplification.

For two-dimensional, viscous compressible flow, the linearized Navier-Stokes equations from Equation 7.4 can be written in the general form:

$$\mathbf{A}_t \frac{\partial \tilde{\mathbf{q}}}{\partial t} + \mathbf{A}_x \frac{\partial \tilde{\mathbf{q}}}{\partial x} + \mathbf{A}_y \frac{\partial \tilde{\mathbf{q}}}{\partial y} + \mathbf{A}_o \tilde{\mathbf{q}} = 0 \quad (7.37)$$

where the \mathbf{A} s are 9×9 matrices given in Appendix C and $\tilde{\mathbf{q}}$ is the column vector of disturbance variables:

$$\tilde{\mathbf{q}} = \left(\tilde{\rho}, \tilde{u}, \tilde{v}, \tilde{\theta}, \tilde{\tau}_{xx}, \tilde{\tau}_{xy}, \tilde{\tau}_{yy}, \tilde{q}_x, \tilde{q}_y \right)^T \quad (7.38)$$

Here $\tilde{\rho}$, \tilde{u} , and \tilde{v} are the fluctuations in density and velocity, $\tilde{\theta}$ is the temperature fluctuation, $\tilde{\tau}_{xx}$, $\tilde{\tau}_{xy}$, and $\tilde{\tau}_{yy}$ are the fluctuations in viscous stresses, and \tilde{q}_x and \tilde{q}_y are the fluctuations in heat fluxes. Expressions for the fluctuating stresses and heat fluxes can be found in Appendix C.

The linearized equations (7.37) are to be solved on the two dimensional, semi-infinite domain $x \in [0, \infty)$, $y \in [0, \infty)$ along with the initial and boundary conditions:

$$\tilde{\mathbf{q}} = \mathbf{q}_o(x, y) \quad t = 0 \quad (7.39a)$$

$$\tilde{u} = \tilde{v} = \tilde{\theta} = 0 \quad y = 0 \quad (7.39b)$$

$$|\tilde{\mathbf{q}}| < \infty \quad y \rightarrow \infty \quad (7.39c)$$

These statements specify no-slip conditions on the velocities, zero temperature fluctuation of the wall's surface, boundedness of the disturbances in the freestream, and an initial disturbance field $\tilde{\mathbf{q}}_o$.

7.10.2 Laplace Transform

Since the initial value problem specified above has constant coefficients in time, solutions can be determined by making use of the Laplace transform pair:

$$\mathbf{q}_\omega(x, y, \omega) = \int_0^\infty \tilde{\mathbf{q}}(x, y, t) e^{i\omega t} dt \quad (7.40a)$$

$$\tilde{\mathbf{q}}(x, y, t) = \frac{1}{2\pi} \int_{i\Gamma-\infty}^{i\Gamma+\infty} \mathbf{q}_\omega(x, y, \omega) e^{-i\omega t} d\omega \quad (7.40b)$$

The frequency $-i\omega$ is chosen as the Laplace transform parameter to highlight the connection with linear stability theory. The real parameter Γ specifies an inversion contour which lies above all singularities in the complex plane. Applying this transform to Equation 7.37, one arrives at the inhomogeneous problem:

$$\mathcal{L}\mathbf{q}_\omega \equiv \mathbf{A}_x \frac{\partial \mathbf{q}_\omega}{\partial x} + \mathbf{A}_y \frac{\partial \mathbf{q}_\omega}{\partial y} + (\mathbf{A}_o - i\omega \mathbf{A}_t) \mathbf{q}_\omega = \mathbf{A}_t \tilde{\mathbf{q}}_o(x, y) \quad (7.41)$$

In principle this equation can be solved for any frequency ω that is not an eigenvalue, and the total solution can be obtained by integrating over frequency space using the inverse Laplace transform (7.40b). This procedure formalizes the conjecture made in the preceding sections that the propagating wave packet consists of a superposition of many waves of different frequencies. Even though the initial disturbance field $\tilde{\mathbf{q}}_o(x, y)$ contains only spatial information, one can think of $\tilde{\mathbf{q}}_o$ as consisting of many different

frequencies since, at time $t = 0$, Equation 7.40b reduces to:

$$\tilde{\mathbf{q}}_o(x, y) = \frac{1}{2\pi} \int_{i\Gamma-\infty}^{i\Gamma+\infty} \mathbf{q}_w(x, y, \omega) d\omega \quad (7.42)$$

Therefore any initial condition contains a spectrum of frequencies, which may be broad-band or narrow-band depending on the characteristics of the initial disturbance field.

In order to solve Equation 7.41, a simplifying assumption is made that the initial condition $\tilde{\mathbf{q}}_o$ is compact in x , such that the change in boundary layer thickness is negligible across the region over which $\tilde{\mathbf{q}}_o$ is nonzero. The region of nonzero $\tilde{\mathbf{q}}_o$ will be assumed to be centered at a streamwise location x_o . Assuming $\tilde{\mathbf{q}}_o$ is sufficiently compact, Equation 7.41 can be solved near the initial location x_o using parallel linear stability theory, in which the change of the boundary layer thickness is ignored. The detailed solution of such a parallel initial-value problem has been worked out by a number of researchers (Fedorov and Tumin, 2003, Forgoston and Tumin, 2005, 2006), but is valid only in the vicinity of the initial point x_o .

Far from the initial point x_o , Equation 7.41 becomes a homogeneous problem which can be solved using the method of multiple-scales. Multiple-scales analyses of this sort have been used in the past to incorporate non-parallelism into boundary layer stability analysis (Nayfeh, 1980, El-Hady, 1991, Fedorov and Khokhlov, 2001). Solutions obtained using the method of multiple scales involve an undetermined constant that accounts for the initial amplitude of the disturbance. This constant can be determined by connecting the multiple-scales solution to the parallel solution at the point x_o , thereby coupling these two solutions together. This procedure has been employed previously by Fedorov in the context of receptivity analysis (Fedorov and Khokhlov, 2001, 2002, Fedorov, 2003, Fedorov et al., 2013), but has never been used to solve an initial-value problem, such as that of a wave packet.

In the sections that follow, formal solutions are derived both near and far from the initial point x_o , and these two solutions are coupled together. Simplifying assumptions are then made in order to reduce the computational expense, and the simple model

obtained in this way is used to investigate wave packet propagation over a wider parameter space than is accessible through the DNS.

7.10.3 Solutions near the initial point

In the vicinity of the initial point x_o where the initial condition $\tilde{\mathbf{q}}_o$ is non-zero, the inhomogeneous problem (7.41) can be solved by neglecting the dependence of the matrices \mathbf{A} on x . Also terms involving the mean vertical velocity \bar{V} and streamwise derivatives of the base flow variables are neglected in the matrices \mathbf{A} , which makes the analysis locally-parallel. One can then apply the Fourier transform and its inverse:

$$\mathbf{q}_{\omega\alpha} = \int_{-\infty}^{\infty} \mathbf{q}_{\omega} e^{-i\alpha(x-x_o)} dx \quad (7.43a)$$

$$\mathbf{q}_{\omega} = \frac{1}{2\pi} \int_{-\infty}^{\infty} \mathbf{q}_{\omega\alpha} e^{i\alpha(x-x_o)} d\alpha \quad (7.43b)$$

Application of this transform to Equation 7.41 produces the parallel problem:

$$\mathcal{L}_o \mathbf{q}_{\omega\alpha} \equiv \mathbf{A}_y \frac{\partial \mathbf{q}_{\omega\alpha}}{\partial y} + (\mathbf{A}_o + i\alpha \mathbf{A}_x - i\omega \mathbf{A}_t) \mathbf{q}_{\omega\alpha} = \mathbf{A}_t \mathbf{q}_{o,\alpha} \quad (7.44)$$

where $\mathbf{q}_{o,\alpha}$ is the Fourier transform of the initial condition \mathbf{q}_o . The homogeneous eigenfunctions of this equation can be computed using the methods of Chapter 4 and have been studied extensively in Chapter 5. The inhomogeneous problem can be solved by expansion onto the homogeneous eigenfunctions; however, such an expansion requires first that the adjoint functions and an orthogonality condition be derived.

Adjoint functions

In this work, the scalar product between two arbitrary vector functions $\mathbf{u}(y)$ and $\mathbf{v}(y)$ is defined by the integral

$$\langle \mathbf{u}, \mathbf{v} \rangle \equiv \int_0^{\infty} \mathbf{v}^H \mathbf{u} dy \quad (7.45)$$

where superscript H designates the conjugate transpose. Making use of this definition and the definition of the direct operator \mathcal{L}_o from Equation 7.44, one can derive an adjoint operator \mathcal{L}_o^+ by requiring that the direct and adjoint operators satisfy Green's formula:

$$\langle \mathcal{L}_o \mathbf{q}, \mathbf{q}^+ \rangle - \langle \mathbf{q}, \mathcal{L}_o^+ \mathbf{q}^+ \rangle = \mathbf{q}^{+H} \mathbf{A}_y \mathbf{q} \Big|_{y=0}^{\infty} \quad (7.46)$$

The adjoint operator that satisfies this property is given by:

$$\mathcal{L}_o^+ \mathbf{q}^+ \equiv -\frac{\partial}{\partial y} (\mathbf{A}_y^H \mathbf{q}^+) + (\mathbf{A}_o^H - i\alpha^* \mathbf{A}_x^H + i\omega^* \mathbf{A}_t^H) \mathbf{q}^+ \quad (7.47)$$

where the asterisk denotes complex conjugation and \mathbf{q}^+ is the solution of the adjoint problem. The boundary conditions on the adjoint function \mathbf{q}^+ are selected such that the boundary term of Equation 7.46 evaluates to zero. The required adjoint boundary conditions are derived in Appendix C, where they are shown to be the same as the boundary conditions of the direct problem:

$$\tilde{u}^+ = \tilde{v}^+ = \tilde{\theta}^+ = 0 \quad y = 0 \quad (7.48a)$$

$$|\mathbf{q}^+| < \infty \quad y \rightarrow \infty \quad (7.48b)$$

Bi-orthogonality

Eigenfunctions of the direct operator \mathcal{L}_o and the adjoint operator \mathcal{L}_o^+ satisfy the homogeneous equations:

$$\mathcal{L}_o \mathbf{q} = 0 \quad \mathcal{L}_o^+ \mathbf{q}^+ = 0 \quad (7.49)$$

Suppose that for some complex frequency ω_k the direct problem has an eigenvalue α_k and an eigenfunction \mathbf{q}_k . Likewise, suppose that the frequency ω_m corresponds to an eigenvalue α_m of the adjoint problem and its adjoint eigenfunction \mathbf{q}_m^+ . Then,

observing that $\mathcal{L}_o \mathbf{q}_k = 0$ identically, one can write the scalar product

$$\langle \mathcal{L}_o \mathbf{q}_k, \mathbf{q}_m^+ \rangle = 0 = \int_0^\infty \mathbf{q}_m^{+H} \left[\mathbf{A}_y \frac{\partial \mathbf{q}_k}{\partial y} + (\mathbf{A}_o + i\alpha_k \mathbf{A}_x - i\omega_k \mathbf{A}_t) \mathbf{q}_k \right] dy$$

Performing integration by parts and making use of the fact that the boundary terms in (7.46) are zero, one can then write:

$$\begin{aligned} 0 = \int_0^\infty \left[-\frac{\partial}{\partial y} (\mathbf{q}_m^{+H} \mathbf{A}_y) + \mathbf{q}_m^{+H} (\mathbf{A}_o + i\alpha_m \mathbf{A}_x - i\omega_m \mathbf{A}_t) \right] \mathbf{q}_k dy \\ + \int_0^\infty i(\alpha_k - \alpha_m) \mathbf{q}_m^{+H} \mathbf{A}_x \mathbf{q}_k - i(\omega_k - \omega_m) \mathbf{q}_m^{+H} \mathbf{A}_t \mathbf{q}_k dy \end{aligned} \quad (7.50)$$

In obtaining this result, the quantity $\mathbf{q}_m^+ (i\alpha_m \mathbf{A}_x - i\omega_m \mathbf{A}_t) \mathbf{q}_k$ has been both added and subtracted. The term in brackets is the conjugate transpose of the adjoint operator $\mathcal{L}_o^+ \mathbf{q}^+$ from Equation 7.47, hence Equation 7.50 can be written

$$0 = \langle \mathbf{q}_k, \mathcal{L}_o^+ \mathbf{q}_m^+ \rangle + i(\alpha_k - \alpha_m) \langle \mathbf{A}_x \mathbf{q}_k, \mathbf{q}_m^+ \rangle - i(\omega_k - \omega_m) \langle \mathbf{A}_t \mathbf{q}_k, \mathbf{q}_m^+ \rangle \quad (7.51)$$

The first term is identically zero since \mathbf{q}_m^+ is an eigenfunction of the adjoint operator \mathcal{L}_o^+ . This leaves the bi-orthogonality relation:

$$(\alpha_k - \alpha_m) \langle \mathbf{A}_x \mathbf{q}_k, \mathbf{q}_m^+ \rangle = (\omega_k - \omega_m) \langle \mathbf{A}_t \mathbf{q}_k, \mathbf{q}_m^+ \rangle \quad (7.52)$$

This relation shows that for spatial analysis with $\omega_k = \omega_m$, two spatial modes \mathbf{q}_k and \mathbf{q}_m^+ either have the same eigenvalue α or are orthogonal under the weight function \mathbf{A}_x . Similarly, for temporal analysis with $\alpha_k = \alpha_m$, two temporal modes \mathbf{q}_k and \mathbf{q}_m^+ either have the same eigenvalue ω or are orthogonal under the weight \mathbf{A}_t .

Eigenfunction expansion

Having derived the adjoint problem and the bi-orthogonality relation, one can now return to the inhomogeneous, locally-parallel problem specified in Equation 7.44. This

equation can be solved by projecting the solution $\mathbf{q}_{\omega\alpha}$ onto the spatial modes:

$$\mathbf{q}_{\omega\alpha} = \sum_k C_k \mathbf{q}_k \quad (7.53)$$

where C_k is the expansion coefficient. For simplicity the symbol \sum_k is used as a shorthand notation to represent both summation over the discrete modes and integration over the continuous spectra, since writing separate expressions for the discrete modes and the continuous spectra leads to equations that are unwieldy. [Fedorov and Tumin \(2003\)](#) have shown that the eigenfunctions of the discrete and continuous spectra together form a complete set by solving the inhomogeneous problem (7.44) using the method of variation of parameters.

One can substitute the expansion (7.53) into Equation 7.44 and then take the inner product against an arbitrary adjoint mode \mathbf{q}_m to obtain:

$$\sum_k C_k \langle \mathcal{L}_o \mathbf{q}_k, \mathbf{q}_m^+ \rangle = \langle \mathbf{A}_t \mathbf{q}_{o,\alpha}, \mathbf{q}_m^+ \rangle \quad (7.54)$$

After expanding out the left hand side, one finds

$$\sum_k C_k \int_0^\infty \mathbf{q}_m^{+H} \left[\mathbf{A}_y \frac{\partial \mathbf{q}_k}{\partial y} + (\mathbf{A}_o + i\alpha \mathbf{A}_x - i\omega \mathbf{A}_t) \mathbf{q}_k \right] dy = \langle \mathbf{A}_t \mathbf{q}_{o,\alpha}, \mathbf{q}_m^+ \rangle \quad (7.55)$$

This equation can be rearranged in the form:

$$\begin{aligned} \sum_k C_k \int_0^\infty \mathbf{q}_m^{+H} \left[\mathbf{A}_y \frac{\partial \mathbf{q}_k}{\partial y} + (\mathbf{A}_o + i\alpha_k \mathbf{A}_x - i\omega \mathbf{A}_t) \mathbf{q}_k \right. \\ \left. + i(\alpha - \alpha_k) \mathbf{A}_x \mathbf{q}_k \right] dy = \langle \mathbf{A}_t \mathbf{q}_{o,\alpha}, \mathbf{q}_m^+ \rangle \end{aligned} \quad (7.56)$$

The first two terms in square brackets are zero because \mathbf{q}_k is an eigenvector of \mathcal{L}_o .

The terms that remain are

$$\sum_k C_k i(\alpha - \alpha_k) \langle \mathbf{A}_x \mathbf{q}_k, \mathbf{q}_m^+ \rangle = \langle \mathbf{A}_t \mathbf{q}_{o,\alpha}, \mathbf{q}_m^+ \rangle \quad (7.57)$$

Making use of the bi-orthogonality relation (7.52), one can solve for the coefficient C_m :

$$C_m = \frac{1}{i(\alpha - \alpha_m)} \frac{\langle \mathbf{A}_t \mathbf{q}_{o,\alpha}, \mathbf{q}_m^+ \rangle}{\langle \mathbf{A}_x \mathbf{q}_m, \mathbf{q}_m^+ \rangle} \quad (7.58)$$

This result describes the projection of the initial condition $\tilde{\mathbf{q}}_o$ onto the m^{th} mode of discrete or continuous spectrum. The total solution is then summed from the expansion (7.53):

$$\mathbf{q}_{\omega\alpha} = \sum_k \frac{1}{i(\alpha - \alpha_k)} \frac{\langle \mathbf{A}_t \mathbf{q}_{o,\alpha}, \mathbf{q}_k^+ \rangle}{\langle \mathbf{A}_x \mathbf{q}_k, \mathbf{q}_k^+ \rangle} \mathbf{q}_k \quad (7.59)$$

Again, it must be emphasized that this solution consists of both a summation over the discrete eigenvalues and integration over the continuous spectra.

Inverse Fourier Transform

The inverse Fourier transform of Equation 7.59 is given by

$$\mathbf{q}_{\omega}(x, y) = \frac{1}{2\pi} \int_{-\infty}^{\infty} \sum_k \frac{1}{i(\alpha - \alpha_k)} \frac{\langle \mathbf{A}_t \mathbf{q}_{o,\alpha}, \mathbf{q}_k^+ \rangle}{\langle \mathbf{A}_x \mathbf{q}_k, \mathbf{q}_k^+ \rangle} \mathbf{q}_k e^{i\alpha(x-x_o)} d\alpha \quad (7.60)$$

Making use of the residue theorem, one finds that the Fourier integral reduces to a summation over the discrete spectrum and an integration over the continuous spectrum. The result is

$$\mathbf{q}_{\omega} = \sum_k \frac{\langle \mathbf{A}_t \mathbf{q}_{o,\alpha_k}, \mathbf{q}_k^+ \rangle}{\langle \mathbf{A}_x \mathbf{q}_k, \mathbf{q}_k^+ \rangle} \mathbf{q}_k e^{i\alpha_k(x-x_o)} \quad (7.61)$$

This result is the formal solution of Equation 7.41 in the vicinity of the initial point x_o , which describes the projection of the Fourier-transformed initial condition $\mathbf{q}_{o,\alpha}(x, y)$ onto the spatial modes $\mathbf{q}_k(y, \omega)$, each of which is evaluated at the point x_o . This result is only valid near x_o since the matrices \mathbf{A} are evaluated at x_o and their streamwise variation has been ignored. Again, the symbol \sum_k should be interpreted as a summation over the discrete modes and an integration over the continuous spectra. Similar

results have been obtained by [Fedorov and Tumin \(2003\)](#) and [Forgoston and Tumin \(2005\)](#), with the exception that they inverted the Laplace transform (temporal) first rather than the Fourier transform (spatial). For the present wave packet analysis, the spatial Fourier transform must be inverted first in order to compute the non-parallel solution \mathbf{q}_ω for each frequency.

7.10.4 Solutions away from the initial point

Having established the solution of the Laplace-transformed initial-value problem in the vicinity of the initial condition, the solution at distances farther downstream can now be determined using the method of multiple scales. The multiple-scales technique employed here is adapted from [Nayfeh \(1980\)](#), and a general exposition on the method is available from [Nayfeh \(1993\)](#).

Far from the initial point x_o , the inhomogeneity of Equation 7.41 disappears leaving the homogeneous problem:

$$\mathcal{L}\mathbf{q} = \mathbf{A}_x \frac{\partial \mathbf{q}_\omega}{\partial x} + \mathbf{A}_y \frac{\partial \mathbf{q}_\omega}{\partial y} + (\mathbf{A}_o \mathbf{q} - i\omega \mathbf{A}_t) \mathbf{q}_\omega = 0 \quad (7.62)$$

To solve this problem, it is assumed that the matrices \mathbf{A} change slowly with the downstream distance x . Also, terms in the matrices \mathbf{A} involving the mean vertical velocity \bar{V} and streamwise derivatives of the base flow are neglected. In keeping with the assumption of a slowly changing base flow, slowly-varying length scale X is introduced:

$$X = \epsilon x \quad \frac{\partial}{\partial x} \rightarrow \frac{\partial}{\partial x} + \epsilon \frac{\partial}{\partial X} \quad (7.63)$$

In this equation, $\epsilon = \delta_L/L$ is a small parameter which is equal to the ratio of the boundary layer thickness to the streamwise distance at some characteristic distance L along the boundary layer. Equivalently, $\epsilon = 1/R_L$ is the inverse of the Reynolds number based on boundary layer thickness at the location L , and hence the approximations made in the multiple-scales analysis improve as the Reynolds number

increases.

The matrices \mathbf{A} are assumed to depend only on the slow scale X , and following [Nayfeh \(1980\)](#) each eigenmode \mathbf{q}_k is assumed to vary in the following way:

$$\mathbf{q}_k = C_k(X) [\mathbf{Q}_{o,k}(X, y) + \epsilon \mathbf{Q}_{1,k}(X, y) + \dots] \exp \left(\int_{x_o}^x i\alpha_k(x) dx \right) \quad (7.64)$$

Here $C_k(X)$ describes the slow disturbance amplitude variation, \mathbf{Q} describes the wall-normal shape of the disturbance, and the exponential models the fast dynamics of the wave. The total solution \mathbf{q}_ω then consists of a summation over all modes k , with contributions from both the discrete modes and from the continuous spectra. Substitution of the expansion (7.64) into Equation 7.62 gives the following problems at the first two powers of ϵ :

$$\epsilon^0 : \quad \sum_k C_k \mathcal{L}_o \mathbf{Q}_{o,k} \exp \left(\int_{x_o}^x i\alpha_k dx \right) = 0 \quad (7.65a)$$

$$\epsilon^1 : \quad \sum_k \left[C_k \mathcal{L}_o \mathbf{Q}_{1,k} + C_k \mathbf{A}_x \frac{\partial \mathbf{Q}_{o,k}}{\partial X} + \frac{\partial C_k}{\partial X} \mathbf{A}_x \mathbf{Q}_{o,k} \right] \exp \left(\int_{x_o}^x i\alpha_k dx \right) = 0 \quad (7.65b)$$

As discussed previously, the summation \sum_k is a shorthand notation which should be regarded as summation over the discrete modes and also integration over the continuous modes. The ϵ^0 equation is automatically satisfied by taking $\mathbf{Q}_{o,k}$ to be an eigenvector of \mathcal{L}_o . As described by [\(Nayfeh, 1993\)](#), the ϵ^1 equation must satisfy a solvability condition in which the second and third terms of Equation 7.65b are orthogonal to each adjoint mode of \mathcal{L}_o^+ . For an arbitrary adjoint mode \mathbf{Q}_m^+ , this solvability condition takes the form:

$$\sum_k \left[C_k \left\langle \mathbf{A}_x \frac{\partial \mathbf{Q}_{o,k}}{\partial X}, \mathbf{Q}_{o,m}^+ \right\rangle + \frac{\partial C_k}{\partial X} \langle \mathbf{A}_x \mathbf{Q}_{o,k}, \mathbf{Q}_{o,m}^+ \rangle \right] \exp \left(\int_{x_o}^x i\alpha_k dx \right) = 0 \quad (7.66)$$

By virtue of the bi-orthogonality relation (7.52), this reduces to

$$\sum_k C_k \left\langle \mathbf{A}_x \frac{\partial \mathbf{Q}_{o,k}}{\partial X}, \mathbf{Q}_{o,m}^+ \right\rangle \exp \left(\int_{x_o}^x i \alpha_k dx \right) = -\frac{\partial C_m}{\partial X} \langle \mathbf{A}_x \mathbf{Q}_{o,m}, \mathbf{Q}_{o,m}^+ \rangle \exp \left(\int_{x_o}^x i \alpha_m dx \right) \quad (7.67)$$

which can be solved for $\partial C_m / \partial X$:

$$\frac{\partial C_m}{\partial X} = -\sum_k C_k \frac{\left\langle \mathbf{A}_x \frac{\partial \mathbf{Q}_{o,k}}{\partial X}, \mathbf{Q}_{o,m}^+ \right\rangle}{\langle \mathbf{A}_x \mathbf{Q}_{o,m}, \mathbf{Q}_{o,m}^+ \rangle} \exp \left(\int_{x_o}^x i(\alpha_k - \alpha_m) dx \right) \quad (7.68)$$

The same expression was derived by Fedorov and Khokhlov (2001) except that they also included the mean vertical velocity \bar{V} and streamwise derivatives of the base flow variables, which produces an additional term in the numerator. This equation represents a coupled system of first order ordinary differential equations for the expansion coefficients C_k , and integration of the system enables each of the constants $C_k(X)$ to be calculated, up to an undetermined constant. The undetermined constant is found by evaluating $C_k(x_o)$, at which point the value of C_k is known from the solution to the locally-parallel initial-value problem, Equation 7.61, which indicates that

$$C_k(x_o) = \frac{\langle \mathbf{A}_t \mathbf{q}_{o,\alpha}, \mathbf{Q}_k^+ \rangle}{\langle \mathbf{A}_x \mathbf{Q}_k, \mathbf{Q}_k^+ \rangle} \quad (7.69)$$

In general, Equation 7.68 must be integrated numerically, for example, by marching the coefficients C_k downstream starting from the initial location x_o where the initial values of $C_k(x_o)$ are known. Since this solution includes all possible modes from both the discrete and continuous spectra, one must truncate the solution space and use a finite number of modes as well as discrete approximations to the integrals over the continuous spectra. It is often possible to consider only a small subset of modes that are relevant to a particular problem of interest, and this approach will be used in the sections that follow.

7.10.5 Single mode solution

In general, the solution (7.68) together with the expansion (7.64) describes the coupled downstream propagation of all possible modes from the discrete and continuous spectra. However, in many cases one is interested in only one or two modes and the result is greatly simplified. For example, if only a single mode is excited then Equation 7.68 reduces to

$$\frac{1}{C} \frac{\partial C}{\partial X} = \frac{\langle \mathbf{A}_x \frac{\partial \mathbf{Q}_o}{\partial X}, \mathbf{Q}_o^+ \rangle}{\langle \mathbf{A}_x \mathbf{Q}_o, \mathbf{Q}_o^+ \rangle} \quad (7.70)$$

which has the solution

$$C(X) = C(x_o) \exp \left[\int_{x_o}^x \frac{\langle \mathbf{A}_x \frac{\partial \mathbf{Q}_o}{\partial X}, \mathbf{Q}_o^+ \rangle}{\langle \mathbf{A}_x \mathbf{Q}_o, \mathbf{Q}_o^+ \rangle} dX \right] \quad (7.71)$$

For second mode waves this is a good approximation except near synchronism points, where the use of a two-mode expansion may be needed. As discussed by Fedorov and Khokhlov (2001), at such points the slow and fast modes (c.f. Section 5.1) become strongly coupled and can exchange their identities, which necessitates a two-mode solution that involves both the slow and fast modes. Further details regarding the treatment of the synchronism point are available from Fedorov and Khokhlov (2001), but for the results that follow the synchronism is not present and a single-mode solution is acceptable.

After combining Equations 7.64 and 7.71, the Laplace-transformed solution for a single second mode wave is

$$\mathbf{q}_\omega = \frac{\langle \mathbf{A}_t \mathbf{q}_{o,\alpha}, \mathbf{Q}_o^+ \rangle}{\langle \mathbf{A}_x \mathbf{Q}_o, \mathbf{Q}_o^+ \rangle} \mathbf{Q}_o \exp \left[\int_{x_o}^x \left(i\alpha(x) - \frac{\langle \mathbf{A}_x \frac{\partial \mathbf{Q}_o}{\partial X}, \mathbf{Q}_o^+ \rangle}{\langle \mathbf{A}_x \mathbf{Q}_o, \mathbf{Q}_o^+ \rangle} \right) dx \right] \quad (7.72)$$

The factor preceding the exponential describes the receptivity problem, that is, the excitation of the second mode wave by the initial disturbance \mathbf{q}_o . The second term in the exponential describes the non-parallel correction. Performing the inverse Laplace

transform, one obtains

$$\mathbf{q}(x, y, t) = \frac{1}{2\pi} \int_{-\infty}^{+\infty} \frac{\langle \mathbf{A}_t \mathbf{q}_{o,\alpha}, \mathbf{Q}_o^+ \rangle}{\langle \mathbf{A}_x \mathbf{Q}_o, \mathbf{Q}_o^+ \rangle} \mathbf{Q}_o \times \exp \left[\int_{x_o}^x \left(i\alpha(\omega, x) - \frac{\langle \mathbf{A}_x \frac{\partial \mathbf{Q}_o}{\partial X}, \mathbf{Q}_o^+ \rangle}{\langle \mathbf{A}_x \mathbf{Q}_o, \mathbf{Q}_o^+ \rangle} \right) dx - i\omega t \right] d\omega \quad (7.73)$$

In the Laplace inversion integral (7.40b), the parameter Γ specifies a line in the complex plane which passes above all singularities of the integrand. For boundary layer flows, one expects the singularities to fall in the lower half plane since poles located in the upper half plane would cause absolute instability, i.e., exponential growth in time of disturbances at a fixed location in the boundary layer. Experiments, linear stability analyses, and DNS all indicate that boundary layers do not experience this type of instability, being instead convectively unstable. Consequently, it suffices to take the limit $\Gamma \rightarrow 0^+$ and perform the Laplace inversion along the real ω axis, and this assumption has been invoked in writing Equation 7.73. Equation 7.73 is the formal solution of a second mode wave packet generated by a compact initial disturbance \mathbf{q}_o . The wavenumber $\alpha(\omega, x)$ and the direct and adjoint eigenfunctions \mathbf{Q}_o and \mathbf{Q}_o^+ needed to evaluate this solution can be found using locally-parallel stability analysis.

7.10.6 Simplification

In the analysis that follows, the solution is further simplified by neglecting the non-parallel correction involving $\partial \mathbf{Q}_o / \partial X$. It should be recalled also that we have neglected terms involving the mean vertical velocity \bar{V} and streamwise derivatives of the base flow in the matrices \mathbf{A} . The results are then analogous to conventional locally-parallel stability analysis, in which growth rates are computed independently at each x location and the results are pieced together to determine the amplification of disturbances in a non-parallel boundary layer. Similarly, in this analysis the evolution of a wave packet in a non-parallel boundary layer is constructed from locally-parallel stability calculations performed independently at each value of x and ω . Therefore the

results obtained here are based on precisely the same approximations that are used in locally-parallel spatial stability analysis. As was shown in Section 7.7, locally-parallel spatial analysis produces the correct qualitative behavior and yields amplification that is within a factor of about 2-3 of fully non-parallel results. For transition prediction, in which waves amplify by several orders of magnitude, this error is usually acceptable for making estimates.

After neglecting the non-parallel correction, the wall pressure $p_{wall}(x, t)$ can be extracted from Equation 7.73 to obtain:

$$p_{wall}(x, t) = \frac{1}{2\pi} \int_{-\infty}^{\infty} \frac{\langle \mathbf{A}_t \mathbf{q}_{o,\alpha}, \mathbf{Q}_o^+ \rangle}{\langle \mathbf{A}_x \mathbf{Q}_o, \mathbf{Q}_o^+ \rangle} \exp \left[\int_{x_o}^x i\alpha(x) dx - i\omega t \right] d\omega \quad (7.74)$$

In writing this result, it has been assumed that the component of \mathbf{Q}_o corresponding to the wall pressure is equal to 1.0, as is the case in the present locally-parallel stability analysis. The term preceding the exponential is a scalar that depends on the frequency, which will be denoted $C(\omega)$. Therefore the wall pressure is of the form:

$$\boxed{p_{wall}(x, t) = \frac{1}{2\pi} \int_{-\infty}^{\infty} C(\omega) \exp \left[\int_{x_o}^x i\alpha(x) dx - i\omega t \right] d\omega} \quad (7.75)$$

Suppose that the initial condition is selected to be of the form:

$$\mathbf{q}_o(x, y) = \mathbf{Q}_o(y) \exp \left(i\alpha_o(x - x_o) - 3\frac{(x - x_o)^2}{R_x^2} \right) \quad (7.76)$$

where \mathbf{Q}_o is the second mode eigenfunction corresponding to some frequency ω_o , α_o is the corresponding second mode wavenumber, and R_x is the half-width of a Gaussian envelope. This is the same form of initial condition that was employed in the DNS of Section 7.8. The Fourier transform of this initial condition is

$$\mathbf{q}_{o,\alpha} = R_x \sqrt{\frac{\pi}{3}} \mathbf{Q}_o(y) \exp \left(-\frac{R_x^2}{12} (\alpha - \alpha_o)^2 \right) \quad (7.77)$$

Therefore the function $C(\omega)$ is given by:

$$C(\omega) = R_x \sqrt{\frac{\pi}{3}} \frac{\langle \mathbf{A}_t \mathbf{Q}_o, \mathbf{Q}_o^+ \rangle}{\langle \mathbf{A}_x \mathbf{Q}_o, \mathbf{Q}_o^+ \rangle} \exp \left[-\frac{R_x^2}{12} \left(\alpha(\omega) - \alpha(\omega_o) \right)^2 \right] \quad (7.78)$$

where $\alpha(\omega, x_o)$ is given by the second mode dispersion relation. The term preceding the exponential is merely a scalar constant and hence its only effect is to set the initial amplitude of the wave packet. In this work we set the initial wave amplitude to 1.0 in physical space rather than evaluating the scalar products in the pre-exponential factor of (7.78).

Having determined $C(\omega)$, the Laplace inversion integral (7.75) can now be evaluated to determine the evolution of the wave packet as a function of time. Since $C(\omega)$ is compact in frequency space because of its Gaussian shape, one can truncate the integration limits to finite values and perform the integration numerically. The steps involved in calculating the wave packet trajectory are then as follows:

1. Compute and tabulate the dispersion curve $\alpha(\omega, x)$ using the locally-parallel stability analysis from Chapter 5.
2. Choose an initial location x_o , a frequency ω_o , and an initial wave packet width R_x .
3. Evaluate $C(\omega)$ using Equation 7.78 and the tabulated dispersion curve $\alpha(\omega, x)$.
4. For any desired point (x, t) , evaluate the wall pressure by numerically integrating Equation 7.75.

7.10.7 Results

The base flow profiles used in this section are the same as those presented previously in Section 7.5 and used in the preceding DNS. Examples of initial wall pressure profiles for several wave packet widths are given in Figure 7.31a, and the corresponding frequency amplitudes $C(\omega)$ are given in Figure 7.31b. The frequency amplitudes C are presented as functions of the dimensionless frequency parameter $F = \omega \nu_e / U_e^2$ and

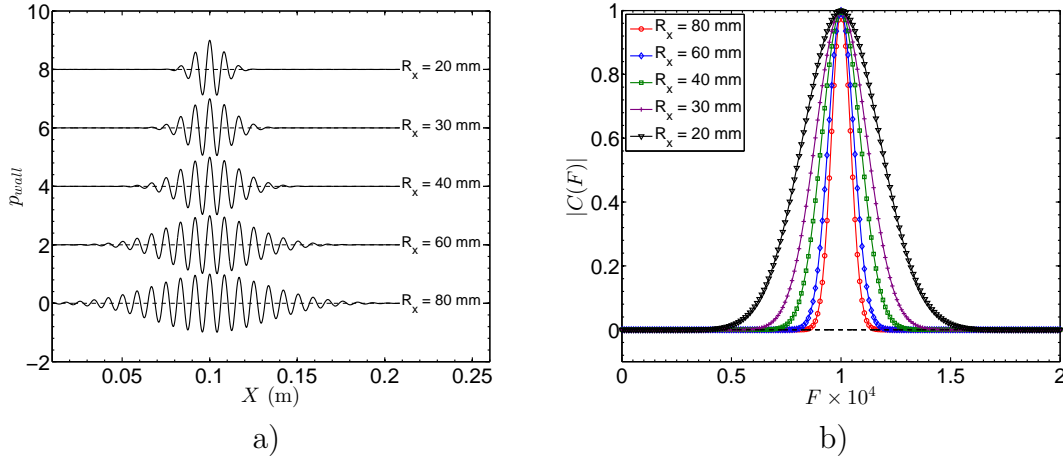


Figure 7.31: a) Initial wall pressure profiles at $t = 0$ for several different wave packet widths. Profiles have been offset vertically for clarity. b) Frequency spectrum $|C(F)|$ for several wave packet widths, normalized by $\max(|C(F)|)$ in each case.

were computed using Equation 7.78. The profiles in physical space, Figure 7.31a, were then calculated by evaluating Equation 7.75 at $t = 0$. It should be noted that $C(\omega)$ is in general complex-valued, but the imaginary part is quite small and does not contribute significantly to the shape of the initial wave packet. As shown in the figure, wider wave packets in physical space lead to narrower packets in frequency space, and vice versa.

When Equation 7.75 is evaluated at different time instants, one obtains the pressure profiles given on an x - t diagram in Figure 7.32. The flow conditions are the same as those pertaining to Figure 7.15, in which an x - t diagram was constructed using DNS. Comparison between the DNS (Figure 7.15) and the simple model (Figure 7.32) shows that the qualitative results from the simple model agree quite favorably with those of the DNS. However, as will be shown in the sections that follow, the amplification predicted by the simple model is somewhat less because of the exclusion of non-parallel effects.

Aside from the mean flow conditions, this simplified wave packet analysis involves only three free parameters: the initial location of the wave x_o , the initial wave packet width R_x , and the frequency F_o (or equivalently, ω_o) used to generate the wave packet (Equation 7.76). We have performed a number of calculations that show that the

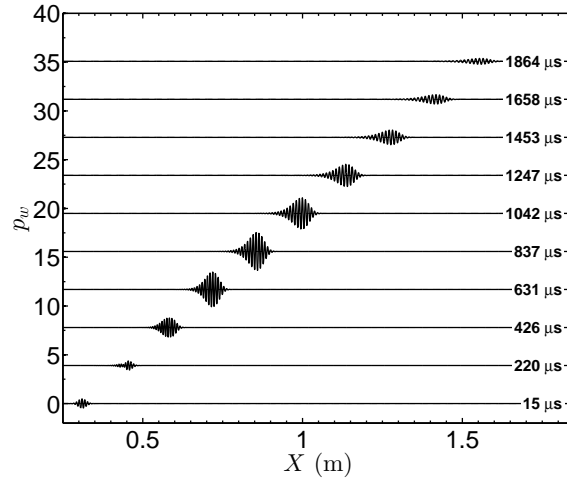


Figure 7.32: x - t diagram of a wave packet with $F_o = 10^{-4}$, $x_o = 0.3$ m, $R_x = 30$ mm. Vertical offset of the traces is proportional to time.

results are quite insensitive to the initial location x_o as long as the wave is upstream of the lower neutral branch ($0 < x_o < 0.5$ m in this case). Consequently, the value $x_o = 0.3$ m is used in the remainder of the results.

The second free parameter is the wave packet width, R_x , which is used in generating the initial condition. To investigate the effect of this parameter, similar calculations to Figure 7.32 were carried out for several values of R_x while keeping the frequency F_o fixed. Figure 7.33 reports the maximum amplitude of the wave packet as a function of downstream distance for several different wave packet widths. The cases shown in this figure are the same as those shown previously in Figure 7.23 using DNS, and the results are qualitatively the same. As the physical width of the initial wave packet grows wider, the disturbance grows narrower in frequency space and the spatial LST result is approached. The only difference is that the amplification predicted by the simple model (Figure 7.33) is less than the amplification achieved in the DNS (Figure 7.23) by a factor of about 1.2-3, depending on the reference location in x from which the amplification is computed. This difference exists because the simple model is based on locally-parallel stability analysis, which was shown in Section 7.7 to under-predict the amplification of each Fourier mode. The difference in amplification between the DNS and the simple model would therefore be remedied

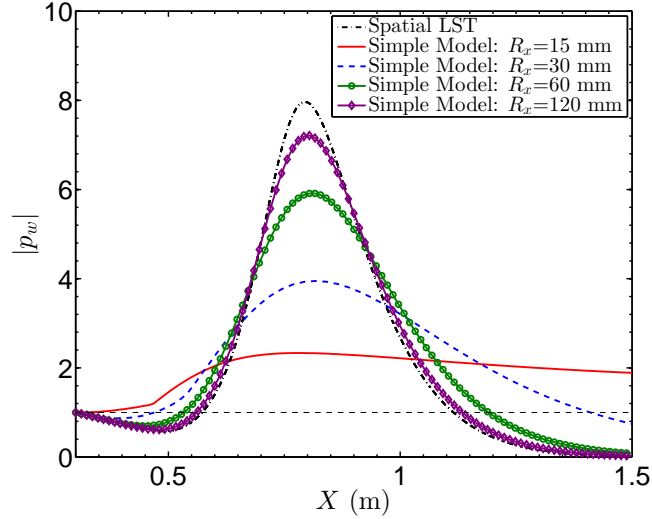


Figure 7.33: Maximum amplitude of wave packet as a function of X for several wave packet widths.

if non-parallel effects were included in the LST analysis, that is, if the second term in the exponential of Equation 7.73 were retained. This would slightly increase the complexity and computational cost of the simple model, but it would remain orders of magnitude cheaper than the DNS.

The third factor that affects the wave packet evolution is the frequency F_o used to generate the initial condition. Figure 7.34 uses the simple wave packet model to study the amplification of wave packets for several values of F_o for fixed $R_x = 30$ mm, and the results are compared with spatial stability theory (LST). Lines with markers describe the amplification of wave packets, whereas dot-dashed lines are the corresponding results from LST. The curves are parameterized by the frequency F_o ; for LST this is the frequency used in the stability analysis and for wave packet analysis this frequency defines ω_o and \mathbf{Q}_o in Equation 7.78.

For high frequency disturbances, which are amplified near the leading edge, the agreement between the LST and the wave packet analysis is fairly good. This is because high frequency disturbances have short wavelengths, so for a fixed initial wave packet width R_x the packet contains more waves when the frequency is higher, and thus is more closely approximated by spatial analysis. For lower frequencies, which are more highly amplified, the growth of the wave packet initially follows the

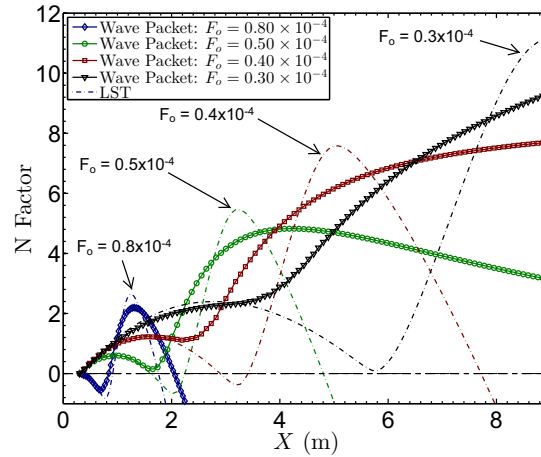


Figure 7.34: Comparison of N factors for wave packets (symbols) and spatial analysis (lines) for several different frequencies F_o . ‘LST’ refers to conventional spatial stability analysis. For wave packet cases, the initial packet width is $R_x = 30$ mm.

LST, but farther downstream there is a significant discrepancy in both the qualitative behavior and the maximum amplification that is achieved.

As an alternative to holding the initial wave packet width R_x fixed as F_o is varied, one can also hold the number of waves in the initial condition fixed. This amounts to holding $\alpha_o R_x$ constant. Figure 7.35 shows the resulting N factors when $2\pi R_x \alpha_o$ is held fixed at 2.5, which means that the initial wave packet contains 5 wavelengths. Similar behavior to Figure 7.34 is observed, except that the amplification of the wave packet is less than that of LST for all frequencies, rather than for low frequencies only. For all frequencies, the N factor of the wave packet is about 1.5-2 less than the N factor from spatial analysis.

The envelopes of the curves for all different frequencies in Figures 7.34-7.35 are the “maximum N factor” curves, which describe the largest possible amplification that can be experienced within the boundary layer. Two different maximum N factor curves can be constructed: one for the spatial LST analysis (lines) and one for the wave packets (symbols). In a similar manner, maximum N factor curves can be generated for any choice of initial wave packet width R_x . This technique provides a way of taking the finite width of instability waves into account during transition prediction. As can be seen, the assumption of a finite width wave packet can lead

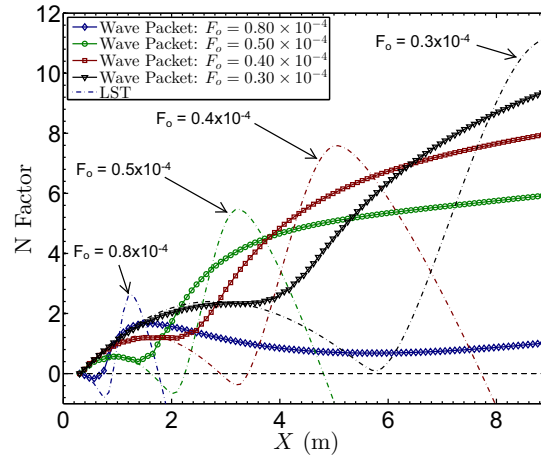


Figure 7.35: Comparison of N factors for wave packets (symbols) and spatial analysis (lines) for several different frequencies F_o . ‘LST’ refers to conventional spatial stability analysis. For wave packet cases, the initial packet contains 5 waves, $2\pi R_x \alpha_o = 2.5$.

to a significant difference in the predicted transition location. For example, if one assumes that transition will occur at $N=8$, the transition locations from LST and from a wave packet initially consisting of 5 waves differ by about 1.5 m, or 30%.

7.11 Conclusion

Experimental evidence suggests that disturbances in a boundary layer take the form of wave packets of finite width, often containing 5-20 individual waves within the packet. The analysis given in this chapter demonstrates that packets of waves initiated near the leading edge of a flat plate experience less amplification than predicted by traditional spatial stability analysis. In the limiting case of a wave packet containing an infinite number of waves, the predictions of spatial linear stability theory and wave packet analysis coincide. But for wave packets of finite width, the amplification is over-predicted by spatial analysis. Since the amplitude of waves in physical space, not frequency space, triggers the nonlinearities that lead to breakdown to turbulence, the finite width of wave packets ought to be taken into account in making predictions of boundary layer transition.

This conclusion may be supported by experimental measurements made on a

compression cone in the Mach 6 quiet tunnel at Purdue. This tunnel is designed to maintain laminar flow along the nozzle wall, which eliminates the acoustic noise radiated from the turbulent boundary layer that is experienced in conventional wind tunnels. As a result, the pitot pressure fluctuations measured in the freestream of this “quiet tunnel” are about 0.04% of the mean pressure (Juliano et al., 2008), as compared to 0.5-1% in conventional wind tunnels. Experiments in this tunnel have reported transition at N factors of 16-20 (Ward et al., 2010, Schneider, 2015) according to spatial stability analysis, which implies amplification on the order of $e^N = 10^7 - 10^8$. Such high levels of amplification seem implausibly large. In the experiments the measured pressure fluctuations at the point of transition were in about 30% of the mean value. Working backward from this final amplitude, one finds that the initial amplitude of the pressure disturbance is on the order of 10 billionths of the mean pressure. This value is not consistent with the 0.04% freestream noise measured in the facility.

This result suggests that disturbances are not actually growing by the amount predicted by spatial stability analysis, and the finite width of the wave packets offers one possible explanation for this. This discrepancy would not be noticed in conventional wind tunnels because of the high noise level; if wave packets in such facilities amplify by less than the prediction of linear stability theory, this will merely cause the computed “N factor at transition” to be larger than the actual amplification of disturbances. There are, of course, other explanations for the high N factors described above. For example, uncertainties regarding the flow conditions could cause the stability analysis to predict unphysically large N factors at the transition point, and there is usually some nonlinear saturation of the disturbances prior to transition. Nevertheless, this may also be an indicator that intermittent “natural” disturbances do not quite amplify in accordance with spatial stability theory.

Chapter 8

Conclusions

Three different mechanisms of linear disturbance amplification in hypersonic boundary layers are investigated in the context of predicting the early stages of laminar-turbulent boundary layer transition. The first mechanism, modal instability, involves unstable discrete eigenmodes of the linearized Navier-Stokes equations that maintain an approximately fixed mode shape as they amplify and travel downstream. The second mechanism, transient growth, involves an optimal initial disturbance that achieves large amounts of short-term amplification despite its eventual exponential decay. The third mechanism is the amplification of finite-width wave packets, which can be thought of as a frequency superposition of modal instabilities.

8.1 Modal Stability Analysis

Although modal stability analysis of compressible boundary layers has a long and rich history, the enormous parameter space, the high sensitivity of the transition point to these parameters, and the complexity and subtleties of the analysis leave much that is not understood about transition of these flows. This is particularly true of high enthalpy flows, where the chemical and thermal nonequilibrium becomes possible. The work presented in this thesis advances the understanding of such flows in several ways.

First, a systematic study of the effects of wall temperature and Mach number on the amplification of instability waves was carried out. Although a few other

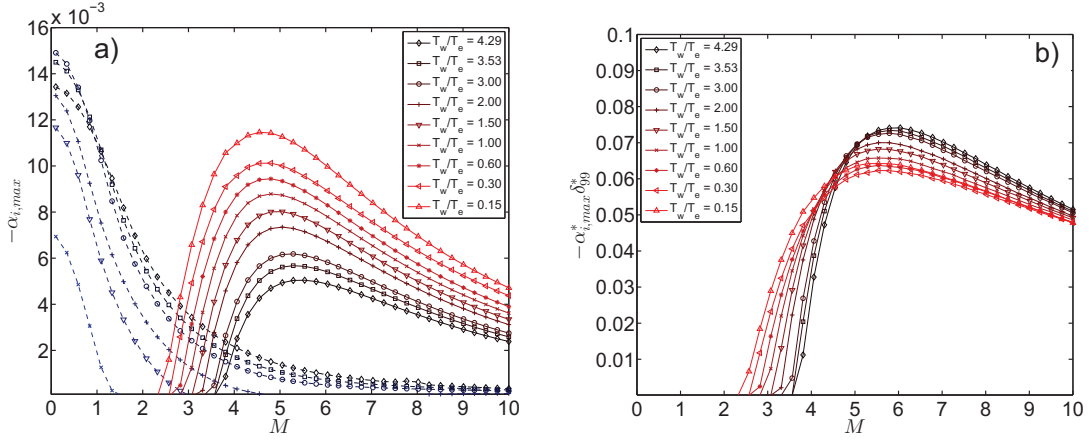


Figure 8.1: Effect of wall cooling on the maximum spatial growth rates of the first and second modes for $R = 1500$, $T_w^* = 300$ K, $T_e^* = 70 - 2000$ K, $P_e^* = 10$ kPa. a) Maximum growth rates for first and second modes. b) Maximum growth rate of second mode normalized by δ_{99} .

researchers have conducted similar systematic studies (Mack, 1969, 1984, Masad et al., 1992), the results given here span a much wider range of parameters that encompasses most conditions that can be reached in impulse-type test facilities. The compilation of stability results over such a wide range of conditions enables several new trends to be identified, including the scaling of second mode frequencies, growth rates, and amplification levels with the δ_{99} boundary layer thickness. This enables the effect of wall temperature to be nearly scaled out of the problem. These results are summarized in Figure 8.1, in which the spatial growth rates are reported for a wide range of conditions and their near collapse upon scaling with the δ_{99} boundary layer thickness is demonstrated.

Second, the effects of vibrational nonequilibrium processes on the second mode instability are explored. It is shown that vibrational nonequilibrium enters the analysis in two ways: by affecting the base flow and by affecting the disturbances. This distinction is important because the influence of nonequilibrium on the base flow and the disturbances can have opposite and competing effects. This has been a source of some confusion in the literature, where conflicting results can be found. This work clarifies this behavior, showing that a vibrational nonequilibrium base flow tends to destabilize the boundary layer relative to the frozen case, while nonequilibrium

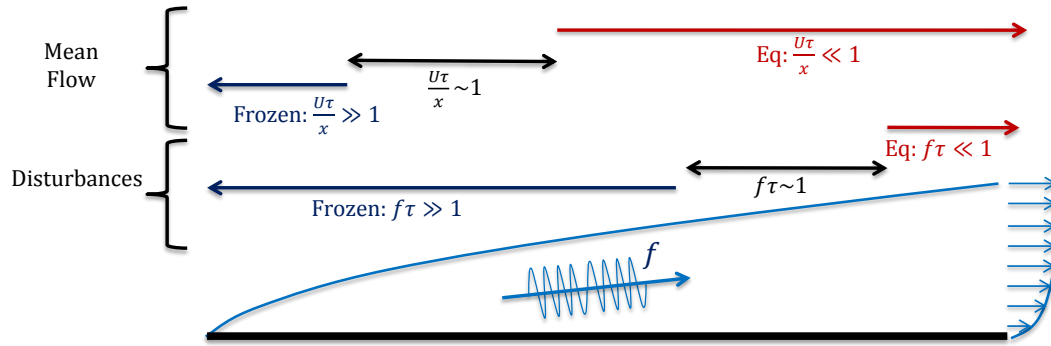


Figure 8.2: Schematic of relaxation times in a boundary layer.

disturbances stabilize it. The net result of these competing effects depends on the Reynolds number, disturbance frequency, and relaxation time scales involved. The importance of these two mechanisms can be assessed on the basis of the schematic of Figure 8.2 along with the Damköhler numbers associated with convection of the freestream ($U\tau/x$) and second mode disturbance fluctuations ($f\tau$).

For slender bodies in air, the stabilizing effect of nonequilibrium disturbances is extremely small since the frequency of the second mode instability is too high for vibrational relaxation to take place. However, vibrational nonequilibrium does slightly alter the base flow profiles, and thereby slightly influences the stability results, though the effect is rather small. For flows of carbon dioxide, on the other hand, the vibrational nonequilibrium produces a net stabilization compared with vibrationally frozen flow at Reynolds numbers relevant to transition.

Third, this work investigates the stability of boundary layers having an extreme level of wall cooling, $T_w/T_e \sim 0.15$, that has not been widely analyzed in the literature, but is highly applicable to flows in high enthalpy shock tunnels because of their high freestream temperature. Such high levels of wall cooling gives rise to supersonic, unstable modes which are unstable over a much wider band of frequencies than the usual subsonic unstable modes. As shown in Figure 8.3 for $T_e = 1000$ and 1500 K, these supersonic modes produce a kink in the dispersion curve that significantly changes its qualitative behavior. Nevertheless, these supersonic modes do not

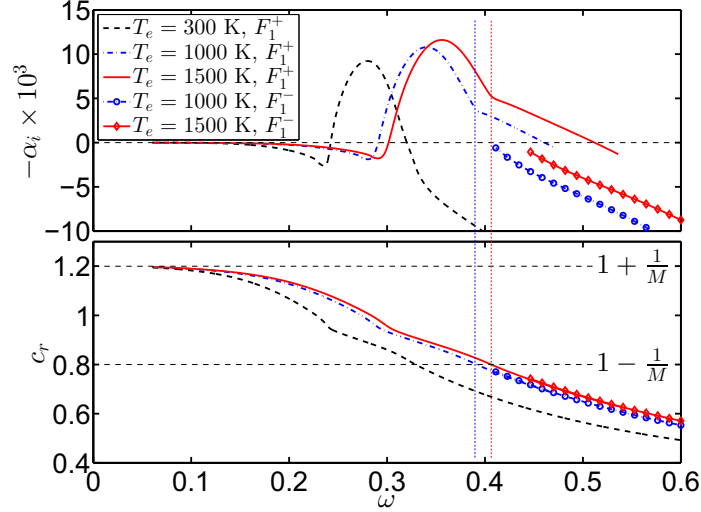


Figure 8.3: Effect of wall cooling on the spatial growth rate (top) and phase speed (bottom). For all cases, the gas is air, $M = 5.0$, $R = 2000$, $T_w^* = 300$ K, $P_e^* = 10$ kPa. Lines with symbols designate an additional mode that appears when $T_w^* \ll T_e^*$.

significantly affect the level of amplification until the Reynolds number is quite high. A new synchronism between freestream acoustic waves and the supersonic modes was also identified, which leads to greater receptivity to the acoustic waves. However, since this synchronism is located downstream of the upper neutral branch it is unlikely to affect the amplification of waves, but it may still influence the nonlinear stages of their downstream development.

8.2 Transient Growth Analysis

Transient growth calculations are reported for a wide range of conditions relevant to impulse-type experimental facilities. These calculations cover a much wider range of conditions than is available in the literature, and hence enables the trends to be clarified. Figure 8.4 summarizes the maximum energy amplification as a function of Mach number and wall temperature ratio T_w/T_e . In general the level of transient growth decreases at higher Mach numbers when the ratio of the wall temperature to the freestream temperature T_w/T_e is held fixed. Transient growth is also minimized with slight wall cooling below $T_w/T_e = 1$, and further wall cooling is needed to

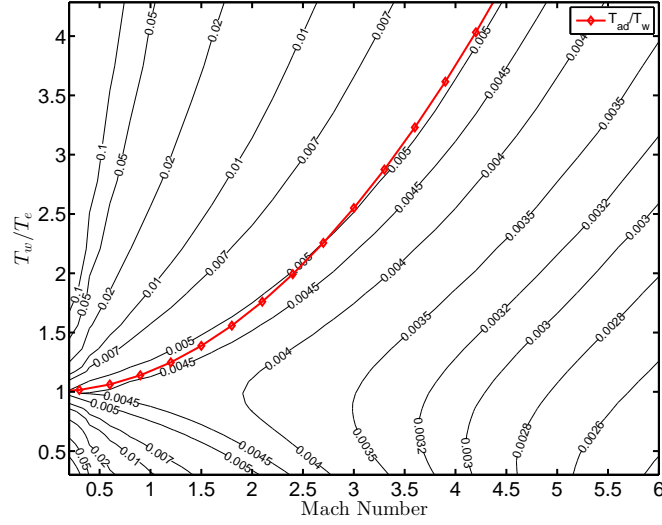


Figure 8.4: Contours of the maximum possible transient growth vs Mach number and wall temperature ratio. Contour levels represent G_{opt}/R^2 and are optimized over all values of time, α , and β . Red line with markers designates the adiabatic wall temperature. Results were calculated at $R = 300$.

minimize transient growth at higher Mach numbers. At low Mach numbers, transient growth is very sensitive to the wall temperature, and high levels of wall cooling (such as are needed to suppress modal instability) result in increased transient growth.

A means of directly comparing the net amplification of modal and non-modal instabilities is developed. This enables the relative importance of these two mechanisms to be explored in different flow regimes. For low enthalpy boundary layers, comparable amplification is observed from transient growth and modal growth, so the transition mechanism is likely to depend on the initial disturbance sources in the flow that initiate the transition process. For high enthalpy boundary layers, on the other hand, modal growth leads to several orders of magnitude larger amplification at Reynolds numbers where transition usually occurs experimentally, indicating that modal instability is dominant at these conditions. An example of this is shown in Figure 8.5, in which the N factors for transient growth (N_{opt}) and modal growth (N_{modal}) are compared. The N factor for modal growth rapidly surpasses that of transient growth and is several orders of magnitude larger at the Reynolds number $Re_x = 2 - 3$ million where transition is observed experimentally. The dominance of modal instability is caused in part by the enormous growth rate of second mode

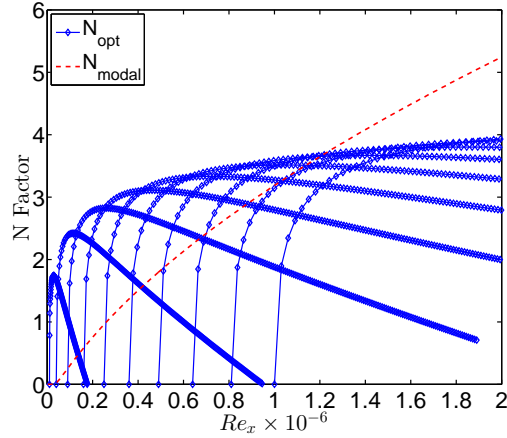


Figure 8.5: Comparison of N factors from modal and non-modal stability calculations. $M = 5.0$, $T_w/T_e = 0.3$, $T_e = 1000$ K.

waves and in part by the reduction of transient growth at higher Mach numbers.

8.3 Wave Packet Analysis

In both the modal analysis and transient growth analysis, either the frequency or the wavenumber of the disturbance is assumed to remain fixed as it travels downstream. Similarly, current state of the art methods for predicting boundary layer transition are based on the spatial growth of fixed-frequency disturbances in the downstream direction. However, experiments (Parziale, 2013, Heitmann et al., 2011, Laurence et al., 2012, 2014) and simulations (Duan and Choudhari, 2013, 2014) indicate that in conventional wind tunnel facilities, both the acoustic waves in the freestream and second mode instability waves in the boundary layer consist of localized packets of waves containing about 5-20 wavelengths. This differs from conventional spatial stability analysis, in which an infinitely long wave train of fixed-frequency waves is assumed. The downstream propagation and amplification of localized wave packets is therefore different from the amplification predicted by spatial stability analysis, yet is highly relevant for predicting boundary layer transition, since the amplitude of the disturbance wave in physical space, not frequency space, triggers the nonlinearities that lead to the breakdown into turbulence.

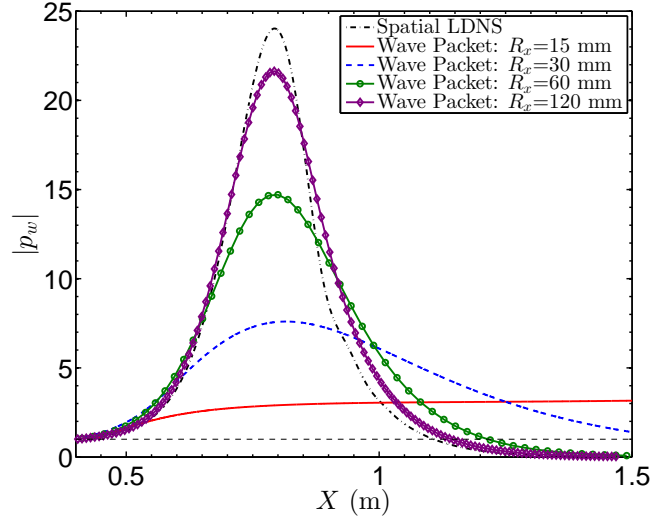


Figure 8.6: Comparison of maximum wave packet amplitude vs streamwise distance for wave packets of four different widths, as well as spatial DNS. $F = 10^{-4}$, $x_o = 0.3$ m.

In this work, linearized direct numerical simulation is used to explore the propagation of such localized instability wave packets. Three sets of simulations are conducted. First, the conventional spatial stability analysis involving fixed-frequency disturbances is conducted as a baseline against which subsequent simulations can be compared. Second, Gaussian-shaped packets of second mode waves are placed into the boundary layer as an initial condition and their downstream development is analyzed. This intentionally neglects the question of receptivity and simplifies the investigation of wave packet propagation. In the final set of simulations, receptivity is reintroduced into the problem and packets of planar acoustic waves in the freestream are caused to impinge on the boundary layer and excite second mode waves, and the downstream growth of these waves is analyzed.

All of the simulations show that finite-width wave packets experience less amplification than the prediction of spatial stability analysis. An example of this is given in Figure 8.6, in which the amplification of wave packets of several different characteristic widths R_x are compared with the prediction of spatial analysis. For wave packets that are wide in physical space (and hence narrow in frequency space), the predictions of spatial analysis are approached, but for narrow packets in physical space (small R_x), the amplification is less and the wave packet persists for a longer

distance downstream. This demonstrates that in order to predict the amplification of instability waves in physical space, it is essential that the finite width of the packet be taken into account. Wave packets appearing in experiments often consist of 5-20 individual waves, which corresponds to $R_x = 20 - 90$ mm for the conditions given in the figure. The amplification of such narrow waves is clearly over-predicted by spatial analysis, and this difference ought to be taken into account in predicting boundary layer transition.

A simple model of wave packet propagation was also proposed that makes use of locally-parallel linear stability analysis and enables wave packet dynamics to be predicted with considerably less expense than for DNS. In this simple model, the wave packet evolution is determined by summing linear stability modes over a broad range of frequencies, which is the first time that wave packet propagation has been investigated in this manner in compressible boundary layers. This simple model is found to produce comparable results to the DNS, although the simple model predicts slightly lower amplification because it excludes non-parallel terms involving the change in wave shape as it propagates downstream. Using this simple model, N factor curves have been constructed for finite-width wave packets, and it has been found that the N factors are smaller for wave packets than for conventional spatial stability analysis. The maximum N factor curves computed in this manner can be used to take finite wave packet width into account in making boundary layer transition predictions.

8.4 Future Work

The investigations of modal stability analysis and transient growth reported in this thesis provide a fairly complete picture of the linear disturbance amplification for flows over simple geometries like flat plates and sharp cones. In contrast, the wave packet analysis provided here considered only a single low enthalpy flow condition, and there is much room for exploration of higher enthalpy flows for which the second mode is further destabilized and the first mode eliminated. The simulations presented here also involve fairly small amounts of amplification of the wave packets, and higher

Reynolds number conditions where greater amplification is experienced should be simulated as well. Additionally, further characterization of nonparallel effects and inclusion of these factors in the simple wave packet model are needed.

The weak point of the e^N method employed in this thesis is the absence of receptivity analysis. Although receptivity was included in a few of the DNS cases, a general framework that ties together receptivity analysis and linear stability calculations remains undeveloped. The multiple-scales analysis described in Section 7.10 establishes the theoretical foundation needed for such receptivity studies. Although a few investigations following a similar procedure are available in the literature (Fedorov and Khokhlov, 2002, Fedorov, 2003, Fedorov et al., 2013), transition prediction models based on this type of analysis remain in their infancy. Future investigations will use this framework to study receptivity of the boundary layer to both wave packets and periodic forcing.

Bibliography

- P. H. Adam and H. G. Hornung. Enthalpy effects on hypervelocity boundary-layer transition: ground test and flight data. *Journal of Spacecraft and Rockets*, 34(5): 614–619, September 1997. [145](#)
- Paul Andersson, Martin Berggren, and Dan S. Henningson. Optimal disturbances and bypass transition in boundary layers. *Physics of Fluids (1994-present)*, 11(1): 134–150, 1999. [111](#), [125](#), [134](#)
- D. E. Ashpis and E. Reshotko. The vibrating ribbon problem revisited. *Journal of Fluid Mechanics*, 213:531–547, 1990. [147](#)
- P. Balakumar. Receptivity of supersonic boundary layers due to acoustic disturbances over blunt cones. In *Proceedings of the 37th AIAA Fluid Dynamics Conference*, Miami, FL, 25-28 June 2007. AIAA-2007-4491. [156](#), [193](#), [194](#)
- P. Balakumar. Receptivity of a supersonic boundary layer to acoustic disturbances. *AIAA Journal*, 47(5):1069–1078, 2009. [5](#), [156](#), [193](#), [194](#)
- P. Balakumar and M.R. Malik. Discrete modes and continuous spectra in supersonic boundary layers. *Journal of Fluid Mechanics*, 239:631–656, 1992. [53](#), [82](#)
- C. M. Bender and S. A. Orszag. *Advanced Mathematical Methods for Scientists and Engineers*. McGraw-Hill Book Co., New York, 1987. [55](#)
- F.P. Bertolotti. The influence of rotational and vibrational energy relaxation on boundary-layer stability. *Journal of Fluid Mechanics*, 372:93–118, 1998. [11](#)

- V. J. Bilardo, F. M. Curran, J. L. Hunt, N. T. Lovell, G. Maggio, A. W. Wilhite, and L. E. McKinney. The benefits of hypersonic airbreathing launch systems for access to space. In *Proceedings of the 39th AIAA Joint Propulsion Conference*, Huntsville, AL, July 20-23 2003. AIAA-2003-5265. [1](#)
- N. P. Bitter and J. E. Shepherd. Stability of highly-cooled hypervelocity boundary layers. *Journal of Fluid Mechanics*, 2015. Submitted 03-Feb, 2015. [69](#)
- N.P. Bitter and J.E. Shepherd. Transient growth in hypersonic boundary layers. In *Proceedings of the 7th AIAA Theoretical Fluid Mechanics Conference*, Atlanta, GA, 2014. AIAA-2014-2497. [111](#)
- G.A. Bres, M.I. Inkman, T. Colonius, and A.V. Fedorov. Second-mode attenuation and cancellation by porous coatings in a high-speed boundary layer. *Journal of Fluid Mechanics*, 726:312–337, 2013. [77](#)
- Kathryn M. Butler and Brian F. Farrell. Three-dimensional optimal perturbations in viscous shear flow. *Physics of Fluids A: Fluid Dynamics (1989-1993)*, 4(8): 1637–1650, 1992. [111](#), [125](#), [134](#), [135](#)
- M. Camac. CO₂ relaxation processes in shock waves. In J.G. Hall, editor, *Fundamental Phenomena in Hypersonic Flow*, pages 195–215. Cornell Univ. Press, Ithaca, NY, 1966. [22](#), [40](#)
- Claudio Canuto, M. Yousuff Hussaini, Alfio Quarteroni, and Thomas A. Zang. *Spectral Methods in Fluid Dynamics*. Springer-Verlag, New York, 1988. [37](#), [51](#)
- K. M. Casper, S. J. Beresh, and S. P. Schneider. Characterization of controlled perturbations in a hypersonic boundary layer. In *Proceedings of the 50th AIAA Aerospace Sciences Meeting*, Nashville, TN, January 2012a. AIAA-2012-0281. [154](#)
- K. M. Casper, S. J. Beresh, and S. P. Schneider. A preliminary study of the longitudinal merging of instability wave packets and turbulent spots in a hypersonic boundary layer. In *Proceedings of the 42nd AIAA Fluid Dynamics Conference*, New Orleans, LA, June 2012b. AIAA-2012-3148. [154](#)

- K. M. Casper, S. J. Beresh, J. F. Henfling, R. W. Spillers, and B. O. M. Pruett. High-speed schlieren imaging of disturbances in a transitional hypersonic boundary layer. In *Proceedings of the 51st AIAA Aerospace Sciences Meeting*, Grapevine, TX, 2013a. AIAA-2013-0376. [12](#), [154](#)
- K. M. Casper, S. J. Beresh, R. M. Wagnild, J. F. Henfling, R. W. Spillers, and B. O. M. Pruett. Simultaneous pressure measurements and high-speed schlieren imaging of disturbances in a transitional hypersonic boundary layer. In *Proceedings of the 43rd AIAA Fluid Dynamics Conference*, San Diego, CA, 2013b. AIAA-2013-2739. [12](#), [154](#)
- K. M. Casper, S. J. Beresh, and S. P. Schneider. Pressure fluctuations beneath instability wavepackets and turbulent spots in a hypersonic boundary layer. *Journal of Fluid Mechanics*, 756:1058–1091, 2014. [154](#)
- C.L. Chang, M.R. Malik, and M.Y. Hussaini. Effects of shock on the stability of hypersonic boundary layers. In *Proceedings of the 21st AIAA Fluid Dynamics, Plasma Dynamics, and Lasers Conference*, Seattle, WA, 1990. AIAA-90-1448. [65](#)
- C.L. Chang, H. Vinh, and M.R. Malik. Hypersonic boundary-layer stability with chemical reactions using PSE. In *Proceedings of the 28th AIAA Fluid Dynamics Conference*, Snowmass Village, CO, 1997. AIAA-97-2012. [78](#)
- Boa-Teh Chu. On the energy transfer to small disturbances in fluid flow (part i). *Acta Mechanica*, 1(3):215–234, 1965. [118](#), [119](#), [120](#)
- J.F. Clarke and M. McChesney. *The Dynamics of Real Gases*. Butterworth, London, 1964. [95](#), [106](#)
- J. Cohen. The initial evolution of a wave packet in a laminar boundary layer. *Physics of Fluids*, 6(3):1133–1143, March 1994. [12](#), [153](#)
- J. Cohen, K. S. Breuer, and J. H. Haritonidis. On the evolution of a wave packet in a laminar boundary layer. *Journal of Fluid Mechanics*, 225:575–606, 1991. [12](#), [153](#)

- W.A. Cole and W.A. Wakeham. The viscosity of nitrogen, oxygen, and their binary mixtures in the limit of zero density. *Journal of physical and chemical reference data*, 14(1):209–226, 1985. [23](#)
- S.D. Conte. The numerical solution of linear boundary value problems. *SIAM Review*, 8(3):309–321, July 1966. [59](#)
- Peter Corbett and Alessandro Bottaro. Optimal perturbations for boundary layers subject to stream-wise pressure gradient. *Physics of Fluids (1994-present)*, 12(1):120–130, 2000. [112](#), [128](#), [134](#), [135](#)
- W.O. Criminale, T.L. Jackson, D.G. Lasseigne, and R.D. Joslin. Perturbation dynamics in viscous channel flows. *Journal of Fluid Mechanics*, 339:55–75, 1997. [114](#)
- A. Davey. An automatic orthonormalization method for solving stiff boundary-value problems. *Journal of Computational Physics*, 51(2):343–356, August 1983. [59](#)
- Defense Science Board. Report of the Defense Science Board task force on the National Aerospace Plane (NASP). Technical Report AD-A201 124, Office of the Secretary of Defense, 1988. [2](#)
- Defense Science Board. Report of the Defense Science Board task force on the National Aero-Space Plane (NASP) program. Technical Report AD-A274 530, Office of the Secretary of Defense, 1992. [2](#)
- A. Demetriades. Laminar boundary layer stability measurements at Mach 7 including wall temperature effects. Technical Report AFOSR-TR-77-1311, U.S. Air Force Office of Scientific Research, 1977. [87](#)
- L. Duan and M. M. Choudhari. Numerical study of pressure fluctuations due to a Mach 6 turbulent boundary layer. In *Proceedings of the 51st AIAA Aerospace Sciences Meeting*, Grapevine, TX, 2013. AIAA-2013-0532. [148](#), [228](#)

- L. Duan and M. M. Choudhari. Analysis of numerical simulation database for pressure fluctuations induced by high-speed turbulent boundary layers. In *Proceedings of the 44th AIAA Fluid Dynamics Conference*, Atlanta, GA, 2014. AIAA-2014-2912. [148](#), [228](#)
- N. M. El-Hady. Nonparallel instability of supersonic and hypersonic boundary layers. *Physics of Fluids*, 3(9):2164–2178, 1991. [204](#)
- T. Ellingsen and E. Palm. Stability of linear flow. *Physics of Fluids*, 18(4):487–488, April 1975. [11](#)
- F. G. Ergin and E. B. White. Unsteady and transitional flows behind roughness elements. *AIAA Journal*, 44(11):2504–2514, November 2006. [12](#)
- B.F. Farrell. Optimal excitation of perturbations in viscous shear flow. *Physics of Fluids*, 31(8):2093–2102, 1988. [128](#)
- H. Fasel and U. Konzelmann. Non-parallel stability of a flat-plate boundary layer using the complete Navier-Stokes equations. *Journal of Fluid Mechanics*, 221:311–347, 1990. [176](#)
- A. Fedorov and A. Khokhlov. Prehistory of instability in a hypersonic boundary layer. *Theoretical and Computational Fluid Dynamics*, 14(6):359–375, 2001. [49](#), [70](#), [82](#), [83](#), [204](#), [212](#), [213](#)
- A. Fedorov and A. Tumin. Initial-value problem for hypersonic boundary-layer flows. *AIAA Journal*, 41(3):379–389, March 2003. [5](#), [204](#), [208](#), [210](#)
- A. Fedorov and A. Tumin. High-speed boundary-layer instability: Old terminology and a new framework. *AIAA Journal*, 49(8):1647–1657, August 2011. [64](#), [71](#), [76](#), [82](#)
- A. V. Fedorov. Receptivity of a high-speed boundary layer to acoustic disturbances. *Journal of Fluid Mechanics*, 491:101–129, 2003. [4](#), [5](#), [156](#), [193](#), [204](#), [231](#)

- A. V. Fedorov and A. P. Khokhlov. Excitation of unstable modes in a supersonic boundary layer by acoustic waves. *Fluid Dynamics*, 9:456–467, 1991. [4](#), [5](#)
- A. V. Fedorov and A. P. Khokhlov. Excitation and evolution of unstable disturbances in supersonic boundary layer. In *Proceedings of the 1993 ASME Fluid Engineering Conference*, Washington, DC, June 20-24 1993. FED-Vol. 151. [4](#), [5](#), [156](#), [193](#)
- A. V. Fedorov and A. P. Khokhlov. Receptivity of hypersonic boundary layer to wall disturbances. *Theoretical and Computational Fluid Dynamics*, 15:231–254, 2002. [204](#), [231](#)
- A. V. Fedorov, G. A. Bres, M. Inkman, and T. Colonius. Instability of hypersonic boundary layer on a wall with resonating micro-cavities. In *Proceedings of the 49th AIAA Aerospace Sciences Meeting*, Orlando, FL, 2011. AIAA-2011-373. [77](#)
- A. V. Fedorov, V. G. Soudakov, and I. A. Leyva. Stability analysis of high-speed boundary-layer flow with gas injection. In *Proceedings of the 7th AIAA Theoretical Fluid Mechanics Conference*, Atlanta, GA, 2014. AIAA-2014-2498. [77](#)
- Alexander Fedorov. Transition and stability of high-speed boundary layers. *Annual Review of Fluid Mechanics*, 43(1):79–95, 2011. [3](#), [9](#)
- A.V. Fedorov, A.A. Ryzhov, V.G. Soudakov, and S.V. Utyuzhnikov. Receptivity of a high-speed boundary layer to temperature spottiness. *Journal of Fluid Mechanics*, 722:533–553, 2013. [5](#), [83](#), [204](#), [231](#)
- E. Forgoston and A. Tumin. Initial-value problem for three-dimensional disturbances in a compressible boundary layer. *Physics of Fluids*, 17(8):084106, 2005. [204](#), [210](#)
- E. Forgoston and A. Tumin. Three-dimensional wave packets in a compressible boundary layer. *Physics of Fluids*, 18(10):104103, 2006. [13](#), [153](#), [204](#)
- K. Fujii and H.G. Hornung. A procedure to estimate the absorption rate of sound propagating through high temperature gas. Technical Report FM 2001.004, GALCIT, August 2001. [106](#)

- K. Fujii and H.G. Hornung. Experimental investigation of high-enthalpy effects on attachment-line boundary-layer transition. *AIAA Journal*, 41(7):1282–1291, July 2003. [67](#), [95](#), [97](#)
- V.K. Garg. Improved shooting techniques for linear boundary value problems. *Computer Methods in Applied Mechanics and Engineering*, 22(1):87–99, April 1980. [59](#)
- M. Gaster. A note on the relation between temporally-increasing and spatially-increasing disturbances in hydrodynamic stability. *Journal of Fluid Mechanics*, 14:222–224, 1962. [114](#), [147](#)
- M. Gaster. A theoretical model of a wave packet in the boundary layer on a flat plate. *Proceedings of the Royal Society of London, A*, 347:271–289, 1975. [13](#), [151](#)
- M. Gaster. Estimates of the errors incurred in various asymptotic representations of wave packets. *Journal of Fluid Mechanics*, 121:365–377, 1982a. [13](#), [153](#)
- M. Gaster. The development of a two-dimensional wavepacket in a growing boundary layer. *Proceedings of the Royal Society of London A*, 384:317–332, 1982b. [13](#), [153](#)
- M. Gaster and I. Grant. An experimental investigation of the formation and development of a wave packet in a laminar boundary layer. *Proceedings of the Royal Society of London, A*, 347:253–269, 1975. [12](#), [151](#), [189](#)
- M. E. Goldstein. The evolution of Tollmien-Schlichting waves near a leading edge. *Journal of Fluid Mechanics*, 127:59–81, 1983. [4](#)
- M. E. Goldstein. Scattering of acoustic waves onto Tollmien-Schlichting waves by small streamwise variations in surface geometry. *Journal of Fluid Mechanics*, 154:509–529, 1985. [4](#)
- D. G. Goodwin. An open-source, extensible software suite for CVD process simulation. In M. Allendorf, F. Maury, and F. Teyssandier, editors, *Proceedings of Chemical Vapor Deposition XVI and EuroCVD Fourteen*, 2003. [17](#), [23](#)

- Ardeshir Hanifi and Dan S. Henningson. The compressible inviscid algebraic instability for streamwise independent disturbances. *Physics of Fluids*, 10(8):1784–1786, 1998. [113](#), [131](#), [145](#)
- Ardeshir Hanifi, Peter J. Schmid, and Dan S. Henningson. Transient growth in compressible boundary layer flow. *Physics of Fluids*, 8(3):826–837, 1996. [112](#), [113](#), [118](#), [120](#), [121](#), [122](#), [123](#), [125](#)
- D. Heitmann, R. Radespiel, and H. Knauss. Experimental study of Mach 6 boundary layer response to laser generated disturbances. In *Proceedings of the 41st AIAA Fluid Dynamics Conference*, Honolulu, HI, June 2011. AIAA-2011-3876. [12](#), [13](#), [149](#), [154](#), [228](#)
- D. Heitmann, N. Parziale, J. E. Shepherd, and N. P. Bitter. Comparative hypersonic boundary layer instability measurements with laser differential interferometer and pressure sensors on a 7° half-angle cone. *AIAA Journal*, 2015. (In preparation). [92](#)
- J. Hilsenrath. Tables of thermodynamic and transport properties. *Circular of the National Bureau of Standards*, 1955. [23](#)
- M. L. Hudson, N. Chokani, and G. V. Candler. Linear stability of hypersonic flow in thermochemical nonequilibrium. *AIAA Journal*, 35(6):958–964, June 1997. [11](#)
- Lennart S. Hultgren and L. Hkan Gustavsson. Algebraic growth of disturbances in a laminar boundary layer. *Physics of Fluids (1958-1988)*, 24(6):1000–1004, 1981. [11](#), [111](#)
- H.B. Johnson, T.G. Seipp, and G.V. Candler. Numerical study of hypersonic reacting boundary layer transition on cones. *Physics of Fluids*, 10(10):2676–2685, October 1998. [11](#), [38](#), [64](#), [100](#)
- Heath B. Johnson. *Thermochemical Interactions in Hypersonic Boundary Layer Stability*. PhD thesis, University of Minnesota, July 2000. [38](#), [64](#)

- T. J. Juliano, S. P. Schneider, S. Aradag, and D. Knight. Quiet-flow Ludwig tube for hypersonic transition research. *AIAA Journal*, 46(7):1757–1763, July 2008. [222](#)
- K. Kadoya, N. Matsunaga, and A. Nagashima. Viscosity and thermal conductivity of dry air in the gaseous phase. *Journal of Physical and Chemical Reference Data*, 14(4):947–970, 1985. [23](#), [24](#)
- J. M. Kendall. Wind tunnel experiments relating to supersonic and hypersonic boundary-layer transition. *AIAA Journal*, 13(3):290–295, 1975. [69](#), [169](#)
- J. Klentzman and A. Tumin. Stability and receptivity of high speed boundary layers in oxygen. In *Proceedings of the 43rd AIAA fluid dynamics conference*, San Diego, CA, 2013. AIAA2013-2882. [77](#)
- E.B. Klunker and F.E. McLean. Effect of thermal properties on laminar-boundary-layer characteristics. Technical Report NACA TN-2916, National Advisory Committee for Aeronautics, 1953. [34](#), [35](#)
- M. T. Landahl. Dynamics of boundary layer turbulence and the mechanism of drag reduction. *Physics of Fluids (1958-1988)*, 20(10):S55–S63, 1977. [112](#), [125](#)
- M.T. Landahl. A note on an algebraic instability of inviscid parallel shear flows. *Journal of Fluid Mechanics*, 98(2):243–251, 1980. [11](#), [112](#), [125](#)
- D.G. Lasseigne, R.D. Joslin, T.L. Jackson, and W.O. Criminale. The transient period for boundary layer disturbances. *Journal of Fluid Mechanics*, 381:89–119, 1999. [114](#)
- K.Y. Lau. Hypersonic boundary-layer transition: Application to high-speed vehicle design. *Journal of Spacecraft and Rockets*, 45(2):176–183, 2008. [1](#)
- J. Laufer. Some statistical properties of the pressure field radiated by a turbulent boundary layer. *Physics of fluids*, 7(8):1191–1197, August 1964. [148](#)
- J. Laufer, J. Williams, and S. Childress. Mechanism of noise generation in the turbulent boundary layer. Technical report, North Atlantic Treaty Organization, November 1964. AGARD-AG-90. [148](#)

- S. J. Laurence, A. Wagner, and K. Hannemann. Time-resolved visualization of instability waves in a hypersonic boundary layer. *AIAA Journal*, 50(1):243–246, January 2012. [12](#), [228](#)
- S. J. Laurence, A. Wagner, H. Ozawa, J. M. Schramm, and K. Hannemann. Visualization of a hypersonic boundary-layer transition on a slender cone. In *Proceedings of the 19th AIAA International Space Planes and Hypersonic Systems and Technologies Conference*, Atlanta, GA, 2014. AIAA-2014-3110. [12](#), [93](#), [228](#)
- L. Lees. The stability of the laminar boundary layer in a compressible fluid. Technical Report 876, National Advisory Committee for Aeronautics, 1947. [8](#)
- L. Lees and C.C. Lin. Investigation of the stability of the laminar boundary layer in a compressible fluid. Technical Report TN-1115, National Advisory Committee for Aeronautics, 1946. [7](#), [80](#)
- L. Lees and E. Reshotko. Stability of the compressible laminar boundary layer. *Journal of Fluid Mechanics*, 12:555–590, 1962. [80](#)
- M.J. Lighthill. Viscosity effects in sound waves of finite amplitude. In G.K. Batchelor and R.M. Davies, editors, *Surveys in Mechanics*, pages 250–351. Cambridge University Press, Cambridge, 1956. [95](#)
- C. C. Lin. On the stability of two-dimensional parallel flows. *Proceedings of the National Academy of Sciences*, 30(10):316–324, 1944. [7](#), [8](#)
- T.C. Lin. Influence of laminar boundary-layer transition on entry vehicle designs. *Journal of Spacecraft and Rockets*, 45(2):165–175, 2008. [1](#)
- Paolo Luchini. Reynolds-number-independent instability of the boundary layer over a flat surface. *Journal of Fluid Mechanics*, 327:101–115, 1996. [112](#)
- Paolo Luchini. Reynolds-number-independent instability of the boundary layer over a flat surface: optimal perturbations. *Journal of Fluid Mechanics*, 404:289–309, 2000. [112](#)

- Y. Ma and X. Zhong. Receptivity of a supersonic boundary layer over a flat plate. Part 1. wave structures and interactions. *Journal of Fluid Mechanics*, 488:31–78, 2003a. [5](#), [69](#), [70](#), [72](#), [169](#), [173](#), [174](#), [175](#), [193](#)
- Y. Ma and X. Zhong. Receptivity of a supersonic boundary layer over a flat plate. Part 2. receptivity to free-stream sound. *Journal of Fluid Mechanics*, 488:79–121, 2003b. [5](#), [156](#), [193](#)
- Y. Ma and X. Zhong. Receptivity of a supersonic boundary layer over a flat plate. Part 3. effects of different types of free-stream disturbances. *Journal of Fluid Mechanics*, 532:63–109, 2005. [5](#), [193](#)
- L. Mack. Boundary-layer linear stability theory. In *AGARD Report No. 709*. North Atlantic Treaty Organization, 1984. [8](#), [85](#), [86](#), [102](#), [111](#), [224](#)
- L. M. Mack. Computations of the stability of the laminar compressible boundary layer. In B. Alder, S. Fernback, and M. Rotenberg, editors, *Methods in Computational Physics*, volume 4, pages 247–299. Academic Press, New York, 1965. [54](#), [111](#)
- L. M. Mack. Boundary layer stability theory. Technical Report JPL Report 900-277, Jet Propulsion Lab, California Institute of Technology, 1969. [8](#), [78](#), [80](#), [85](#), [111](#), [118](#), [120](#), [224](#)
- L. M. Mack. Transition and laminar instability. Technical report, Jet Propulsion Laboratory, Pasadena, CA, 1977. NACA-CP-153203. [7](#)
- L.M. Mack. Linear stability theory and the problem of supersonic boundary-layer transition. *AIAA Journal*, 13(3):278–289, 1975. [8](#)
- L.M. Mack. *Review of Linear Compressible Stability Theory*, pages 164–187. Springer-Verlag, New York, 1987. [8](#), [78](#)
- M. R. Malik. Stability theory for chemically reacting flows. In D. Arnal and

- R. Michel, editors, *Laminar-Turbulent Transition*, pages 251–260. IUTAM Symposium Toulouse/France, September 1989. [85](#)
- M. R. Malik. Numerical methods for hypersonic boundary layers. *Journal of Computational Physics*, 86:376–413, 1990. [52](#), [123](#), [159](#), [258](#), [262](#)
- M. R. Malik and P. Balakumar. Acoustic receptivity of Mach 4.5 boundary layer with leading-edge bluntness. *Theoretical and Computational Fluid Dynamics*, 21:323–342, 2007. [156](#), [194](#)
- M.R. Malik and E.C. Anderson. Real gas effects on hypersonic boundary-layer stability. *Physics of Fluids*, 3(5):803–821, 1991. [44](#)
- E. C. Marineau, G. Moraru, D. R. Lewis, J. D. Norris, J. F. Lafferty, R. M. Wagnild, and J. A. Smith. Mach 10 boundary-layer transition experiments on sharp and blunted cones. In *Proceedings of the 19th AIAA International Space Planes and Hypersonic Systems and Technologies Conference*, Atlanta, GA, 2014. AIAA-2014-3108. [88](#), [92](#)
- J.A. Masad, A.H. Nayfeh, and A.A. Al-Maaitah. Effect of heat transfer on the stability of compressible boundary layers. *Computers and Fluids*, 21(1):43–61, 1992. [8](#), [85](#), [86](#), [224](#)
- C. S. Mayer, A. C. Laible, and H. F. Fasel. Numerical investigation of wave packets in a mach 3.5 cone boundary layer. *AIAA Journal*, 49(1):67–85, 2011. [13](#), [153](#), [185](#)
- J. F. McKenzie and K. O. Westphal. Interaction of linear waves with oblique shock waves. *Physics of Fluids*, 11(11):2350–2362, 1968. [4](#), [156](#)
- D.A. McQuarrie. *Statistical Mechanics*. Harper Collins, New York, 1976. [20](#)
- M. Medeiros and M. Gaster. The influence of phase on the nonlinear evolution of wavepackets in boundary layers. *Journal of Fluid Mechanics*, 397:259–283, 1999. [153](#)

- R.C. Millikan and D.R. White. Systematics of vibrational relaxation. *Journal of Chemical Physics*, 139(12):3209–3213, December 1963. [21](#), [22](#), [40](#)
- M.V. Morkovin, E. Reshotko, and T. Herbert. Transition in open flow systems – a reassessment. *Bulletin of the American Physical Society*, 39:1882, 1994. [3](#)
- A. H. Nayfeh. Stability of three-dimensional boundary layers. *AIAA Journal*, 18(4):406–416, 1980. [49](#), [73](#), [204](#), [210](#), [211](#), [253](#)
- A. H. Nayfeh. *Introduction to Perturbation Techniques*. John Wiley & Sons, New York, 1993. [210](#), [211](#)
- I. Nompelis, G. V. Candler, and M. S. Holden. Effect of vibrational nonequilibrium on hypersonic double-cone experiments. *AIAA Journal*, 41(11):2162–2169, November 2003. [28](#)
- C. Park. *Nonequilibrium Hypersonic Aerothermodynamics*. John Wiley & Sons, New York, 1990. [18](#), [21](#)
- N. Parziale. *Slender-Body Hypervelocity Boundary-Layer Instability*. PhD thesis, California Institute of Technology, 2013. [12](#), [92](#), [149](#), [228](#)
- T. J. Poinso and S. K. Lele. Boundary conditions for direct simulations of compressible viscous flows. *Journal of computational physics*, 101:104–129, 1992. [163](#)
- Lord Rayleigh. On the stability, or instability, of certain fluid motions. *Proceedings of the London Mathematical Society*, s1-11(1):57–72, 1879. [7](#)
- Lord Rayleigh. On the stability, or instability, of certain fluid motions. *Proceedings of the Mathematical Society of London*, 11:57–70, 1880. [7](#)
- Satish C. Reddy and Dan S. Henningson. Energy growth in viscous channel flows. *Journal of Fluid Mechanics*, 252:209–238, 1993. [112](#)
- E Reshotko. Boundary-layer stability and transition. *Annual Review of Fluid Mechanics*, 8(1):311–349, 1976. [5](#), [111](#)

- E. Reshotko. Transient growth: A factor in bypass transition. *Physics of Fluids*, 13(5):1067–1075, May 2001. [6](#)
- E. Reshotko and A. Tumin. Role of transient growth in roughness-induced transition. *AIAA Journal*, 42(4):766–770, April 2004. [113](#), [131](#), [145](#)
- W. S. Saric, H. L. Reed, and E. J. Kerschen. Boundary-layer receptivity to freestream disturbances. *Annual Review of Fluid Mechanics*, 34:291–319, 2002. [4](#)
- H. Schlichting and K. Gersten. *Boundary Layer Theory*. Springer, eighth edition, 2000. [26](#), [33](#), [43](#), [45](#), [49](#), [107](#)
- P.J. Schmid. Nonmodal stability theory. *Annual Review of Fluid Mechanics*, 39:129–162, 2007. [128](#)
- P.J. Schmid and D.S. Henningson. Optimal energy density growth in Hagen-Poiseuille flow. *Journal of Fluid Mechanics*, 277:197–225, 1994. [122](#)
- P.J. Schmid and D.S. Henningson. *Stability and Transition in Shear Flows*. Springer, New York, 2001. [11](#), [112](#)
- S. P. Schneider. Hypersonic laminar instability on round cones near zero angle of attack. Technical report, NATO Research and Technology Organization, RTO-AVT-007-V3, pp. 1-1-24, 2006. [93](#)
- S. P. Schneider. Developing mechanism-based methods for estimating hypersonic boundary-layer transition in flight: The role of quiet tunnels. *Progress in Aerospace Science*, 72:17–29, 2015. [5](#), [75](#), [222](#)
- S.P. Schneider. Effects of high-speed tunnel noise on laminar-turbulent transition. *Journal of Spacecraft and Rockets*, 38(3):323–333, May 2001. [5](#)
- G. B. Schubauer and H. K. Skramstad. Laminar boundary-layer oscillations and stability of laminar flow. *Journal of the Aeronautical Sciences*, 14(2):69–78, 1947. [7](#), [148](#), [189](#)

- J. Sivasubramanian and H. F. Fasel. Numerical investigation of the development of three-dimensional wavepackets on a sharp cone boundary layer at Mach 6. *Journal of Fluid Mechanics*, 756:600–649, 2014. [13](#), [153](#), [155](#), [185](#)
- A. M. Smith and N. Gamberoni. Transition, pressure gradient and stability theory. Technical Report ES-26388, Douglas Aircraft Company, 1956. [74](#)
- K. F. Stetson. Hypersonic boundary layer transition experiments. Technical Report AFWAL-TR-80-3062, Air Force Wright Aeronautical Laboratories, 1980. [93](#)
- K. F. Stetson, E. R. Thompson, J. C. Donaldson, and L. G. Siler. Laminar boundary layer stability experiments on a cone at Mach 8, Part 1: sharp cone. In *Proceedings of the 16th AIAA Fluid and Plasma Dynamics Conference*, Danvers, MA, July 1983. AIAA-83-1761. [87](#), [93](#)
- K. F. Stetson, E. R. Thompson, J. C. Donaldson, and L. G. Siler. Laminar boundary layer stability experiments on a cone at Mach 8, Part 2: blunt cone. In *Proceedings of the 22nd AIAA Aerospace Sciences Meeting*, Reno, NV, January 9-12 1984. AIAA-84-0006. [93](#)
- M. E. Tauber, G. P. Menees, and H. G. Adelman. Aerothermodynamics of transatmospheric vehicles. *Journal of Aircraft*, 24(9):594–602, 1987. [1](#)
- R.L. Taylor and S. Bitterman. Survey of vibrational relaxation data for processes important in the CO₂-N₂ laser system. *Reviews of Modern Physics*, 41(1):26–47, January 1969. [20](#), [21](#)
- D. Tempelmann, A. Hanifi, and D.S. Henningson. Spatial optimal growth in three-dimensional compressible boundary layers. *Journal of Fluid Mechanics*, 704:251–279, August 2012. [112](#), [113](#), [114](#), [127](#)
- David Tempelmann, Ardeshir Hanifi, and Dan S. Henningson. Spatial optimal growth in three-dimensional boundary layers. *Journal of Fluid Mechanics*, 646:5–37, 2010. [112](#)

- K. W. Thompson. Time dependent boundary conditions for hyperbolic systems. *Journal of Computational Physics*, 68(1):1–24, 1987. [163](#), [165](#)
- W. Tollmien. General instability criterion of laminar velocity distributions. Technical Report 792, National Advisory Committee for Aeronautics, 1936. [7](#)
- L.N. Trefethen, A.E. Trefethen, S.C. Reddy, and T.A. Driscoll. Hydrodynamic stability without eigenvalues. *Science*, 261(5121):578–584, 1993. [6](#), [11](#), [111](#), [117](#)
- R. D. Trengove and W. A. Wakeham. The viscosity of carbon dioxide, methane, and sulfur hexafluoride in the limit of zero density. *Journal of Physical and Chemical Reference Data*, 16(2):175–187, 1987. [23](#)
- A. Tumin. Three-dimensional spatial normal modes in compressible boundary layers. *Journal of Fluid Mechanics*, 586:295–322, 2007. [54](#)
- A. Tumin and E. Reshotko. Spatial theory of optimal disturbances in boundary layers. *Physics of Fluids*, 13(7):2097–2104, July 2001. [112](#), [113](#), [121](#), [123](#), [124](#), [125](#), [144](#)
- A. Tumin and E. Reshotko. Optimal disturbances in compressible boundary layers. *AIAA Journal*, 41(12):2357–2363, December 2003. [112](#), [113](#), [117](#), [125](#), [131](#), [134](#), [144](#)
- E.R. Van Driest. Calculation of the stability of the laminar boundary layer in a compressible fluid on a flat plate with heat transfer. *Journal of the Aeronautical Sciences*, 19(12):801–812, 1952. [8](#)
- W. G. Vincenti and C. H. Kruger. *Introduction to Physical Gas Dynamics*. John Wiley and Sons, New York, 1967. [18](#), [20](#), [22](#), [95](#), [102](#), [106](#)
- C. A. Ward, B. M. Wheaton, A. Chou, P. L. Gilbert, L. E. Steen, and S. P. Schneider. Boundary-layer transition measurements in a Mach-6 quiet tunnel. In *Proceedings of the 40th AIAA Fluid Dynamics Conference*, June 2010. AIAA-2010-4721. [222](#)
- E. B. White. Transient growth of stationary disturbances in a flat plate boundary layer. *Physics of Fluids*, 14(12):4429–4439, December 2002. [12](#)

- E. B. White, J. M. Rice, and F. G. Ergin. Receptivity of stationary transient disturbances to surface roughness. *Physics of Fluids*, 17:064109, 2005. [12](#)
- F.M. White. *Viscous Fluid Flow*. McGraw-Hill, New York, 1974. [1](#), [23](#), [24](#), [43](#), [45](#), [107](#)
- C.R. Wilke. A viscosity equation for gas mixtures. *Journal of Chemical Physics*, 18(4):517–519, April 1950. [22](#)
- M.J. Wright, G.V. Candler, and D. Bose. Data-parallel line relaxation method for the Navier-Stokes equations. *AIAA Journal*, 36(9):1603–1609, September 1998. [38](#), [64](#)
- X. Zhong. High-order finite-difference schemes for numerical simulation of hypersonic boundary-layer transition. *Journal of computational physics*, 144:662–709, 1998. [159](#)
- X. Zhong and Y. Ma. Boundary-layer receptivity of Mach 7.99 flow over a blunt cone to free-stream acoustic waves. *Journal of Fluid Mechanics*, 556:55–103, 2006. [5](#)
- S. Zuccher and A. Tumin. Optimal disturbances in compressible boundary layers – complete energy norm analysis. In *Proceedings of the 4th AIAA Theoretical Fluid Mechanics Meeting*, Toronto, Ontario Canada, 2005. AIAA-2005-5314. [120](#)
- S. Zuccher, A. Tumin, and E. Reshotko. Parabolic approach to optimal perturbations in compressible boundary layers. *Journal of Fluid Mechanics*, 556:189–216, June 2006. [112](#)

Appendices

Appendix A

Stability Equations

In this appendix the linear stability equations with vibrational energy exchange are derived. The objective is to reduce the linearized Navier-Stokes equations to one of several forms. For the “global” stability analysis, in which all the eigenvalues are found simultaneously, the desired form is a set of six second-order differential equations:

$$\left(\mathbf{A} \frac{\partial^2}{\partial y^2} + \mathbf{B} \frac{\partial}{\partial y} + \mathbf{C} \right) \mathbf{q} = 0 \quad (\text{A.1})$$

where \mathbf{A} , \mathbf{B} , and \mathbf{C} are 6×6 matrices and $\mathbf{q} = \left(\hat{u}, \hat{v}, \hat{p}, \hat{\theta}, \hat{w}, \hat{\theta}_v \right)^T$. For “local” stability analysis, in which a single eigenvalue is found with high accuracy, the preferred form of the equations is a set of ten first order differential equations:

$$\frac{\partial \mathbf{q}}{\partial y} = \mathbf{a} \mathbf{q} \quad (\text{A.2})$$

where \mathbf{a} is a 10×10 matrix and here \mathbf{q} is the vector

$$\mathbf{q} = \left(\hat{u}, \frac{\partial \hat{u}}{\partial y}, \hat{v}, \hat{p}, \hat{\theta}, \frac{\partial \hat{\theta}}{\partial y}, \hat{w}, \frac{\partial \hat{w}}{\partial y}, \hat{\theta}_v, \frac{\partial \hat{\theta}_v}{\partial y} \right)^T \quad (\text{A.3})$$

A.1 General Linearized Stability Equations

Starting with the compressible Navier-Stokes equations (2.14), one can assume fluctuations of the following form:

$$\begin{aligned}
 u &= \bar{U} + \tilde{u} & v &= \bar{V} + \tilde{v} & w &= \bar{W} + \tilde{w} \\
 p &= \bar{P} + \tilde{p} & \rho &= \bar{\rho} + \tilde{\rho} & T &= \bar{T} + \tilde{\theta} \\
 T_v &= \bar{T}_v + \tilde{\theta}_v & \mu &= \bar{\mu} + \tilde{\mu} & k &= \bar{k} + \tilde{k} \\
 k_v &= \bar{k}_v + \tilde{k}_v & Q &= \bar{Q} + \tilde{Q}
 \end{aligned}$$

where overbars signify mean flow variables and a tilde designates fluctuations. The fluctuations in viscosity, thermal conductivity, and vibrational source term are related to the fluctuations in temperature and pressure:

$$\tilde{\mu} = \frac{\partial \mu}{\partial T} \tilde{\theta} \quad (\text{A.4a})$$

$$\tilde{k} = \frac{\partial k}{\partial T} \tilde{\theta} \quad (\text{A.4b})$$

$$\tilde{k}_v = \frac{\partial k_v}{\partial T} \tilde{\theta} + \frac{\partial k_v}{\partial T_v} \tilde{\theta}_v \quad (\text{A.4c})$$

$$\tilde{Q} = \frac{\partial Q}{\partial T} \tilde{\theta} + \frac{\partial Q}{\partial T_v} \tilde{\theta}_v + \frac{\partial Q}{\partial p} \tilde{p} \quad (\text{A.4d})$$

where all partial derivatives are evaluated at the conditions of the mean flow. We also define the mean and fluctuating viscous stresses:

$$\begin{aligned}
 \bar{\tau}_{ij} &= \bar{\mu} \left(\frac{\partial \bar{U}_i}{\partial x_j} + \frac{\partial \bar{U}_j}{\partial x_i} + r \delta_{ij} \frac{\partial \bar{U}_k}{\partial x_k} \right) \\
 \tilde{\tau}_{ij} &= \bar{\mu} \left(\frac{\partial \tilde{u}_i}{\partial x_j} + \frac{\partial \tilde{u}_j}{\partial x_i} + r \delta_{ij} \frac{\partial \tilde{u}_k}{\partial x_k} \right) + \tilde{\mu} \left(\frac{\partial \bar{U}_i}{\partial x_j} + \frac{\partial \bar{U}_j}{\partial x_i} + r \delta_{ij} \frac{\partial \bar{U}_k}{\partial x_k} \right)
 \end{aligned}$$

where δ_{ij} is the Kronecker delta and r is the ratio of the second viscosity coefficient to the shear viscosity; in this work $r = -2/3$ is assumed in accordance of Stokes' hypothesis of zero bulk viscosity; however, it should be noted that some of the effects of nonzero bulk viscosity are retained through the explicit modeling of vibrational

nonequilibrium. After replacing the variables in Equation 2.14 by the perturbations above and linearizing, the result is:

Continuity:

$$\begin{aligned} \frac{\partial \tilde{\rho}}{\partial t} + \bar{U} \frac{\partial \tilde{\rho}}{\partial x} + \bar{V} \frac{\partial \tilde{\rho}}{\partial y} + \bar{W} \frac{\partial \tilde{\rho}}{\partial z} + \tilde{u} \frac{\partial \bar{\rho}}{\partial x} + \tilde{v} \frac{\partial \bar{\rho}}{\partial y} + \tilde{w} \frac{\partial \bar{\rho}}{\partial z} \\ + \tilde{\rho} \left(\frac{\partial \bar{U}}{\partial x} + \frac{\partial \bar{V}}{\partial y} + \frac{\partial \bar{W}}{\partial z} \right) + \bar{\rho} \left(\frac{\partial \tilde{u}}{\partial x} + \frac{\partial \tilde{v}}{\partial y} + \frac{\partial \tilde{w}}{\partial z} \right) = 0 \end{aligned} \quad (\text{A.5a})$$

X Momentum:

$$\begin{aligned} \bar{\rho} \left(\frac{\partial \tilde{u}}{\partial t} + \bar{U} \frac{\partial \tilde{u}}{\partial x} + \bar{V} \frac{\partial \tilde{u}}{\partial y} + \bar{W} \frac{\partial \tilde{u}}{\partial z} \right) + \bar{\rho} \left(\tilde{u} \frac{\partial \bar{U}}{\partial x} + \tilde{v} \frac{\partial \bar{U}}{\partial y} + \tilde{w} \frac{\partial \bar{U}}{\partial z} \right) \\ + \tilde{\rho} \left(\bar{U} \frac{\partial \bar{U}}{\partial x} + \bar{V} \frac{\partial \bar{U}}{\partial y} + \bar{W} \frac{\partial \bar{U}}{\partial z} \right) + \frac{\partial \tilde{p}}{\partial x} = \frac{1}{R} \left[\frac{\partial \tilde{\tau}_{xx}}{\partial x} + \frac{\partial \tilde{\tau}_{xy}}{\partial y} + \frac{\partial \tilde{\tau}_{xz}}{\partial z} \right] \end{aligned} \quad (\text{A.5b})$$

Y Momentum:

$$\begin{aligned} \bar{\rho} \left(\frac{\partial \tilde{v}}{\partial t} + \bar{U} \frac{\partial \tilde{v}}{\partial x} + \bar{V} \frac{\partial \tilde{v}}{\partial y} + \bar{W} \frac{\partial \tilde{v}}{\partial z} \right) + \bar{\rho} \left(\tilde{u} \frac{\partial \bar{V}}{\partial x} + \tilde{v} \frac{\partial \bar{V}}{\partial y} + \tilde{w} \frac{\partial \bar{V}}{\partial z} \right) \\ + \tilde{\rho} \left(\bar{U} \frac{\partial \bar{V}}{\partial x} + \bar{V} \frac{\partial \bar{V}}{\partial y} + \bar{W} \frac{\partial \bar{V}}{\partial z} \right) + \frac{\partial \tilde{p}}{\partial y} = \frac{1}{R} \left[\frac{\partial \tilde{\tau}_{yx}}{\partial x} + \frac{\partial \tilde{\tau}_{yy}}{\partial y} + \frac{\partial \tilde{\tau}_{yz}}{\partial z} \right] \end{aligned} \quad (\text{A.5c})$$

Z Momentum:

$$\begin{aligned} \bar{\rho} \left(\frac{\partial \tilde{w}}{\partial t} + \bar{U} \frac{\partial \tilde{w}}{\partial x} + \bar{V} \frac{\partial \tilde{w}}{\partial y} + \bar{W} \frac{\partial \tilde{w}}{\partial z} \right) + \bar{\rho} \left(\tilde{u} \frac{\partial \bar{W}}{\partial x} + \tilde{v} \frac{\partial \bar{W}}{\partial y} + \tilde{w} \frac{\partial \bar{W}}{\partial z} \right) \\ + \tilde{\rho} \left(\bar{U} \frac{\partial \bar{W}}{\partial x} + \bar{V} \frac{\partial \bar{W}}{\partial y} + \bar{W} \frac{\partial \bar{W}}{\partial z} \right) + \frac{\partial \tilde{p}}{\partial z} = \frac{1}{R} \left[\frac{\partial \tilde{\tau}_{zx}}{\partial x} + \frac{\partial \tilde{\tau}_{zy}}{\partial y} + \frac{\partial \tilde{\tau}_{zz}}{\partial z} \right] \end{aligned} \quad (\text{A.5d})$$

Energy:

$$\begin{aligned}
& \bar{\rho}\bar{c}_p \left(\frac{\partial\tilde{\theta}}{\partial t} + \bar{U}\frac{\partial\tilde{\theta}}{\partial x} + \bar{V}\frac{\partial\tilde{\theta}}{\partial y} + \bar{W}\frac{\partial\tilde{\theta}}{\partial z} \right) + \bar{\rho}\bar{c}_p \left(\tilde{u}\frac{\partial\bar{T}}{\partial x} + \tilde{v}\frac{\partial\bar{T}}{\partial y} + \tilde{w}\frac{\partial\bar{T}}{\partial z} \right) \\
& + (\bar{\rho}\bar{c}_p + \bar{\rho}\bar{c}_p) \left(\bar{U}\frac{\partial\bar{T}}{\partial x} + \bar{V}\frac{\partial\bar{T}}{\partial y} + \bar{W}\frac{\partial\bar{T}}{\partial z} \right) \\
& - M^2(\gamma_e - 1) \left(\frac{\partial\tilde{p}}{\partial t} + \bar{U}\frac{\partial\tilde{p}}{\partial x} + \bar{V}\frac{\partial\tilde{p}}{\partial y} + \bar{W}\frac{\partial\tilde{p}}{\partial z} + \tilde{u}\frac{\partial\bar{P}}{\partial x} + \tilde{v}\frac{\partial\bar{P}}{\partial y} + \tilde{w}\frac{\partial\bar{P}}{\partial z} \right) = \\
& \frac{1}{\sigma_e R} \left\{ \frac{\partial}{\partial x} \left[\bar{k}\frac{\partial\tilde{\theta}}{\partial x} + \tilde{k}\frac{\partial\bar{T}}{\partial x} \right] + \frac{\partial}{\partial y} \left[\bar{k}\frac{\partial\tilde{\theta}}{\partial y} + \tilde{k}\frac{\partial\bar{T}}{\partial y} \right] + \frac{\partial}{\partial z} \left[\bar{k}\frac{\partial\tilde{\theta}}{\partial z} + \tilde{k}\frac{\partial\bar{T}}{\partial z} \right] \right\} \\
& + \frac{M^2(\gamma_e - 1)}{R} \left[\tilde{\tau}_{ij}\frac{\partial\bar{U}_i}{\partial x_j} + \bar{\tau}_{ij}\frac{\partial\tilde{u}_i}{\partial x_j} \right] - R \left(\frac{\partial Q}{\partial T}\tilde{\theta} + \frac{\partial Q}{\partial T_v}\tilde{\theta}_v + \frac{\partial Q}{\partial p}\tilde{p} \right) \tag{A.5e}
\end{aligned}$$

Vibrational Energy:

$$\begin{aligned}
& \bar{\rho}\bar{c}_{v,v} \left(\frac{\partial\tilde{\theta}_v}{\partial t} + \bar{U}\frac{\partial\tilde{\theta}_v}{\partial x} + \bar{V}\frac{\partial\tilde{\theta}_v}{\partial y} + \bar{W}\frac{\partial\tilde{\theta}_v}{\partial z} \right) + \bar{\rho}\bar{c}_{v,v} \left(\tilde{u}\frac{\partial\bar{T}_v}{\partial x} + \tilde{v}\frac{\partial\bar{T}_v}{\partial y} + \tilde{w}\frac{\partial\bar{T}_v}{\partial z} \right) \\
& + (\bar{\rho}\bar{c}_{v,v} + \bar{\rho}\bar{c}_{v,v}) \left(\bar{U}\frac{\partial\bar{T}_v}{\partial x} + \bar{V}\frac{\partial\bar{T}_v}{\partial y} + \bar{W}\frac{\partial\bar{T}_v}{\partial z} \right) = \\
& \frac{1}{\sigma_e R} \left\{ \frac{\partial}{\partial x} \left[\bar{k}_v\frac{\partial\tilde{\theta}_v}{\partial x} + \tilde{k}_v\frac{\partial\bar{T}_v}{\partial x} \right] + \frac{\partial}{\partial y} \left[\bar{k}_v\frac{\partial\tilde{\theta}_v}{\partial y} + \tilde{k}_v\frac{\partial\bar{T}_v}{\partial y} \right] + \frac{\partial}{\partial z} \left[\bar{k}_v\frac{\partial\tilde{\theta}_v}{\partial z} + \tilde{k}_v\frac{\partial\bar{T}_v}{\partial z} \right] \right\} \\
& + R \left(\frac{\partial Q}{\partial T}\tilde{\theta} + \frac{\partial Q}{\partial T_v}\tilde{\theta}_v + \frac{\partial Q}{\partial p}\tilde{p} \right) \tag{A.5f}
\end{aligned}$$

A.2 Locally Parallel Flow

For stability analysis, the flow is assumed to be locally parallel, which involves three assumptions: x derivatives of the mean flow variables are neglected, the mean vertical velocity \bar{V} is neglected, and x derivatives of the amplitude coefficients of the disturbances (designated by tildes) are ignored. The locally parallel assumption can be derived as the first term in a multiple-scales analysis (Nayfeh, 1980), in which successive terms in the perturbation expansion are proportional to inverse powers of

R . Therefore the accuracy of the locally-parallel approximation improves at higher Reynolds numbers. After eliminating nonparallel terms, there is a substantial reduction to the following equations:

Continuity:

$$\frac{\partial \tilde{\rho}}{\partial t} + \bar{U} \frac{\partial \tilde{\rho}}{\partial x} + \bar{W} \frac{\partial \tilde{\rho}}{\partial z} + \tilde{v} \frac{\partial \bar{\rho}}{\partial y} + \bar{\rho} \left(\frac{\partial \tilde{u}}{\partial x} + \frac{\partial \tilde{v}}{\partial y} + \frac{\partial \tilde{w}}{\partial z} \right) = 0 \quad (\text{A.6a})$$

Momentum:

$$\bar{\rho} \left(\frac{\partial \tilde{u}}{\partial t} + \bar{U} \frac{\partial \tilde{u}}{\partial x} + \bar{W} \frac{\partial \tilde{u}}{\partial z} \right) + \bar{\rho} \tilde{v} \frac{\partial \bar{U}}{\partial y} + \frac{\partial \tilde{p}}{\partial x} = \frac{1}{R} \left[\frac{\partial \tilde{\tau}_{xx}}{\partial x} + \frac{\partial \tilde{\tau}_{xy}}{\partial y} + \frac{\partial \tilde{\tau}_{xz}}{\partial z} \right] \quad (\text{A.6b})$$

$$\bar{\rho} \left(\frac{\partial \tilde{v}}{\partial t} + \bar{U} \frac{\partial \tilde{v}}{\partial x} + \bar{W} \frac{\partial \tilde{v}}{\partial z} \right) + \frac{\partial \tilde{p}}{\partial y} = \frac{1}{R} \left[\frac{\partial \tilde{\tau}_{yx}}{\partial x} + \frac{\partial \tilde{\tau}_{yy}}{\partial y} + \frac{\partial \tilde{\tau}_{yz}}{\partial z} \right] \quad (\text{A.6c})$$

$$\bar{\rho} \left(\frac{\partial \tilde{w}}{\partial t} + \bar{U} \frac{\partial \tilde{w}}{\partial x} + \bar{W} \frac{\partial \tilde{w}}{\partial z} \right) + \bar{\rho} \tilde{v} \frac{\partial \bar{W}}{\partial y} + \frac{\partial \tilde{p}}{\partial z} = \frac{1}{R} \left[\frac{\partial \tilde{\tau}_{zx}}{\partial x} + \frac{\partial \tilde{\tau}_{zy}}{\partial y} + \frac{\partial \tilde{\tau}_{zz}}{\partial z} \right] \quad (\text{A.6d})$$

Energy:

$$\begin{aligned} & \bar{\rho} \bar{c}_p \left(\frac{\partial \tilde{\theta}}{\partial t} + \bar{U} \frac{\partial \tilde{\theta}}{\partial x} + \bar{W} \frac{\partial \tilde{\theta}}{\partial z} \right) + \bar{\rho} \bar{c}_p \tilde{v} \frac{\partial \bar{T}}{\partial y} \\ & - M^2 (\gamma_e - 1) \left(\frac{\partial \tilde{p}}{\partial t} + \bar{U} \frac{\partial \tilde{p}}{\partial x} + \bar{W} \frac{\partial \tilde{p}}{\partial z} \right) = \\ & \frac{1}{\sigma_e R} \left\{ \bar{k} \frac{\partial^2 \tilde{\theta}}{\partial x^2} + \frac{\partial}{\partial y} \left[\bar{k} \frac{\partial \tilde{\theta}}{\partial y} + \tilde{k} \frac{\partial \bar{T}}{\partial y} \right] + \bar{k} \frac{\partial^2 \tilde{\theta}}{\partial z^2} \right\} \\ & + \frac{M^2 (\gamma_e - 1)}{R} \left[\tilde{\tau}_{ij} \frac{\partial \bar{U}_i}{\partial x_j} + \bar{\tau}_{ij} \frac{\partial \tilde{u}_i}{\partial x_j} \right] - R \left(\frac{\partial Q}{\partial T} \tilde{\theta} + \frac{\partial Q}{\partial T_v} \tilde{\theta}_v + \frac{\partial Q}{\partial p} \tilde{p} \right) \end{aligned} \quad (\text{A.6e})$$

Vibrational Energy:

$$\begin{aligned} & \bar{\rho} \bar{c}_{v,v} \left(\frac{\partial \tilde{\theta}_v}{\partial t} + \bar{U} \frac{\partial \tilde{\theta}_v}{\partial x} + \bar{W} \frac{\partial \tilde{\theta}_v}{\partial z} \right) + \bar{\rho} \bar{c}_{v,v} \tilde{v} \frac{\partial \bar{T}_v}{\partial y} = \\ & \frac{1}{\sigma_e R} \left\{ \bar{k}_v \frac{\partial^2 \tilde{\theta}_v}{\partial x^2} + \frac{\partial}{\partial y} \left[\bar{k}_v \frac{\partial \tilde{\theta}_v}{\partial y} + \tilde{k}_v \frac{\partial \bar{T}_v}{\partial y} \right] + \bar{k}_v \frac{\partial^2 \tilde{\theta}_v}{\partial z^2} \right\} + R \left(\frac{\partial Q}{\partial T} \tilde{\theta} + \frac{\partial Q}{\partial T_v} \tilde{\theta}_v + \frac{\partial Q}{\partial p} \tilde{p} \right) \end{aligned} \quad (\text{A.6f})$$

For locally-parallel flow, the components of the viscous stress tensor are also greatly simplified. The non-zero components of the mean and fluctuating viscous stress tensors are:

$$\begin{aligned} \bar{\tau}_{xy} &= \bar{\mu} \frac{\partial \bar{U}}{\partial y} & \bar{\tau}_{zy} &= \bar{\mu} \frac{\partial \bar{W}}{\partial z} \\ \tilde{\tau}_{xx} &= \bar{\mu} \left((2+r) \frac{\partial \tilde{u}}{\partial x} + r \frac{\partial \tilde{v}}{\partial y} + r \frac{\partial \tilde{w}}{\partial z} \right) & \tilde{\tau}_{xy} &= \bar{\mu} \left(\frac{\partial \tilde{u}}{\partial y} + \frac{\partial \tilde{v}}{\partial x} \right) + \tilde{\mu} \frac{\partial \bar{U}}{\partial y} \\ \tilde{\tau}_{yy} &= \bar{\mu} \left((2+r) \frac{\partial \tilde{v}}{\partial y} + r \frac{\partial \tilde{u}}{\partial x} + r \frac{\partial \tilde{w}}{\partial z} \right) & \tilde{\tau}_{yz} &= \bar{\mu} \left(\frac{\partial \tilde{w}}{\partial y} + \frac{\partial \tilde{v}}{\partial z} \right) + \tilde{\mu} \frac{\partial \bar{W}}{\partial z} \\ \tilde{\tau}_{zz} &= \bar{\mu} \left((2+r) \frac{\partial \tilde{w}}{\partial z} + r \frac{\partial \tilde{u}}{\partial x} + r \frac{\partial \tilde{v}}{\partial y} \right) & \tilde{\tau}_{xz} &= \bar{\mu} \left(\frac{\partial \tilde{u}}{\partial z} + \frac{\partial \tilde{w}}{\partial x} \right) \end{aligned}$$

As a result, the viscous dissipation term in the energy equation becomes:

$$\begin{aligned} \tilde{\tau}_{ij} \frac{\partial \bar{U}_i}{\partial x_j} + \bar{\tau}_{ij} \frac{\partial \tilde{u}_i}{\partial x_j} &= 2\bar{\mu} \frac{\partial \bar{U}}{\partial y} \left(\frac{\partial \tilde{u}}{\partial y} + \frac{\partial \tilde{v}}{\partial x} \right) + 2\bar{\mu} \frac{\partial \bar{W}}{\partial y} \left(\frac{\partial \tilde{w}}{\partial y} + \frac{\partial \tilde{v}}{\partial z} \right) \\ &+ \tilde{\mu} \left(\frac{\partial \bar{U}}{\partial y} \right)^2 + \bar{\mu} \left(\frac{\partial \bar{W}}{\partial y} \right)^2 \end{aligned} \quad (\text{A.7})$$

A.3 Normal Modes

Using the above results, one can now write Equations A.6 in terms of normal modes, in which fluctuations are proportional to exponentials in space and time:

$$\tilde{\mathbf{q}} = \hat{\mathbf{q}} \exp(i\alpha x + i\beta z - i\omega t) \quad (\text{A.8})$$

where \mathbf{q} is the vector containing the disturbance components of velocity, pressure, temperature, and vibrational temperature. After writing Equations A.6 in terms of normal modes, the result is:

Continuity:

$$(i\alpha\bar{U} + i\beta\bar{W} - i\omega) \hat{\rho} + \hat{v} \frac{\partial \bar{\rho}}{\partial y} + \bar{\rho} \left(i\alpha \hat{u} + \frac{\partial \hat{v}}{\partial y} + i\beta \hat{w} \right) = 0 \quad (\text{A.9a})$$

X Momentum:

$$\begin{aligned} \bar{\rho} (i\alpha\bar{U} + i\beta\bar{W} - i\omega) \hat{u} + \bar{\rho} \hat{v} \frac{\partial \bar{U}}{\partial y} + i\alpha \hat{p} = & \frac{\bar{\mu}}{R} \left[-\alpha^2(2+r)\hat{u} + i\alpha r \frac{\partial \hat{v}}{\partial y} - \alpha\beta r \hat{w} \right] \\ & + \frac{1}{R} \left[\frac{\partial \bar{\mu}}{\partial y} \left(\frac{\partial \hat{u}}{\partial y} + i\alpha \hat{v} \right) + \bar{\mu} \left(\frac{\partial^2 \hat{u}}{\partial y^2} + i\alpha \frac{\partial \hat{v}}{\partial y} \right) + \frac{\partial \hat{\mu}}{\partial y} \frac{\partial \bar{U}}{\partial y} + \hat{\mu} \frac{\partial^2 \bar{U}}{\partial y^2} \right] \\ & - \frac{\bar{\mu}}{R} \left[\beta^2 \hat{u} + \alpha\beta \hat{w} \right] \end{aligned} \quad (\text{A.9b})$$

Y Momentum:

$$\begin{aligned} \bar{\rho} (i\alpha\bar{U} + i\beta\bar{W} - i\omega) \hat{v} + \frac{\partial \hat{p}}{\partial y} = & \frac{1}{R} \left[\bar{\mu} \left(i\alpha \frac{\partial \hat{u}}{\partial y} - \alpha^2 \hat{v} \right) + i\alpha \hat{\mu} \frac{\partial \bar{U}}{\partial y} \right] \\ & + \frac{1}{R} \left[\frac{\partial \bar{\mu}}{\partial y} \left((2+r) \frac{\partial \hat{v}}{\partial y} + r i \alpha \hat{u} + r i \beta \hat{w} \right) + \bar{\mu} \left((2+r) \frac{\partial^2 \hat{v}}{\partial y^2} + r i \alpha \frac{\partial \hat{u}}{\partial y} + r i \beta \frac{\partial \hat{w}}{\partial y} \right) \right] \\ & + \frac{1}{R} \left[\bar{\mu} \left(i\beta \frac{\partial \hat{w}}{\partial y} - \beta^2 \hat{v} \right) + i\beta \hat{\mu} \frac{\partial \bar{W}}{\partial y} \right] \end{aligned} \quad (\text{A.9c})$$

Z Momentum:

$$\begin{aligned}
\bar{\rho} (i\alpha\bar{U} + i\beta\bar{W} - i\omega) \hat{w} + \bar{\rho}\hat{v} \frac{\partial\bar{W}}{\partial y} + i\beta\hat{p} = & -\frac{\bar{\mu}}{R} \left[\alpha\beta\hat{u} + \alpha^2\hat{w} \right] \\
& + \frac{1}{R} \left[\frac{\partial\bar{\mu}}{\partial y} \left(i\beta\hat{v} + \frac{\partial\hat{w}}{\partial y} \right) + \bar{\mu} \left(i\beta \frac{\partial\hat{v}}{\partial y} + \frac{\partial^2\hat{w}}{\partial y^2} \right) + \frac{\partial\hat{\mu}}{\partial y} \frac{\partial\bar{W}}{\partial y} + \hat{\mu} \frac{\partial^2\bar{W}}{\partial y^2} \right] \\
& + \frac{\bar{\mu}}{R} \left[-\beta^2(2+r)\hat{w} - r\alpha\beta\hat{u} + i\beta r \frac{\partial\hat{v}}{\partial y} \right]
\end{aligned} \tag{A.9d}$$

Energy:

$$\begin{aligned}
\bar{\rho}\bar{c}_p (i\alpha\bar{U} + i\beta\bar{W} - i\omega) \hat{\theta} + \bar{\rho}\bar{c}_p\hat{v} \frac{\partial\bar{T}}{\partial y} - M^2(\gamma_e - 1) (i\alpha\bar{U} + i\beta\bar{W} - i\omega) \hat{p} = \\
\frac{1}{\sigma_e R} \left[-(\alpha^2 + \beta^2)\bar{k}\hat{\theta} + \frac{\partial\bar{k}}{\partial y} \frac{\partial\hat{\theta}}{\partial y} + \bar{k} \frac{\partial^2\hat{\theta}}{\partial y^2} + \frac{\partial\hat{k}}{\partial y} \frac{\partial\bar{T}}{\partial y} + \hat{k} \frac{\partial^2\bar{T}}{\partial y^2} \right] \\
+ \frac{M^2(\gamma_e - 1)}{R} \left[2\bar{\mu} \frac{\partial\bar{U}}{\partial y} \left(\frac{\partial\hat{u}}{\partial y} + i\alpha\hat{v} \right) + 2\bar{\mu} \frac{\partial\bar{W}}{\partial y} \left(\frac{\partial\hat{w}}{\partial y} + i\beta\hat{v} \right) \right. \\
\left. + \hat{\mu} \left(\frac{\partial\bar{U}}{\partial y} \right)^2 + \hat{\mu} \left(\frac{\partial\bar{W}}{\partial y} \right)^2 \right]
\end{aligned} \tag{A.9e}$$

$$- R \left(\frac{\partial Q}{\partial T} \hat{\theta} + \frac{\partial Q}{\partial T_v} \hat{\theta}_v + \frac{\partial Q}{\partial p} \hat{p} \right) \tag{A.9f}$$

Vibrational Energy:

$$\begin{aligned}
\bar{\rho}\bar{c}_{v,v} (i\alpha\bar{U} + i\beta\bar{W} - i\omega) \hat{\theta}_v + \bar{\rho}\bar{c}_{v,v}\hat{v} \frac{\partial\bar{T}_v}{\partial y} = \\
\frac{1}{\sigma_e R} \left[-(\alpha^2 + \beta^2)\bar{k}_v\hat{\theta}_v + \frac{\partial\bar{k}_v}{\partial y} \frac{\partial\hat{\theta}_v}{\partial y} + \bar{k}_v \frac{\partial^2\hat{\theta}_v}{\partial y^2} + \frac{\partial\hat{k}_v}{\partial y} \frac{\partial\bar{T}_v}{\partial y} + \hat{k}_v \frac{\partial^2\bar{T}_v}{\partial y^2} \right] \\
+ R \left(\frac{\partial Q}{\partial T} \hat{\theta} + \frac{\partial Q}{\partial T_v} \hat{\theta}_v + \frac{\partial Q}{\partial p} \hat{p} \right)
\end{aligned} \tag{A.9g}$$

We can now replace $\bar{\rho}$ by $1/\bar{T}$ using the mean equation of state and then solve each of the equations A.9 for the highest derivative. Following the notation of Malik (1990), we also introduce the definition:

$$\xi \equiv \alpha\bar{U} + \beta\bar{W} - \omega \quad (\text{A.10})$$

We also write the fluctuations in viscosity and thermal conductivity, $\hat{\mu}$, \hat{k} , and \hat{k}_v in terms of the temperature fluctuations using Equation A.4. Making these substitutions, the result is:

X Momentum:

$$\begin{aligned} \hat{u}'' &= \left(\alpha^2(2+r) + \beta^2 \right) \hat{u} - (1+r)(i\alpha\hat{v}' - \alpha\beta\hat{w}) - \frac{\bar{\mu}'}{\bar{\mu}}(\hat{u}' + i\alpha\hat{v}) \\ &\quad - \frac{1}{\bar{\mu}} \frac{\partial \bar{\mu}}{\partial \bar{T}} \bar{U}'' \hat{\theta} - \frac{1}{\bar{\mu}} \frac{\partial^2 \bar{\mu}}{\partial \bar{T}^2} \bar{T}' \bar{U}' \hat{\theta} - \frac{1}{\bar{\mu}} \frac{\partial \bar{\mu}}{\partial \bar{T}} \bar{U}' \hat{\theta}' + \frac{R}{\bar{\mu}} \left(i \frac{\xi \hat{u}}{\bar{T}} + \frac{\hat{v} \bar{U}'}{\bar{T}} + i\alpha \hat{p} \right) = 0 \end{aligned} \quad (\text{A.11})$$

Y Momentum:

$$\begin{aligned} \hat{v}'' &= \frac{\alpha^2 + \beta^2}{2+r} \hat{v} - \frac{1+r}{2+r} \left(i\alpha\hat{u}' + i\beta\hat{w}' \right) - \frac{1}{\bar{\mu}(2+r)} \frac{\partial \bar{\mu}}{\partial \bar{T}} (i\alpha\bar{U}' + i\beta\bar{W}') \hat{\theta} \\ &\quad - \frac{\bar{\mu}'}{\bar{\mu}(2+r)} \left((2+r)\hat{v}' + r(i\alpha\hat{u} + i\beta\hat{w}) \right) + \frac{R}{\bar{\mu}(2+r)} \left(i \frac{\xi}{\bar{T}} \hat{v} + \hat{p}' \right) \end{aligned} \quad (\text{A.12})$$

Continuity

$$\hat{v}' = - \left[i\xi \left(\gamma M^2 \hat{p} - \frac{\hat{\theta}}{\bar{T}} \right) - \hat{v} \frac{1}{\bar{T}} \frac{\partial \bar{T}}{\partial y} + i\alpha\hat{u} + i\beta\hat{w} \right] \quad (\text{A.13})$$

Energy:

$$\hat{\theta}'' = (\alpha^2 + \beta^2) \hat{\theta} - \left(\frac{\bar{k}'}{\bar{k}} \hat{\theta}' + \left(\frac{\partial \bar{k}}{\partial \bar{T}} \right)' \bar{T}' \hat{\theta} + \frac{\partial \bar{k}}{\partial \bar{T}} \bar{T}' \hat{\theta}' + \frac{\partial \bar{k}}{\partial \bar{T}} \bar{T}'' \hat{\theta} \right)$$

$$\begin{aligned}
& - \frac{M^2(\gamma_e - 1)\bar{\mu}\sigma_e}{\bar{k}} \left[2\bar{U}'(\hat{u}' + i\alpha\hat{v}) + 2\bar{W}'(\hat{w}' + i\beta\hat{v}) + \frac{1}{\bar{\mu}} \frac{\partial\bar{\mu}}{\partial\bar{T}} (\bar{U}'^2 + \bar{W}'^2) \hat{\theta} \right] \\
& + \frac{R\sigma_e}{\bar{k}} \left(\frac{i\xi\bar{c}_p}{\bar{T}} \hat{\theta} + \frac{\bar{c}_p\bar{T}'}{\bar{T}} \hat{v} - i\xi M^2(\gamma_e - 1)\hat{p} \right) \\
& + \frac{R^2\sigma_e}{\bar{k}} \left(\frac{\partial Q}{\partial T} \hat{\theta} + \frac{\partial Q}{\partial T_v} \hat{\theta}_v + \frac{\partial Q}{\partial p} \hat{p} \right) \tag{A.14}
\end{aligned}$$

Z Momentum:

$$\begin{aligned}
\hat{w}'' &= \left(\alpha^2 + (2+r)\beta^2 \right) \hat{w} - (1+r) \left(i\beta\hat{v}' - \alpha\beta\hat{u} \right) - \frac{\bar{\mu}'}{\bar{\mu}} (\hat{w}' + i\beta\hat{v}) \\
& - \frac{1}{\bar{\mu}} \frac{\partial\bar{\mu}}{\partial\bar{T}} \bar{W}'' \hat{\theta} - \frac{1}{\bar{\mu}} \frac{\partial^2\bar{\mu}}{\partial\bar{T}^2} \bar{T}' \bar{W}' \hat{\theta} - \frac{1}{\bar{\mu}} \frac{\partial\bar{\mu}}{\partial\bar{T}} \bar{W}' \hat{\theta}' + \frac{R}{\bar{\mu}} \left(i\frac{\xi\hat{w}}{\bar{T}} + \frac{\hat{v}\bar{W}'}{\bar{T}} + i\beta\hat{p} \right) \tag{A.15}
\end{aligned}$$

Vibrational Energy:

$$\begin{aligned}
\hat{\theta}_v'' &= (\alpha^2 + \beta^2) \hat{\theta}_v + \frac{R\sigma_e}{\bar{k}_v} \left(\frac{i\xi\bar{c}_{v,v}}{\bar{T}} \hat{\theta}_v + \frac{\bar{c}_{v,v}\bar{T}'_v}{\bar{T}} \hat{v} \right) - \frac{R^2\sigma_e}{\bar{k}_v} \left(\frac{\partial Q}{\partial T} \hat{\theta} + \frac{\partial Q}{\partial T_v} \hat{\theta}_v + \frac{\partial Q}{\partial p} \hat{p} \right) \\
& - \frac{\bar{k}'_v}{\bar{k}_v} \hat{\theta}'_v - \frac{\bar{T}'_v}{\bar{k}_v} \left(\frac{\partial\bar{k}_v}{\partial\bar{T}} \hat{\theta} + \frac{\partial\bar{k}_v}{\partial\bar{T}_v} \hat{\theta}_v \right) - \frac{\bar{T}'_v}{\bar{k}_v} \left[\left(\frac{\partial\bar{k}_v}{\partial\bar{T}} \right)' \hat{\theta} + \left(\frac{\partial\bar{k}_v}{\partial\bar{T}_v} \right)' \hat{\theta}_v \right] \\
& - \frac{\bar{T}'_v}{\bar{k}_v} \left(\frac{\partial\bar{k}_v}{\partial\bar{T}} \hat{\theta}' + \frac{\partial\bar{k}_v}{\partial\bar{T}_v} \hat{\theta}'_v \right) \tag{A.16}
\end{aligned}$$

In these equations, primes refer to differentiation in the wallnormal direction.

A.4 Second order equations

The equations are now in the form of Equation A.1, and the nonzero coefficients of the matrices **A**, **B**, and **C** can be tabulated:

$$A_{11} = A_{22} = A_{44} = A_{55} = A_{66} = 1$$

$$B_{11} = \frac{\bar{\mu}'}{\bar{\mu}}$$

$$B_{12} = i\alpha(1+r)$$

$$B_{14} = \frac{1}{\bar{\mu}} \frac{\partial\bar{\mu}}{\partial\bar{T}} \bar{U}'$$

$$\begin{aligned}
B_{21} &= i\alpha \frac{1+r}{2+r} \\
B_{22} &= \frac{\bar{\mu}'}{\bar{\mu}} \\
B_{23} &= -\frac{R}{(2+r)\bar{\mu}} \\
B_{25} &= i\beta \frac{1+r}{2+r} \\
B_{32} &= 1 \\
B_{41} &= \frac{M^2(\gamma_e - 1)\bar{\mu}\sigma_e}{\bar{k}} 2\bar{U}' \\
B_{44} &= 2\frac{\bar{k}'}{\bar{k}} \\
B_{45} &= \frac{M^2(\gamma_e - 1)\bar{\mu}\sigma_e}{\bar{k}} 2\bar{W}' \\
B_{52} &= i\beta(1+r) \\
B_{54} &= \frac{1}{\bar{\mu}} \frac{\partial \bar{\mu}}{\partial \bar{T}} \bar{W}' \\
B_{55} &= \frac{\bar{\mu}'}{\bar{\mu}} \\
B_{64} &= \frac{\bar{T}'_v}{\bar{k}_v} \frac{\partial \bar{k}_v}{\partial \bar{T}} \\
B_{66} &= \frac{\bar{T}'_v}{\bar{k}_v} \frac{\partial \bar{k}_v}{\partial \bar{T}_v} + \frac{\bar{k}'_v}{\bar{k}_v} \\
C_{11} &= -(2+r)\alpha^2 - \beta^2 - i\xi \frac{R}{\bar{\mu}\bar{T}} \\
C_{12} &= i\alpha \frac{\bar{\mu}'}{\bar{\mu}} - \frac{R}{\bar{\mu}\bar{T}} \bar{U}' \\
C_{13} &= -i\alpha \frac{R}{\bar{\mu}} \\
C_{14} &= \frac{1}{\bar{\mu}} \frac{\partial \bar{\mu}}{\partial \bar{T}} \bar{U}'' + \frac{1}{\bar{\mu}} \frac{\partial^2 \bar{\mu}}{\partial \bar{T}^2} \bar{T}' \bar{U}' \\
C_{15} &= -\alpha\beta(1+r) \\
C_{21} &= \frac{i\alpha r \bar{\mu}'}{(2+r)\bar{\mu}} \\
C_{22} &= -\frac{i\xi R}{\bar{\mu}\bar{T}(2+r)} - \frac{\alpha^2 + \beta^2}{2+r} \\
C_{24} &= \frac{1}{\bar{\mu}(2+r)} \frac{\partial \bar{\mu}}{\partial \bar{T}} (i\alpha \bar{U}' + i\beta \bar{W}')
\end{aligned}$$

$$C_{25} = \frac{i\beta\bar{\mu}'r}{\bar{\mu}(2+r)}$$

$$C_{31} = i\alpha$$

$$C_{32} = -\frac{\bar{T}'}{\bar{T}}$$

$$C_{33} = i\xi\gamma_e M_e^2$$

$$C_{34} = -i\xi/T$$

$$C_{35} = i\beta$$

$$C_{42} = \frac{M^2(\gamma_e - 1)\bar{\mu}\sigma_e}{\bar{k}} (2i\alpha\bar{U}' + 2i\beta\bar{W}') - \frac{\bar{c}_p\bar{T}'\sigma_e R}{\bar{T}\bar{k}}$$

$$C_{43} = i\xi\frac{R\sigma_e}{\bar{k}} M^2(\gamma_e - 1) - \frac{R^2\sigma_e}{\bar{k}} \frac{\partial\bar{Q}}{\partial\bar{p}}$$

$$C_{44} = \left(\frac{\partial\bar{k}}{\partial\bar{T}}\right)' + \frac{\partial\bar{k}}{\partial\bar{T}}\bar{T}' + \frac{M^2(\gamma_e - 1)\sigma_e}{\bar{k}} \frac{\partial\bar{\mu}}{\partial\bar{T}} (\bar{U}'^2 + \bar{W}'^2) \\ - i\xi\frac{\bar{c}_p R\sigma_e}{\bar{T}\bar{k}} - (\alpha^2 + \beta^2) - \frac{R^2\sigma_e}{\bar{k}} \frac{\partial\bar{Q}}{\partial\bar{T}}$$

$$C_{46} = -\frac{R^2\sigma_e}{\bar{k}} \frac{\partial\bar{Q}}{\partial\bar{T}_v}$$

$$C_{51} = -(1+r)\alpha\beta$$

$$C_{52} = i\beta\frac{\bar{\mu}'}{\bar{\mu}} - \frac{R}{\bar{T}\bar{\mu}}\bar{W}'$$

$$C_{53} = -i\beta\frac{R}{\bar{\mu}}$$

$$C_{54} = \frac{1}{\bar{\mu}} \frac{\partial\bar{\mu}}{\partial\bar{T}}\bar{W}'' + \frac{1}{\bar{\mu}} \frac{\partial^2\bar{\mu}}{\partial\bar{T}^2}\bar{T}'\bar{W}'$$

$$C_{55} = -\frac{i\xi R}{\bar{T}\bar{\mu}} - \alpha^2 - (2+r)\beta^2$$

$$C_{62} = -\frac{R\sigma_e}{\bar{k}_v\bar{T}}\bar{c}_{v,v}\bar{T}'_v$$

$$C_{63} = \frac{R^2\sigma_e}{\bar{k}_v} \frac{\partial\bar{Q}}{\partial\bar{p}} 6$$

$$C_{64} = \frac{\bar{T}''_v}{\bar{k}_v} \frac{\partial\bar{k}_v}{\partial\bar{T}} + \frac{\bar{T}'_v}{\bar{k}_v} \left(\frac{\partial\bar{k}_v}{\partial\bar{T}}\right)' + \frac{R^2\sigma_e}{\bar{k}_v} \frac{\partial\bar{Q}}{\partial\bar{T}}$$

$$C_{66} = \frac{\bar{T}''_v}{\bar{k}_v} \frac{\partial\bar{k}_v}{\partial\bar{T}_v} + \frac{\bar{T}'_v}{\bar{k}_v} \left(\frac{\partial\bar{k}_v}{\partial\bar{T}_v}\right)' + \frac{R^2\sigma_e}{\bar{k}_v} \frac{\partial\bar{Q}}{\partial\bar{T}_v} - (\alpha^2 + \beta^2) - i\xi\frac{R\sigma_e}{\bar{k}_v\bar{T}}\bar{c}_{v,v}$$

Underlined terms involve vibrational energy transfer and are the only differences between the present method and the vibrationally frozen analysis described by [Malik \(1990\)](#).

A.5 First order equations

For the local stability solver described in Section 4.2, it is more convenient to express these equations as a first-order system of the form

$$\frac{d\mathbf{q}}{dy} = \mathbf{a}\mathbf{q} \quad \mathbf{q} = \left[\hat{u}, \hat{u}', \hat{v}, \hat{p}, \hat{\theta}, \hat{\theta}', \hat{w}, \hat{w}'\hat{\theta}_v, \hat{\theta}'_v \right]^T \quad (\text{A.17})$$

To obtain a system of this form, the continuity equation (A.13) is differentiated to get:

$$\begin{aligned} \hat{v}'' = & -i\xi \left(\gamma_e M_e^2 \hat{p}' - \frac{\hat{\theta}'}{\bar{T}} + \frac{\hat{\theta}T'}{T^2} \right) - i(\alpha\bar{U}' + \beta\bar{W}') \left(\gamma_e M^2 \hat{p} - \frac{\hat{\theta}}{T} \right) \\ & - i\alpha\hat{u}' - i\beta\hat{w}' + \frac{\bar{T}'}{\bar{T}}\hat{v}' + \left(\frac{\bar{T}'}{\bar{T}} \right)' \hat{v} \end{aligned} \quad (\text{A.18})$$

After substituting this expression for \hat{v}'' into the Y momentum equation (A.12) and solving for \hat{p}' , one finds

$$\begin{aligned} \frac{\hat{p}'}{\chi} = & -(\alpha^2 + \beta^2)\hat{v} + (1+r) \left(i\alpha\hat{u}' + i\beta\hat{w}' \right) + \frac{1}{\bar{\mu}} \frac{\partial \bar{\mu}}{\partial \bar{T}} (i\alpha\bar{U}' + i\beta\bar{W}') \hat{\theta} \\ & + \frac{\bar{\mu}'}{\bar{\mu}} \left((2+r)\hat{v}' + r(i\alpha\hat{u} + i\beta\hat{w}) \right) - \frac{R}{\bar{\mu}} \frac{i\xi}{\bar{T}} \hat{v} - i\xi(2+r) \left(-\frac{\hat{\theta}'}{\bar{T}} + \frac{\hat{\theta}T'}{T^2} \right) \\ & + (2+r) \left[-i(\alpha\bar{U}' + \beta\bar{W}') \left(\gamma_e M^2 \hat{p} - \frac{\hat{\theta}}{T} \right) - i\alpha\hat{u}' - i\beta\hat{w}' + \frac{\bar{T}'}{\bar{T}}\hat{v}' + \left(\frac{\bar{T}'}{\bar{T}} \right)' \hat{v} \right] \end{aligned} \quad (\text{A.19})$$

where, following the notation of [Malik \(1990\)](#), we define the quantity χ by

$$\chi = \left[\frac{R}{\bar{\mu}} + i\xi\gamma_e M^2(2+r) \right]^{-1} \quad (\text{A.20})$$

After factoring each of the disturbance components, one finds

$$\begin{aligned}
\frac{\hat{p}'}{\chi} &= \left[i\alpha r \frac{\bar{\mu}'}{\bar{\mu}} \right] \hat{u} - i\alpha \hat{u}' - \left[\alpha^2 + \beta^2 + i\xi \frac{R}{\bar{\mu}\bar{T}} - (2+r) \left(\frac{\bar{T}'}{\bar{T}} \right)' \right] \hat{v} \\
&- \left[(2+r)i(\alpha\bar{U}' + \beta\bar{W}')\gamma_e M^2 \right] \hat{p} \\
&+ \left[\frac{1}{\bar{\mu}} \frac{\partial \bar{\mu}}{\partial \bar{T}} (i\alpha\bar{U}' + i\beta\bar{W}') - i\xi(2+r) \frac{\bar{T}'}{\bar{T}^2} + (2+r)i(\alpha\bar{U}' + \beta\bar{W}') \frac{1}{\bar{T}} \right] \hat{\theta} \\
&+ \left[\frac{i\xi(2+r)}{\bar{T}} \right] \hat{\theta}' + \left[i\beta r \frac{\bar{\mu}'}{\bar{\mu}} \right] \hat{w} - i\beta \hat{w}' + (2+r) \left[\frac{\bar{\mu}'}{\bar{\mu}} + \frac{\bar{T}'}{\bar{T}} \right] \hat{v}' \quad (\text{A.21})
\end{aligned}$$

The final step is to eliminate the term \hat{v}' using the continuity equation (A.13). After substituting this quantity and collecting terms, the Y momentum equation reads:

$$\begin{aligned}
\frac{\hat{p}'}{\chi} &= -i\alpha \left[(2+r) \frac{\bar{T}'}{\bar{T}} + 2 \frac{\bar{\mu}'}{\bar{\mu}} \right] \hat{u} - i\alpha \hat{u}' \\
&- \left[\alpha^2 + \beta^2 + i\xi \frac{R}{\bar{\mu}\bar{T}} - (2+r) \left(\frac{\bar{T}''}{\bar{T}} + \frac{\bar{\mu}'\bar{T}'}{\bar{\mu}\bar{T}} \right) \right] \hat{v} \\
&- i(2+r)\gamma_e M^2 \left[(\alpha\bar{U}' + \beta\bar{W}') + \xi \left(\frac{\bar{T}'}{\bar{T}} + \frac{\bar{\mu}'}{\bar{\mu}} \right) \right] \hat{p} \\
&+ \left[i(\alpha\bar{U}' + \beta\bar{W}') \left(\frac{1}{\bar{\mu}} \frac{\partial \bar{\mu}}{\partial \bar{T}} + \frac{2+r}{\bar{T}} \right) + \frac{i\xi}{\bar{T}} (2+r) \frac{\bar{\mu}'}{\bar{\mu}} \right] \hat{\theta} \\
&+ \left[\frac{i\xi(2+r)}{\bar{T}} \right] \hat{\theta}' \\
&- i\beta \left[(2+r) \frac{\bar{T}'}{\bar{T}} + 2 \frac{\bar{\mu}'}{\bar{\mu}} \right] \hat{w} - i\beta \hat{w}' \quad (\text{A.22})
\end{aligned}$$

In the same way, the continuity equation can be used to eliminate the quantity \hat{v}' from the X and Z momentum equations:

$$\begin{aligned}
\hat{u}'' &= \left(\alpha^2(2+r) + \beta^2 \right) \hat{u} - (1+r) \left(\alpha\xi \left[\gamma_e M^2 \hat{p} - \frac{\hat{\theta}}{\bar{T}} \right] + \alpha^2 \hat{u} + i\alpha \hat{v} \frac{\bar{T}'}{\bar{T}} \right) \\
&- \frac{\bar{\mu}'}{\bar{\mu}} (\hat{u}' + i\alpha \hat{v}) \\
&- \left(\frac{1}{\bar{\mu}} \frac{\partial \bar{\mu}}{\partial \bar{T}} \bar{U}'' + \frac{1}{\bar{\mu}} \frac{\partial^2 \bar{\mu}}{\partial \bar{T}^2} \bar{T}' U' \right) \hat{\theta} - \frac{1}{\bar{\mu}} \frac{\partial \bar{\mu}}{\partial \bar{T}} \bar{U}' \hat{\theta}' + \frac{R}{\bar{\mu}} \left(\frac{i\xi}{\bar{T}} \hat{u} + \frac{\bar{U}'}{\bar{T}} \hat{v} + i\alpha \hat{p} \right) = 0 \quad (\text{A.23})
\end{aligned}$$

$$\begin{aligned}
\hat{w}'' &= \left(\alpha^2 + (2+r)\beta^2 \right) \hat{w} - (1+r) \left(\beta\xi \left[\gamma_e M^2 \hat{p} - \frac{\hat{\theta}}{\bar{T}} \right] + \beta^2 \hat{w} + i\beta \hat{v} \frac{\bar{T}'}{\bar{T}} \right) \\
&\quad - \frac{\bar{\mu}'}{\bar{\mu}} (\hat{w}' + i\beta \hat{v}) \\
&\quad - \left(\frac{1}{\bar{\mu}} \frac{\partial \bar{\mu}}{\partial \bar{T}} \bar{W}'' + \frac{1}{\bar{\mu}} \frac{\partial^2 \bar{\mu}}{\partial \bar{T}^2} \bar{T}' \bar{W}' \right) \hat{\theta} - \frac{1}{\bar{\mu}} \frac{\partial \bar{\mu}}{\partial \bar{T}} \bar{W}' \hat{\theta}' + \frac{R}{\bar{\mu}} \left(\frac{i\xi}{\bar{T}} \hat{w} + \frac{\bar{W}'}{\bar{T}} \hat{v} + i\beta \hat{p} \right) \quad (\text{A.24})
\end{aligned}$$

The coefficients of the matrix \mathbf{a} are then:

$$a_{12} = 1$$

$$a_{21} = i\xi \frac{R}{\bar{\mu}\bar{T}} + \alpha^2 + \beta^2$$

$$a_{22} = -\frac{\bar{\mu}'}{\bar{\mu}}$$

$$a_{23} = -i\alpha \frac{\bar{\mu}'}{\bar{\mu}} + \frac{R}{\bar{\mu}\bar{T}} \bar{U}' - i\alpha(1+r) \frac{\bar{T}'}{\bar{T}}$$

$$a_{24} = i\alpha \frac{R}{\bar{\mu}} - \alpha\xi(1+r)\gamma_e M^2$$

$$a_{25} = -\frac{1}{\bar{\mu}} \left(\frac{\partial \bar{\mu}}{\partial \bar{T}} \bar{U}'' + \frac{\partial^2 \bar{\mu}}{\partial \bar{T}^2} \bar{T}' \bar{U}' \right) + (1+r) \frac{\alpha\xi}{\bar{T}}$$

$$a_{26} = -\frac{1}{\bar{\mu}} \frac{\partial \bar{\mu}}{\partial \bar{T}} \bar{U}'$$

$$a_{31} = -i\alpha$$

$$a_{33} = \frac{\bar{T}'}{\bar{T}}$$

$$a_{34} = -i\xi\gamma_e M^2$$

$$a_{35} = \frac{i\xi}{\bar{T}}$$

$$a_{37} = -i\beta$$

$$a_{41} = -i\alpha\chi \left[(2+r) \frac{\bar{T}'}{\bar{T}} + 2 \frac{\bar{\mu}'}{\bar{\mu}} \right]$$

$$a_{42} = -i\alpha\chi$$

$$a_{43} = -\chi \left[\alpha^2 + \beta^2 + i\xi \frac{R}{\bar{\mu}\bar{T}} - (2+r) \left(\frac{\bar{T}''}{\bar{T}} + \frac{\bar{T}'\bar{\mu}'}{\bar{\mu}\bar{T}} \right) \right]$$

$$\begin{aligned}
a_{44} &= -i\chi(2+r)\gamma_e M^2 \left[(\alpha\bar{U}' + \beta\bar{W}') + \xi \left(\frac{\bar{T}'}{\bar{T}} + \frac{\bar{\mu}'}{\bar{\mu}} \right) \right] \\
a_{45} &= \chi \left[i(\alpha\bar{U}' + \beta\bar{W}') \left(\frac{1}{\bar{\mu}} \frac{\partial \bar{\mu}}{\partial \bar{T}} + \frac{2+r}{\bar{T}} \right) + \frac{i\xi}{\bar{T}}(2+r) \frac{\bar{\mu}'}{\bar{\mu}} \right] \\
a_{46} &= \frac{i\xi\chi(2+r)}{\bar{T}} \\
a_{47} &= -i\beta\chi \left[(2+r) \frac{\bar{T}'}{\bar{T}} + 2 \frac{\bar{\mu}'}{\bar{\mu}} \right] \\
a_{48} &= -i\beta\chi \\
a_{56} &= 1 \\
a_{62} &= -\frac{M^2(\gamma_e - 1)\bar{\mu}\sigma_e}{\bar{k}} 2\bar{U}' \\
a_{63} &= -\frac{M^2(\gamma_e - 1)\bar{\mu}\sigma_e}{\bar{k}} (2i\alpha\bar{U}' + 2i\beta\bar{W}') + \frac{R\sigma_e}{\bar{T}\bar{k}} \bar{c}_p \bar{T}' \\
a_{64} &= -i\xi(\gamma_e - 1)M^2 \frac{R\sigma_e}{\bar{k}} + \frac{R^2\sigma_e}{\bar{k}} \frac{\partial \bar{Q}}{\partial \bar{p}} \\
a_{65} &= \alpha^2 + \beta^2 - \left(\frac{\partial \bar{k}}{\partial \bar{T}} \right)' \bar{T}' - \frac{\partial \bar{k}}{\partial \bar{T}} \bar{T}'' - \frac{M^2(\gamma_e - 1)\sigma_e}{\bar{k}} \frac{\partial \bar{\mu}}{\partial \bar{T}} (\bar{U}'^2 + \bar{W}'^2) \\
&\quad + i\xi \frac{R\sigma_e}{\bar{k}\bar{T}} \bar{c}_p + \frac{R^2\sigma_e}{\bar{k}} \frac{\partial \bar{Q}}{\partial \bar{T}} \\
a_{66} &= -2 \frac{\bar{k}'}{\bar{k}} \\
a_{68} &= -\frac{M^2(\gamma_e - 1)\bar{\mu}\sigma_e}{\bar{k}} 2\bar{W}' \\
a_{69} &= \frac{R^2\sigma_e}{\bar{k}} \frac{\partial \bar{Q}}{\partial \bar{T}_v} \\
a_{78} &= 1 \\
a_{83} &= \frac{R\bar{W}'}{\bar{\mu}\bar{T}} - i\beta \frac{\bar{\mu}'}{\bar{\mu}} - i\beta(1+r) \frac{\bar{T}'}{\bar{T}} \\
a_{84} &= i\beta \frac{R}{\bar{\mu}} - (1+r)\beta\xi\gamma_e M^2 \\
a_{85} &= \frac{\beta\xi(1+r)}{\bar{T}} - \frac{1}{\bar{\mu}} \left(\frac{\partial \bar{\mu}}{\partial \bar{T}} \bar{W}'' + \frac{\partial^2 \bar{\mu}}{\partial \bar{T}^2} \bar{T}' \bar{W}' \right) \\
a_{86} &= -\frac{1}{\bar{\mu}} \frac{\partial \bar{\mu}}{\partial \bar{T}} \bar{W}' \\
a_{87} &= i\xi \frac{R}{\bar{\mu}\bar{T}} + \alpha^2 + \beta^2 \\
a_{88} &= -\frac{\bar{\mu}'}{\bar{\mu}}
\end{aligned}$$

$$a_{9,10} = \underline{1}$$

$$a_{10,3} = \frac{R\sigma_e}{\bar{k}_v \bar{T}} \bar{c}_{v,v} \bar{T}'$$

$$a_{10,4} = -\frac{R^2 \sigma_e}{\bar{k}_v} \frac{\partial \bar{Q}}{\partial \bar{p}}$$

$$a_{10,5} = \frac{-\frac{R^2 \sigma_e}{\bar{k}_v} \frac{\partial \bar{Q}}{\partial \bar{T}} - \frac{\bar{T}''}{\bar{k}_v} \frac{\partial \bar{k}_v}{\partial \bar{T}} - \frac{\bar{T}'}{\bar{k}_v} \left(\frac{\partial \bar{k}_v}{\partial \bar{T}} \right)'}{\quad}$$

$$a_{10,6} = -\frac{\bar{T}'}{\bar{k}_v} \frac{\partial \bar{k}_v}{\partial \bar{T}}$$

$$a_{10,9} = \alpha^2 + \beta^2 + i\xi \frac{R\sigma_e}{\bar{k}_v \bar{T}} \bar{c}_{v,v} - \frac{R^2 \sigma_e}{\bar{k}_v} \frac{\partial \bar{Q}}{\partial \bar{T}_v} - \frac{\bar{T}''}{\bar{k}_v} \frac{\partial \bar{k}_v}{\partial \bar{T}_v} - \frac{\bar{T}'}{\bar{k}_v} \left(\frac{\partial \bar{k}_v}{\partial \bar{T}_v} \right)'$$

$$a_{10,10} = -\frac{\bar{T}'}{\bar{k}_v} \frac{\partial \bar{k}_v}{\partial \bar{T}_v} - \frac{\bar{k}'_v}{\bar{k}_v}$$

Appendix B

Mean Flow Jacobian

In this section, the elements of the Jacobian matrix used in the non-self-similar boundary layer solver of Section 3.3 are derived. For numerical calculations, it is convenient to re-write the boundary layer equations from Equation 3.15 in the following form:

$$E = 0 = \frac{x}{\Delta x} \left(\bar{U} - \bar{U}^{(k-1)} \frac{\bar{T}}{\bar{T}^{(k-1)}} \right) - \frac{\eta}{2} \frac{\partial \bar{U}}{\partial \eta} + \frac{\partial \bar{V}}{\partial \eta} - \left(\bar{V} - \frac{\eta \bar{U}}{2} \right) \frac{1}{\bar{T}} \frac{\partial \bar{T}}{\partial \eta} \quad (\text{B.1a})$$

$$F = 0 = \frac{\bar{U}x}{\Delta x} (\bar{U} - \bar{U}^{(k-1)}) + \left(\bar{V} - \frac{\eta \bar{U}}{2} \right) \frac{\partial \bar{U}}{\partial \eta} - \bar{T} \left(\bar{\mu} \frac{\partial^2 \bar{U}}{\partial \eta^2} + \frac{\partial \bar{\mu}}{\partial \bar{T}} \frac{\partial \bar{T}}{\partial \eta} \frac{\partial \bar{U}}{\partial \eta} \right) \quad (\text{B.1b})$$

$$G = 0 = \frac{\bar{U}x}{\Delta x} (\bar{T} - \bar{T}^{(k-1)}) + \left(\bar{V} - \frac{\eta \bar{U}}{2} \right) \frac{\partial \bar{T}}{\partial \eta} - \frac{\bar{T}}{\sigma_e} \left(\bar{k} \frac{\partial^2 \bar{T}}{\partial \eta^2} + \frac{\partial \bar{k}}{\partial \bar{T}} \left(\frac{\partial \bar{T}}{\partial \eta} \right)^2 \right) - \bar{T} (\gamma_e - 1) M_e^2 \bar{\mu} \left(\frac{\partial \bar{U}}{\partial \eta} \right)^2 + \bar{T} Re_x \bar{Q} \quad (\text{B.1c})$$

$$H = 0 = \frac{\bar{U} \bar{c}_{v,v} x}{\Delta x} (\bar{T}_v - \bar{T}_v^{(k-1)}) + \bar{c}_{v,v} \left(\bar{V} - \frac{\eta \bar{U}}{2} \right) \frac{\partial \bar{T}_v}{\partial \eta} - \frac{\bar{T}}{\sigma_e} \left(\bar{k}_v \frac{\partial^2 \bar{T}_v}{\partial \eta^2} + \frac{\partial \bar{k}_v}{\partial \bar{T}} \frac{\partial \bar{T}}{\partial \eta} \frac{\partial \bar{T}_v}{\partial \eta} + \frac{\partial \bar{k}_v}{\partial \bar{T}_v} \left(\frac{\partial \bar{T}_v}{\partial \eta} \right)^2 \right) - \bar{T} Re_x \bar{Q} \quad (\text{B.1d})$$

In this equation \bar{V} is the mean vertical velocity, re-scaled using the Reynolds number according to the definition: $\bar{V} \equiv \sqrt{Re_x} \bar{V}$. Terms with superscript $(k-1)$ are

evaluated at the previous location along the boundary layer, whereas all other terms are evaluated at the current location k for which the solution is not yet known. Each of these residuals E , F , G , and H must be driven to zero using Newton iteration in order to determine the solution at streamwise location k .

Suppose that we define a column vector \mathbf{R} that contains the residuals E , F , G , and H defined above as its elements. We also define a vector \mathbf{X} which contains discrete values of the flow variables \bar{V} , \bar{U} , \bar{T} , \bar{T}_v as its elements at the position k along the boundary layer where the solution is sought. One can then drive the residual \mathbf{R} to zero using Newton iteration:

$$\mathbf{J}(\mathbf{X}^{n+1} - \mathbf{X}^n) = -\mathbf{R} \quad (\text{B.2})$$

where n is the current iteration step. In performing these iterations, the elements of the Jacobian matrix \mathbf{J} are required, where

$$J_{ij} = \frac{\partial R_i}{\partial X_j} \quad (\text{B.3})$$

The elements of the Jacobian matrix are provided in the following equations:

Continuity:

$$\frac{\partial E}{\partial \bar{V}} = \mathcal{D} - \frac{\mathcal{D}\bar{T}}{\bar{T}} \quad (\text{B.4a})$$

$$\frac{\partial E}{\partial \bar{U}} = \frac{x}{\Delta x} - \frac{\eta}{2}\mathcal{D} + \frac{\eta}{2}\frac{\mathcal{D}\bar{T}}{\bar{T}} \quad (\text{B.4b})$$

$$\frac{\partial E}{\partial \bar{T}} = -\frac{x}{\Delta x}\frac{\bar{U}^{(k-1)}}{\bar{T}^{(k-1)}} - \left(\bar{V} - \frac{\eta\bar{U}}{2}\right)\left(\frac{\mathcal{D}}{\bar{T}} - \frac{\mathcal{D}\bar{T}}{\bar{T}^2}\right) \quad (\text{B.4c})$$

$$\frac{\partial E}{\partial \bar{T}_v} = 0 \quad (\text{B.4d})$$

X Momentum:

$$\frac{\partial F}{\partial \bar{V}} = \mathcal{D}\bar{U} \quad (\text{B.5a})$$

$$\begin{aligned} \frac{\partial F}{\partial \bar{U}} &= \frac{x}{\Delta x} (2\bar{U} - \bar{U}^{(k-1)}) + \left(\bar{V} - \frac{\eta\bar{U}}{2} \right) \mathcal{D} - \frac{\eta}{2} \mathcal{D}\bar{U} \\ &\quad - \bar{T} \left(\bar{\mu} \mathcal{D}^2 + \frac{\partial \bar{\mu}}{\partial T} \mathcal{D}\bar{T} \mathcal{D} \right) \end{aligned} \quad (\text{B.5b})$$

$$\begin{aligned} \frac{\partial F}{\partial \bar{T}} &= - \left(\bar{\mu} \mathcal{D}^2 \bar{U} + \frac{\partial \bar{\mu}}{\partial \bar{T}} \frac{\partial \bar{T}}{\partial \eta} \frac{\partial \bar{U}}{\partial \eta} \right) \\ &\quad - \bar{T} \left(\frac{\partial \mu}{\partial T} \mathcal{D}^2 \bar{U} + \frac{\partial \bar{\mu}}{\partial T} \frac{\partial \bar{U}}{\partial \eta} \mathcal{D} + \frac{\partial^2 \bar{\mu}}{\partial T^2} \mathcal{D}\bar{T} \mathcal{D}\bar{U} \right) \end{aligned} \quad (\text{B.5c})$$

$$\frac{\partial F}{\partial \bar{T}_v} = 0 \quad (\text{B.5d})$$

Energy:

$$\frac{\partial G}{\partial \bar{V}} = \mathcal{D}\bar{T} \quad (\text{B.6a})$$

$$\frac{\partial G}{\partial \bar{U}} = \frac{x}{\Delta x} (\bar{T} - \bar{T}^{(k-1)}) - \frac{\eta}{2} \mathcal{D}\bar{T} - 2\bar{T}(\gamma_e - 1)M_e^2 \bar{\mu} \mathcal{D}\bar{U} \mathcal{D} \quad (\text{B.6b})$$

$$\begin{aligned} \frac{\partial G}{\partial \bar{T}} &= \frac{x\bar{U}}{\Delta x} + \left(\bar{V} - \frac{\eta\bar{U}}{2} \right) \mathcal{D} - \frac{1}{\sigma_e} \left(\bar{k} \mathcal{D}^2 \bar{T} + \frac{\partial \bar{k}}{\partial T} (\mathcal{D}\bar{T})^2 \right) \\ &\quad - \frac{\bar{T}}{\sigma_e} \left(\bar{k} \mathcal{D}^2 + \frac{\partial \bar{k}}{\partial T} \mathcal{D}^2 \bar{T} + \frac{\partial^2 \bar{k}}{\partial T^2} (\mathcal{D}\bar{T})^2 + 2 \frac{\partial \bar{k}}{\partial T} \mathcal{D}\bar{T} \mathcal{D} \right) \\ &\quad - (\gamma_e - 1)M_e^2 (\mathcal{D}\bar{U})^2 \left(\bar{\mu} + \bar{T} \frac{\partial \bar{\mu}}{\partial T} \right) + Re_x \bar{Q} + Re_x \bar{T} \frac{\partial \bar{Q}}{\partial T} \end{aligned} \quad (\text{B.6c})$$

$$\frac{\partial G}{\partial \bar{T}_v} = \bar{T} Re_x \frac{\partial Q}{\partial T_v} \quad (\text{B.6d})$$

Vibrational Energy:

$$\frac{\partial H}{\partial \bar{V}} = \bar{c}_{v,v} \mathcal{D} \bar{T}_v \quad (\text{B.7a})$$

$$\frac{\partial H}{\partial \bar{U}} = \frac{\bar{c}_{v,v} x}{\Delta x} (\bar{T}_v - \bar{T}_v^{(k-1)}) - \bar{c}_{v,v} \frac{\eta}{2} \mathcal{D} \bar{T}_v \quad (\text{B.7b})$$

$$\begin{aligned} \frac{\partial H}{\partial \bar{T}} = & -\frac{1}{\sigma_e} \left(\bar{k}_v \mathcal{D}^2 \bar{T}_v + \frac{\partial \bar{k}_v}{\partial T} \mathcal{D} \bar{T} \mathcal{D} \bar{T}_v + \frac{\partial \bar{k}_v}{\partial T_v} (\mathcal{D} \bar{T}_v)^2 \right) \\ & - \frac{\bar{T}}{\sigma_e} \left(\frac{\partial \bar{k}_v}{\partial T} \mathcal{D}^2 \bar{T}_v + \frac{\partial^2 \bar{k}_v}{\partial T^2} \mathcal{D} \bar{T} \mathcal{D} \bar{T}_v + \frac{\partial \bar{k}_v}{\partial T} \mathcal{D} \bar{T}_v \mathcal{D} + \frac{\partial^2 \bar{k}_v}{\partial T \partial T_v} (\mathcal{D} \bar{T}_v)^2 \right) \\ & - Re_x \bar{Q} - \bar{T} Re_x \frac{\partial \bar{Q}}{\partial \bar{T}} \end{aligned} \quad (\text{B.7c})$$

$$\begin{aligned} \frac{\partial H}{\partial \bar{T}_v} = & \frac{\bar{U} \bar{c}_{v,v} x}{\Delta x} + \frac{\bar{U} x}{\Delta x} \frac{\partial \bar{c}_{v,v}}{\partial T_v} (\bar{T}_v - \bar{T}_v^{(k-1)}) \\ & + \left(\bar{V} - \frac{\eta \bar{U}}{2} \right) \left(\frac{\partial \bar{c}_{v,v}}{\partial T_v} \mathcal{D} \bar{T}_v + \bar{c}_{v,v} \mathcal{D} \right) \\ & - \frac{\bar{T}}{\sigma_e} \left(\bar{k}_v \mathcal{D}^2 + \frac{\partial \bar{k}_v}{\partial T} \mathcal{D} \bar{T} \mathcal{D} + 2 \frac{\partial \bar{k}_v}{\partial T_v} \mathcal{D} \bar{T}_v \mathcal{D} + \frac{\partial \bar{k}_v}{\partial T_v} \mathcal{D}^2 \bar{T}_v \right. \\ & \quad \left. + \frac{\partial^2 \bar{k}_v}{\partial T \partial T_v} \mathcal{D} \bar{T} \mathcal{D} \bar{T}_v + \frac{\partial^2 \bar{k}_v}{\partial T_v^2} (\mathcal{D} \bar{T}_v)^2 \right) \\ & - \bar{T} Re_x \frac{\partial Q}{\partial T_v} \end{aligned} \quad (\text{B.7d})$$

In these equations, \mathcal{D} designates the wallnormal differentiation operator, which is carried out using fourth order finite differences. In performing the updates described by Equation B.2, the solution vector \mathbf{X} must also respect the boundary conditions. This is enforced by replacing the rows of \mathbf{J} and \mathbf{R} with the appropriate boundary conditions:

No Slip Velocity:

$$\bar{V}(0) = 0 \quad (\text{B.8})$$

$$\bar{U}(0) = 0 \quad (\text{B.9})$$

Freestream Conditions:

$$\bar{U}(y_{max}) = 1 \quad (\text{B.10})$$

$$\bar{T}(y_{max}) = 1 \quad (\text{B.11})$$

$$\bar{T}_v(y_{max}) = T_{v,e}^*/T_e^* \quad (\text{B.12})$$

Isothermal Wall:

$$\bar{T}(0) = T_w \quad (\text{B.13})$$

$$\bar{T}_v(0) = T_w \quad (\text{B.14})$$

Adiabatic Wall:

$$\bar{k} \frac{\partial \bar{T}}{\partial y} \Big|_{y=0} + \bar{k}_v \frac{\partial \bar{T}_v}{\partial y} \Big|_{y=0} = 0 \quad (\text{B.15})$$

$$\bar{T}(0) - \bar{T}_v(0) = 0 \quad (\text{B.16})$$

Appendix C

Multiple-Scales Model

In this section, the equations of motion and adjoint boundary conditions are derived for the analysis described in Section 7.10.

C.1 Governing equations

The flow is modeled as a calorically perfect ideal gas, for which the compressible Navier-Stokes equations can be written in the form:

$$\frac{D\rho}{Dt} + \rho \nabla \cdot \mathbf{u} = 0 \quad (\text{C.1a})$$

$$\rho \frac{D\mathbf{u}}{Dt} + \frac{1}{\gamma M^2} \nabla(\rho T) = \frac{1}{Re_L} \nabla \cdot \boldsymbol{\tau} \quad (\text{C.1b})$$

$$\rho \frac{DT}{Dt} + (\gamma - 1)(\rho T) \nabla \cdot \mathbf{u} = \frac{\gamma(\gamma - 1)M^2}{Re_L} \nabla \mathbf{u} : \boldsymbol{\tau} - \frac{\gamma}{\sigma Re_L} \nabla \cdot \mathbf{q} \quad (\text{C.1c})$$

These equations are nondimensionalized using the scheme from Equation 2.13, and the pressure has been eliminated using the equation of state $\gamma M^2 p = \rho T$. After linearization about a time-averaged base flow, one reaches

$$\frac{\partial \tilde{\rho}}{\partial t} + \bar{U} \frac{\partial \tilde{\rho}}{\partial x} + \bar{V} \frac{\partial \tilde{\rho}}{\partial y} + \tilde{u} \frac{\partial \bar{\rho}}{\partial x} + \tilde{v} \frac{\partial \bar{\rho}}{\partial y} + \bar{\rho} \left(\frac{\partial \tilde{u}}{\partial x} + \frac{\partial \tilde{v}}{\partial y} \right) + \tilde{\rho} \left(\frac{\partial \bar{U}}{\partial x} + \frac{\partial \bar{V}}{\partial y} \right) = 0 \quad (\text{C.2a})$$

$$\begin{aligned} & \left(\frac{\partial \tilde{u}}{\partial t} + \bar{U} \frac{\partial \tilde{u}}{\partial x} + \bar{V} \frac{\partial \tilde{u}}{\partial y} + \tilde{u} \frac{\partial \bar{U}}{\partial x} + \tilde{v} \frac{\partial \bar{U}}{\partial y} \right) + \tilde{\rho} \bar{T} \left(\bar{U} \frac{\partial \bar{U}}{\partial x} + \bar{V} \frac{\partial \bar{U}}{\partial y} \right) \\ & + \frac{1}{\gamma M^2} \left(\tilde{\rho} \bar{T} - \frac{\tilde{\theta}}{\bar{T}} \right) \frac{\partial \bar{T}}{\partial x} + \frac{1}{\gamma M^2} \left(\bar{T}^2 \frac{\partial \tilde{\rho}}{\partial x} + \frac{\partial \tilde{\theta}}{\partial x} \right) - \frac{\bar{T}}{Re_L} \left(\frac{\partial \tilde{\tau}_{xx}}{\partial x} + \frac{\partial \tilde{\tau}_{xy}}{\partial y} \right) = 0 \quad (\text{C.2b}) \end{aligned}$$

$$\left(\frac{\partial \tilde{v}}{\partial t} + \bar{U} \frac{\partial \tilde{v}}{\partial x} + \bar{V} \frac{\partial \tilde{v}}{\partial y} + \tilde{u} \frac{\partial \bar{V}}{\partial x} + \tilde{v} \frac{\partial \bar{V}}{\partial y}\right) + \tilde{\rho} \bar{T} \left(\bar{U} \frac{\partial \bar{V}}{\partial x} + \bar{V} \frac{\partial \bar{V}}{\partial y}\right) + \frac{1}{\gamma M^2} \left(\tilde{\rho} \bar{T} - \frac{\tilde{\theta}}{\bar{T}}\right) \frac{\partial \bar{T}}{\partial y} + \frac{1}{\gamma M^2} \left(\bar{T}^2 \frac{\partial \tilde{\rho}}{\partial y} + \frac{\partial \tilde{\theta}}{\partial y}\right) - \frac{\bar{T}}{Re_L} \left(\frac{\partial \tilde{\tau}_{yx}}{\partial x} + \frac{\partial \tilde{\tau}_{yy}}{\partial y}\right) = 0 \quad (\text{C.2c})$$

$$\left(\frac{\partial \tilde{\theta}}{\partial t} + \bar{U} \frac{\partial \tilde{\theta}}{\partial x} + \bar{V} \frac{\partial \tilde{\theta}}{\partial y} + \tilde{u} \frac{\partial \bar{T}}{\partial x} + \tilde{v} \frac{\partial \bar{T}}{\partial y}\right) + \tilde{\rho} \bar{T} \left(\bar{U} \frac{\partial \bar{T}}{\partial x} + \bar{V} \frac{\partial \bar{T}}{\partial y}\right) + (\gamma - 1) \bar{T} \left(\frac{\partial \tilde{u}}{\partial x} + \frac{\partial \tilde{v}}{\partial y}\right) + (\gamma - 1) (\tilde{\rho} \bar{T}^2 + \tilde{\theta}) \left(\frac{\partial \bar{U}}{\partial x} + \frac{\partial \bar{V}}{\partial y}\right) - \frac{\gamma(\gamma - 1) M^2 \bar{T}}{Re_L} \left(\tilde{\tau}_{ij} \frac{\partial \tilde{u}_i}{\partial x_j} + \tilde{\tau}_{ij} \frac{\partial \bar{U}_i}{\partial x_j}\right) + \frac{\gamma \bar{T}}{\sigma Re_L} \left(\frac{\partial \tilde{q}_x}{\partial x} + \frac{\partial \tilde{q}_y}{\partial y}\right) = 0 \quad (\text{C.2d})$$

In these equations bars are used to denote the time-averaged base flow and tildes designate small amplitude fluctuations. These equations of motion are supplemented by the definitions of the fluctuating shear stresses and heat fluxes:

$$\tilde{\tau}_{xx} = \bar{\mu} \left[(2+r) \frac{\partial \tilde{u}}{\partial x} + r \frac{\partial \tilde{v}}{\partial y} \right] + \left[(2+r) \frac{\partial \bar{U}}{\partial x} + r \frac{\partial \bar{V}}{\partial y} \right] \frac{\partial \bar{\mu}}{\partial \bar{T}} \tilde{\theta} \quad (\text{C.3a})$$

$$\tau_{xy} = \bar{\mu} \left[\frac{\partial \tilde{u}}{\partial y} + \frac{\partial \tilde{v}}{\partial x} \right] + \left[\frac{\partial \bar{U}}{\partial y} + \frac{\partial \bar{V}}{\partial x} \right] \frac{\partial \bar{\mu}}{\partial \bar{T}} \tilde{\theta} \quad (\text{C.3b})$$

$$\tilde{\tau}_{yy} = \bar{\mu} \left[(2+r) \frac{\partial \tilde{v}}{\partial y} + r \frac{\partial \tilde{u}}{\partial x} \right] + \left[(2+r) \frac{\partial \bar{V}}{\partial y} + r \frac{\partial \bar{U}}{\partial x} \right] \frac{\partial \bar{\mu}}{\partial \bar{T}} \tilde{\theta} \quad (\text{C.3c})$$

$$\tilde{q}_x = -\bar{k} \frac{\partial \tilde{\theta}}{\partial x} - \frac{\partial \bar{k}}{\partial \bar{T}} \frac{\partial \bar{T}}{\partial x} \tilde{\theta} \quad (\text{C.3d})$$

$$\tilde{q}_y = -\bar{k} \frac{\partial \tilde{\theta}}{\partial y} - \frac{\partial \bar{k}}{\partial \bar{T}} \frac{\partial \bar{T}}{\partial y} \tilde{\theta} \quad (\text{C.3e})$$

where r is the ratio of the bulk viscosity to the shear viscosity, which is assumed to be constant. This system of equations can be written compactly in the form:

$$\mathbf{A}_t \frac{\partial \tilde{\mathbf{q}}}{\partial t} + \mathbf{A}_x \frac{\partial \tilde{\mathbf{q}}}{\partial x} + \mathbf{A}_y \frac{\partial \tilde{\mathbf{q}}}{\partial y} + \mathbf{A}_o \tilde{\mathbf{q}} = 0 \quad (\text{C.4})$$

where $\tilde{\mathbf{q}}$ is the vector of disturbance variables given by

$$\tilde{\mathbf{q}} = \left(\tilde{\rho}, \tilde{u}, \tilde{v}, \tilde{\theta}, \tilde{\tau}_{xx}, \tilde{\tau}_{xy}, \tilde{\tau}_{yy}, \tilde{q}_x, \tilde{q}_y \right)^T \quad (\text{C.5})$$

As written, this system of equations remains fully non-parallel. The non-zero elements of these matrices are:

Matrix \mathbf{A}_t :

$$A_{t,11} = 1$$

$$A_{t,22} = 1$$

$$A_{t,33} = 1$$

$$A_{t,44} = 1$$

Matrix \mathbf{A}_x :

$$A_{x,11} = \bar{U}$$

$$A_{x,12} = \bar{\rho}$$

$$A_{x,21} = \frac{\bar{T}^2}{\gamma M^2}$$

$$A_{x,22} = \bar{U}$$

$$A_{x,24} = \frac{1}{\gamma M^2}$$

$$A_{x,25} = -\frac{\bar{T}}{Re_L}$$

$$A_{x,33} = \bar{U}$$

$$A_{x,36} = -\frac{\bar{T}}{Re_L}$$

$$A_{x,42} = (\gamma - 1)\bar{T} - K\bar{\tau}_{xx}$$

$$A_{x,43} = -K\bar{\tau}_{xy}$$

$$A_{x,44} = \bar{U}$$

$$A_{x,48} = \frac{\gamma \bar{T}}{\sigma Re_L}$$

$$A_{x,52} = (2 + r)\bar{\mu}$$

$$A_{x,63} = \bar{\mu}$$

$$A_{x,72} = r\bar{\mu}$$

$$A_{x,84} = -\bar{k}$$

Matrix \mathbf{A}_y :

$$A_{y,11} = \bar{V}$$

$$A_{y,13} = \bar{\rho}$$

$$A_{y,22} = \bar{V}$$

$$A_{y,26} = -\frac{\bar{T}}{Re_L}$$

$$A_{y,31} = \frac{\bar{T}^2}{\gamma M^2}$$

$$A_{y,33} = \bar{V}$$

$$A_{y,34} = \frac{1}{\gamma M^2}$$

$$A_{y,37} = -\frac{\bar{T}}{Re_L}$$

$$A_{y,42} = -\bar{K}\bar{\tau}_{xy}$$

$$A_{y,43} = (\gamma - 1)\bar{T} - K\bar{\tau}_{yy}$$

$$A_{y,44} = \bar{V}$$

$$A_{y,49} = \frac{\gamma \bar{T}}{\sigma Re_L}$$

$$A_{y,53} = r\bar{\mu}$$

$$A_{y,62} = \bar{\mu}$$

$$A_{y,73} = (2 + r)\bar{\mu}$$

$$A_{y,94} = -\bar{k}$$

Matrix \mathbf{A}_o :

$$A_{o,11} = \frac{\partial \bar{U}}{\partial x} + \frac{\partial \bar{V}}{\partial y}$$

$$A_{o,12} = \frac{\partial \bar{\rho}}{\partial x}$$

$$A_{o,13} = \frac{\partial \bar{\rho}}{\partial y}$$

$$A_{o,21} = \bar{T} \left(\bar{U} \frac{\partial \bar{U}}{\partial x} + \bar{V} \frac{\partial \bar{U}}{\partial y} \right) + \frac{\bar{T}}{\gamma M^2} \frac{\partial \bar{T}}{\partial x}$$

$$A_{o,22} = \frac{\partial \bar{U}}{\partial x}$$

$$A_{o,23} = \frac{\partial \bar{U}}{\partial y}$$

$$A_{o,24} = -\frac{1}{\gamma M^2 \bar{T}} \frac{\partial \bar{T}}{\partial x}$$

$$A_{o,31} = \bar{T} \left(\bar{U} \frac{\partial \bar{V}}{\partial x} + \bar{V} \frac{\partial \bar{V}}{\partial y} \right) + \frac{\bar{T}}{\gamma M^2} \frac{\partial \bar{T}}{\partial y}$$

$$A_{o,32} = \frac{\partial \bar{V}}{\partial x}$$

$$A_{o,33} = \frac{\partial \bar{V}}{\partial y}$$

$$A_{o,34} = -\frac{1}{\gamma M^2 \bar{T}} \frac{\partial \bar{T}}{\partial y}$$

$$A_{o,41} = \bar{T} \left(\bar{U} \frac{\partial \bar{T}}{\partial x} + \bar{V} \frac{\partial \bar{T}}{\partial y} \right) + \bar{T}^2 (\gamma - 1) (\nabla \cdot \vec{U})$$

$$A_{o,42} = \frac{\partial \bar{T}}{\partial x}$$

$$A_{o,43} = \frac{\partial \bar{T}}{\partial y}$$

$$A_{o,44} = (\gamma - 1) (\nabla \cdot \vec{U})$$

$$A_{o,45} = -K \frac{\partial \bar{U}}{\partial x}$$

$$A_{o,46} = -K \left(\frac{\partial \bar{V}}{\partial x} + \frac{\partial \bar{U}}{\partial y} \right)$$

$$A_{o,47} = -K \frac{\partial \bar{V}}{\partial y}$$

$$A_{o,54} = \frac{\partial \bar{\mu}}{\partial T} \left((2+r) \frac{\partial \bar{U}}{\partial x} + r \frac{\partial \bar{V}}{\partial y} \right)$$

$$A_{o,55} = -1$$

$$A_{o,64} = \frac{\partial \bar{\mu}}{\partial T} \left(\frac{\partial \bar{U}}{\partial y} + \frac{\partial \bar{V}}{\partial x} \right)$$

$$A_{o,66} = -1$$

$$A_{o,74} = \frac{\partial \bar{\mu}}{\partial T} \left((2+r) \frac{\partial \bar{V}}{\partial y} + r \frac{\partial \bar{U}}{\partial x} \right)$$

$$A_{o,77} = -1$$

$$A_{o,84} = -\frac{\partial \bar{k}}{\partial T} \frac{\partial \bar{T}}{\partial x}$$

$$A_{o,88} = -1$$

$$A_{o,94} = -\frac{\partial \bar{k}}{\partial T} \frac{\partial \bar{T}}{\partial y}$$

$$A_{o,99} = -1$$

where

$$K = \frac{\gamma(\gamma - 1)M^2 \bar{T}}{Re_L} \tag{C.6}$$

$$\bar{\tau}_{xx} = \bar{\mu} \left((2+r) \frac{\partial \bar{U}}{\partial x} + r \frac{\partial \bar{V}}{\partial y} \right) \tag{C.7}$$

$$\bar{\tau}_{yy} = \bar{\mu} \left((2+r) \frac{\partial \bar{V}}{\partial y} + r \frac{\partial \bar{U}}{\partial x} \right) \tag{C.8}$$

$$\bar{\tau}_{xy} = \bar{\mu} \left(\frac{\partial \bar{U}}{\partial y} + \frac{\partial \bar{V}}{\partial x} \right) \tag{C.9}$$

C.2 Adjoint Boundary Conditions

The boundary conditions of the adjoint problem (Eq. 7.47) must be selected such that the boundary terms of Equation 7.46 are zero:

$$\mathbf{q}^{+H} \mathbf{A}_y \mathbf{q} \Big|_{y=0}^{\infty} = 0 \quad (\text{C.10})$$

In matrix form, the matrix \mathbf{A}_y is:

$$\mathbf{A}_y = \begin{bmatrix} \bar{V} & 0 & \bar{\rho} & 0 & 0 & 0 & 0 & 0 & 0 \\ 0 & \bar{V} & 0 & 0 & 0 & -\frac{\bar{T}}{Re_L} & 0 & 0 & 0 \\ \frac{\bar{T}^2}{\gamma M^2} & 0 & \bar{V} & \frac{1}{\gamma M^2} & 0 & 0 & -\frac{\bar{T}}{Re_L} & 0 & 0 \\ 0 & -K\bar{\tau}_{xy} & (\gamma - 1)\bar{T} - K\bar{\tau}_{yy} & \bar{V} & 0 & 0 & 0 & 0 & \frac{\gamma\bar{T}}{\sigma Re_L} \\ 0 & 0 & r\bar{\mu} & 0 & 0 & 0 & 0 & 0 & 0 \\ 0 & \bar{\mu} & 0 & 0 & 0 & 0 & 0 & 0 & 0 \\ 0 & 0 & (2+r)\bar{\mu} & 0 & 0 & 0 & 0 & 0 & 0 \\ 0 & 0 & 0 & 0 & 0 & 0 & 0 & 0 & 0 \\ 0 & 0 & 0 & -\bar{k} & 0 & 0 & 0 & 0 & 0 \end{bmatrix} \quad (\text{C.11})$$

After multiplying out the boundary product (C.10), assuming decaying disturbances as $y \rightarrow \infty$, and assuming no-slip conditions $\tilde{u}(0) = \tilde{v}(0) = 0$ for the direct problem,

one finds

$$\left(\tilde{\rho}^{+*}, \tilde{u}^{+*}, \tilde{v}^{+*}, \tilde{\theta}^{+*}, \tilde{\tau}_{xx}^{+*}, \tilde{\tau}_{xy}^{+*}, \tilde{\tau}_{yy}^{+*}, \tilde{q}_x^{+*}, \tilde{q}_y^{+*} \right) \begin{pmatrix} 0 \\ -\frac{\bar{T}}{Re_L} \tilde{\tau}_{xy} \\ \frac{\bar{T}^2}{\gamma M^2} \tilde{\rho} + \frac{\tilde{\theta}}{\gamma} M^2 - \frac{\bar{T}}{Re_L} \tilde{\tau}_{yy} \\ \frac{\gamma \bar{T}}{\sigma Re_L} \tilde{q}_y \\ 0 \\ 0 \\ 0 \\ 0 \\ -\bar{k} \tilde{\theta} \end{pmatrix}_{y=0} = 0 \quad (\text{C.12})$$

which evaluates to

$$-\frac{\bar{T}}{Re_L} \tilde{\tau}_{xy} \tilde{u}^{+*} + \left[\frac{\bar{T}^2}{\gamma M^2} \tilde{\rho} + \frac{\tilde{\theta}}{\gamma} M^2 - \frac{\bar{T}}{Re_L} \tilde{\tau}_{yy} \right] \tilde{v}^{+*} + \frac{\gamma \bar{T}}{\sigma Re_L} \tilde{q}_y \tilde{\theta}^{+*} - \bar{k} \tilde{\theta} \tilde{q}_y^{+*} = 0 \quad (\text{C.13})$$

The adjoint boundary conditions are selected such that each of these terms is zero.

The result is:

Isothermal disturbances, $\tilde{\theta}(0) = 0$:

$$\tilde{u}^+ = \tilde{v}^+ = \tilde{\theta}^+ = 0 \quad y = 0 \quad (\text{C.14})$$

Adiabatic disturbances, $\tilde{q}_y(0) = 0$:

$$\tilde{u}^+ = \tilde{v}^+ = \tilde{q}_y^+ = 0 \quad y = 0 \quad (\text{C.15})$$

Thus the adjoint boundary conditions are exactly the same as those of the direct problem.